Title
Design Strategies for Controlling Optoelectronic Properties and Solid-State Order of Conjugated Materials in Organic Photovoltaics

Author
Lee, Olivia Pei-Hua

Publication Date
2013

Peer reviewed|Thesis/dissertation

Design Strategies for Controlling Optoelectronic Properties and Solid-State Order of Conjugated Materials in Organic Photovoltaics

by

Olivia Pei-Hua Lee

A dissertation submitted in partial satisfaction of the

requirements for the degree of

Doctor of Philosophy

in

Chemistry

in the

Graduate Division

of the

University of California, Berkeley

Committee in Charge:
Professor Jean M. J. Fréchet, Chair
Professor T. Don Tilley
Professor Alex Zettl

Fall 2013

Design Strategies for Controlling Optoelectronic Properties and Solid-State Order of Conjugated Materials in Organic Photovoltaics

by

Olivia Pei-Hua Lee

ABSTRACT

Design Strategies for Controlling Optoelectronic Properties and Solid-State Order of Conjugated Materials in Organic Photovoltaics

by

Olivia Pei-Hua Lee

Doctor of Philosophy in Chemistry

University of California, Berkeley

Professor Jean M. J. Fréchet, Chair

Organic photovoltaics (OPVs) have emerged as an alternative technology to current silicon-based systems for harvesting solar energy. The solution-processability of conjugated materials offers the potential for scalable, low-cost production of lightweight, flexible solar cells. In particular, OPVs containing a bulk-heterojunction (BHJ) architecture, where electron-donors and electron-acceptors form an interpenetrating network within the device active layer, have demonstrated high solar cell performance. The active layer components serve a crucial role in light absorption, charge generation and carrier transport. Through synthetic design and device characterization, this work focuses on elucidating design strategies and principles for the development of high-performing electron-donors for OPVs.

Molecular packing parameters of conjugated materials can strongly impact charge transport in the solid state. With a model polymer backbone containing thiophene comonomers, it was shown that strategic substitution of furan for thiophene improved material solubility and allowed for the use of linear alkyl side chains to reduce insulating contents in devices. These structural modifications yielded polymers with sufficient solubility, favorable solid-state morphology, enhanced long-range packing order, and efficient OPV performance. In a separate study, conjugated small molecules were functionalized with symmetric, planar end-groups so that they could self-assemble and form an interpenetrating network with electron-acceptors in the active layer. This investigation demonstrates that directing self-assembly via end-groups is an effective strategy to enhance molecular interconnectivity and improve the performance of molecular semiconductors in organic solar cells.

Alongside solid-state morphology, semiconducting materials need to exhibit optical and electronic properties that enable effective light absorption and charge generation in solar cells. We showed that incorporating antiaromatic units into conjugated molecules effectively redshifted and broadened absorption to cover a significant portion of the visible spectrum. The impact of atomic substitution on optoelectronics was also explored with the design of an electron-poor monomer, oxadiazolopyridine, which yielded efficient OPV materials upon copolymerization with electron-donors. Furthermore, gold and silver nanoparticles were embedded in one of the device interlayers to enhance light absorption *via* surface plasmon resonance, improving OPV performance.

Finally, influence of chemical structures on photoexcited charge transfer processes was investigated in a system containing organic electron-donors and inorganic electron-acceptor. Characterization by femtosecond-stimulated Raman spectroscopy provided information on electron transfer dynamics and molecular structural changes in the excited state. The results revealed that organic molecules containing *trans*-double bonds could isomerize into *cis*-double bonds upon photoexcitation, subsequently decreasing charge separation and device efficiency.

TABLE OF CONTENTS

Dedication ..... **v**

Acknowledgements ..... **vi**

Chapter I. An Overview of Bulk-Heterojunction Organic Photovoltaics **1**

1.1. Background and Motivation 2
1.2. Device Configurations of Organic Solar Cells 3
1.2.1. Bilayer (Lamellar) Devices 4
1.2.2. Bulk-Heterojunction Devices 4
1.3. Operation and Performance of Organic Photovoltaics 5
1.3.1. Elementary steps for photocurrent generation 5
1.3.2. Quantification of Photovoltaic Performance 8
1.4. The Active Layer: Conjugated Materials for OPVs 10
1.4.1. Band Structure of Organic Semiconducting Materials 10
1.4.2. Basic Design Criteria and Characterization Methods of OPV Active Layer Materials 11
1.4.3. An Overview of Conjugated Polymers and Small Molecules 14
1.5. Approaches for Modulating Optical and Electronic Properties of Conjugated Materials 17
1.5.1. Donor-Acceptor Approach: Functionality/Substituent Effects 17
1.5.2. Competing Aromaticity 19
1.5.3. Sterics 21
1.6. Strategies for Controlling Nanostructural Order of the OPV Active Layer and Impact on Device Performance 21
1.7. Dissertation Overview 22
1.8. References 23

Chapter II. Controlling Solubility and Thin-Film Nanostructural Order of Diketopyrrolopyrrole (DPP)-Furan Polymers via Furan Incorporation and Side-Chain Modulation **31**

2.1. Introduction: Viability of Furan as a Building Block for Conjugated Materials 32
2.2. Solubility Enhancement through the Incorporation of Furan into Polymer Backbones 33
2.2.1. Design and Synthesis of Furan-Containing Diketopyrrolopyrrole Polymers 34
2.2.2. Effects on Polymer Optoelectronics When Substituting Furan for Thiophene 34
2.3. Incorporation of Furan Comonomers Allows for the Use of Linear Side Chains 35
2.3.1. Exploiting Solubility Enhancement from the Alternating Furan-Thiophene Motif 35

2.3.2. Synthesis and Optoelectronics of Polymers Functionalized with Linear Alkyl Groups 36
2.3.3. Solar Cell Testing and Performance 38
2.3.4. Surface Morphology of Thin Films 39
2.4. The Use of Linear Side Chains Improves Polymer Long-Range Order in Thin Films 39
2.4.1. π-π Stacking Distances between the Polymer Backbones 39
2.4.2. Polymer Long-Range Order by Determination of Correlation Lengths 42
2.5. Conclusion 43
2.6. Experimental 43
2.6.1. Synthetic Details 43
2.6.2. Organic Photovoltaic Device Fabrication and Mobility Measurements 54
2.6.3. Instrumentation for Characterization of Optoelectronic Properties and Active Layer Morphology 56
2.7. References 57

Chapter III. Enhancing Intermolecular Connectivity of Conjugated Small Molecules via Pyrene-Directed Self-Assembly 61
3.1. Introduction: Improving Interconnectivity of Conjugated Small Molecules 62
3.2. Molecular Design: End-Group-Facilitated Self-Assembly via π-π Interactions 62
3.3. Results and Discussion 63
3.3.1. Synthesis and Optoelectronic Properties 63
3.3.2. Photovoltaic Performance and Mobility Measurements 65
3.3.3. Active Layer Morphology 68
3.3.4. Effect of Thermal Annealing on the Solar Cell Performance of DPP-C2-Pyrene 69
3.4. Determination of Small Molecule Packing by Single Crystal X-ray Diffraction 70
3.5. Conclusion 71
3.6. Experimental 71
3.6.1. Synthetic Details 71
3.6.2. UV-visible Absorption and Cyclic Voltammetry 79
3.6.3. Organic Solar Cell Fabrication, Performance Testing and Mobility Measurements 80
3.6.4. Morphology and Crystal Packing by AFM, GIXS and Single-Crystal X-Ray Diffraction 81
3.7. References 81

Chapter IV. Antiaromatic Pentalenes in Conjugated Small Molecules 85
4.1. Introduction: Tuning Band Gaps of Conjugate Materials via Antiaromaticity 86
4.2. Synthesis and Characterization of Pentalenodithiophene 87

4.2.1. Design and Theoretical Calculations of Pentalenodithiophene Small Molecules 87
4.2.2. Synthesis of Pentalenodithiophene Small Molecules 89
4.2.3. Optical and Electrochemical Properties of Pentalenodithiophene 92
4.3. Conclusion 93
4.4. Experimental 94
4.4.1. Synthetic Details 94
4.4.2. Optical and Electrochemical Characterization 105
4.4.3. Acquisition and Analysis of Single-Crystal X-Ray Diffraction 105
4.5. References 111

Chapter V. Ester-Functionalized Oxadiazolopyridine (ODP) as an Electron-Deficient Comonomer in Semiconducting Polymers for Efficient Organic Solar Cells 113
5.1. Introduction: Development of New Building Blocks via Atomic Substitution 114
5.2. Molecular Designs, Synthesis and Optoelectronic Characterization 116
5.2.1. Choice of Electron-Rich Comonomer and Material Synthesis 116
5.2.2. Assessment of Molecular Geometry by DFT Calculations 117
5.2.3. Electrochemical and Optical Characterization 119
5.3. Solar Cell Performance 120
5.4. Plasmon-Enhanced OPV Device Performance—Preliminary Results 122
5.5. Conclusion 123
5.6. Experimental 124
5.6.1. Synthetic Materials and Methods 124
5.6.2. Monomer Syntheses and Characterization 124
5.6.3. Polymer Syntheses 129
5.6.4. OPV Device Fabrication 132
5.6.5. Characterization by UV-vis spectroscopy and Cyclic Voltammetry 133
5.7. References 133

Chapter VI. Electron Transfer Dynamics of Triphenylamine Dyes Bound to TiO_2 Nanoparticles from Femtosecond Stimulated Raman Spectroscopy (FSRS) 137
6.1. Introduction: Photoexcited Electron Transfer at the Organic/Inorganic Interface 138
6.2. Design and Synthesis of Metal-Free Organic Dyes and Dye-TiO_2 Conjugates 139
6.3. Results 141
6.3.1. Ground-State UV-Visible Absorption 141
6.3.2. Transient Absorption 142
6.3.3. Transient Stimulated Raman Spectra of TPAC1 and TPAC2 145
6.3.4. Transient Stimulated Raman Spectra of TPAC3 149
6.4. Discussion 152

6.4.1. Analysis of the Kinetic Data from Transient Absorption and FSRS 152
6.4.2. Comparison of Excited State Kinetics between TPAC3 and trans-Stilbene 152
6.4.3. Proposed Model for Charge Transfer Dynamics at the Metal-Free Dye/TiO_2 Interface 153
6.5. Conclusion 154
6.6. Experimental 154
6.6.1. TPAC Syntheses 154
6.6.2. Femtosecond Stimulated Raman Spectroscopy 160
6.7. References 162

To Mommy and Daddy
for
their unconditional support and infinite patience,
and for giving me all the love in the world

AND

To Uncle Jimmy
for
inspiring me to pursue scientific research

ACKNOWLEDGEMENTS

The Chemistry Department at Berkeley has been my home away from home for the last four years. There was a great deal of camaraderie among the students (see the 2012 Holiday Party "Call Me Maybe" parody), and the faculty has provided me with so much support and encouragement. While graduate school is not made up of rainbows and butterflies, my Berkeley experience has been an amazing journey because of my research group, friends, and family. I owe so much of my growth and accomplishments to them, and my time at Berkeley would have been so dramatically different without them.

First and foremost, I whole-heatedly thank Professor Jean Fréchet for his guidance and support, and for being an exceptionally inspirational mentor. Under his direction and with the freedom that he has given us, I have learned to be an independent, self-motivated chemist capable of communicating and collaborating with scientists from different fields. I truly respect his high standards for scientific integrity and excellence, and as an advisor, he is sensible, encouraging, and inspiring. While I only caught a small glimpse of his wisdom in each of our conversations, I always felt that I learned so much just by talking to him. As I move on in life, his advice will always stay with me: work hard, play hard.

I also acknowledge my thesis and qualifying exam committee members: Professors T. Don Tilley, Ting Xu, Alex Zettl, and Miquel Salmeron. I especially want to thank Don for his guidance and encouragement. Ting has been extremely supportive throughout my time at Berkeley, and I deeply appreciate her insightful, constructive criticisms and invaluable advice.

If I were to choose my research group all over again, I would still choose the Fréchet group without hesitation, for no other reason but that the group was amazingly wonderful. I love my group. I am greatly indebted to Dr. Mark Chen, Dr. Tom Holcombe, Professor Jill Millstone, and Dr. Claire Woo for their friendship and mentorship. I thank Mark for being the fearless leader of the lab while boss is away, and for being the super synthetic chemist and awesome writer from whom I have learned so much. I thank Tom for helping me start off in the Fréchet group in the first two years; chemistry is always more exciting than ever with him around. I thank Jill for her tremendous support and for teaching me everything, ranging from nanoparticle synthesis, project development, scientific writing, collaboration management, and many other things in life. I appreciate her always being there for me even after starting her own successful, independent career at Pitt. I also thank Claire for being the rock in Team Solar and for being calm, reasonable, encouraging voice.

My day-to-day life would have been very boring and different without the company of Jessica Douglas, with whom I have shared the same lab room since our first day in the group. She has been a great labmate who is kind, enthusiastic, and respectful, and I am grateful to her, for putting up with me everyday for four years. I also acknowledge Alan Yiu, aka partner-in-crime, for working with me on several projects, testing my materials in devices, and patiently teaching me how to make solar cells. I would like give many thanks to all the past and present Fréchet group members for their help and encouragement during my time at Berkeley: Dr. Kyle Broaders, Dr. Tabitha Clem, Professor Haifeng Gao, Gianmarco Griffini, Dr. David Kavulak, Paul Kierstead, Dr. Jeremy Niskala, Seita Onishi, Dr. Claudia Piliego, Dr. David Unruh, Anna Yang, and Eric Young. I also want to give both Cezar Ramiro and Chona de Mesa the biggest hugs and thank them for keeping the logistics running smoothly and being the super cheerleaders.

In addition to working with the Fréchet group member, I have had the pleasure collaborating with David Hoffman, who performed all of the Raman spectroscopic measurements and analyses in my final thesis chapter. I also thank Alex Buyanin, Dr. Yi Liu, David Hanifi, Professor Alan

Sellinger, and Jason Bloking for being great collaborators. I am grateful to Dr. Chris Canlas, incredibly kind and knowledgeable, for giving me the opportunity to work in the NMR Facility, learn so much about various NMR experiments and operations from him, and stay connected with the department through meeting all the synthetic students and postdocs. In terms of teaching, I would like to thank Professor Felix Fischer for letting me be one of his GSIs. I enjoyed teaching for him, along with working on problem sets and quizzes with Justin Bours, and I am thankful for the experience.

I am deeply indebted to all of my friends who have been with me through thick and thin, and I treasure our friendship. I especially want to express my sincere gratitude to Vivian Lin, aka "the better-half" with whom I often have the same thinking wavelengths, for listening, being the voice of reason, and taking care of me at various times. To Katherine Mackenzie, for her pure awesomeness and for being the best workout/running buddy ever. To Talha Siddiqui, for always cheering me up and reminding me that I will always have you on my side. To Heather Buckley, for listening to my craziness and bringing excitement to conversations. To the Changstas—Sara Thoi, Annie Chantarojsiri, Jess Lee, and Dr. Ho-Yu Au-Yeung—for making me an honorary Chang group member. Also to Miriam Bowring, Jeff and Melissa Chan, Dan Finley, Chelsea Gordon, Sisi Guo, Miles Johnson, Stephanie Jones, Colleen Kellenberger, Jessica Kisunzu, Hsueh-Ju (Rick) Liu, Rebecca Murphy, Tiffany Pham, Chandra Richards, Maggie Yandell, and Chan Zhao, for all of their assistance, encouragement, and support. I am also grateful to my summer research mentors, Professor Denise Fitzgerald and Dr. Zoë Fonseca-Kelly, for introducing me to the scientific research, and to my undergraduate research advisor and mentor at NYU, Professor David Schuster and Dr. Mike Fazio, for starting me off in the world of chemistry. I also want to thank Tiffany Hong for being a great friend and video game buddy since middle school.

And I express my deepest heartfelt gratitude and love for the most amazing family in the world. I am forever grateful and indebted to my parents, Chin-Sheng and Chiung-Yi, who not only sacrificed their comfortable lives in Taiwan and moved to the States for their children's education, but also provided me with unlimited freedom and means to pursue my career goal. Their unconditional love and care made me who I am today, and their encouraging words always help me persist through various obstacles. I thank my creatively artistic sister, Gloria, and my adorably hilarious brother, Andrew, for being the awesome siblings who always make me laugh until I cannot stand up straight. I also send my greatest appreciation and love to all of my grandparents, particularly A-Mama Hsiu-Yu, and Uncle Chun-Yu for their kindness and continuous support. Lastly, I want to give very special thanks to Uncle Chun-Chieh, for being a major influence of my pursuing research in materials and for providing me with his precious experience in scientific research.

Chapter I

An Overview of Bulk-Heterojunction Organic Photovoltaics

1.1. Background and Motivation

Meeting current worldwide energy demand while mitigating the social and environmental impact will require a diversified portfolio of resources. Yet, fossil fuel based energy sources dominate the marketplace (82%).[1] One particularly attractive alternative to a fossil fuel based infrastructure is one that uses renewable and abundant solar energy.[2] However, the development and implementation of solar technology has been hampered by the cost of producing, installing, and integrating photovoltaic devices (PVs). In fact, solar energy provided less than 0.2% of the nation's energy supply in 2011 (Figure 1-1).[1]

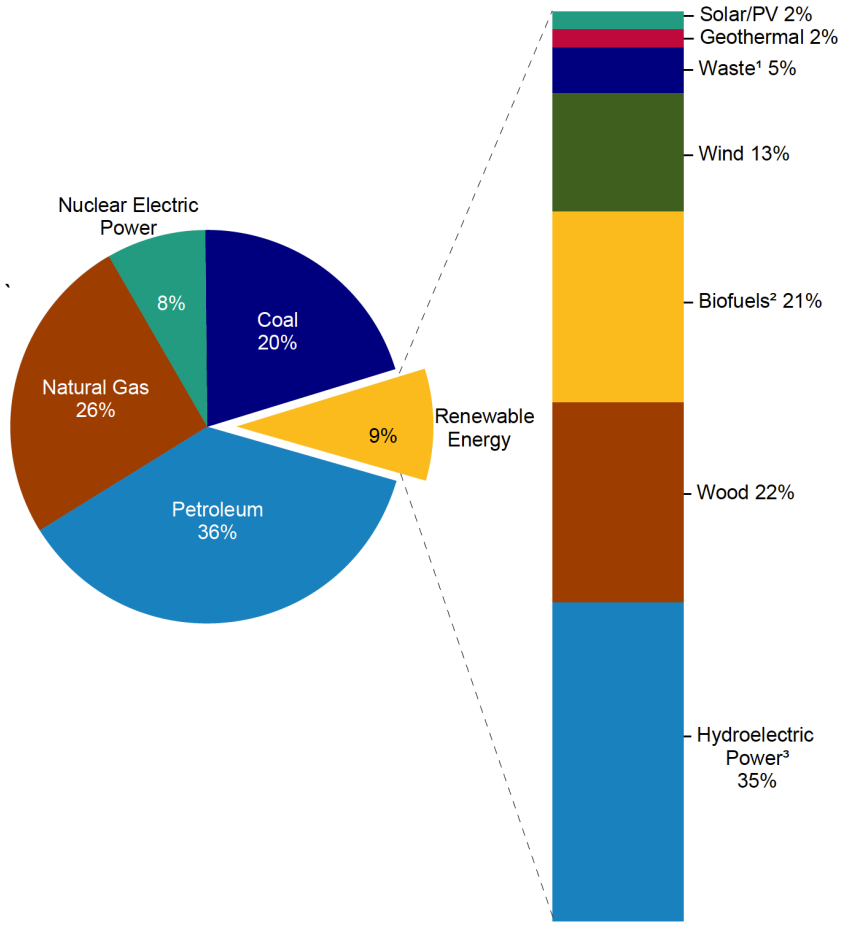

Figure 1-1. Renewable energy as share of total primary energy consumption in 2011.

For solar energy to be widely adopted, the efficiency and manufacturing cost of the devices must reach market parity.[3] To achieve this goal, many types of materials, such as solution-processable, semiconducting organic molecules and nanocrystals, are being investigated as alternatives to the traditional silicon-based technologies.[4–12] Organic photovoltaics (OPVs) are particularly attractive in applications requiring operation at low light intensity or with mechanical flexibility.[13–15] In terms of material design, organic materials exhibit optical and electronic properties that can be finely tuned through chemical modification of the molecular structures.[16] Furthermore, their solution-processability allows for low-temperature manufacture of these devices on a large-scale with existing infrastructure and technology, such as roll-to-roll printing and gravure offset printing.[17–20] Over the last decade, research and development into OPVs has led to devices with power conversion efficiencies surpassing 10%.[21,22]

To introduce the readers to this field, Chapter 1 provides a description on the basic operations of OPVs and an overview of conjugated materials. It also briefly explains common strategies used for tuning the optical, electronic, and solid-state packing properties of organic semiconductors.

1.2. Device Configurations of Organic Solar Cells

Organic photovoltaics are classified as excitonic solar cells, which generate electrically neutral, Coulombically bound electron-hole pairs, or excitons, upon photoexcitation.[23,24] Different from other inorganic materials such as silicon and CdTe, the low dielectric constants of organic materials limit the exciton dissociation (binding energy of Frenkel excitons ≈ 0.3–1 eV), thereby hindering the charge generation process.[25–27] Figure 1-2 depicts a schematic representation of an organic solar cell built on a transparent substrate, such as a piece of glass or plastic.[28] A typical device contains a light-absorbing active layer sandwiched between a transparent electrode and a back electrode. The two electrodes should exhibit different work functions so that the built-in electric field can assist the separation and transport of charges generated in OPV devices. Between the electrodes and the active layer, thin interlayers are often deposited to facilitate charge extraction at the organic/inorganic interface.[29,30] These interlayers can also modify the work functions of the electrodes and change the direction of charge transport. To ensure long-term stability of OPV devices, commercially viable solar cells must be encapsulated to prevent degradation caused by moisture and oxygen.[31-33]

Prior to the seminal publication by Tang, OPV devices were fabricated with only a single layer of electroactive materials.[34] The built-in potential from the electrodes' work functions or from the organic/metal contact was insufficient for driving efficient exciton dissociation. These single-junction devices suffered from low device performance due to the insulating nature and field-dependent charge generation of organic materials. This section describes the OPVs that contain two different electroactive organic materials for photocurrent generation. Based on the morphology of the active layer, OPVs can be classified as either bilayer or bulk-heterojunction solar cells. Other device configurations such as tandem solar cells will not be discussed here.[35-37]

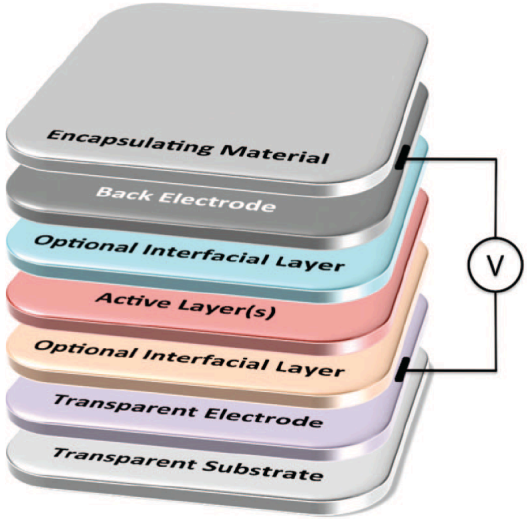

Figure 1-2. A generic scheme of an organic solar cell built on a piece of transparent substrate. An active layer is sandwiched between two electrodes of different work functions, and charge-transporting interlayers can be deposited between the active components and the metals to facilitate charge extraction. In addition, encapsulating the entire device can protect it from moisture and air, thereby extending the long-term stability and lifetime of a solar cell. Reprinted with permission from reference 28. Copyright 2010 American Chemical Society.

1.2.1. Bilayer (Lamellar) Devices

In 1986, Tang reported the first heterojunction OPV device containing copper phthalocyanine (CuPc) and a perylene tetracarboxylic derivative, which have different electron affinities, as two distinct layers sandwiched between indium tin oxide (ITO) and silver electrodes (Figure 1-3a).[34] In this system, CuPc, which exhibits the lower ionization potential (lower oxidation potential) of the two, serves as the electron-donor (p-type) while the perylene molecule serves as the electron-acceptor (n-type). It was discovered that the separation of strongly bound excitons occurs almost exclusively at the interface because the energy level offset between the two organic components provides the required driving force for electron transfer. With an efficiency approaching 1 % at AM 2 (see Section 1.4), this heterojunction solar cell not only demonstrated the efficacy of using two organic molecules to generate electrical energy from light but also revolutionized the design of OPVs, making the previously used single-junction devices obsolete.[34]

For fabricating bilayer devices, conjugated materials are often deposited by evaporation under ultra-high vacuum (on the order of 10^{-7} mBar).[28] Alternatively, the two different active layer materials can be solution-processed in orthogonal solvents, or one of the two materials is solution-deposited and the other is evaporated.[38–40] In all of these cases, there is slight mixing of the two materials at the interface. Electron-donors consist of molecular entities, such as porphyrins, phthalocyanines, subphthalocyanines, and polyacenes, while typical n-type materials include perylene derivatives or unfunctionalized fullerenes (most commonly C_{60} and C_{70}).[28] Although the bilayer configuration provides a simple system for studying charge separation at the interface between the p- and n-type materials, the probability of exciton dissociation is reduced due to the limited surface area of the donor-acceptor interface and short exciton diffusion lengths in organic materials (see Section 1.3).[41]

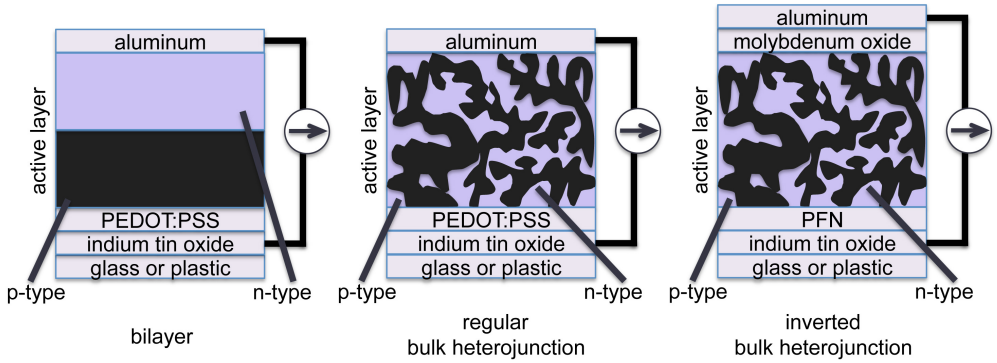

Figure 1-3. Schematic diagrams of (a) a bilayer solar cell, (b) a regular BHJ solar cell and (c) an inverted BHJ solar cell. The dark grey region represents organic electron-donors (p-type materials), and the purple region represents electron-acceptors (n-type materials), which are typically derivatives of fullerenes. Al work function = 4.3 eV. ITO work function = 4.7–5.0 eV. PEDOT:PSS = poly(3,4-ethylenedioxythiophene):poly(styrenesulfonate). PFN = poly[(9,9-*bis*(3′-(*N*,*N*-dimethylamino)propyl)-2,7-fluorene)-*alt*-2,7-(9,9-dioctylfluorene)]. For bilayer and regular bulk heterojunction devices, a hole-blocking layer, such as LiF or Ca, is occasionally deposited between the active layer and the Al electrode.[28]

1.2.2. Bulk-Heterojunction Devices

In 1995, Heeger and Friend independently reported organic solar cells that contain polymer-fullerene and polymer-polymer composites, respectively, as photocurrent-generating layers.[42-44] These OPV devices are termed “bulk-heterojunction” (BHJ) solar cells because the electron-donor and -acceptor materials form an interpenetrating network in the active layer, which is often co-deposited from a solution consisting of both components. The formation of a BHJ maximizes

the interfacial area between the two materials, thereby increasing the probability of exciton dissociation and, consequently, improving device efficiency.[8,23,25,45–47] These solar cells often perform better than bilayer cells, and devices described in this dissertation all contain BHJ active layers.

In regular device configuration, transparent ITO serves as the anode and collects holes while Al serves as the cathode and extracts electrons (Figure 1-3). Before spin-coating the active layer onto a substrate, a thin layer of PEDOT:PSS is first deposited on ITO for three reasons: (1) to smooth rough, sputtered ITO surface, and (2) to prevent electrons from entering ITO by being negatively charged, and (3) to improve contact with the organic active layer. For certain electron-donor and -acceptor combinations, the performance of the solar cells improves when a hole-blocking layer is deposited between the active layer and the Al electrode. Common HTL material includes LiF, Ca, poly[(9,9-*bis*(3′-(*N*,*N*-dimethylamino)propyl)-2,7-fluorene)-*alt*-2,7-(9,9-dioctylfluorene)] (PFN) and metal oxides, and they can improve the contact at the organic/metal interface or adjust the work function of the counter electrode.[29,30,48-58] In inverted OPV devices, ITO is still used as the transparent electrode but it now serves as the cathode upon PFN deposition and collects electrons. Molybdenum oxide (MoO_x) is commonly evaporated as the interlayer to raise the work function of the Al electrode such that the directions of hole and electron extractions are reversed.[59–62]

1.3. Operation and Performance of Organic Photovoltaics

1.3.1. Elementary steps for photocurrent generation

Designing appropriate materials for efficient solar cells requires an understanding of the properties and behaviors of OPV systems at the molecular level. Regardless of device configuration, the mechanism of photocurrent generation in OPV devices can be simplified into four basic steps: (1) light absorption and exciton generation, (2) exciton diffusion, (3) charge separation, and (4) charge transport and extraction (Figure 1-4).[29]

In most OPVs, electron-donors comprise the major light-absorbing component since their extinction coefficients in the visible region are often higher than those of the commonly used fullerene electron-acceptors. When the electron-donor in the active layer absorbs a photon, an exciton forms as an electron in the highest-occupied molecular orbital (HOMO), is promoted to the lowest-unoccupied molecular orbital (LUMO) upon excitation (Figure 1-4a). As previously mentioned, an exciton is strongly bound electron-hole pair due to Coulombic attraction, which can be described by

$$E_{\text{Coulomb}} = \frac{e^2}{4\pi\varepsilon_0\varepsilon R} \quad (1)$$

where e is the elementary charge, ε_0 is the permittivity of vacuum, ε is the dielectric constant of the medium, and R is the distance between two point charges. The small dielectric constants of organic materials (ε = 3–4) lead to attraction energy that is greater than the thermal energy at room temperature; thus, these excitons do not dissociate spontaneously under ambient conditions.[24,28,39]

Upon formation, neutral excitons can then diffuse through Brownian motion to an interface between electron-donors and -acceptors (Figure 1-4b). Excitons in organic semiconducting materials typically possess lifetimes on the order of tens to hundreds of picoseconds, which correspond to diffusion lengths ranging from 5-10 nm depending on the material diffusion coefficients.[45, 63-66] If the distance between the site of exciton generation and donor-acceptor

interface is greater than the exciton diffusion length, then the exciton has a high probability of decaying back to its ground state prior to charge separation.[67] Thus, it is imperative that an OPV device active layer exhibits domain sizes on the order of nanometers to minimize the distance an exciton must travel to an interface.

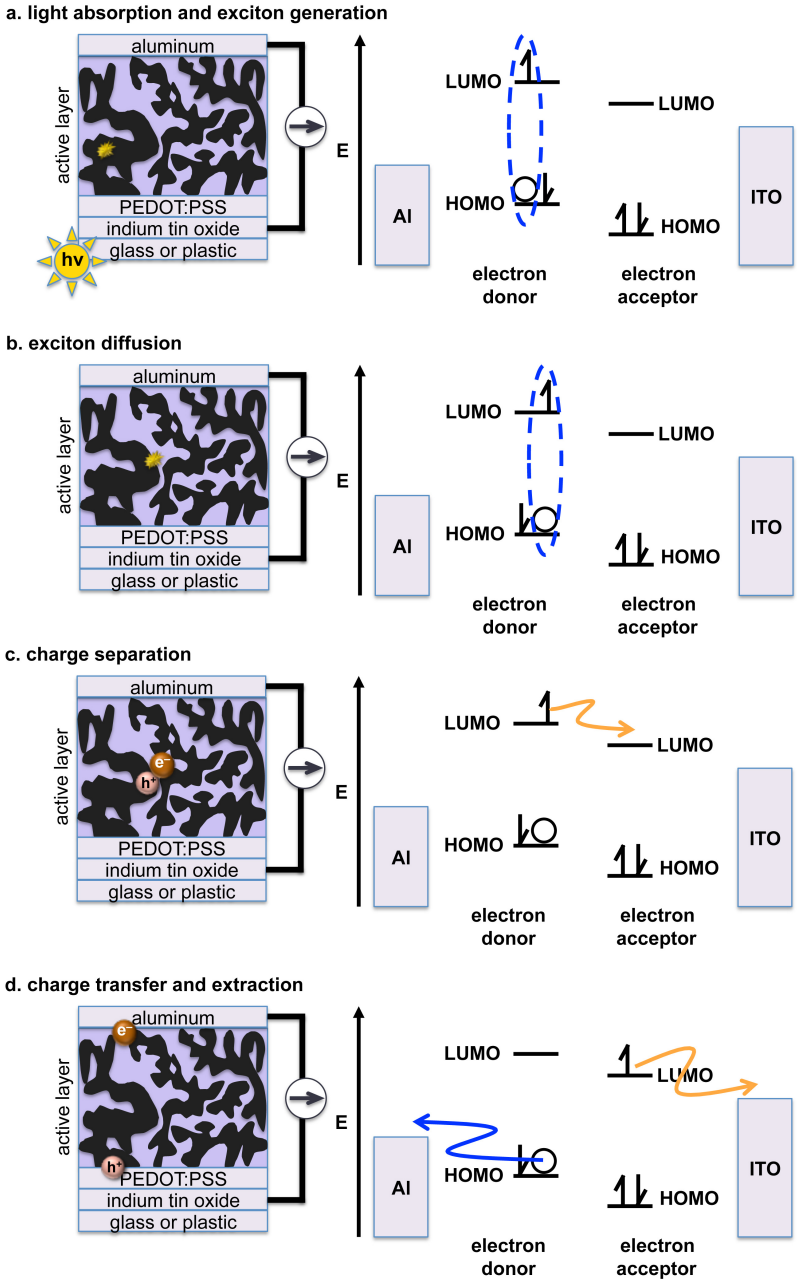

Figure 1-4. Mechanism of photocurrent generation. This scheme illustrates with a regular BHJ device and assumes that the electron-donor is responsible for the majority of light absorption. (a) When an electron-donor absorbs a photon, an electron is promoted from its HOMO to LUMO, and an exciton is generated. (b) The exciton, a Coulombically bound electron-hole pair, can diffuse to a donor-acceptor interface. (c) At this interface, the excited electron is transferred to the electron-acceptor while the hole remains on the electron-donor material. (d) The separated hole and electron are transported to the ITO and Al electrodes, respectively.

At the donor-acceptor interface, a favorable energy difference between the LUMO levels of the two materials is required to drive exciton dissociation (Figure 1-4c).[66,68] Electron transfer from the LUMO of an electron-donor to the LUMO of an electron-acceptor leads to the formation of a geminate pair, also known as a charge-transfer (CT) complex or a CT state (Figure 1-5).[69,70] A geminate pair is an intermediate state where the hole and the electron are still Coulombically attracted but localize on different materials.[71] Potential loss mechanisms at this stage include geminate recombination to form the triplet excitons via intersystem crossing ($k_{(T)RC}$) or to form singlet excitons ($k_{(S)RC}$).[72,73] A geminate pair can undergo further dissociation to generate free charges under the influence of the intrinsic electric field.[74,75] In order to probe the fate of these transient species (i.e. excitons, geminate pairs, etc.), ultrafast, pump-probe spectroscopic methods are extensively used to elucidate the charge transfer, separation, and recombination processes.[76-78] Upon the formation of free charges, energy of the final charge-separated (CS) state can be described by summing the ionization potential (IP) of the donor and the electron affinity (EA) of the acceptor.[66]

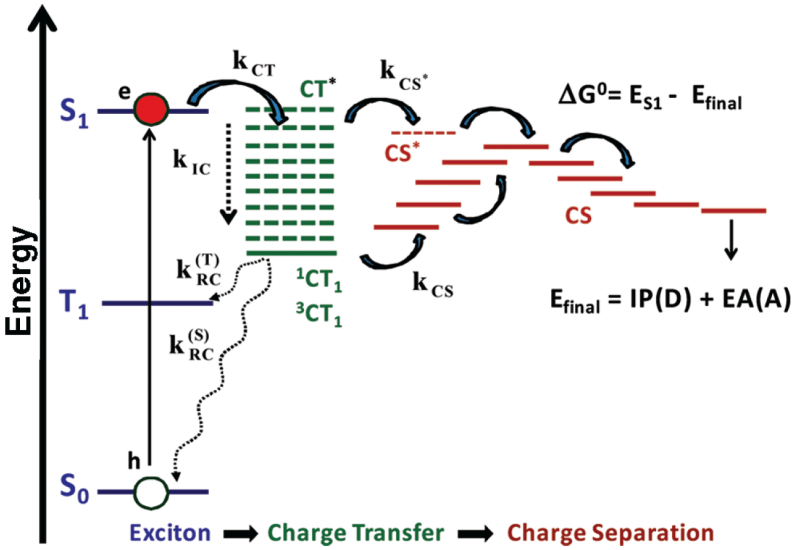

Figure 1-5. A schematic diagram showing some of the possible photophysical processes that an excited electron can undergo. Reprinted with permission from Reference 66. Copyright 2009 American Chemical Society.

In the final elementary step, free holes and electrons are transported through the electron-donor and -acceptor, respectively, and extracted at the electrodes under the influence of the built-in electric field generated by the work function difference between the two electrodes (Figure 1-4d).[79] In regular device configuration, holes are extracted at the ITO electrode while electrons are collected at the Al electrode. Charge carriers in organic semiconducting materials can travel via hopping or band-like mechanisms. In disordered materials (e.g. amorphous polymers), charge transport mainly relies on thermally activated hopping across several localized states, while it tends to proceed through delocalized, band-like states in highly crystalline materials (e.g. acenes).[80] For an OPV device, charge mobility is dependent on factors including morphology, intrinsic conductivity of the materials, crystallinity, and solid-state packing, particularly π-π spacing and long-range order (i.e. correlation lengths).[81–83] Potential loss mechanisms at this step include charge trapping and bimolecular recombination, a process by which a free hole and a free electron annihilate each other.[14,72,84,85]

1.3.2. Quantification of Photovoltaic Performance

To determine and quantify photovoltaic performance, a solar cell is first placed under simulated sunlight with a standardized spectrum to allow for comparisons among results obtained from different laboratories and various types of photovoltaics. The Air Mass 1.5 global (AM 1.5G) spectrum is the reference solar spectrum used for all PV efficiency measurements. It accounts for the interaction between solar photon flux and Earth's air masses, mainly atmospheric water, oxygen, and ozone, at 48.19° incident angle relative to the zenith. The solar irradiation intensity of the AM 1.5G spectrum is calibrated to 100 mW/cm^2, as found on the continental United States.[28] Figure 1-6 shows a comparison between the AM 1.5G spectrum and the solar spectrum before sunlight enters the atmosphere (AM 0).

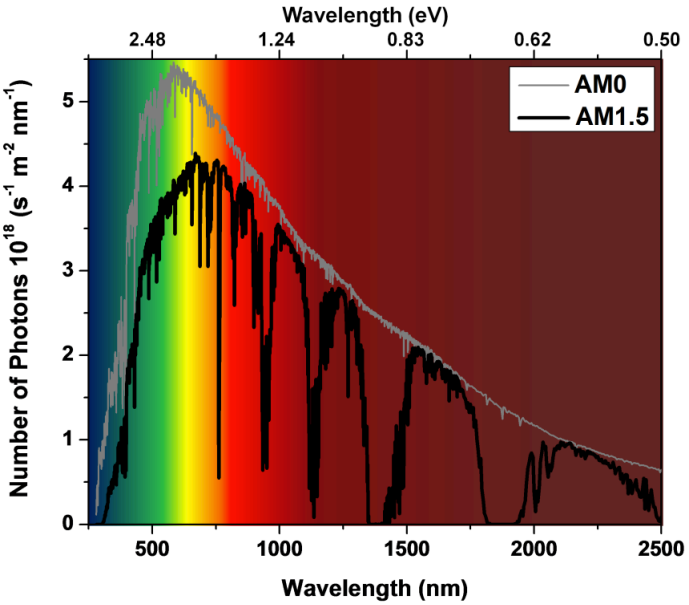

Figure 1-6. The extraterrestrial (AM 0) and the AM 1.5G solar spectra are plotted as a function of wavelengths. The characteristic absorption bands in the AM 1.5G spectrum are due to interactions between the solar flux and atmospheric molecules, mainly water, oxygen and ozone. Also note that the majority of the photon flux is located in the visible and near-infrared (400-1300 nm) regions.

Under simulated sunlight, the photocurrent output of a solar cell is measured as a function of applied voltage (V) until it reaches 0 mA due to the reverse current, and the photocurrent density (J) can then be determined based on the area of the solar cell used (J = photocurrent/device area, mA/cm^2). Figure 1-7 shows a typical J-V output curve generated from this measurement. Open-circuit voltage (V_{OC}), the x-intercept, is the applied voltage at which the photocurrent equals the reverse current; it is the maximum load that can be applied to the solar cell tested. Short-circuit current density (J_{SC}), the y-intercept, is the density of the photocurrent generated by the PV at zero externally applied voltage.[23]

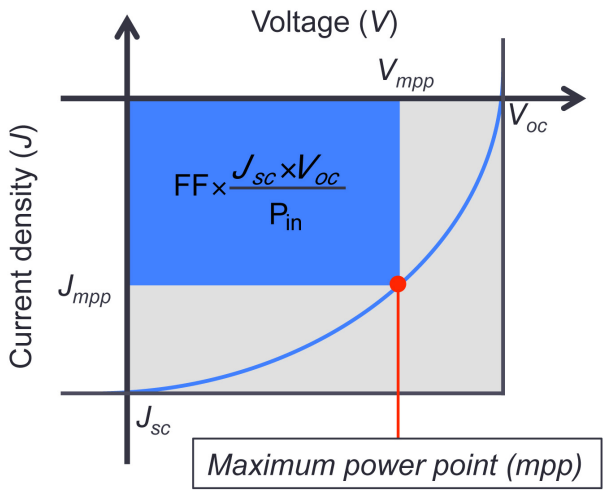

Figure 1-7. Typical current density-voltage (*J*-*V*) curve obtained for measuring PV performance.

The theoretical power output (at absolute power point) of a solar cell is the product of V_{OC} and J_{SC} as illustrated by the grey rectangle in the figure, and the blue line represents the experimental *J*-*V* curve. Along this curve lies a maximum power point (mpp), and the largest experimental power output of a device is shown as the blue rectangle in the figure. The position of the mpp is dependent on the shape of the *J*-*V* curve. This curvature is a result of non-idealities and loss mechanisms in the photocurrent generation process, and it can be described by fill-factor (FF). In mathematical terms, fill-factor is defined as the ratio of the maximum power output ($V_{mpp} \times J_{mpp}$) to the theoretical power output ($V_{OC} \times J_{SC}$): [23]

$$FF = \frac{J_{mpp} \times V_{mpp}}{J_{SC} \times V_{OC}} \tag{2}$$

The product of V_{OC}, J_{SC} and FF represents the device power output, which can be used to determine the efficiency of a solar cell. The power conversion efficiency (PCE, η) is defined by the ratio between the power produced by the cell (P_{out}) and the power input (P_{in}), shown in equation (3): [23]

$$\eta = \frac{P_{out}}{P_{in}} = FF \times \frac{J_{SC} \times V_{OC}}{P_{in}} \tag{3}$$

where J_{SC} has units in mA/cm^2 and V_{OC} has units in V.[23] The value of J_{SC} depends primarily on the amount of light absorbed by the active layer, and other factors influencing J_{SC} include film morphology, charge carrier mobility and charge transport.[29,86–89] In addition to measuring *J*-*V* curves, the J_{SC} can be calculated from integrating the external quantum efficiency (EQE) spectra.[7] The value of V_{OC} is mainly determined by the energy difference between the highest-occupied molecular orbital (HOMO) of the donor and the lowest-unoccupied molecular orbital (LUMO) of the acceptor (see Section 1.4.).[91–95] As electron-acceptors are reduced, electrons collected at the Al electrode travel through the circuit and recombine with the hole at the HOMO level of the electron-donor. It has also been demonstrated that intermolecular interactions can influence device V_{OC}. FF can be influenced by charge mobility, imbalanced carrier transport, and charge extraction at the electrodes.[96,97] The interplay of these three parameters can be modeled using an equivalent circuit.[28,88] While some aspects of device architecture influence one of the cell components more than they do to another, all of the three parameters, J_{SC}, V_{OC} and

FF, remain interdependent. Furthermore, the morphology of active layers governs several factors, including charge mobility and exciton diffusion, thereby serving as a key contributor in determining the interplay among the three parameters.[98–100]

1.4. The Active Layer: Conjugated Materials for OPVs

1.4.1. Band Structure of Organic Semiconducting Materials

Organic semiconducting materials are conjugated macromolecules with continuous sp^2-hybridized carbon centers. In these molecules, the sp^2 orbitals form the molecular structure through σ-bonds while the valence electrons in the remaining *p*-orbitals, which are perpendicular to the σ-framework, delocalize extensively. Since the delocalized π-electron density render these materials conductive, their electronic band structures and band gap formation can be most easily explained by molecular orbital (MO) theory.[101] In particular, the frontier molecular orbitals, HOMO and LUMO, are the most crucial in determining the optical and electronic properties of a conjugated material.

Most semiconducting molecules contain covalently linked or fused aromatic units. As shown in Figure 1-8, when two aromatic rings, such as thiophene, are bonded, the mixing of MOs raises the HOMO and lowers the LUMO energy levels, decreasing the HOMO-LUMO gap, or the band gap (E_g).[102] Further addition of aromatic rings leads to a reduction of E_g and energy spacings between MOs, which can be approximated as continuous energy bands similar to the band structures of inorganic semiconducting materials (HOMO and LUMO of organic materials are analogous to valence and conduction bands of inorganic semiconductors, respectively).[103,104]

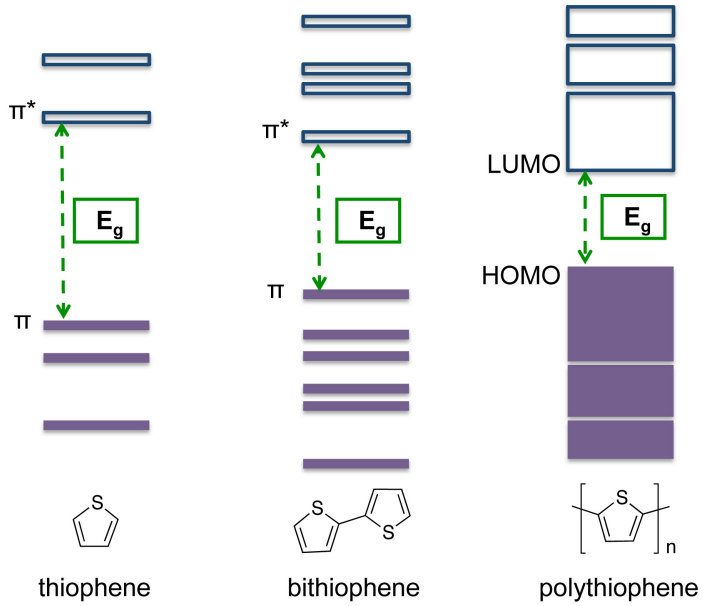

Figure 1-8. Origin of the band structures of polyaromatics. In the case of 2,2'-bithiophene, the newly generated HOMO (π) is higher and LUMO (π*) is lower than the HOMO and LUMO of thiophene, respectively, leading to a narrower band gap. Extending conjugation by linking additional aromatic monomers results in closely located, almost continuous energy levels that resemble the band structures of inorganic semiconductors, and the band gap (E_g) also decreases because of electron density delocalization. At conjugation length, the band gap does not continue to decrease due to Peierls distortion.

An organic semiconductor reaches its conjugation length when additional aromatic units do not significantly alter its band gap; molecular band gaps do not decrease infinitely due to Peierls

distortion, the solid-state equivalent of the Jahn-Teller effect.[103,104] In brief, molecular structure will deform from highly symmetric, nearly degenerate states in order to stabilize partially filled electronic states, subsequently lowering the energy of the overall system. This structural distortion is reflected on the extent of bond-length alternation (BLA).[105,106] In perfectly degenerate π-systems of polyaromatics, all of the bonds should be 1.5 bonds, as in the case of benzene, and enable complete delocalization of electron density. However, because of Peierls' distortion, the double bonds tend to localize in the aromatic rings while the inter-ring bonds exhibit similar bond lengths to single bonds. As a consequence, band gaps of organic semiconducting materials do not reach zero, and the greater the bond lengths alternate between the double and single bonds in a chain, the wider the band gap. The conjugation length of a semiconducting polymer generally ranges from 5 to 20 repeat units.[107–110]

1.4.2. Basic Design Criteria and Characterization Methods of OPV Active Layer Materials

Careful consideration of OPV operating mechanisms (Section 1.3.1) will enable the design and development of conjugated materials with appropriate properties for efficient devices. First, organic semiconductors in an active layer must exhibit absorption spectra that match the solar emission spectrum to maximize the number of photons harvested. As previously shown in Figure 1-6, the greatest photon flux from the sun concentrates between 400 and 1100 nm; thus, an active layer material should absorb strongly in the visible and near infrared (NIR) regions. Thiophene homopolymers show solid-state absorption onset around 670 nm, and most of the newly developed, high-performing copolymers exhibit redshifted absorption onset.[111–114] In addition to absorption breadth, extinction coefficients must also be high, preferably on the order of 10^4 or 10^5 M^{-1} cm^{-1}. Common strategies used for band gaps engineering are described in Section 1.5.

As previously mentioned, exciton diffusion lengths in organic semiconductors are short (5-10 nm); thus, electron-donor and -acceptor should phase separate on the nanometer scale and form an interpenetrating network. However, there is an optimal domain size. On the one hand, phase domains larger than exciton diffusion lengths can limit the probability of an exciton's reaching donor-acceptor interface. On the other hand, fine mixing of the phases increases the occurrence of recombination events.[98–100,115,116] The extent of phase segregation depends on the solubility and miscibility of the two materials. In addition to intrinsic material properties, the extent of phase separation can vary significantly depending on device processing solvents and conditions, along with the use of high boiling-point additives.[117–119]

Facilitating exciton dissociation requires an appropriate energy level alignment between the frontier MOs of electron-donors and -acceptors. It has been empirically determined that a 0.3 eV difference between the energy levels is necessary for efficient charge transfer, though in some cases, working devices can still be fabricated from two materials with a smaller energetic offset.[23,120–122] If there is insufficient energetic driving force for exciton dissociation, other photophysical pathways such as charge recombination will dominate and decrease solar cell efficiency. Proper energy level alignment is also important for achieving high device V_{OC}, which correlates with the difference between the HOMO of the electron-donor and the LUMO of the electron-acceptor used. In general, large V_{OC} values can be obtained with electron-donors with low-lying HOMO levels and electron-acceptor with high-lying LUMO levels.

Tuning the optical and electronic properties of active layer components can be complicated (Figure 1-9).[123–125] To develop an electron-donor with a narrow band gap requires the energy difference between HOMO and LUMO to be small, and the material should possess a low HOMO level for generating a large V_{OC}. To implement both of these criteria then necessitates

the LUMO level of the electron-donor to be low; however, a low-lying LUMO may not provide sufficient energetic driving force for charge separation. One possible way to maintain charge separation efficiency is to reduce the LUMO energy level of the corresponding electron-acceptor, yet this method will subsequently lower the device V_{OC}. In short, an ideal organic semiconducting material should (i) have sufficient energy level offsets in comparison with the other active layer component for efficient charge separation while maximizing the open-circuit voltage, (ii) display an absorption spectrum extending across the visible spectrum and into the near-IR, and (iii) maintain high extinction coefficients over this spectral range.[126]

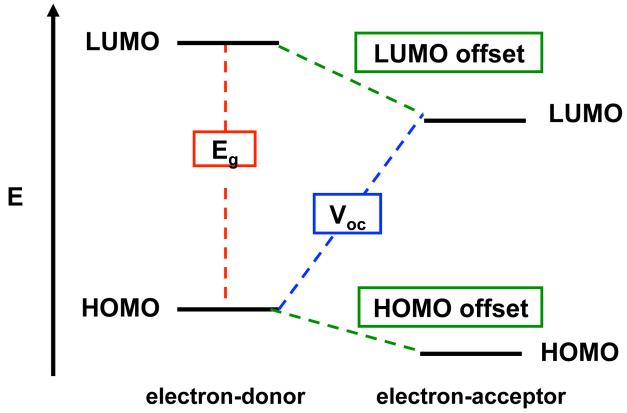

Figure 1-9. An energy level diagram illustrating the tradeoff between the width of a band gap, energy level offsets, and the size of device V_{OC}. Achieving a balance between all three parameters is necessary for designing materials with high device efficiency.

To ensure efficient transport of free charges through device active layer, electron-donors and -acceptors should exhibit high hole and electron mobility, respectively. Charge transport along a molecular backbone typically proceeds via a band-like mechanism where the holes or electrons travel through the delocalized π-system.[79,80] Crystallinity and solid-state packing also contribute significantly to carrier transport properties of conjugated materials.[81–83,127,128] Cofacial packing is preferred due to the stabilizing effect of π-π interactions, and the short π-π packing distances favors intermolecular charge hopping because of intermolecular orbital overlap (Figure 1-10). Although planar molecules often pack more tightly, some nonplanar molecules, such as rubrene and isoindigo-containing polymers, can exhibit high hole mobility.[129-132]

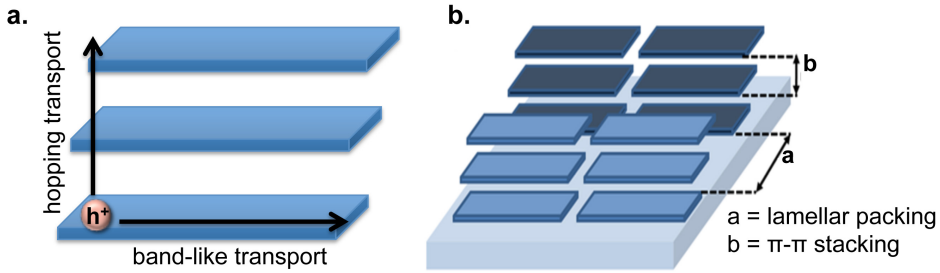

Figure 1-10. (a) Within a crystallite, intermolecular charge transport proceeds through hopping mechanism while charges travel through the delocalized π-system along the molecular backbone. (b) Molecular packing in the side-to-side direction, or lamellar packing, typically show larger distance than cofacial packing, π-π stacking; thus, intermolecular hopping transport is more efficient through the π-stacks.

Typical methods for characterizing band gaps and energy levels of organic semiconducting materials include ultraviolet-visible (UV-vis) absorption spectroscopy and cyclic voltammetry (CV). An optical band gap (E_g) corresponds to the minimal energy required to promote an electron from the HOMO to the LUMO, and it can be determined by the onset of a UV-vis absorption spectrum. Compared to absorption profiles collected in solution, thin-film spectra often exhibit redshifted onset of absorption and spectral broadening due to further delocalization of electron density through two- or three-dimensional intermolecular π-π interactions.[133]

Cyclic voltammetry is the most common method for measuring MO energy levels. HOMO energy level (E_{HOMO}) corresponds to the ionization potential (IP) of a conjugated material and can be calculated based on the oxidation wave onset; LUMO energy level (E_{LUMO}) represents the electron-affinity (EA) and can be determined by the reduction wave onset. In literary references, most of the energy levels are reported with respect to vacuum after calibrating each measurement to the half-wave potential ($E_{1/2}$) of ferrocene/ferrocenium redox couple (Fc/Fc^+). There have been discrepancies in the general reporting of CV data where some publications use –4.8 eV[134] (vs. vacuum) for Fc/Fc^+ while others use –5.1 eV.[39,135] A recent paper by Bazan and coworkers clarified that $E_{1/2}$ = –4.8 eV had been derived from data that are incongruent with the currently accepted experimental potential of the Fc/Fc^+ redox couple.[136]

In determining band gaps, there is a subtle distinction between the data collected with optical and with electrochemical techniques. LUMO level measured by CV yields the energy required for radical anion formation while optical band gap is the energy necessary for an electronic transition from the S_0 to the S_1 state, not the addition of an electron to the LUMO level. Since photoexcitation is the first step in the charge generation mechanism, optically determined E_g by UV-vis spectroscopy is the more appropriate band gap measurement. Other techniques for characterizing HOMO energy level include photoelectron spectroscopy in air (PESA) and ultraviolet photoelectron spectroscopy (UPS).

Surface morphology of an active layer can be characterized by atomic force microscopy (AFM). From both the height and phase images, the domain sizes can be measured. However, the exact composition of the phases cannot be determined because a domain can be pure electron-donors or acceptors or a mixture of the two. While AFM images only reflect the surface morphology, which may be different from the bulk of the active layer, it still provides insights into the separated phase-domains. Active layers that exhibit large, distinct features and rough surfaces or that appear completely amorphous often correlate with low device efficiencies, and high-performing devices frequently show corresponding AFM images with domain sizes of 10-20 nm. To characterize the bulk of the active layer morphology, transmission electron microscopy (TEM) has been used to acquire images of the bulk-heterojunction.[119,137–139]

Grazing incidence X-ray scattering or diffraction (GIXS or GIXD)[82,140] is the most commonly used technique to determine solid-state packing of conjugated materials in thin films (~100 nm). As shown in Figure 1-11, an incident X-ray beam irradiates at a very shallow angle (~0.1 °) relative to the sample surface, and the scattered beam is collected using an area detector. Because the penetration wave is limited to the nanometer length scale, this technique is suitable for thin-film measurements by increasing the path length and, subsequently, signal-to-noise ratio. The scattering pattern reveals information about crystallinity, crystallite alignment, packing distances, and long-range order. With GI wide-angle scattering (GIWAXS), molecular packing distances are revealed in thin-film diffraction patterns based on peaks that correspond to either π-stacking ($q \sim 1.7$ Å^{-1}) or lamellar spacing ($q \sim 0.3$ Å^{-1}). As shown in Figure 1-10b, if diffraction peaks of π-π packing, for example, are observed along the q_z axis ($q_{xy} = 0$), it means the

molecules orient face-on relative to the substrate (out-of-plane π-stacking); if the peaks appear along the q_{xy} axis ($q_z = 0$), it means the molecules orient edge-on relative to the substrate (in-plane π-stacking). Diffraction peaks that are not on either axis are much more difficult to analyze and interpret. Films with an isotropic distribution of π-stacking will display diffraction patterns with an arc of scattering intensity across all polar angles, suggesting that the film is crystalline but the crystallites are not aligned.

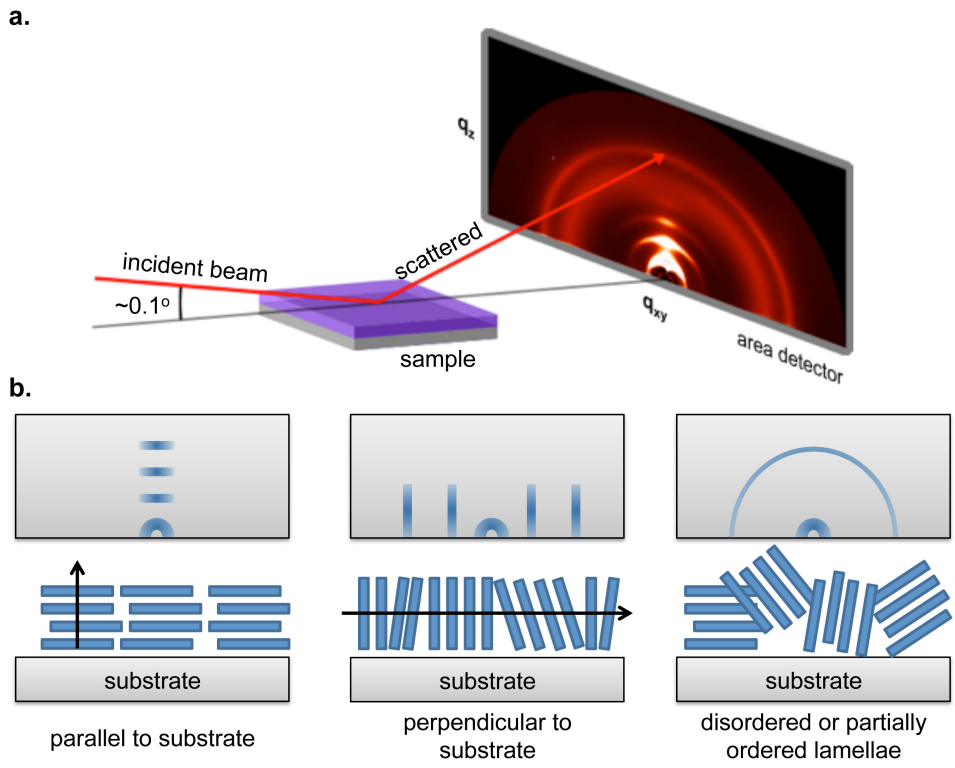

Figure 1-11. (a) A schematic diagram showing the acquisition of grazing-incidence X-ray diffraction. (b) Using π-π stacking as an example: a scattering pattern with peaks along the q_z axis indicates that the molecules pack face-on and orient parallel to the substrate (left); a scattering pattern with peaks along the q_{xy} axis indicates that the molecules pack edge-on and orient perpendicular to the substrate (middle). When a scattering pattern shows a semicircular ring, it suggests that the molecules in the film form crystallites with disordered alignment with respect to the substrate (right).

Charge mobility of thin films can be determined using hole-only or electron-only diodes or field-effect transistors. The mobility measured from space-charge-limited current (SCLC) is more relevant because the device architecture is similar to an OPV device, where a film of conjugated materials is sandwiched between two electrodes. Depending on the electrodes used, the forward bias preferentially extracts holes or electrons from the diode in the vertical direction, and as space charges build up at the electrodes, the current-voltage plot can be modeled to yield a mobility value. For a device of known thickness that operates in the SCLC regime, the mobility can be calculated following the Mott-Gurney Law.[141-143]

1.4.3. An Overview of Conjugated Polymers and Small Molecules

Conjugated materials can be divided into two major classes, polymers and small molecules, based on the number of repeat units covalently linked together. Small molecules can either be

oligomers, such as oligothiophenes, or large molecules, such as porphyrins, phthalocyanines, fullerenes, and hexabenzocoronenes. Polymers are macromolecules containing at least 20 repeat units (a degree of polymerization > 20) with a distribution of molecular weights described by the polydispersity index (PDI, M_n/M_w).

For solar cell applications, polymers exhibit more extensive conjugation, greater absorption breadth, and typically larger extinction coefficients than small molecules. Their long chains may allow for the formation of an interconnected, interpenetrating network in the device active layer, thereby promoting nanoscale phase separation.[7,8,41,45] While conjugated polymers are promising materials for OPVs, they are intrinsically polydisperse, and the variability in molecular weights leads to synthetic and device inconsistency from batch to batch. Polymeric materials also tend to be difficult to purify. Since most of the conjugated polymers are synthesized via transition metal-catalyzed cross couplings, including Kumada, Suzuki, and Stille reactions,[144–147] residual nickel or palladium from polymerizations may affect long-term OPV device stability.[33,148,149] Palladium byproducts from Suzuki and Stille polycondensation can be chelated and removed using scavengers such as *N*,*N*-diethylphenylazothioformamide (Figure 1-12).[150,151] Furthermore, cross-coupling reactions lead to contaminated polymer chain-ends, introducing undesired bromide, stannane, borylates into the active layer. These unreacted end-groups can be capped by adding monofunctionalized benezenes, such as iodobenzene, into the reaction mixture after the polymerization is complete.[152-155] Other impurities that might ultimately affect OPV device lifetime include oligomeric species that cannot be separated from the high molecular weight polymers by Soxhlet extraction. It has been shown that residual low molecular weight materials can reduce OPV device efficiency over time, and, by purification with preparatory recycling size-exclusion chromatography (SEC), OPV device efficiency can be maintained for an extended period of time.[156]

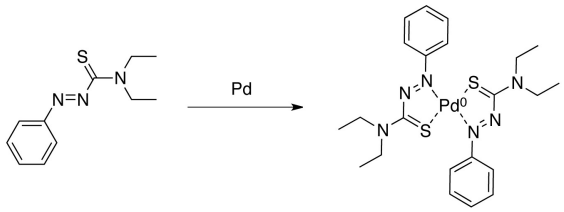

Figure 1-12. Structure of *N*,*N*-diethylphenylazothioformamide, which is used to chelate residual palladium (0) after Stille or Suzuki polycondensation.

In contrast to polymers, small molecules are single molecular entities that can be readily synthesized, purified, and characterized.[28,157–161] Purification of small molecules can be done with traditional methods such as column chromatography and recrystallization. Their purity can be definitively determined by nuclear magnetic resonance spectroscopy, mass spectrometry, elemental analysis, and single-crystal X-ray diffraction. These characteristics of small molecules eliminate the sort of device variability that can arise from material inhomogeneity. Despite these potential advantages, solutions of planar small molecules often lack appropriate viscosity, likely leading to poor film-forming capabilities.[161,162] They also tend to form large crystallites and may phase-segregate into domains greater than nanoscale in active layers, thereby decreasing OPV device J_{SC} and FF.

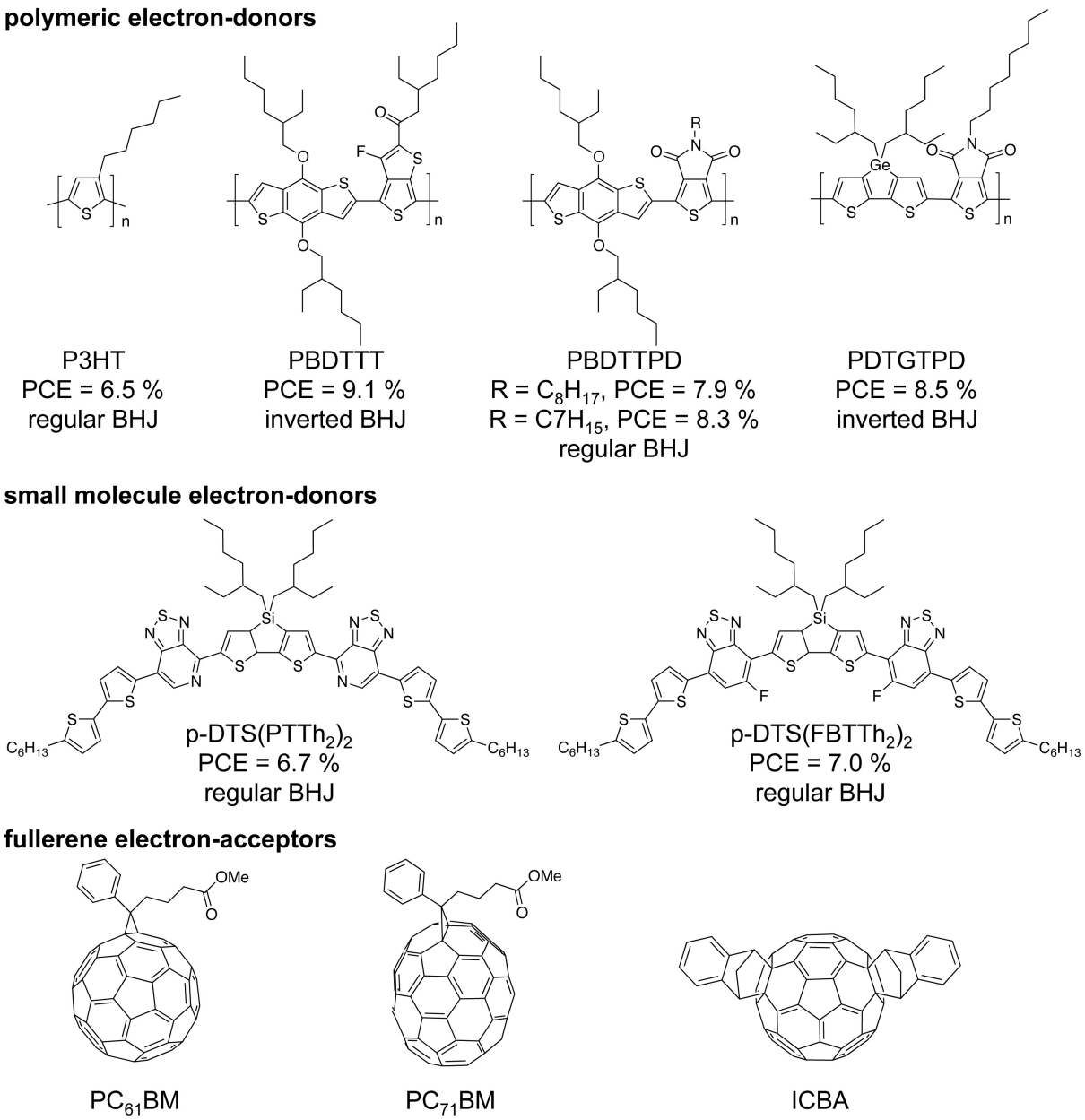

Figure 1-13. Chemical structures of high-performing electron-donors and -acceptors. The efficiency values listed for the electron-donors are maximum OPV performance with $PC_{71}BM$ as the electron-acceptor, except for P3HT, the device of which is fabricated with ICBA.

Figure 1-13 shows the structures of several high-performing electron-donors and electron-acceptors. The most-studied, well-known homopolymer for OPV application is poly(3-hexylthiophene), or P3HT,[23,116,163,164] which performs with device PCE as high as 6.5%.[165] State-of-the-art, polymeric electron-donors demonstrate OPV device efficiency above 8% in both regular[54,166–169] and inverted[59,170] device architectures while the best-performing p-type small molecule devices exhibit device PCE up to 7%.[171] All of these devices use molecular fullerene derivatives, phenyl-C_{61}/C_{71}-butyric acid methyl ester ($PC_{61}BM$ or $PC_{71}BM$)[172,173] or indene-C_{60}-bisadduct (ICBA)[174], as the electron-acceptor. Wudl and coworkers first reported the synthesis

of $PC_{61}BM$, which has become one of the most popular electron-acceptor for OPV devices. Fullerene derivatives are promising n-type materials because they exhibit low reduction potential, small reorganization energy, reasonable solubility in common device-processing solvents (e.g. chlorobenzene, dichlorobenzene), and high electron mobility. In particular, $PC_{71}BM$ contributes significantly to device J_{SC} because it shows greater extinction coefficients in the visible region than $PC_{61}BM$, which does not absorb much light due to symmetry-forbidden electronic transitions.[175] ICBA is another commonly used fullerene derivative that has a higher LUMO energy level than PCBM, thereby enhancing device V_{OC} given appropriate energy level offset with the p-type material used. Other polymeric and molecular electron-acceptors have been synthesized and investigated as substitutes for fullerene acceptors, which are expensive to produce and difficult to purify.[39.122,160,176,177] Yet, fullerene-containing devices still perform much better than these alternative materials.

1.5. Approaches for Modulating Optical and Electronic Properties of Conjugated Materials

Implementing the design criteria discussed in Section 1.4.2. requires a fundamental understanding of how changes in molecular structure influences the optical and electronic properties of conjugated polymers and small molecules. Since their first reported syntheses in 1986, soluble, alkylated thiophene homopolymers, specifically poly(3-hexylthiophene) (P3HT), have shown great promise as semiconducting materials for organic electronics. While BHJ solar cells with P3HT:PCBM active layers have demonstrated PCE up to 6.7 %,[165] further performance optimization becomes increasingly difficult. The V_{OC} values of P3HT:PCBM devices are limited to 0.6 V due to energy level alignment between the two components ($E_{HOMO, P3HT}$ = 5.2 eV, $E_{LUMO, PCBM}$ = 4.2 eV, charge separation energy ≈ 0.3 eV), and the J_{SC} values are restricted by the relatively wide E_g of P3HT (λ_{onset} in film ≈ 670 nm).[23] As mentioned previously, OPV materials should absorb strongly between 400 nm and 1100 nm; thus, strategies have been developed to reduce bond-length alternation of conjugated materials, thereby narrowing band gaps and redshifting absorption, and to adjust their energy levels, allowing for ideal alignment between the frontier MO levels of the active layer materials.

1.5.1. Donor-Acceptor Approach: Functionality/Substituent Effects

The most popular strategy for designing low-band-gap materials is the donor-acceptor (D-A) approach, where an electron-rich moiety (donor) and an electron-poor moiety ("acceptor) are covalently linked together.[6,112,178–180] Electron-rich units typically exhibit high HOMO and LUMO levels due to electron-rich substituents, such as electron-rich heteroatoms (S, P, Se), alkyl and alkoxy functionalities. Electron-poor units are often functionalized with electron-withdrawing groups, including electronegative atoms and carbonyl groups, which lower both of the frontier MO energy levels. When these two kinds of monomers are bonded together, the rehybridized HOMO preferentially locate on the donor and the LUMO on the acceptor, leading to electron delocalization and reduction of bond-length alternation. As a result, the band gaps of donor-acceptor materials are narrower than those of homopolymers (Figure 1-14). However, their extinction coefficients are often lowered to the order of 10^3 to 10^4 M^{-1} cm^{-1} compared to that of homopolymers (10^5 M^{-1} cm^{-1}) because their HOMOs and LUMOs tend to localize on different moieties, resulting in weak overlap between electronic states.[23] Since not all D-A materials exhibit appropriate energy levels and band gaps for OPV applications, the donor and acceptor pairs must be carefully chosen.

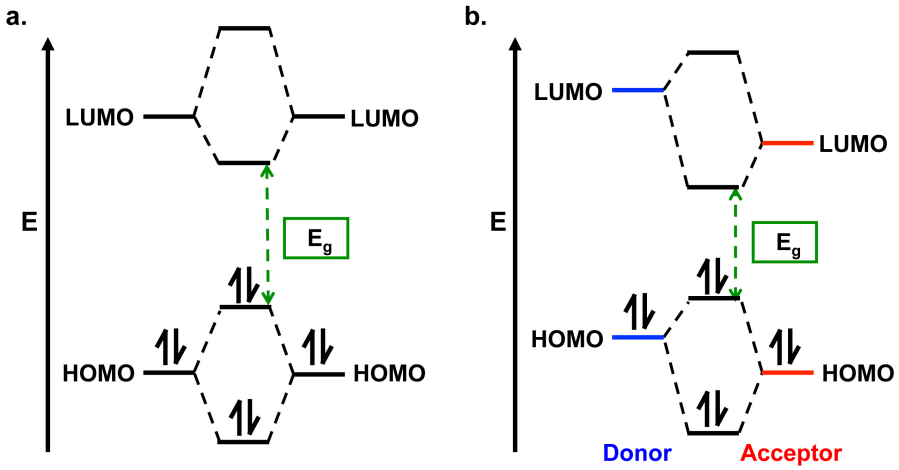

Figure 1-14. When (a) two of the same aromatic units are covalently linked, the reduction in band gap is less than (b) the band gap generated from the linkage between a donor moiety and an acceptor moiety. The D-A approach results in polymers and small molecules with decreased BLA, increased electron delocalization, and reduced E_g. Although D-A materials display broadened absorption spectra, they tend to exhibit lower extinction coefficients than homopolymers due to offset in electronic states.

Poly[2,6-(4,4-bis-(2-ethylhexyl)-4H-cyclopenta[2,1-*b*;3,4-*b*′]-dithiophene)-*alt*-4,7-(2,1,3-benzothiadiazole)] (PCPDTBT), synthesized by Brabec and coworkers in 2006[181] and optimized by Heeger and coworkers in 2007,[182] is the first donor-acceptor p-type polymer performed at a 5.5% device PCE with $PC_{61}BM$. Over the last several years, many high-performing polymers and small molecules are synthesized with the D-A motif (Figure 1-12). However, this approach does not guarantee the development of materials with high device performance. To achieve a balance between band gaps and device V_{OC}, You proposed the "weak donor, strong acceptor" strategy for designing materials with efficient OPV devices.[6,183] The use of a weak donor moiety keeps the energy level of the rehybridized HOMO low, ensuring a large V_{OC}, while the use of a strong acceptor maintains a narrow E_g by significantly lowering the LUMO energy level.

A literature survey reveals that the "weak donor, strong acceptor" concept can be demonstrated with the chemical structure of several high-performing, solution-processable polymers and small molecules. In particular, incorporating benzo[1,2*b*;4,5*b*′]dithiophene (BDT) derivatives as a "weak donor" into conjugated materials often lead to low HOMO levels because the fused benzene ring is less electron-rich than thiophene and provides aromatic stabilization to the entire moiety; thus, many BDT-containing materials exhibit high device V_{OC}.[184–186] Other weak donors include dibenzo[*b*,*d*]germole (DBG)[187] and germolo[3,2-*b*:4,5-*b*′]dithiophene (DTG).[188] A number of "strong acceptors" building blocks have also been developed, including thienopyrrole dione (TPD),[189–191] thieno[3,4-*b*]thiophene (TT),[114,192] diketopyrrolopyrrole (DPP),[193–196] mono- and di-fluorinated benzothiadiazole (BT),[171,197] and pyridalthiadiazole (PT)[198] (Figure 1-15). TPD, simultaneously developed by Fréchet and Leclerc, and DPP are electron poor because of imide and amide carbonyls, respectively. The electron deficiency of PT and BT is due to the fused nitrogen-containing heterocycles while fluorination of BT further reduces its energy levels. Several derivatives of TT have been synthesized, and the most electron poor TT moiety is fluorinated and functionalized with an acyl side chain. While this fluoride and pendant carbonyl contribute to lowering the energy levels, the use of TT moiety allows for extensive electron delocalization, decreased BLA, and reduced band gap through a different mechanism (Section 1.5.2.).

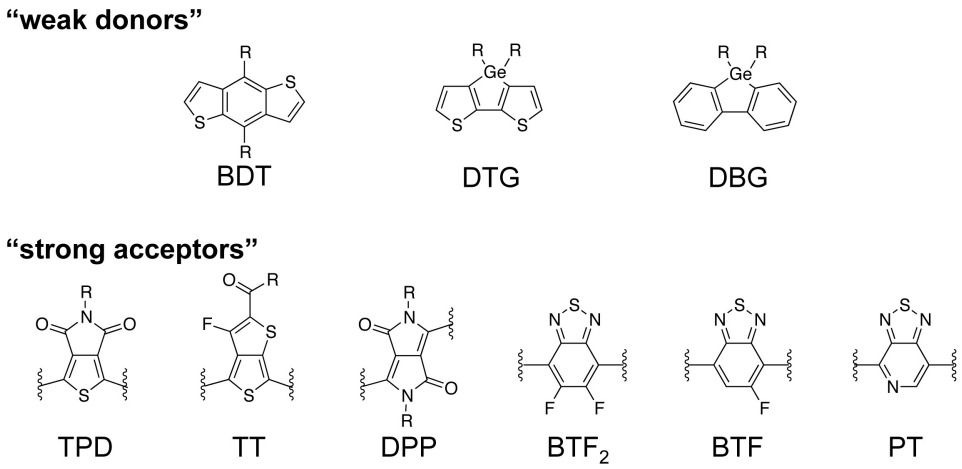

Figure 1-15. Chemical structures of promising electron-rich and electron-deficient building blocks used in conjugated materials for efficient OPV devices. R = alkyl or alkoxy.

1.5.2. Competing Aromaticity

Conjugated materials can be drawn with two major resonance structures, the aromatic and the quinoidal forms (Figure 1-16).[6,103,113] In the aromatic form, the double bonds localized in the rings while in the quinoidal form, the inter-ring bonds exhibit greater double bond character, suggesting greater electron delocalization throughout the conjugated system. When resonance character of one is much greater than the other, there is much alternation of the bond lengths, and the band gap is wide. Conversely, similar resonance contribution from both forms (i.e. less Peierls distortion) leads to greater electron delocalization, and the BLA is reduced.

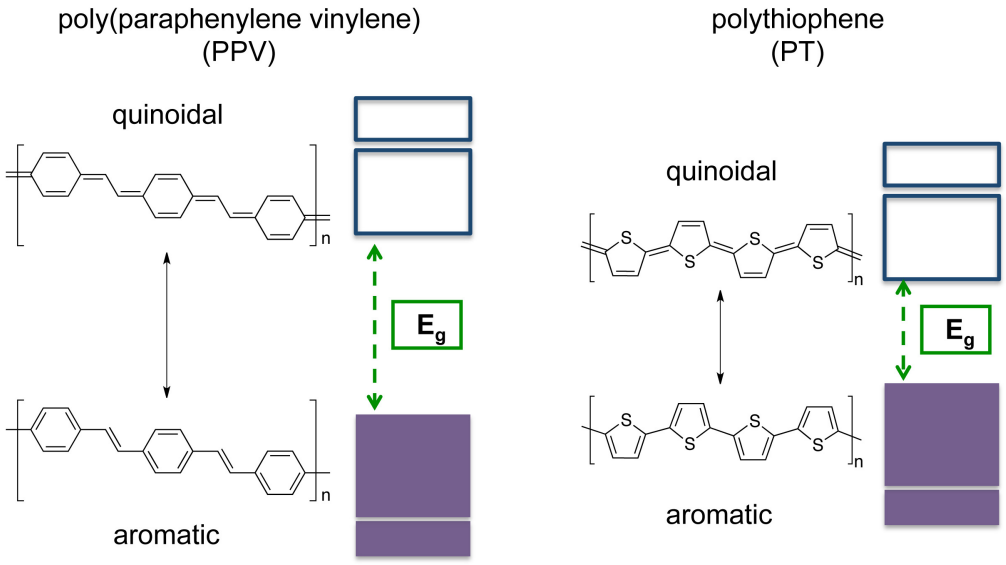

Figure 1-16. Any conjugated material has two major resonance forms, aromatic and quinoidal. The similarity between the two states dictates the band gap. If aromatic contribution is much greater than quinoidal contribution, then E_g is large. However, similar quinoidal and aromatic states lead to reduced BLA, increased electron delocalization, and redshifted absorption onset. PPV shows greater BLA than PT and exhibits a band gap of 2.3–3 eV, while the E_g of PT is 2 eV

The aromatic form is often favored because aromatic stabilization, the extent of which influences the contribution of each resonance structure. The aromatic stabilization energy of benzene is the largest (36 kcal/mol), and this energy other heteroaromatic molecules decreases in this order: thiophene (29 kcal/mol) > pyrrole (21 kcal/mol) > furan (16 kcal/mol).[199] Thus, in polyaromatics, derivatives of poly(*p*-phenylene vinylene) (PPV) exhibit band gaps ranging from 2.2–3 eV while various polythiophenes (PT) display E_g around 2 eV (Figure 1-16).[113]

The situation becomes complicated with systems containing fused rings where the aromatic stabilization of individual rings competes with the other. As a classic example, isothianaphthene (ITN) consists of a benzene ring fused to the C3-C4 bond of a thiophene (Figure 1-17). In poly(isothianaphthene) (PITN), since aromatic stabilization energy is greater for benzene than for thiophene in each monomer, only the benzene portion is aromatized, thereby destabilizing the HOMO level while stabilizing the LUMO. Thus, the thiophene backbone PITN exhibits greater quinoidal character than PT, and its band gap (1.1 eV) is much lower than that of PT.[200] Substituting the benzene portion of ITN with another thiophene shows a similar effect, although poly(thieno[3,4-*b*]thiophene) (PTT) is expected to exhibit higher HOMO and LUMO levels than PITN because thiophene is more electron-rich than benzene.

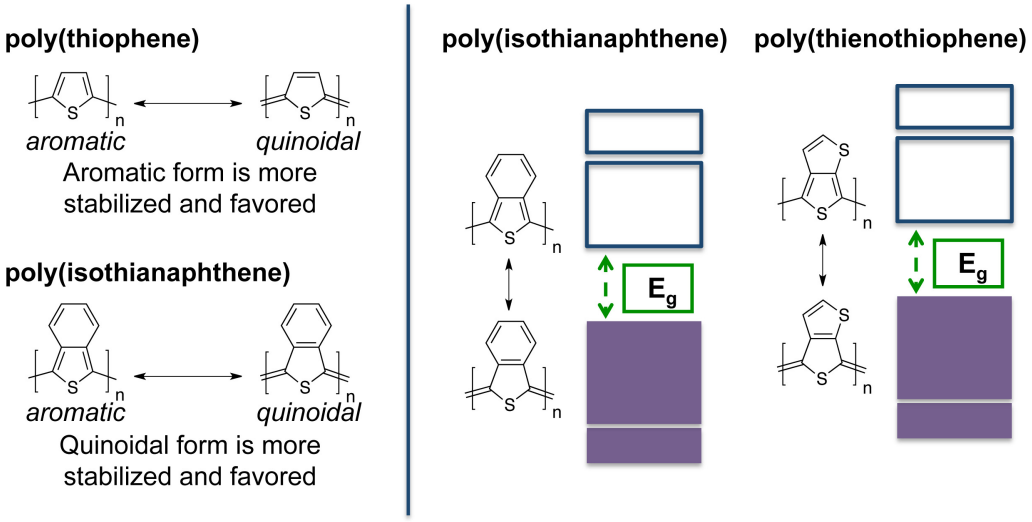

Figure 1-17. Compared to polythiophene, the quinoidal resonance form of poly(isothianaphthene) is stabilized because the fused benzene ring is aromatized. Since the quinoidal form contributes significantly to the overall structure, PITN exhibits reduced BLA, leading to narrow E_g (left). Similar effect of the fused system is observed in poly(thienothiophene) though its frontier MO levels are higher because thiophene is more electron rich than benzene.

Further substitution of fused monomers with functional groups allows for fine-tuning of energy levels, which subsequently affects V_{OC}.[201] Yu and coworkers showed this substituent effect with several copolymers based on the same backbone, PDBTTTs, where the TT comonomers are fluorinated or functionalized with ketones or esters.[114] With the same donor monomer, the best-performing polymer in the series contains a TT monomer appended with a fluoride and a ketone side chain. In another example, Fréchet and coworkers developed a series of BDT-copolymer containing ITN comonomers functionalized with diesters, imide, or dinitriles. It was found that PBDTITNs substituted with diester or imide groups perform as electron donors (p-type) while the installment of dinitrile dramatically lowers the energy levels of PBDTITN, making it perform as an electron acceptor (n-type) in OPV devices.[202]

1.5.3. Sterics

Delocalization of π-electron density relies on p-orbital overlaps. Since this overlap is maximized when the π-system is completely planar, any inter-ring twists break conjugation and reduce conjugation lengths, thereby broadening material band gaps.[203,204] The interannular twists (dihedral angles) can be determined by the torsional angle about the bond that connects two neighboring aromatic rings. Sources that can disrupt molecular planarity include synthetic defects, solvent-molecule interactions, heat, and intrinsic steric hindrance within molecular structures.[205,206]

Deviation from planarity is often undesired, yet steric effects can be used to adjust molecular band gaps, energy levels, and device V_{OC}. In an unpublished work, Fréchet and coworkers synthesized a series of D-A polymers containing benzo-thieno-isoindigo (BTII) or thieno-isoindigo (TII) as the electron-poor comonomer (Figure 1-18). It was demonstrated that PTII2Ts, which possess nearly coplanar backbones, exhibit absorption onset between 889 and 903 nm and perform poorly in OPV devices due to high HOMO energy level. Replacing one of the fused thiophene with benzene yields PBTII2Ts; the six-member fused ring introduces steric hindrance and decreases coplanarity of the entire backbone, thereby widening the band gap and blueshifting the absorption onset to between 769 and 801 nm. Thus, PBTII2Ts display lower HOMO energy levels, larger device J_{SC} and V_{OC}, and higher PCE than do PTII2Ts.[207] In addition to material optoelectronics, sterics strongly influence intermolecular interactions, packing in the solid state, and, subsequently, charge transport (see Section 1.6.).

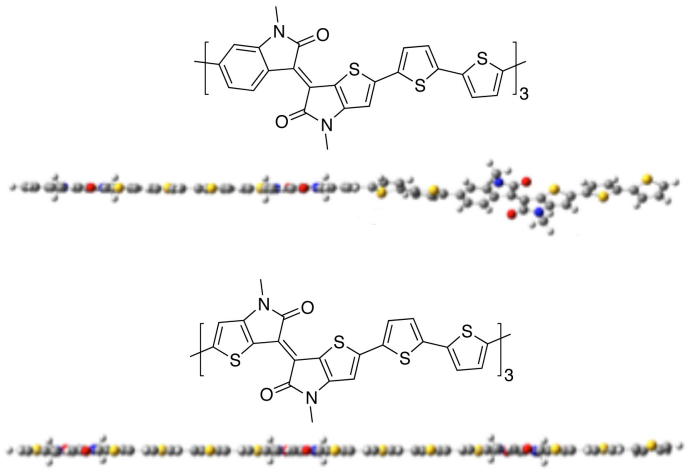

Figure 1-18. Molecular and geometry-optimized (density functional theory, B3LYP/6-31G(d)) structures of BTII2T (top) and TII2T (bottom) trimers. The BTII2T trimer twists because of the steric interactions between benzene and thiophene while the TII2T trimer is completely planar. The complete coplanarity of the TII2T backbone makes its absorption onset much more redshifted than that of BTII2T.

1.6. Strategies for Controlling Nanostructural Order of the OPV Active Layer and Impact on Device Performance

For bulk-heterojunction devices, solution-processability, tight π-π stacking, and long-range crystalline order are important material characteristics that allow for effective charge transport and high power conversion efficiency. Thus, correlating and elucidating the relationship between chemical structures and molecular packing properties can enable the development of promising materials for OPVs. As discussed in the last section, molecules with planar backbones

tend to pack closely since reduced steric hindrance enhances intermolecular interactions. In addition, monomers consist of fused rings (e.g. benzodithiophene) may lead to increased π-π interactions because they exhibit limited degrees of rotational freedom when compared to bonded aromatic rings (e.g. bithiophene).

Chemical structures of side chains appended to conjugated backbones can also be modified to tune the solid-state packing of semiconducting molecules, as well as controlling their solubility.[208–211] These solubilizing side chains are often alkyl groups containing only sp^3-hybridized carbons, which do not conduct charges. Ensuring solution-processability of conjugated materials often requires the use of bulky, branched alkyl substituents, yet materials substituted with excess alkyl groups not only reduces material crystallinity but also increases insulating contents of the active layer. Furthermore, large, branched alkyl groups can prevent conjugated backbones from packing closely due to steric hindrance from substituents with branching points located near the π-system (Figure 1-19). In comparison, substituting conjugated materials with linear alkyl side chains allows for short π-π stacking distance, thereby improving charge transport properties; however, strong intermolecular interactions leads to polymers and small molecules with limited solubility. Thus, finding a balance between solubility, processability, and crystallinity is crucial for developing high-performing OPV materials.[89,190]

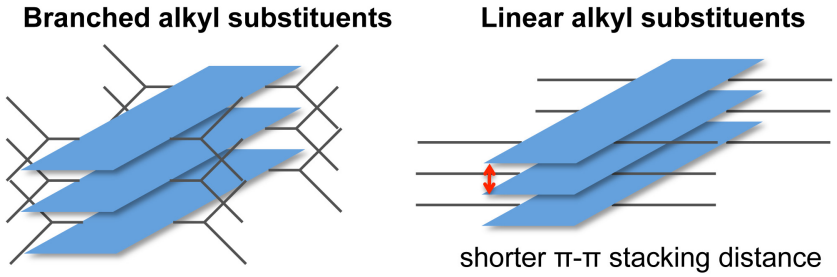

Figure 1-19. Although branched alkyl groups impart solubility to conjugated materials, their branching points can prevent the backbones from packing closely and limit π-π interactions. On the other hand, linear substituents allow molecules to stack with small π-spacing and increased crystallinity; however, strong intermolecular interactions reduce material solubility and processability.

1.7. Dissertation Overview

All of the work presented in this dissertation attempts to elucidate structure-property relationships and new design strategies that will enable future development of efficient materials for organic photovoltaics. The chapters mainly focus on the synthetic progress of novel p-type polymers and small molecules.

Chapter 2 explores the possibility of tuning material solubility via backbone modification. In combination with atomic substitution, the side-chains are modified to further control the solid-state nanostructural order of the polymers. Along with controlling films morphology and solid-state packing of materials, Chapter 3 describes the use of molecular self-assembly as a method to improve the performance of small molecule materials.

Chapter 4 introduces the use of antiaromaticity as a new method to decrease the BLA and, subsequently, the band gap of conjugated materials. Extensive synthetic efforts were explored to develop these new materials that are interesting from the perspective of fundamental, physical organic chemistry. As an extension from the work described in Chapters 2 and 4, we continue to

examine the effect of atomic substitution and side-chain functionalization on the optoelectronics of conjugated materials. Chapter 5 describes the design, development and synthesis of a new building block that, upon copolymerization with benzodithiophene, leads to one of the highest performing polymers in the literature.

The final chapter explores a slightly different system that involves an inorganic component as the electron-acceptor. Using ultrafast spectroscopy, we are able to probe both the electronic and structural dynamics during the charge transfer process.

1.8. References

(1) Table 1.2 Primary Energy Production by Source, Selected Years 1949-2011 (Quadrillion Btu). *US. Energy Information Administration. Annual Energy Review 2011.*
(2) Lewis, N. S.; Nocera, D. G. *Proc. Natl. Acad. Sci.* **2006**, *103*, 15729.
(3) Wadia, C.; Alivisatos, A. P.; Kammen, D. M. *Environ. Sci. Technol.* **2009**, *43*, 2072.
(4) Liu, J.; Tanaka, T.; Sivula, K.; Alivisatos, A. P.; Fréchet, J. M. J. *J. Am. Chem. Soc.* **2004**, *126*, 6550.
(5) Gur, I.; Fromer, N. A.; Chen, C.-P.; Kanaras, A. G.; Alivisatos, A. P. *Nano Lett.* **2007**, *7*, 409-414.
(6) Zhou, H.; Yang, L.; You, W. *Macromolecules* **2012**, *45*, 607.
(7) Li, G.; Zhu, R.; Yang, Y. *Nature Photon*. **2012**, *6*, 153.
(8) Brabec, C. J.; Gowrisanker, S.; Halls, J. J. M.; Laird, D.; Jia, S.; Williams, S. P. *Adv. Mater*. **2010**, *22*, 3839.
(9) Hagfeldt, A.; Boschloo, G.; Sun, L.; Kloo, L; Pettersson, H. *Chem. Rev.*, **2010**, *110*, 6595.
(10) Graetzel, M.; Janssen, R. A. J.; Mitzi, D. B.; Sargent, E. H. *Nature* **2012**, *488*, 304.
(11) Nayak, P. K.; Bisquert, J.; Cahen, D. *Adv. Mater.* **2011**, *23*, 2870.
(12) Law, M.; Greene, L. E.; Johnson, J. C.; Saykally, R.; Yang, P. *Nature Mater.* **2005**, *4*, 455.
(13) Guo, J.; Ohkita, H.; Benten, H.; Ito, S. *J. Am. Chem. Soc*. **2010**, *132*, 6154
(14) Tumbleston, J. R.; Liu, Y.; Samulski, E. T.; Lopez, R. *Adv. Energ. Mater.* **2012**, *2*, 477.
(15) Cheng, Y.-J.; Yang, S.-H.; Hsu, C.-S. *Chem. Rev.* **2009**, *109*, 5868.
(16) Robb, M. J.; Ku, S.-Y.; Brunetti, F. G.; Hawker, C. J. *J. Polym. Sci.: A Polym. Chem.* **2013**, *51*, 1263.
(17) Krebs, F. C. *Sol. Eng. Mater. Sol. Cells* **2009**, 93, 394.
(18) Krebs, F. C.; Tromholt, T.; Jørgensen, M. *Nanoscale* **2010**, *2*, 873.
(19) Pudas, M.; Hagberg, J.; Leppävuori, S. *Progr. Org. Coatings* **2004**, *49*, 324.
(20) Krebs, F. C., Gevorgyan, S. A. & Alstrup, J. *J. Mater. Chem.* **2009**, *19*, 5442.
(21) Green, M. A.; Emery, K.; Hishikawa, Y.; Warta, W.; Dunlop, E. D. *Prog. Photovolt: Res. Appl.* **2013**, *21*, 1.
(22) Service, R. F. *Science* **2011**, *332*, 293.
(23) Thompson, B. C.; Fréchet, J. M. J. *Angew. Chem. Int. Ed.* **2008**, *47*, 58.
(24) Gregg, B. A. *J. Phys. Chem. B* **2003**, *107*, 4688
(25) Tvingstedt, K; Vandewal, K.; Zhang, F.; Inganäs, O. *J. Phys. Chem. C* **2010**, *114*, 21824.
(26) Marks, R. N.; Halls, J. J. M.; Bradley, D. D. C.; Friend, R. H.; Homes, A. B. *J. Phys.: Condens. Matter* **1994**, *6*, 1379.
(27) Knupfer, M. *Appl. Phys. A* **2003**, *77*, 623.
(28) Hains, A. W.; Liang, Z.; Woodhouse, M. A.; Gregg, B. A. *Chem. Rev.* **2010**, 110, 6689.
(29) Blom, P. W. M.; Mihailetchi, V. D.; Koster, L. J. A.; Markov, D. E. *Adv. Mater.* **2007**, *19*, 1551.

(30) Groenendaal, L.; Jonas, F.; Freitag, D.; Pielartzik, H.; Reynolds, J. R. *Adv. Mater.* **2000**, *12*, 481
(31) Norrman, K.; Madsen, M. V.; Gevorgyan, S. A.; Krebs, F. C. *J. Am. Chem. Soc.* **2010**, *132*, 16883.
(32) Jørgensen, M.; Norrman, K.; Gevorgyan, S. A.; Tromholt, T.; Andreasen, B.; Krebs, F. C. *Adv. Mater.* **2012**, *24*, 580.
(33) Grossiord, N.; Kroon, J. M.; Andriessen, R.; Blom, P. W. M. *Org. Electron.* **2012**, *13*, 432.
(34) Tang, C. W. *Appl. Phys. Lett.* **1986**, *48*, 183.
(35) Hadipour, A.; de Boer, B.; Wildeman, J.; Kooistra, F. B.; Hummelen, J. C.; Turbiez, M. G. R.; Wienk, M. M.; Janssen, R. A. J.; Blom, P. W. M. *Adv. Funct. Mater.* **2006**, *16*, 1897.
(36) Hadipour, A.; de Boer, B.; Blom, P. W. M. *Adv. Funct. Mater.* **2008**, *18*, 169.
(37) Dou, L.; You, J.; Yang, J.; Chen, C.-C.; He, Y.; Murase, S.; Moriarty, T.; Emery, K.; Li, G.; Yang Y. *Nature Photon.* **2012**, *6*, 180.
(38) Granström, M.; Petritsch, K.; Arias, A. C.; Lux, A.; Andersson, M. R.; Friend, R. H. *Nature* **1998**, *395*, 257.
(39) Woo, C. H.; Holcombe, T. W.; Unruh, D. A.; Sellinger, A.; Fréchet, J. M. J. *Chem. Mater.* **2010**, *22*, 1673.
(40) Lee, K. H.; Schwenn, P. E.; Smith, A. R. G.; Cavaye, H.; Shaw, P. E.; James, M.; Krueger, K. B.; Gentle, I. R.; Meredith, P.; Burn, P. L. *Adv. Mater.* **2011**, *23*, 766.
(41) Facchetti, A. *Chem. Mater.* **2011**, *23*, 733.
(42) Sariciftci, N. S.; Smilowitz, L.; Heeger, A. J.; Wudl, F. *Science* **1992**, *258*, 1474.
(43) Yu, G.; Gao, J.; Hummelen, J. C.; Wudl, F.; Heeger, A. J. *Science* **1995**, *270*, 1789.
(44) Halls, J. J. M.; Walsh, C. A.; Greenham, N. C.; Marseglia, E. A.; Friend, R. H.; Moratti, S. C.; Holmes, A. B. *Nature* **1995**, *376*, 498.
(45) Günes, S.; Neugebauer, H.; Sariciftci, N. S. *Chem. Rev.* **2007**, *107*, 1324.
(46) Dennler, G.; Scharber, M. C.; Brabec, C. J. *Adv. Mater.* **2009**, *21*, 1323.
(47) Nelson, J. *Mater. Today* **2011**, *14*, 462.
(48) Hung, L. S.; Tang, C. W.; Mason, M. G. *Appl. Phys. Lett.* **1997**, *70*, 152.
(49) Liang, Y; Wu, Y.; Feng, D.; Tsai, S.-T.; Son, H.-J.; Li, G.; Yu, L. *J. Am. Chem. Soc.* **2009**, *131*, 56.
(50) Carsten, B.; Szarko, J. M.; Son, H. J.; Wang, W.; Lu, L.; He, F.; Rolczynski, B. S.; Lou, S. J.; Chen, L. X.; Yu, L. *J. Am. Chem. Soc.* **2011**, *133*, 20468.
(51) White, M. S.; Olson, D. C.; Shaheen, S. E.; Kopidakis, N.; Ginley, D. S. *Appl. Phys. Lett.* **2006**, *89*, 143517.
(52) Ahiswede, E.; Hanisch, J.; Powalla, M. *Appl. Phys. Lett.* **2007**, *90*, 163504.
(53) Jönsson, S. K. M.; Carlegrim, E.; Zhang, F.; Salaneck, W. R.; Fahlman, M. *Jpn. J. Appl. Phys.* **2005,** *44*, 3695.
(54) He, Z.; Zhong, C.; Huang, X.; Wong, W.-Y.; Wu, H.; Chen, L.; Su, S.; Cao, Y. *Adv. Mater.* **2011**, *23*, 4636.
(55) Liao, S. H.; Li, Y.-L.; Jen, T.-H.; Cheng, Y.-S.; Chen, S.-A. *J. Am. Chem. Soc.* **2012**, *134*, 14271.
(56) Na, S-I.; Kim, T. S.; Oh, S-H.; Kim, J-Y.; Kim, S-S.; Kim, D-Y. *Appl. Phys. Lett*. **2010**, *97*, 223305.
(57) Chang, C.-Y.; Cheng, Y.-J; Hung, S.-H.; Wu, J.-S.; Kao, W.-S.; Lee, C.-H.; Hsu, C. S. *Adv. Mater.* **2012**, *24*, 549.

(58) Hau, S. K.; Yip, H.-L.; Baek, N. S.; Zou, J.; O'Malley, K.; Jen, A. K.-Y. *Appl. Phys. Lett.* **2008**, *92*, 253301.
(59) Small, C. E.; Chen, S.; Subbiah, J.; Amb, C. M.; Tsang, S. W.; Lai, T. H.; Reynolds, J. R.; So, F. *Nature Photon.* **2012**, *6*, 115.
(60) Irfan; Ding, H.; Gao, Y.; Kim, D. Y.; Subbiah, J.; So, F. *Appl. Phys. Lett.* **2010**, *96*, 073304.
(61) Kroger, M.; Hamwi, S.; Meyer, J.; Riedl, T.; Kowalsky, W.; Kahn, A. *Appl. Phys. Lett.* **2009**, *95*, 1233019
(62) Schmidt, H.; Flugge, H.; Winkler, T.; Bulow, T.; Riedl, T.; Kowalsky, W. *Appl. Phys. Lett.* **2009**, *94*, 243302.
(63) Yoo, S.; Domercq, B.; Kippelen, B. *Appl. Phys. Lett.* **2004**, *85*, 5427.
(64) Terao, Y.; Sasabe, H.; Adachi, C. *Appl. Phys. Lett.* **2007**, *90*, 103515.
(65) Stübinger, T.; Brütting, W. *J. Appl. Phys.* **2001**, *90*, 3632.
(66) Brédas, J.-L.; Norton, J. E.; Cornil, J.; Coropceanu, V. *Acc. Chem. Res.* **2009**, *42*, 1691.
(67) Haugeneder, A.; Neges, M.; Kallinger, C.; Spirkl, W.; Lemmer, U.; Feldmann, J.; Scherf, U.; Harth, E.; Gügel, A.; Müllen, K. *Phys. Rev. B* **1999**, *59* 15346.
(68) Brédas, J.-L.; Beljonne, D.; Coropceanu, V.; Cornil, J. *Chem. Rev.* **2004,** 104, 4971.
(69) Holcombe,T. W.; Norton, J. E.; Rivnay, J.; Woo, C. H.; Goris, L.; Piliego, C.; Griffini, G.; Sellinger, A.; Brédas, J.-L.; Salleo, A.; Fréchet, J. M. J. *J. Am. Chem. Soc.* **2011**, *133*, 12106.
(70) Tvingstedt, K.; Vandewal, K.; Gadisa, A.; Zhang, F.; Manca, J.; Inganäs, O. *J. Am. Chem. Soc.* **2009**, *131*, 11819.
(71) Bakulin, A. A.; Rao, A.; Pavelyev, V. G.; van Loosdrecht, P. H. M.; Pshenichnikov, M. S.; Niedzialek, D.; Cornil, J.; Beljonne, D.; Friend, R. H. *Science* **2012**, *335*, 1340.
(72) Credgington, D.; Jamieson, F. C.; Walker, B.; Nguyen, T.-Q.; Durrant, J. R. *Adv. Mater.* **2012**, *24*, 2135.
(73) Faist, M. A.; Kirchartz, T.; Gong, W.; Ashraf, R. S.; McCulloch, I.; de Mello, J. C.; Ekins-Daukes, N. J.; Bradley, D. D. C.; Nelson, J. *J. Am. Chem. Soc.* **2012**, *134*, 685.
(74) Thomas J. K. Brenner,† Zhe Li,† and Christopher R. McNeill *J. Phys. Chem. C*, **2011**, *115*, 22075.
(75) Yamamoto, S.; Ohkita, H.; Benten, H.; Ito, S. *Adv. Funct. Mater.* **2012**, *22*, 3075.
(76) Howard, I. A.; Mauer, R.; Meister, M.; Laquai, F. *J. Am. Chem. Soc.* **2010**, *132*, 14866.
(77) Carsten, B.; Szarko, J. M.; Son, H. J.; Wang, W.; Lu, L.; He, F.; Rolczynski, B. S.; Lou, S. J.; Chen, L. X.; Yu, L. *J. Am. Chem. Soc.* **2011**, *133*, 20468.
(78) Ohkita, H.; Cook, S.; Astuti, Y.; Duffy, W.; Tierney, S.; Zhang, W.; Heeney, M.; McCulloch, I.; Nelson, J.; Bradley, D. D. C.; Durrant, J. R. *J. Am. Chem. Soc.* **2008**, *130*, 3030.
(79) Coropceanu, V.; Cornil, J.; da Silva Filho, D. A.; Olivier, Y.; Silbey, R.; Brédas, J.-L. *Chem. Rev.* **2007**, *107*, 926.
(80) Zaumseil, J.; Sirringhaus, H. *Chem. Rev.* **2007,** *107*, 1296.
(81) Zhang, L.; Colella, N. S.; Liu, F.; Trahan, S.; Baral, J. K.; Winter, H. H.; Mannsfeld, S. C. B.; Briseno, A. L. *J. Am. Chem. Soc.* **2013**, *135*, 844.
(82) Cho, E.; Risko, C.; Kim, D.; Gysel, R.; Miller, N. C.; Breiby, D. W.; McGehee M. D.; Toney, M. F.; Kline, R. J.; Brédas, J.-L. *J. Am. Chem. Soc.* **2012**, *134*, 6177.
(83) Rogers, J. T.; Schmidt, K.; Toney, M. F.; Kramer, E. J.; Bazan, G. C. *Adv. Mater.* **2011**, *23*, 2284.

(84) Koster, L. J. A.; Kemerink, M.; Wienk, M. M.; Maturová, K.; Janssen, R. A. J. *Adv. Mater.* **2011**, *23*, 1670.
(85) Keivanidis, P. E.; Kamm, V.; Zhang, W.; Floudas, G.; Laquai, F.; McCulloch, I.; Bradley, D. D. C.; Nelson, J. *Adv. Funct. Mater.* **2012**, *22*, 2318.
(86) Chen, H.-C.; Chen, Y.-H.; Liu, C.-C.; Chien, Y.-C.; Chou, S.-W.; Chou, P.-T. *Chem. Mater.* **2012**, *24*, 4766.
(87) Khlyabich, P. P.; Burkhart, B.; Ng, C. F.; Thompson, B. C. *Macromolecules* **2011**, *44*, 5079.
(88) Moliton, A.; Nunzi J.-M. *Polym. Int.* **2006**, *55*, 583.
(89) Yiu, A. T.; Beaujuge, P. M.; Lee, O. P.; Woo, C. H.; Toney, M. F.; Fréchet, J. M. J. *J. Am. Chem. Soc.* **2012**, *134*, 2180.
(90) Gong, X.; Tong, M.; Brunetti, F. G.; Seo, J.; Sun, Y.; Moses, D.; Wudl, F.; Heeger, A. J. *Adv. Mater.* **2011**, *23*, 2272.
(91) Vandewal, K.; Tvingstedt, K.; Gadisa1, A.; Inganäs, O.; Manca, J. V. *Nature Mater.* **2009**, *8*, 904.
(92) Yamamoto, S.; Orimo, A.; Ohkita, H.; Benten, H.; Ito, S. *Adv. Energy Mater.* **2012**, *2*, 229.
(93) Ko, S.; Hoke, E. T.; Pandey, L.; Hong, S.; Mondal, R.; Risko, C.; Yi, Y.; Noriega, R.; McGehee, M. D.; Brédas, J.-L.; Salleo, A.; Bao, Z. *J. Am. Chem. Soc.*, **2012**, *134*, 5222
(94) Mutolo, K. L.; Mayo, E. I.; Rand, B. P.; Forrest, S. R.; Thompson, M. E. *J. Am. Chem. Soc.* **2006**, *128*, 8108.
(95) Albrecht, S.; Janietz, S.; Schindler, W.; Frisch, J.; Kurpiers, J.; Kniepert, J.; Inal, S.; Pingel, P.; Fostiropoulos, K.; Koch, N.; Neher, D. *J. Am. Chem. Soc.* **2012**, *134*, 14932.
(96) Perez, M. D.; Borek, C.; Forrest, S. R.; Thompson, M. E. *J. Am. Chem. Soc.* **2009**, *131*, 9281.
(97) Yang, L.; Zhou, H., You, W. *J. Phys. Chem. C* **2010**, *114*, 16793.
(98) Brabec, C. J.; Heeney, M.; McCulloch, I.; Nelson, J. *Chem. Soc. Rev.* **2011**, *40*, 1185.
(99) Moulé, A. J.; Meerholz, K. *Adv. Funct. Mater.* **2009**, *19*, 3028.
(100) Hoppe, H.; Sariciftci, N. S. *J. Mater. Chem.* **2006**, *16*, 45.
(101) Anslyn, E. V.; Dougherty, D. A. *Advanced Concepts in Electronic Structure Theory.* In *Modern Physical Organic Chemistry*; University Science Books; 2006, pp 807–876.
(102) Gettinger, C. L.; Heeger, A. J.; Drake, J. M.; Pine, D. J. *J. Chem. Phys.* **1994**, *101*, 1673.
(103) Hoffman, R. *Angew. Chem. Int. Ed. Engl.* **1987**, *26*, 846
(104) Anslyn, E. V.; Dougherty, D. A. *Electronic Organic Materials.* In *Modern Physical Organic Chemistry*; University Science Books; 2006, pp 1001–1045.
(105) Brédas, J.-L. *J. Chem. Phys.* **1985**, *82*, 3808.
(106) Lowe, J. P.; Kafafi, S. A. *J. Am. Chem. Soc.* **1984**, *106*, 5837.
(107) Bredas, J.-L.; Silbey, R.; Boudreaux, D. S.; Chance, R. R. *J. Am. Chem. Soc.* **1983**, *105*, 6555.
(108) Meier, H.; Stalmach, U.; Kolshorn, H. *Acta Polym.* 1997, *48*, 379.
(109) Klaerner, G.; Miller, R. D. *Macromolecules* **1998**, *31*, 2007.
(110) Sirringhaus, H.; Brown, P. J.; Friend, R. H.; Nielsen, M. M.; Bechgaard, K.; Langeveld-Voss, B. M. W.; Spiering, A. J. H.; Janssen, R. A. J.; Meijer, E. W.; Herwig, P.; de Leeuw, D. M. *Nature* **1999**, *401*, 685.
(111) Patil, A. O.; Heeger, A. J.; Wudl, F. *Chem. Rev.* 1988, 88, 183.
(112) Bundgaard, E.; Krebs, F. C. *Sol. Energ. Mat. Sol. C.* **2007**, *91*, 954.
(113) Roncali, J. *Macromol. Rapid Commun.* **2007**, *28*, 1761.

(114) Chen, H.-Y.; Hou, J.; Zhang, S.; Liang, Y.; Yang, G.; Yang, Y.; Yu, L.; Wu, Y.; Li, G. *Nature Photon.* **2009**, *3*, 649.
(115) Fabiano, S.; Chen, Z.; Vahedi, S.; Facchetti, A.; Pignataroc, B.; Loi, M. A. *J. Mater. Chem.* **2011**, *21*, 5891.
(116) Dang, M. T.; Hirsch, L.; Wantz, G.; Wuest, J. D. *Chem. Rev.*, **2013**, *113*, 3734.
(117) Lou, S. J.; Szarko, J. M.; Xu, T.; Yu, L.; Marks, T. J.; Chen, L. X. *J. Am. Chem. Soc.* **2011**, *133*, 20661.
(118) Liu, X.; Huettner, S.; Rong, Z.; Sommer, M.; Friend, R. H. *Adv. Mater.* **2012**, *24*, 669.
(119) Moon, J. S.; Takacs, C. J.; Cho, S.; Coffin, R. C.; Kim, H.; Bazan, G. C.; Heeger, A. J. *Nano Lett.* **2010**, *10*, 4005.
(120) Brabec, C. J.; Winder, C.; Sariciftci, N. S.; Hummelen, J. C.; Dhanabalan, A.; van Hal, P. A.; Janssen, R. A. J. *Adv. Funct. Mater.* **2002**, *12*, 709.
(121) Rand, B. P.; Burk, D. P.; Forrest, S. R. *Phys. Rev. B* **2007**, *75*, 116327.
(122) Holcombe, T. W.; Woo, C. H.; Kavulak, D. F. J.; Thompson, B. C.; Fréchet, J. M. J. *J. AM. Chem. Soc.* **2009**, *131*, 14160.
(123) Zhou, H.; Yang, L.; Liu, S.; You, W. *Macromolecules* **2010**, *43*, 10390.
(124) He, F.; Yu, L. *J. Phys. Chem. Lett.* **2011**, *2*, 3102.
(125) Kooistra, F. B.; Knol, J.; Kastenberg, F.; Popescu, L. M.; Verhees, W. J. H.; Kroon, J. M.; Hummelen, J. C. *Org. Lett.* **2007**, *9*, 551.
(126) Heremans, P.; Cheyns, D.; Rand, B. P. *Acc. Chem. Res.* **2009**, *42*, 1740.
(127) Zhang, L.; Colella, N. S.; Liu, F.; Trahan, S.; Baral, J. K.; Winter, H. H.; Mannsfeld, S. C. B.; Briseno, A. L. *J. Am. Chem. Soc.* **2013**, *135*, 844
(128) Rivnay, J.; Jimison, L. H.; Northrup, J. E.; Toney, M. F.; Noriega, R.; Lu, S.; Marks, T. J. Facchetti, A.; Salleo, A. *Nature Mater.* **2009**, *8* 952.
(129) Reyes-Martinez, M. A.; Ramasubramaniam, A.; Briseno, A. L.; Crosby, A. J. *Adv. Mater.* **2012**, *24*, 5548.
(130) Anthony, J. E. *Angew. Chem. Int. Ed.* **2008**, *47*, 452.
(131) Lei, T.; Cao, Y.; Fan, Y.; Liu, C.-J.; Yuan, S.-C.; Pei, J. *J. Am. Chem. Soc.* **2011**, *133*, 6099.
(132) Wang, E.; Ma, Z.; Zhang, Z.; Vandewal, K.; Henriksson, P.; Inganäs, O.; Zhang, F.; Andersson, M. R. *J. Am. Chem. Soc.* **2011**, *133*, 14244.
(133) Brown, P. J.; Thomas, D. S.; Köhler, A.; Wilson, J. S.; Kim, J.-S.; Ramsdale, C. M.; Sirringhaus, H.; Friend, R. H. *Phys. Rev. B* **2003**, *67*, 064203.
(134) Liang, Y.; Wu, Y.; Feng, D.; Tsai, S.-T.; Son, H. J.; Li, G.; Yu, L. *J. Am. Chem. Soc.* **2009**, *131*, 56.
(135) Amb, C. M.; Chen, S.; Graham, K. R.; Subbiah, J.; Small, C. E.; So, F.; Reynolds, J. R. *J. Am. Chem. Soc.* **2011**, *133*, 10062.
(136) Cardona, C. M.; Li, W.; Kaifer, A. E.; Stockdale, D.; Bazan, G. C. *Adv. Mater.* **2011**, *23*, 2367.
(137) Drees, M.; Hoppe, H.; Winder, C.; Neugebauer, H.; Sariciftci, N. S.; Schwinger, W.; Schäffler, F.; Topf, C.; Scharber, M. C.; Zhu, Z.; Gaudiana, R. *J. Mater. Chem.* **2005**, *15*, 5158.
(138) Drummy, L. F.; Davis, R. J.; Moore, D. L.; Durstock, M.; Vaia, R. A.; Hsu, J. W. P. *Chem. Mater.* **2011**, *23*, 907.
(139) Verhees, W. J. H.; Wienk, M. M.; Kroon, J. M.; Michels, M. A. J.; Janssen, R. A. J.; Yang, X.; Loos, J.; Veenstra, S. C. *Nano Lett.* **2005**, *5*, 579.

(140) DeLongchamp, D. M.; Kline, R. J.; Fischer, D. A.; Richter, L. J.; Toney, M. F. *Adv. Mater.* **2011**, *23*, 319.
(141) Mihailetchi, V. D.; Wildeman, J.; Blom, P. W. M. *Phys. Rev. Lett.* **2005**, *94*, 126602.
(142) Melzer, C.; Koop, E. J.; Mihailetchi, V. D.; Blom, P. W. M. *Adv. Funct. Mater.* **2004**, *14*, 865.
(143) Shrotriya, V.; Li, G.; Yao, Y.; Moriarty, T.; Emery, K.; Yang, Y. *Adv. Funct. Mater.* **2006**, *16*, 2016.
(144) Carsten, B.; He, F.; Son, H. J.; Xu, T.; Yu, L. *Chem. Rev.* **2011**, *111*, 1493.
(145) Sakamoto, J.; Rehahn, M.; Wegner, G.; Schlüter, A. D. *Macromol. Rapid Commun.* **2009**, *30*, 653.
(146) Chen, T.-A.; Wu, X.; Rieke, R. D. *J. Am. Chem. Soc.* **1995**, *117*, 233.
(147) Jeffries-El, M.; Sauvé, G.; McCullough, R. D. *Macromolecules* **2005**, *38*, 10346.
(148) Nikiforov, M. P.; Lai, B.; Chen, W.; Chen, S.; Schaller, R. D.; Strzalka, J.; Maser, J.; Darling, S. B. *Energy Environ. Sci.* **2013**, *6*, 1513.
(149) Jørgensen, M.; Norrman, K.; Krebs, F. C. *Sol. Energy. Mat. Sol. C.* **2008**, *92*, 686.
(150) Nielsen, K. T.; Bechgaard, K.; Krebs, F. C. *Macromolecules* **2005**, *38*, 658.
(151) Helgesen, M.; Sondergaard, R.; Krebs, F. C. *J. Mater. Chem.* **2010**, *20*, 36.
(152) Blouin, N.; Michaud, A.; Leclerc, M. *Adv. Mater.* **2007**, *19*, 2295.
(153) Shi, Q.; Fan, H.; Liu, Y.; Chen, J.; Shuai, Z.; Hu, W.; Li, Y.; Zhan, X. *J. Polym. Sci. A: Polym. Chem.* **2011**, *49*, 4875.
(154) Zou, Y.; Gendron, D.; Badrou-Aïch, R.; Najari, A.;Tao, Y.; Leclerc, M. *Macromolecules* **2009**, *42*, 2891.
(155) Peters, C. H.; Sachs-Quintana, I. T.; Mateker, W. R.; Heumueller, T.; Rivnay, J.; Noriega, R.; Beiley, Z. M.; Hoke, E. T.; Salleo, A.; McGehee, M. D. *Adv. Mater.* **2012**, *24*, 663.
(156) Mateker, W. R.; Douglas, J. D.; Cabanetos, C; Beaujuge, P. M. B.; Fréchet J. M. J.; McGehee, M. D. *Unpublished results*.
(157) Roncali, J. *Acc. Chem. Res.* **2009**, *42*, 1719.
(158) Walker, B.; Kim, C.; Nguyen, T.-Q. *Chem. Mater.* **2011**, *23*, 470.
(159) Mishra, A.; Bäuerle, P. *Angew. Chem. Int. Ed.* **2012**, *51*, 2020.
(160) Anthony, J. E. *Chem. Mater.* **2011**, *23*, 583.
(161) Lin, Y.; Li, Y.; Zhan, X. *Chem. Soc. Rev.* **2012**, *41*, 4245.
(162) Stingelin-Stutzmann, N.; Smits, E.; Wondergem, H.; Tanase, C.; Blom, P.; Smith, P.; de Leeuw, D. *Nature Mater.* **2005**, *4*, 601.
(163) Sato, M.; Tanaka, S.; Kaeriyama, K. *J. Chem. Soc., Chem. Commun.* **1986**, 873.
(164) Bao, Z.; Dodabalapur, A.; Lovinger, A. J. *Appl. Phys. Lett.* **1996**, *69*, 23.
(165) Zhao, G.; He, Y.; Li, Y. *Adv. Mater.* **2010**, *22*, 4355.
(166) Chen, H.-C.; Chen, Y.-H.; Liu, C.-C.; Chien, Y.-C.; Chou, S.-W.; Chou, P. T. *Chem. Mater.* **2012**, *24*, 4766.
(167) Cabanetos, C.; El Labban, A.; Bartelt, J. A.; Douglas, J. D.; Mateker, W. R.; Fréchet, J. M. J.; McGehee, M. D.; Beaujuge, P. M. B. *J. Am. Chem. Soc.* **2013**, *135*, 4656.
(168) Lu, L.; Luo, Z.; Xu, T.; Yu, L. *Nano Lett.* **2013**, *13*, 59.
(169) Choi, H.; Lee, J.-P.; Ko, S.-J.; Jung, J.-W.; Park, H.; Yoo, S.; Park, O.; Jeong, J.-R.; Park, S.; Kim, J. Y. *Nano Lett.* **2013**, *13*, 2204.
(170) He, Z.; Zhong, C.; Su, S.; Xu, M.; Wu, H.; Cao, Y. *Nature Photon.* **2012**, *6*, 591.
(171) van der Poll, T. S.; Love, J. A.; Nguyen, T.-Q.; Bazan, G. C. *Adv. Mater.* **2012**, *24*, 3646.
(172) Hummelen, J. C.; Knight, B. W.; LePeq, F.; Wudl F. *J. Org. Chem.* **1995**, *60*, 532.

(173) Wienk, M. M.; Kroon, J. M.; Verhees, W. J. H.; Knol, J. K.; Hummelen, J. C.; van Hal, P. A.; Janssen R. A. J. *Angew. Chem. Int. Ed.* **2003**, *42*, 3371.
(174) He, Y.; Chen, H.-Y.; Hou, J.; Li, Y. *J. Am. Chem. Soc.* **2010**, *132*, 1377.
(175) Arbogast, J. W.; Foote, C. S. *J. Am. Chem. Soc.* **1991**, *113*, 8886.
(176) Bloking, J. T.; Han, X.; Higgs, A. T.; Kastrop, J. P.; Pandey, L.; Norton, J. E.; Risko, C.; Chen, C. E.; Brédas, J.-L.; McGehee, M. D.; Sellinger, A. *Chem. Mater.* **2011**, *23*, 5484.
(177) Zhou, E.; Cong, J.; Wei, Q.; Tajima, K.; Yang, C.; Hashimoto, K. *Angew. Chem. Int. Ed*. **2011**, *50*, 2799.
(178) Henson, Z. B.; Müllen, K.; Bazan, G. C. *Nature Chem.* **2012**, *4*, 699.
(179) Boudreault, P.-L. T.; Najari, A.; Leclerc, M. *Chem. Mater.* **2011**, *23*, 456.
(180) Kroon, R.; Lenes, M.; Hummelen, J. C.; Blom, P. W. M.; de Boer, B. *Polym. Rev.* **2008**, *48*, 531.
(181) Mühlbacher, D.; Scharber, M.; Morana, M.; Zhu, Z.; Waller, D.; Gaudiana, R.; Brabec, C.; *Adv. Mater.* **2006**, *18*, 2884.
(182) Peet, J.; Kim, J. Y.; Coates, N. E.; Ma, W. L.; Moses, D.; Heeger, A. J.; Bazan, G. C. *Nature Mater.* **2007**, *6*, 497.
(183) Zhou, H.; Yang, L.; Stoneking, S.; You, W. *ACS Appl. Mater. Interfaces* **2010**, *2*, 1377.
(184) Hou, J.; Park, M.-H.; Zhang, S.; Yao, Y.; Chen, L.-M.; Li, J.-H.; Yang, Y. *Macromolecules* **2008**, *41*, 6012.
(185) Li, Y. *Acc. Chem. Res.* **2012**, *45*, 723.
(186) Liang, Y.; Yu, L. *Acc. Chem. Res.*, **2010**, *43*, 1227.
(187) Allard, N.; Aïch, R. d. B.; Gendron, D.; Boudreault, P.-L. T.; Tessier, C.; Alem, S.; Tse, S.-C.; Tao, Y.; Leclerc, M. *Macromolecules* **2010**, *43*, 2328.
(188) Amb, C. M.; Chen, S.; Graham, K. R.; Subbiah, J.; Small, C. E.; So, F.; Reynolds, J. R. *J. Am. Chem. Soc.* **2011**, *133*, 10062.
(189) Zou, Y.; Najari, A.; Berrouard, P.; Beaupré, S.; Réda-Aïch, B.; Tao, Y.; Leclerc, M. *J. Am. Chem. Soc.* **2010**, *132*, 5330.
(190) Piliego, C.; Holcombe, T. W.; Douglas, J. D.; Woo, C. H.; Beaujuge, P. M.; Fréchet, J. M. J. *J. Am. Chem. Soc.* **2010**, *132*, 7595.
(191) Chu, T.-Y.; Lu, J.; Beaupré, S.; Zhang, Y.; Pouliot, J.-R.; Wakim, S.; Zhou, J.; Leclerc, M.; Li, Z.; Ding, J.; Tao, Y. *J. Am. Chem. Soc.* **2011**, *133*, 4250.
(192) Liang, Y.; Feng, D.; Wu, Y.; Tsai, S.-T.; Li, G.; Ray, C.; Yu, L. *J. Am. Chem. Soc.*, **2009**, *131*, 7792.
(193) Li, W.; Roelofs, W. S. C.; Wienk, M. M.; Janssen, R. A. J. *J. Am. Chem. Soc.* **2012**, *134*, 13787.
(194) Yiu, A. T.; Beaujuge, P. M.; Lee, O. P.; Woo, C. H.; Toney, M. F.; Fréchet, J. M. J. *J. Am. Chem. Soc.* **2012**, *134*, 2180.
(195) Bronstein, H.; Chen, Z.; Ashraf, R. S.; Zhang, W.; Du, J.; Durrant, J. R.; Tuladhar, P. S.; Song, K.; Watkins, S. E.; Geerts, Y.; Wienk, M. M.; Janssen, R. A. J.; Anthopoulos, T.; Sirringhaus, H.; Heeney, M.; McCulloch, I. *J. Am. Chem. Soc.* **2011**, *133*, 3272.
(196) Walker, B.; Tamayo, A. B.; Dang, X. D.; Zalar, P.; Seo, J. H.; Garcia, A.; Tantiwiwat, M.; Nguyen, T.-Q. *Adv. Funct. Mater.* **2009**, *19*, 3063.
(197) Zhou, H.; Yang, L.; Stuart, A. C.; Price, S. C.; Liu, S.; You, W. *Angew. Chem. Int. Ed.* **2011**, *50*, 2995.
(198) Sun, Y.; Welch, G. C.; Leong, W. L.; Takacs, C. J.; Bazan, G. C.; Heeger, A. J. *Nature Mater.* **2012**, *11*, 44.

(199) Peart, P. A.; Repka, L. M.; Tovar, J. D. *Eur. J. Org. Chem.* **2008**, 2193.
(200) Bredas, J.-L.; Heeger, A. J.; Wudl, F. *J. Chem. Phys.* **1986**, *85*, 4673.
(201) Kleinhenz, N.; Yang, L.; Zhou, H.; Price, S. C.; You, W. *Macromolecules* **2011**, *44*, 872.
(202) Douglas, J. D.; Griffini, G.; Holcombe, T. H.; Young, E. P.; Lee, O. P.; Chen, M. S.; Fréchet, J. M. J. *Macromolecules* **2012**, *45*, 4069.
(203) McCullough, R. D.; Tristram-Nagle, S.; Williams, S. P.; Lowe, R. D.; Jayaraman, M. *J. Am. Chem. Soc.* **1993**, *115*, 4910.
(204) Ko, S.; Hoke, E. T.; Pandey, L.; Hong, S.; Mondal, R.; Risko, C.; Yi, Y.; Noriega, R.; McGehee, M. D.; Brédas, J.-L.; Salleo, A.; Bao, Z. *J. Am. Chem. Soc.* **2012**, *134*, 5222.
(205) Guo, J.; Ohkita, H.; Benten, H.; Ito, S. *J. Am. Chem. Soc.* **2010**, *132*, 6154.
(206) Inganäs, O.; Salaneck, W.; Österholm, J.; Laakso, J. *Synthetic Metals* **1988**, *22*, 395.
(207) Chen, M. S.; Niskala, J. R.; Unruh, D. A.; Chu, C. K.; Lee, O. P.; Moreton, J. C.; Fréchet, J. M. J. *In preparation*.
(208) Uy, R. L.; Price, S. C.; You, W. *Macromol. Rapid Commun.* **2012***, 33*, 1162.
(209) Zhang, X.; Richter, L. J.; DeLongchamp, D. M.; Kline, R. J.; Hammond, M. R.; McCulloch, I.; Heeney, M.; Ashraf, R. S.; Smith, J. N.; Anthopoulos, T. D.; Schroeder, G.; Geerts, Y. H.; Fischer, D. A.; Toney, M. F. *J. Am. Chem. Soc.* **2011**, *133*, 15073.
(210) Massip, S.; Oberhumer, P. M.; Tu, G.; Albert-Seifried, S.; Huck, W. T. S.; Friend, R. H.; Greenham, N. C. *J. Phys. Chem. C* **2011**, *115*, 25046.
(211) Mei, J.; Kim, D. H.; Ayzner, A. L.; Toney, M. F.; Bao, Z. *J. Am. Chem. Soc.* **2011**, *133*, 20130.

Chapter II

Controlling Solubility and Thin-Film Nanostructural Order of Diketopyrrolopyrrole (DPP)-Furan Polymers via Furan Incorporation and Side-Chain Modulation

2.1. Introduction: Viability of Furan as a Building Block for Conjugated Materials

Organic photovoltaic (OPV) technology has the potential for low-cost, high-throughput energy generation. To date, much research has been directed toward developing low band-gap donor polymers that can be used in bulk-heterojunction (BHJ) devices with fullerene-derived electron-acceptors.[1–10] The search for new building blocks for semiconducting polymers continues as we gain understanding of the structure-property relationships that govern material performance and establish design rules relevant to organic electronic applications.[3,11,12]

The chemical structure of a conjugated polymer, including backbone repeat units and the solubilizing side chains, has been shown to influence properties such as light absorption,[10,13,14] electronic compatibility with the fullerene acceptor,[15–19] charge transport characteristics,[20–23] thin-film morphology,[24–26] and molecular packing.[27–30] However, structural changes often have competing effects on these properties and, in turn, on device performance. For instance, while using a longer or larger solubilizing alkyl side chain generally improves solution-processability, it is also expected to increase insulating content and decrease material crystallinity. Thus, overcoming performance limitations imposed by these competing effects requires a means of optimizing one property with minimal adverse effect on others. In this regard, strategies to reduce the length, bulkiness, and density of solubilizing groups along the polymer backbone while maintaining polymer solubility and processability are well worth exploring.

A survey of state-of-the-art BHJ solar cells reveals that most high-performance polymers reported so far rely on thiophene or thiophene-based heterocycles.[31–41] While thiophene-containing conjugated materials have attracted much attention in the area of organic electronics, only a limited number of studies have examined furan-containing materials for device applications.[41–44] Recently, furans have been used as an alternative to thiophenes in organic dyes for dye-sensitized solar cells and have shown very similar optoelectronic properties.[45,46] Furan-based heterocycles have also been introduced as peripheral substituents on a high-performing small molecule for OPVs.[47] Based on these considerations, we designed two furan-containing semiconducting polymers: PDPP2FT-2EH and PDPP3F-2EH, which are based on the analogous, thiophene-containing PDPP3T-2HD previously reported by Janssen *et al.*, and investigated their performance in OPVs (Figure 2-1).[48] We show that furan heterocycles can be advantageously incorporated into conjugated polymer backbones without hindering their photovoltaic device performance. We further demonstrate that furans can be used to reduce a significant amount of aliphatic side-chain material necessary to solubilize polymer backbones. This discovery allows for the replacement of branched alkyl side chains with linear ones, thereby enhancing polymer nanostructural order in thin films and subsequently improving polymer performance in solar cells.

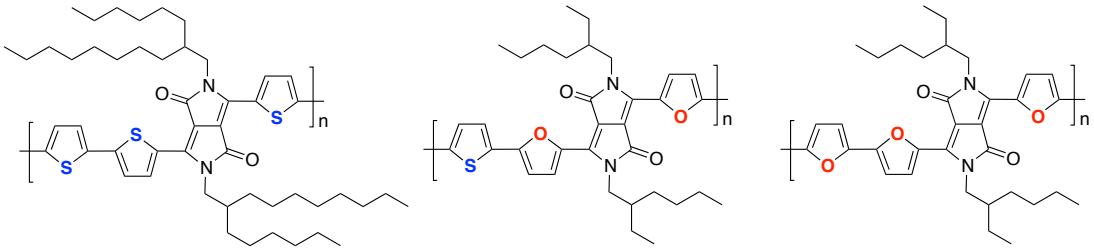

Figure 2-1. Structures of PDPP3T-2HD, PDPP2FT-2EH, and PDPP3F-2EH (DPP = diketopyrrolopyrrole, T = thiophene, F = furan, 2HD = 2-hexyldecyl, and 2EH = 2-ethylhexyl).

2.2. Solubility Enhancement through the Incorporation of Furan into Polymer Backbones

2.2.1. Design and Synthesis of Furan-Containing Diketopyrrolopyrrole Polymers

To demonstrate our concept, we chose our model system based on a previously reported polymer containing an electron-deficient diketopyrrolopyrrole (DPP)[17,47–58] moiety—PDPP3T. This particular structure enables us to systematically replace the thiophene comonomers with furan and determine the effect of this substitution on polymer properties and device performance. Modifying the synthesis of 2,5-dialkyl-3,6-di(thiophen-2-yl)-diketopyrrolepyrrole allows us to obtain the dibrominated DPP-comonomers, and PDPP2FT and PDPP3F are polymerized through Stille cross-coupling reaction (Scheme 2-1).

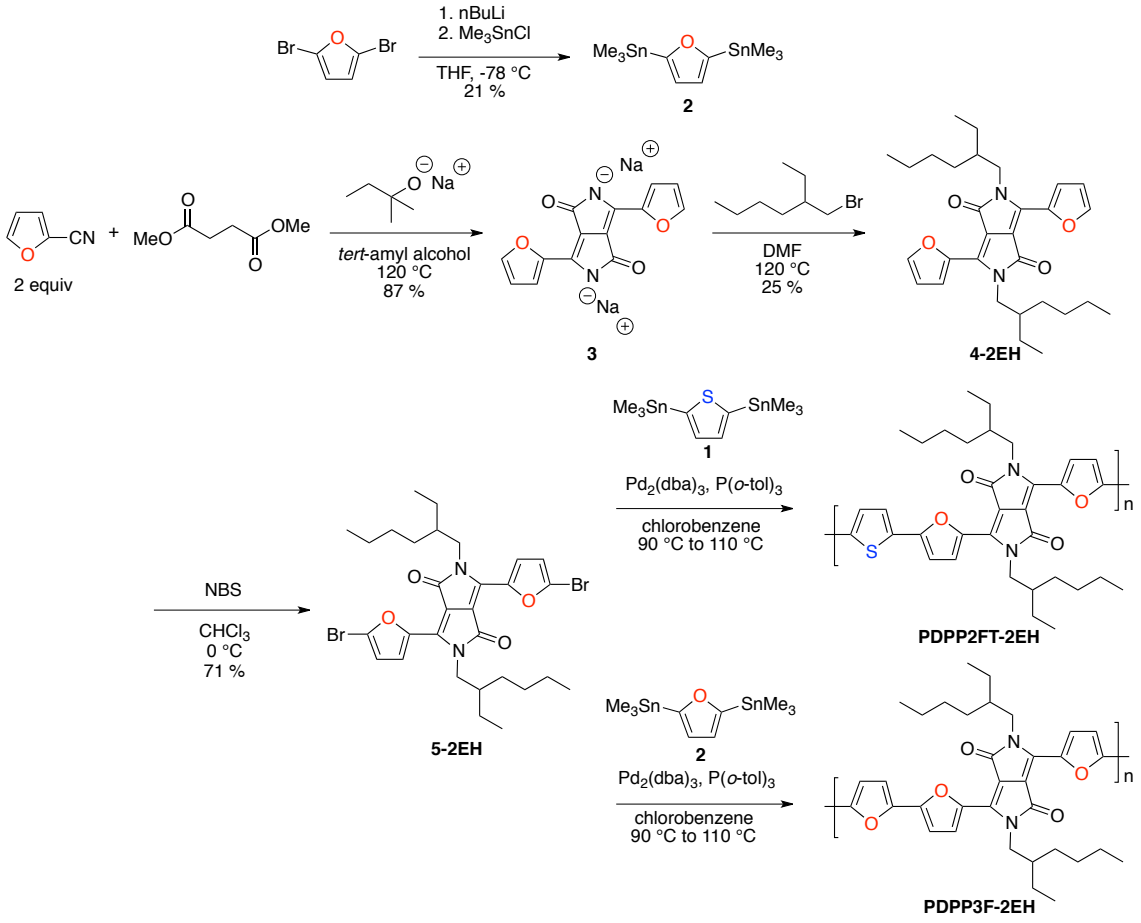

Scheme 2-1. Synthesis of PDPP2FT-2EH and PDPP3F-2EH.

Briefly, 2,5-bis(trimethylstannyl)thiophene **1** was recrystallized from the commercially available reagent, and 2,5-bis(trimethylstannyl)furan **2** was synthesized by lithiation of 2,5-dibromofuran followed by the addition of trimethyltin chloride. High-purity comonomer **2** was obtained after distillation under reduced pressure. A condensation reaction, promoted by *tert*-amyl alkoxide, between 2-furonitrile and dimethylsuccinate afforded the disodium salt of 3,6-di(furan-2-yl)-diketopyrrolopyrrole **3**, which was then alkylated with the 2-ethylhexyl bromide to yield **4**. Subsequent bromination of **4** with *N*-bromosuccinimide furnishes comonomer **5**. Stille polycondensation of comonomers **5** and either **1** or **2** yields PDPP2FT-2EH or PDPP3F-2EH, respectively. It is important to note that both PDPP2FT-2EH and PDPP3F-2EH were

synthesized with 2-ethylhexyl (2EH) groups as the side-chains, while the reported PDPP3T-2HD was functionalized with 2-hexyldecyl (2HD) groups.[48]

We found that PDPP2FT-2EH could be obtained with high molecular weight (M_n = 66 kDa) and was readily soluble. The use of 2-ethylhexyl substituents was sufficient to impart PDPP2FT-2EH with appropriate solubility in common organic solvents (e.g., tetrahydrofuran, chloroform, chlorobenzene) for device fabrication. In contrast, PDPP3F-2EH, synthesized using the same polymerization protocol only achieved moderate molecular weight (M_n = 29 kDa), and it was found to possess slightly reduced solubility in the same organic solvents. While the improved solubility of oligofurans over oligothiophenes has been reported,[59] it appears that the ratio of furan to thiophene in alternating oligomers also impacts solubility.[60,61] As a control experiment, we attempted to synthesize the 2-ethylhexyl-substituted PDPP3T following the same polymerization procedure. However, the polymerization yielded only low-molecular-weight fractions that were minimally soluble in all common organic solvents (M_n = 2 kDa).

2.2.2. Effects on Polymer Optoelectronics When Substituting Furan for Thiophene

The optical and electronic properties of PDPP2FT-2EH and PDPP3F-2EH were characterized by UV-visible spectroscopy and cyclic voltammetry, and the measured data were compared to the published thiophene analogue, PDPP3T-2HD. The onset of optical absorption of PDPP2FT in a thin film was measured to be 880 nm (E_g = 1.41 eV), while the λ_{max} was observed at 789 nm (see Figure 2-2a), which is comparable to the optical properties of PDPP3T-2HD reported earlier by Janssen *et al.* (E_g = 1.3 eV).34 PDPP3F-2EH also possesses similar optical properties, with E_g = 1.35 eV and λ_{max} at 767 nm. Figure 2-2b shows the cyclic voltammograms of the two polymers. The onsets of oxidation and reduction of PDPP2FT-2EH were observed at +0.28 and -1.34 V vs. Fc/Fc^+, corresponding to HOMO and LUMO levels at -5.4 and -3.8 eV vs. vacuum. For PDPP3F, the onsets were observed at +0.35 and -1.34 V, corresponding to HOMO and LUMO levels at -5.5 and -3.8 eV. These values are also comparable to those obtained for the low-molecular-weight thiophene analogue, PDPP3T-2EH.

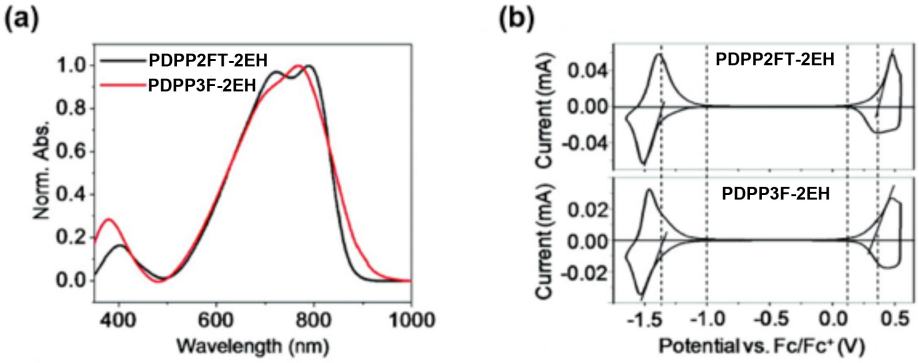

Figure 2-2. (a) Thin-film absorption spectra and (b) cyclic voltammograms of PDPP2FT-2EH and PDPP3F-2EH.

2.2.3. Solar Cell Performance of Furan-Containing Materials

Solar cells were fabricated using PDPP2FT-2EH as the electron-donor and [6,6]-phenyl-C_{71}-butyric acid methyl ester ($PC_{71}BM$) as the electron-acceptor, with the device structure ITO/PEDOT:PSS/polymer:$PC_{71}BM$/LiF/Al. The active layers were spin-coated from solutions of chlorobenzene containing a small amount of the high boiling-point additive 1-chloronaphthalene (CN), which was added to optimize blend morphology for enhanced device performance.[62] Figure 2-3 shows the *J-V* curves of optimized devices fabricated from blends of PDPP2FT-

2EH:$PC_{71}BM$ at a 1:3 weight ratio in chlorobenzene. With the addition of 9% (v/v) CN to the blend solution, the best performing OPV device achieved a V_{OC} of 0.74 V, a J_{SC} of 11.2 mA cm^{-2}, a FF of 60 %, and a PCE of 5.0% (average 4.7%), a result comparable to that obtained by Janssen *et al.* with PDPP3T.[48] Solar cells containing a blend of PDPP3F-2EH and $PC_{71}BM$ were also fabricated and achieved a maximum PCE of 4.1 % (average 3.8%) after optimization (Figure 2-3). These device results strongly support the potential of furan-based polymeric systems in organic photovoltaic devices.

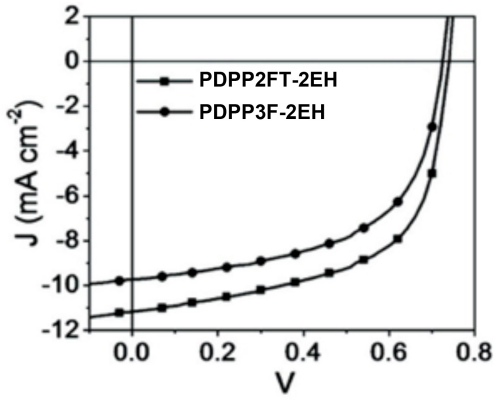

Figure 2-3. *J-V* curves for solar cells fabricated with PDPP2FT-2EH:$PC_{71}BM$ and PDPP3F-2EH:$PC_{71}BM$

2.3. Incorporation of Furan Comonomers Allows for the Use of Linear Side Chains

2.3.1. Exploiting Solubility Enhancement from the Alternating Furan-Thiophene Motif

In the previous section, we show that furan (F) is a viable alternative to thiophene (T) as a building block in conjugated polymers for OPV applications. Our results demonstrate that polymer solubility can be improved while the same OPV device performance was maintained upon incorporating furan as a comonomer. In attempting to exploit this enhanced solubility, we noticed that, as is the case with PDPP3T-2HD, the vast majority of polymer donors exhibiting high PCEs in BHJ devices have branched solubilizing side chains of various size and sterics.[18,29,31,63−65] While such branching centers and substituents greatly improve polymer solution-processability in organic solvents, they may not be coplanar with the backbone. We hypothesized that increasing overall polymer planarity may ultimately promote self-assembly into extended crystalline domains with longer-range backbone alignment. Increased molecular ordering in the active layer has often been shown to improve OPV performance, as a result of improved continuity of charge transport pathways.[66,67] The choice of alkyl side-chain structure has been shown to have a pronounced effect on molecular packing and, therefore, on overall device performance.[29]

In order to study the effects of side-chain branching and lengths on polymer nanostructural order, we functionalized a series of PDPP2FT derivatives, each with linear alkyl substituents of a different length. We found that, because of the enhanced solubility of the PDPP2FT backbone, these *n*-alkyl-substituted derivatives can be solution-processed despite the absence of conventional side-chain branching. In contrast, PDPP3T derivatives with the same *n*-alkyl side chains are not soluble enough to be processed into functional devices. We also compared the OPV performance and solid-state packing behavior of these polymers with their analogues bearing branched side chains.

2.3.2. Synthesis and Optoelectronics of Polymers Functionalized with Linear Alkyl Groups

To demonstrate the influence of side-chain design on polymer nanostructural order in films, PDPP2FT derivatives were synthesized with *n*-$C_{12}H_{25}$ (C12), *n*-$C_{14}H_{29}$ (C14), or *n*-$C_{16}H_{33}$ (C16) side chains (Figure 2-4). This progression of side chains was chosen in order to determine the optimal side-chain length. The route used for synthesizing these polymers is the same as the one shown in Scheme 2-1, and details regarding procedures and yields are described in Section 2.7.

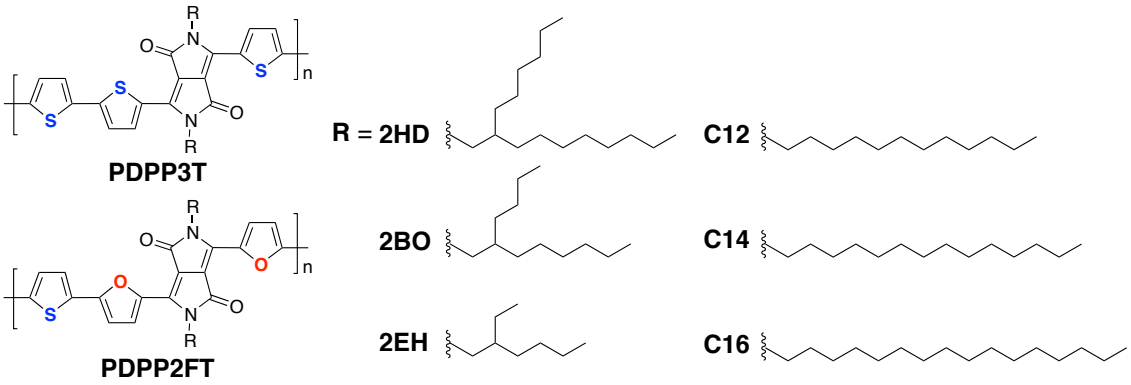

Figure 2-4. PDPP2FT and PDPP3T (control polymers) derivatives with branched and linear alkyl substituents.

To characterize the optical and electronic properties of these polymers, their solid-state UV-visible spectra were measured (Figure 2-5), and other parameters including thin-film absorption coefficients, optical band gaps, and photoelectron spectroscopy in air (PESA)-estimated highest occupied molecular orbital (HOMO) energy levels are summarized in Table 2-1. The optical and electronic properties of all three derivatives are nearly identical and closely match those of the branched-alkyl-substituted analogues PDPP2FT-2EH29 and PDDP3T-2HD.[48] The branched-alkyl-substituted derivative PDPP2FT-2BO (Figure 2-4, 2BO = 2-butyloctyl) was also prepared in order to further correlate the size of the branched substituents with structural order and solar cell device performance. Further shortening the side chain to *n*-$C_{10}H_{21}$ resulted in a polymer with greatly reduced solubility, and the polymerization product could not be solution-processed. As control experiments, PDPP3T-C14 and -C16 were synthesized, but these analogues also showed limited solubility and could not be solution-processed.

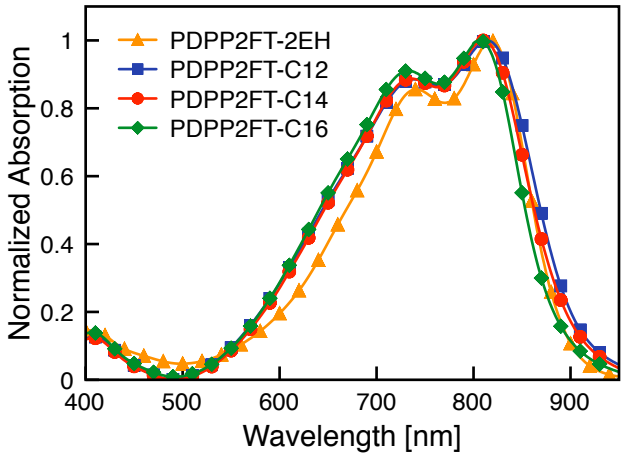

Figure 2-5. Thin-film UV-vis absorption spectra of PDPP2FT-2EH, -C12, -C14 and -C16.

Table 2-1. Molecular weights, PDI, and optoelectronic properties of *n*-alkyl PDPP2FT.

R	M_n [kDa]	PDI	attenuation coefficient [cm^{-1}]	HOMO by PESA [eV]	optical band gap [eV]
n-$C_{12}H_{25}$	46	1.70	1×10^5	-5.2	1.4
n-$C_{14}H_{29}$	58	1.59	8×10^4	-5.2	1.4
n-$C_{16}H_{33}$	55	1.60	7×10^4	-5.3	1.4

The solubility difference between PDPP2FT and PDPP3T derivatives demonstrates that the integration of furan in the backbone allows access to polymer structures that are not otherwise soluble or processable. Previous studies comparing oligofurans to oligothiophenes have similarly reported that oligofurans and alternating furan-thiophene oligomers are more soluble than the analogous oligothiophenes.[59–61] Although the mechanism behind the improved solubility imparted by the furan co-monomer is not well established, we attempt to rationalize this observation by performing density functional theory calculations on methyl-substituted trimers of DPP3T, DPP2FT, and DPP3F using Gaussian 09 at the B3LYP/6-31G(d) level.[68] Geometry-optimized structures reveal that the molecular curvature, determined based on the through-space distance between DPP carbonyls, varies greatly for the three different trimers (Figure 2-6). DPP2FT shows the shortest inter-carbonyl distance of 6.83 Å due to the largest bend in the conjugated backbone; DPP3F has the next shortest distance of 7.88 Å, and DPP3T exhibits the longest distance (11.25 Å). By this analysis, DPP3T is considerably more linear than the backbones of DPP2FT and DPP3F trimers. Interestingly, the backbone that displays the greatest amount of curvature among the trimers (DPP2FT) also provides the most qualitatively soluble polymers (PDPP2FT). These data support prior studies[69] that correlate increased conjugated backbone curvature with improved polymer solubility. Compared to linear polymers, polymers with curved backbones exhibit weaker interchain interactions, leading to diminished aggregation and enhanced solubility. Additionally, polymers with curved geometries may form coils in solution that are entropically favored. Thus, the significant backbone curvature due to the furan substitution likely leads to the increased solubility of PDPP2FT compared to PDPP3T.

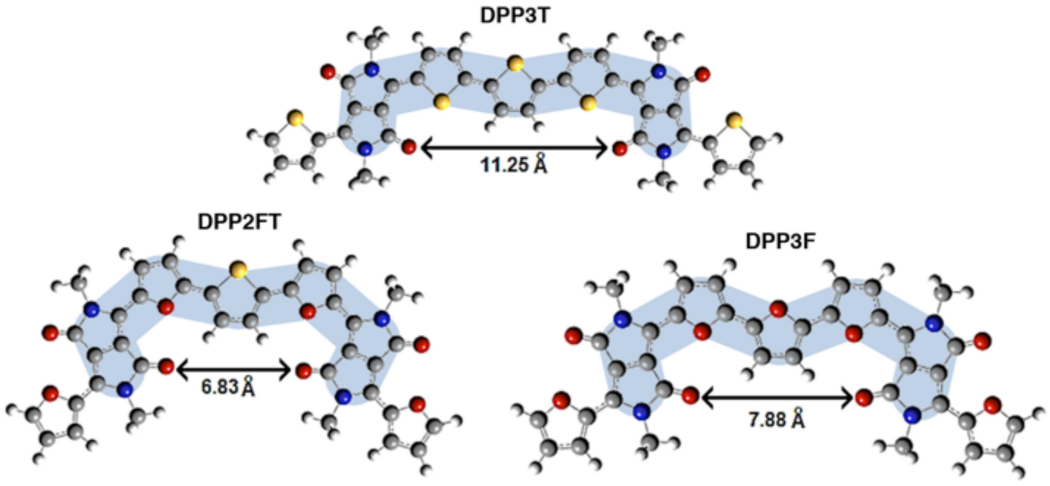

Figure 2-6. Geometry optimized structures of DPP3T, DPP2FT, and DPP3F trimers obtained by DFT calculations. The extent of backbone curvature is depicted for each structure (blue highlight), along with the inter-ketone distance between DPP subunits.

2.3.2. Solar Cell Testing and Performance

Thin-film BHJ solar cells were fabricated using PDPP2FT-C12, -C14, and -C16 as electron donors and $PC_{71}BM$ as the electron acceptor, with a PDPP2FT:$PC_{71}BM$ blend ratio of 1:3 by weight. This blend ratio was determined for each derivative individually as part of an optimization process encompassing a wide range of device fabrication parameters (e.g., spin-coater speed, solvent, solution concentrations). The optimized device architecture was ITO/PEDOT:PSS/polymer:$PC_{71}BM$/LiF/Al. Active layers were spin-coated from chloroform solutions, with a small amount of the processing additive 1-chloronaphthalene (CN)[62] used to improve device performance.[24,33,70] Devices fabricated from the PDPP2FT-C12, -C14, and -C16 derivatives achieved average PCEs of 4.8%, 6.2%, and 5.7%, respectively, with PDPP2FT-C14 based devices reaching as high as 6.5% (Table 2-2). PDPP2FT-C12 proved relatively difficult to solution-process due to its lower solubility. The performance of the PDPP2FT-C14 and -C16, on the other hand, is substantially improved over that of the branched-alkyl-substituted analogues PDPP2FT-2EH (4.7%), PDPP2FT-2BO (1.3%) and PDPP3T-2HD (4.7%). This improvement of PCE is mostly attributed to increases in photocurrent and fill factor (FF). As shown in the device current density-voltage (*J-V*) curves and external quantum efficiency (EQE) spectra (Figure 2-7), PDPP2FT-C14-based devices exhibit particularly high short-circuit current (J_{SC}) approaching 15 mA/cm^2 and a broad EQE spectrum approaching 50% efficiency at 500 nm. As all of the derivatives exhibit similar light absorption and electrical properties, it is likely that these performance improvements are due to changes in properties such as charge carrier mobility, film morphology (donor/acceptor phase separation), and nanostructural order.

Table 2-1. PV performance of PDPP2FT derivatives with $PC_{71}BM$.

R	J_{SC} [mA/cm^2]	V_{OC} [V]	FF	avg PCE [%]	max PCE [%]
2-butyloctyl	-3.8	0.61	0.55	1.3	--
2-ethylhexyl	-11.2	0.74	0.60	4.7	5.0
n-$C_{12}H_{25}$	-12.2	0.65	0.60	4.8	5.2
n-$C_{14}H_{29}$	-14.8	0.65	0.64	6.2	6.5
n-$C_{16}H_{33}$	-12.3	0.65	0.69	5.7	6.2

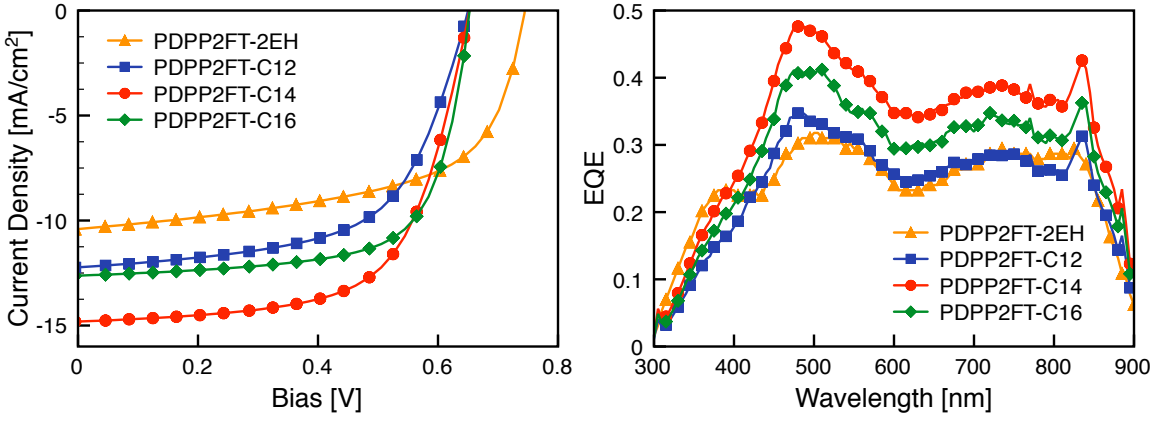

Figure 2-7. Representative *J-V* curves (left) and external quantum efficiency (EQE) spectra (right) of solar cells fabricated from PDPP2FT-2EH, -C12, -C14 and C16. The J_{SC} values obtained from integration of the EQE spectra are in agreement with those determined from the *J-V* curves.

To determine the impact of side chains on carrier mobility, hole mobility was measured using the space-charge-limited current (SCLC) model. In these hole-only devices, neat films of PDPP2FT-C12, -C14, and -C16 showed mobilities of 4×10^{-4}, 7×10^{-4}, and 2×10^{-3} $cm^2/V\bullet s$, respectively. The high carrier mobility of these *n*-alkyl-substituted PDPP2FT derivatives is expected to contribute in part to the high photocurrents and fill factors observed in optimized BHJ devices (Figure 2-7). For comparison, neat films of PDPP2FT-2EH showed a hole mobility of 2×10^{-3} $cm^2/V\bullet s$. Since this value is similar to the mobilities observed with PDPP2FT-C14 and -C16, it is likely that the performance improvement seen with the *n*-alkyl-substituted derivatives arises from other thin-film parameters.

2.3.3. Surface Morphology of Thin Films

As a polymer's solubilizing side chains are expected to impact its solubility and miscibility with $PC_{71}BM$, they could in turn affect the film morphology that forms during the spin-coating process. Atomic force microscopy (AFM) was used to investigate the nanoscale topography networks of features on the order of 20 nm in size. Excitons generated in donor phases of this size scale can diffuse to a donor/acceptor interface, assuming an exciton diffusion length of 10 nm.[71,72] Films of PDPP2FT-C12, -C14, and -C16 have root-mean-square (rms) roughnesses of 2.2, 1.6, and 3.3 nm, respectively. The relative smoothness of the PDPP2FT-C14 active layer may point to finer and more evenly distributed morphological features, which could reduce charge recombination. These results suggest that, with PDPP2FT, *n*-$C_{14}H_{29}$ side chains may provide the most adequate combination of polymer solubility and miscibility with $PC_{71}BM$ to achieve optimal film morphology.

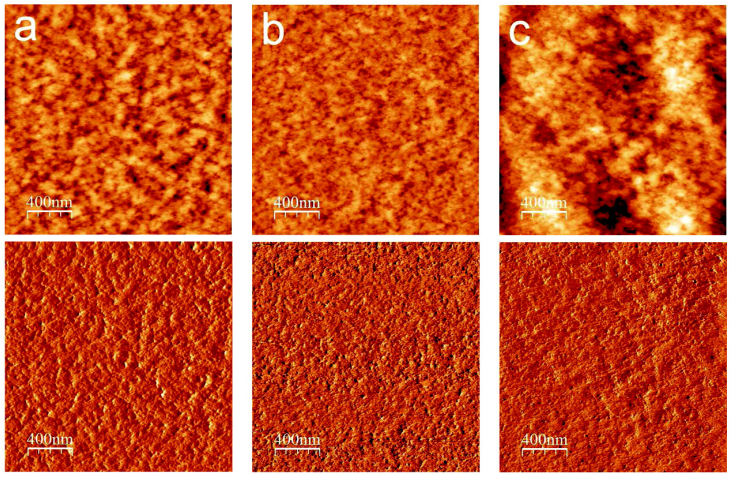

Figure 2-8. AFM height (top) and phase (bottom) images of the *n*-alkyl-substituted polymers (a) PDPP2FT-C12, (b) PDPP2FT-C14, and (c) PDPP2FT-C16

2.4. The Use of Linear Side Chains Improves Polymer Long-Range Order in Thin Films

2.4.1. π-π Stacking Distances between the Polymer Backbones

To determine the influence of side-chain substitutions on nanostructural order within the active layer, grazing-incidence X-ray scattering (GIXS) was used to examine thin-films of PDPP2FT-C12, -C14, -C16, -2EH, and -2BO in both neat polymer films (Figure 2-9) and optimized BHJ films with $PC_{71}BM$ (Figure 2-10).

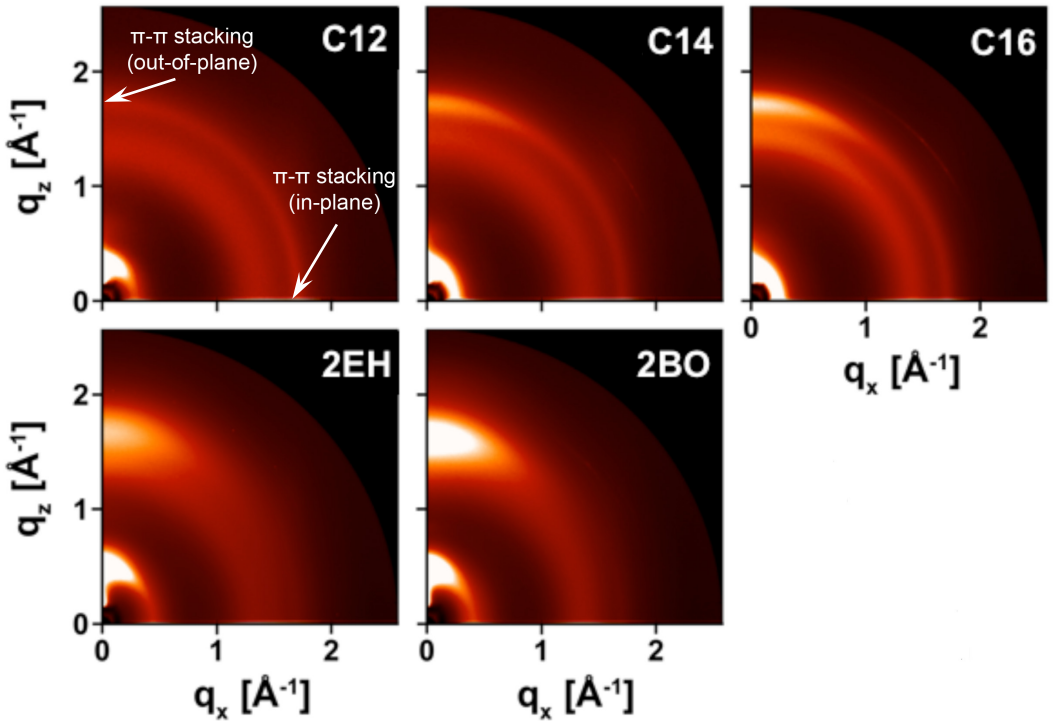

Figure 2-9. 2-D grazing incidence X-ray scattering (GIXS) patterns of neat films of PDPP2FT-C12, -C14, -C16, -2EH and -2BO.

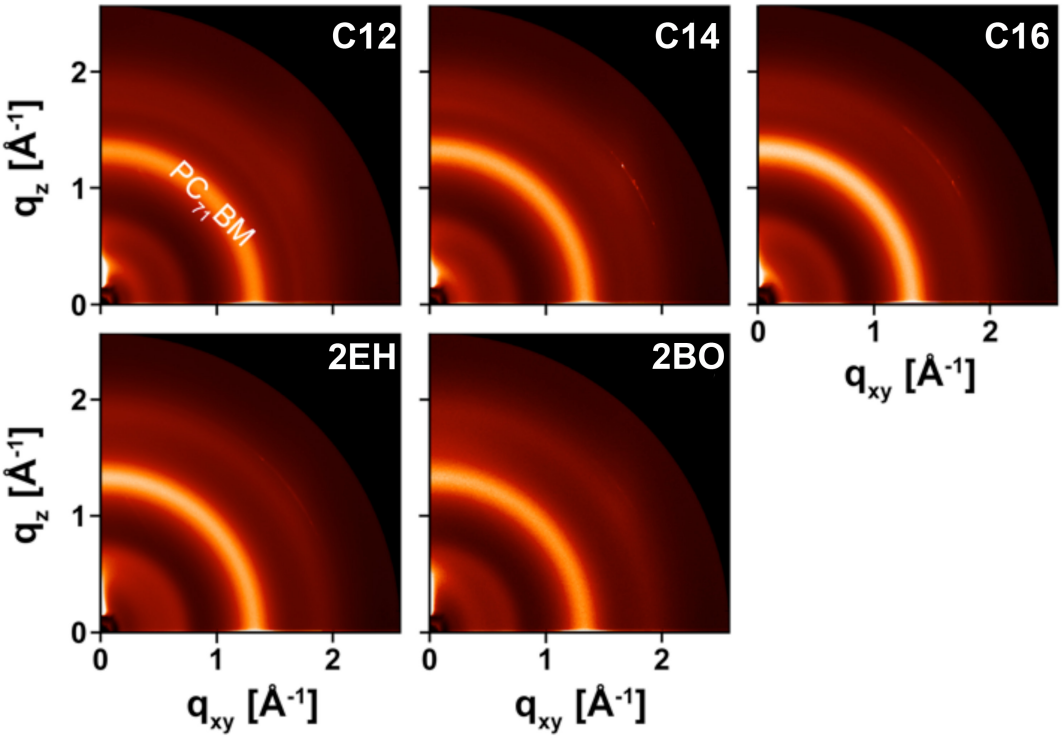

Figure 2-10. 2-D GIXS scattering profiles of blend (BHJ) films of PDPP2FT-C12, -C14, -C16, -2EH and -2BO with $PC_{71}BM$.

GIXS data collected for the neat films was used to determine the nature and extent of the face-to-face packing of conjugated polymer backbones (π-π stacking). While GIXS scattering profiles of blend (BHJ) films exhibit peaks similar peaks to those of the neat films, the intensity of the $PC_{71}BM$ ring adds difficulty the solid-state order analysis. The scattering patterns of neat films of all four derivatives exhibit a π-π stacking peak, visible as a ring or partial arc at $q \approx 1.7$ Å^{-1}. The stronger peak intensity near $q_{xy} \approx 0$ means that the π-π stacking is preferentially oriented out-of-plane, which has been often correlated with high OPV performance.[30,73,74] As shown in Figure 2-9, the extent of out-of-plane orientation of each derivative increases in this order: PDPP2FT-C12, -C14, -C16, -2EH, and -2BO. This order agrees well with the SCLC hole mobilities presented earlier, as SCLC measures hole mobility in the out-of- plane direction.

In assessing the effect of these π-π interactions on solar cell performance, it is important to consider π-stacking distances. A shorter distance is thought to reduce the energetic barrier for charge hopping between adjacent molecules, promoting charge transport and improving device performance.[22,75,76] Brédas and co-workers have shown in model systems that, for cofacial π-π stacking, electronic couplings decay exponentially with the stacking distance and can vary by as much as a factor of 4 when the stacking distance increases from 3.4 to 4.0 Å.[22] It is expected that the solubilizing substituents of a polymer will impact this π-stacking distance. Compared to branched side chains, which can create steric hindrance to prevent polymer chains from packing tightly, linear solubilizing groups are expected to be able to organize coplanar with the backbone, allowing for closer π-π stacking distances. In agreement with this hypothesis, the π-stacking distances of PDPP2FT-C12, -C14, and -C16 are all measured to be 3.6 Å, while the π-stacking distances of PDPP2FT-2EH and -2BO are measured to be 3.7 and 3.9 Å, respectively (Table 2-3). This result suggests that branched side chains do keep the backbones farther apart via steric hindrance. Empirically, a negative correlation is observed between π-stacking distance and device performance. PDPP2FT-2BO, in particular, exhibits a much larger stacking distance (3.9 Å) and achieves the lowest solar cell performance. Furthermore, it is important to note that charge transfer between two molecules also depends strongly on their in-plane offset and not just on their cofacial separation distance, as wave function overlap plays a critical role in electronic coupling.[22] Nevertheless, as suggested by the empirical correlation drawn above, π-π stacking distance provides a valuable first-order metric for evaluating the charge transport characteristics of complex polymer systems.

Table 2-3. GIXS peak parameters for PDPP2FT derivatives

R	π-π stacking peak		lamellar spacing peak	
	d [Å]	L_C [nm]	d [Å]	L_C [nm]
2-butyloctyl	3.9	1.2	14	2.5
2-ethylhexyl	3.7	1.1	13	2.7
n-$C_{12}H_{25}$	3.6	3.3	21	3.4
n-$C_{14}H_{29}$	3.6	3.6	23	3.6
n-$C_{16}H_{33}$	3.6	3.0	25	4.1

2.4.2. Polymer Long-Range Order by Determination of Correlation Lengths

In addition to describing the molecular packing distances and orientation of crystallites in thin films, GIXS provides information on the extent of nanostructural order. Specifically, GIXS can be used to determine the correlation length (L_C),[27,77] which is a measure of the length scale over which one can expect a crystal lattice to be preserved. In polymer systems, order is expected to improve with the reduction of (1) the variability in chain position and rotation and (2) the density of chain ends and lamellar folds.[75] Correlation length can be determined using the Scherrer equation,[50,51] which takes scattering peak breadth as an input. As the order of crystalline domains increases, the corresponding scattering peaks become narrower. To determine the full width at half-maximum (fwhm) peak breadths, peaks were fit to GIXS data averaged over quasipolar angle (χ) for $\chi = 20° \pm 2°$ and $\chi = 60° \pm 2°$. The resulting average correlation lengths are shown for π-π stacking and lamellar spacing peaks in Table 2-3 and Figure 2-11, which also contains solar cell efficiencies (PCEs) for ease of comparison. Notably, the *n*-alkyl-substituted PDPP2FT derivatives pack with significantly longer π-π stacking correlation lengths (> 3 nm) than do PDPP2FT-2EH and PDPP2FT-2BO (appx. 1 nm). Furthermore, device performance is substantially improved in BHJs made with PDPP2FT-C14, which also shows the largest π-π stacking correlation length at 3.6 nm.

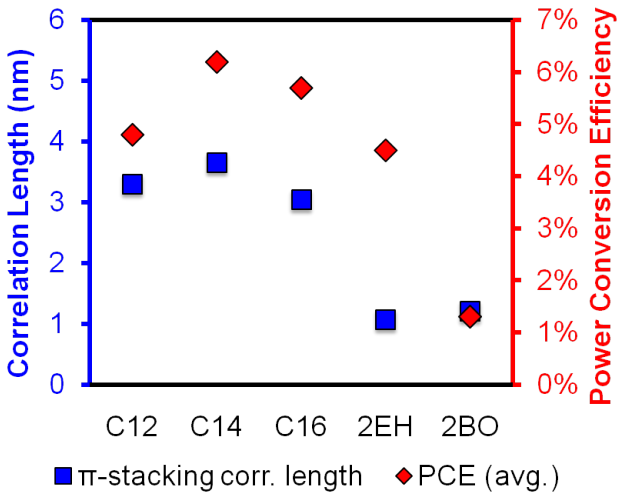

Figure 2-11. π-π stacking correlation lengths (blue squares) for PDPP2FT derivatives in thin-film. Power conversion efficiency in devices is shown (red diamond) to demonstrate the relationship between π-π stacking correlation length and device performance.

Recall that PDPP2FT-C12 had the lowest solubility of all the derivatives, which may have affected device PCE. A similar trend is observed for lamellar spacing correlation lengths, which are greater for the *n*-alkyl-substituted derivatives (3−4 nm) than for the branched-alkyl-substituted derivatives (< 3 nm). Although additional studies will be required to determine the interdigitation and packing structure of the side chains, it is important to note the likely contribution of the linear chains to overall solid-state order and device performance. Increased order, particularly of π-π stacking, likely minimizes the number of defects that can trap charge carriers and hinder their percolation across the active layer.[67,78] As discussed earlier, the π-π stacking in these systems is preferentially oriented out-of-plane, which is also the desired direction for hole transport. As a result, the effect of π-π stacking correlation length on solar cell

device performance is expected to be particularly significant among factors contributing to improved performance.

2.5. Conclusion

In summary, we have shown that furans can be advantageously used as an alternative to thiophenes and thiophene-based building units in the design and synthesis of low band-gap conjugated polymers with efficient solar cell performance. The polymers first examined, PDPP2FT-2EH and PDPP3F-2EH, exhibit nearly identical optical and electronic properties and demonstrate a maximum power conversion efficiency of 5% in BHJ devices with $PC_{71}BM$. The incorporation of furan into the conjugated backbone allowed for shorter solubilizing groups to be used, compared to those required to solubilize the analogous polymer PDPP3T-2HD. In particular, polymer solubility was found to improve substantially when a combination of thiophene and furan heterocycles is incorporated. The 4.1 % efficiency achieved with the PDPP3F-2EH demonstrates the potential of furans as thiophene alternatives in the design of high-performance organic solar cell materials.

We subsequently exploited the increased polymer solubility imparted by the alternating furan-thiophene motif and explored the use of linear alkyl substituents as solubilizing groups for polymers. Despite the absence of side-chain branching, the *n*-alkyl-functionalized PDPP2FT derivatives retain their solution-processability and exhibit long-range nanostructural order in thin-film solar cells. GIXS shows that linear side chains in these systems reduce the π-stacking distances between backbones and increase π-π stacking and lamellar spacing correlation lengths within polymer crystallites. Building from these design principles, we show that BHJ solar cells fabricated from *n*-alkyl-substituted PDPP2FT electron-donors and the electron-acceptor $PC_{71}BM$ exhibit PCEs reaching 6.5% (PDPP2FT-C14). This high performance represents a substantial improvement over the PCE of 5% achieved with the branched-alkyl-substituted derivative PDPP2FT-2EH and the original thiophene-based analogue PDPP3T-2HD. This work demonstrates the potential of furan moieties in expanding the structural design flexibility of polymer donors for efficient OPV applications. By leveraging the enhanced solubility imparted by the furan moiety, this work also shows that side-chain structural design can be used to control thin-film nanostructural order and device performance. This combination of design principles paves a path to reaching PCE values exceeding those presently obtained using other thiophene-based polymer donors with branched side chains.

2.6. Experimental

2.6.1. Synthetic Details

All reagents from commercial sources were used without further purification, unless otherwise noted. *N*-bromosuccinimide (NBS) was purified by recrystallization in distilled water prior to use. Flash chromatography was performed using Silicycle SiliaFlash ® P60 (particle size 40-63 μm, 230 – 400 mesh) silica gel. All compounds were characterized by ^{1}H and ^{13}C NMR spectroscopy on a Bruker AVQ-400 or AV-600 instrument. Notations for proton splitting patterns: s = singlet, d = doublet, t = triplet, q = quartet, dd = doublet of doublet, m = multiplet, and a = apparent. Matrix-assisted laser desorption/ionization mass spectrometry (MALDI-TOF MS) was performed on a PerSeptive Biosystems Voyager-DE using 2,2':5',2''-terthiophene as the matrix. Samples were prepared by diluting the monomers in chloroform with the matrix.

For the molecular weight determination of polymers, samples were dissolved in HPLC grade chloroform at a concentration of 1 mg/mL. The resulting solution was briefly heated and then allowed to return to room temperature prior to filtering through a 0.2 μm polyvinylidene fluoride (PVDF) filter. Size exclusion chromatography (SEC) was performed with HPLC grade chloroform at an elution rate of at 1.0 mL/min through three PLgel Mixed-C columns at room temperature. The particle size in the columns was 5 μm and the columns were maintained at room temperature. The SEC system consisted of a Waters 2695 Separation Module and a Waters 486 Tunable Absorption Detector. The apparent molecular weights and polydispersities (PDI, M_w/M_n) were determined with a calibration based on linear polystyrene standards using Millennium software from Waters.

2,5-Bis(trimethylstannyl)thipohene (**1**).

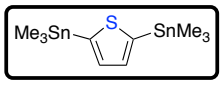

Recrystallized (EtOH) from the commercially available reagent.

2,5-Bis(trimethylstannyl)furan (**2**).

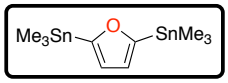

2,5-Dibromofuran (2.0 g, 8.85 *m*mol) and 30 mL of dry THF were added to a 100-mL two-neck flask with stir bar, and placed under N_2 atmosphere. The mixture was cooled to -78 °C, and *n*-BuLi (2.5 M in hexanes, 18.2 *m*mol, 7.4 mL) was added dropwise over 30 min while at -78 °C). Following complete addition of *n*-BuLi, the reaction mixture was stirred for an additional 15 min at -78 °C. It was subsequently allowed to reach room temperature and stirred for 1 h. The reaction mixture was again cooled down to -78 °C prior to the addition of Me_3SnCl (18.6 *m*mol, 3.70 g) and stirred at -78 °C for 15 min. It was then warmed room temperature and stirred for 12 h. The organic layer was extracted with diethyl ether, washed with water, dried over $MgSO_4$ and filtered. The solvent was evaporated, and the resulting oil (yellow) was passed through a plug of basic alumina using hexanes as eluent. Hexanes were evaporated, and the resulting oil (colorless) was distilled under reduced pressure (68-72 °C at 180 *m*Torr) and 0.74 g of **2** was isolated (21% yield).

^{1}H NMR (400 MHz, $CDCl_3$): δ (ppm) = 6.71 (s, 2 H), 0.40 (m, 18 H). ^{13}C NMR (100 MHz, $CDCl_3$): δ (ppm) = 165.2, 120.3, -9.0. GC-MS (EI, *m/z*): calc'd for $C_{10}H_{20}OSn_2$ [M^+] = 396.0; found 398.0.

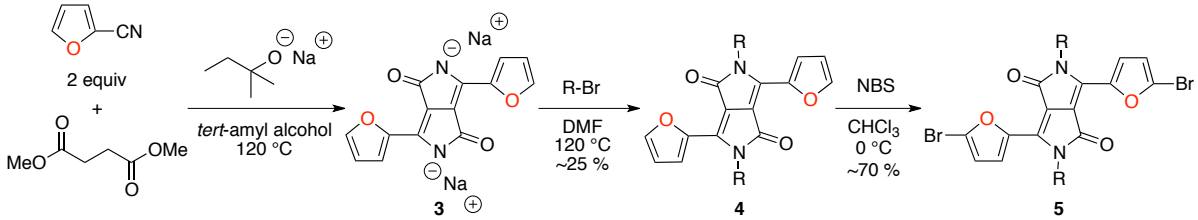

Disodium Salt of 3,6-di(furan-2-yl)pyrrolo[3,4-c]pyrrole-1,4(2H,5H)-dione (**3**)**.**

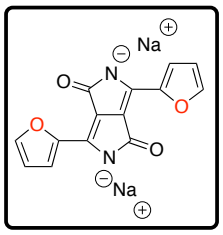

A 500-mL three-neck flask, connected to a condenser and dry nitrogen flow, was charged with a *tert*-amyl alcohol (250 mL). Sodium metal pieces (2.47 g, 107 mmol) were progressively added to the warmed solution of *tert*-amyl alcohol (60-70 °C). After complete addition of the sodium, the temperature was raised to 120 °C. The mixture was stirred for 16 h at 120 °C. Furan-2-carbonitrile (10.0 g, 107 *m*mol) was added to the solution of sodium alkoxide. Dimethyl succinate (5.23 g, 35.8 *m*mol) was added dropwise over a period of 20 min (the reaction mixture turned dark orange-red), and the resulting mixture was stirred for 1.5 h. The reaction mixture was then cooled to rt and precipitated onto ice. Vacuum filtration of the suspension yielded 14.7 g of red solid (87 %), which was used without further purification.

2,5-Bis(2-ethylhexyl)-3,6-di(furan-2-yl)pyrrolo[3,4-c]pyrrole-1,4(2H,5H)-dione (**4-2EH**)**.**

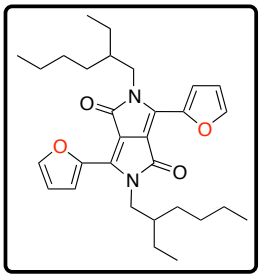

A 250-mL flask attached to a condenser was charged with **3** (3.36 g, 10.8 *m*mol) and 100 mL dry DMF. The mixture was heated at 120 °C for 30 min, and 2-ethylhexylbromide (6.05 g, 31.3 *m*mol) was added in one portion. The reaction mixture was then stirred at 140 °C for 6 h. The organic layer was extracted with diethyl ether, washed with water, dried over $MgSO_4$ and filtered. The solvent was removed under reduced pressure, and the residual solid was purified by flash chromatography (silica gel, chloroform) to afford 1.30 g of red solid (25 %).

^{1}H NMR (400 MHz, $CDCl_3$): δ (ppm) = 8.33 (d, *J* = 3.6 Hz, 2 H), 7.61 (d, *J* = 1.3 Hz, 2 H), 6.69 (dd, *J* = 1.7 Hz, 3.6 Hz, 2 H), 4.04 (d, *J* = 7.8 Hz, 4 H), 1.80 – 1.68 (m, 2 H), 1.39 – 1.26 (m, 16 H), 0.95 – 0.85 (m, 12 H). ^{13}C (100 MHz, $CDCl_3$): δ (ppm) = 161.4, 145.0, 144.8, 134.1, 120.4, 113.6, 106.6, 46.3, 40.1, 30.7, 28.8, 24.0, 23.2, 14.2, 10.9. MALDI-TOF MS (*m/z*): calc'd for $C_{30}H_{40}N_2O_4$ [M^+] = 492.3; found 492.9.

2,5-Di-(2-butyloctyl)-3,6-di(furan-2-yl)pyrrolo[3,4-c]pyrrole-1,4(2H,5H)-dione (**4-2BO**)**.**

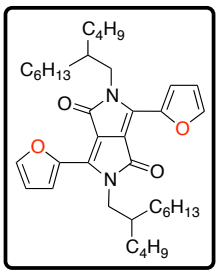

Reaction conditions were the same as for 4-2EH, except 2-butyloctyl iodide was used.

^{1}H NMR (400 MHz, $CDCl_3$): δ (ppm) = 8.37 (d, *J* = 3.6 Hz, 2 H), 7.65 (d, *J* = 1.5 Hz, 2 H), 6.73 (dd, *J* = 1.7 Hz, 3.7 Hz, 2 H), 4.08 (d, *J* = 7.5 Hz, 4 H), 1.91–1.76 (m, 2 H), 1.48–1.18 (m, 32 H), 1.00 – 0.82 (m, 12 H). ^{13}C NMR (100 MHz, $CDCl_3$): δ (ppm) = 161.3, 144.8, 144.7, 133.9, 120.2, 113.5, 106.5, 46.5, 38.5, 31.8, 31.5, 29.7, 26.5, 23.1, 22,7, 14.1. MALDI-TOF MS (*m/z*): calc'd for $C_{38}H_{56}N_2O_4$ [M^+] = 604.42; found 604.65.

2,5-Didodecyl-3,6-di(furan-2-yl)pyrrolo[3,4-c]pyrrole-1,4(2H,5H)-dione (**4-C12**).

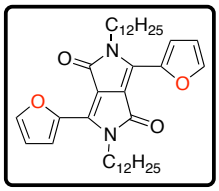

Reaction conditions were the same as for **4-2EH**, except 1-dodecylbromide was used.

^{1}H NMR (400 MHz, $CDCl_3$): δ (ppm) = 8.30 (d, *J* = 3.6 Hz, 2 H), 7.63 (d, *J* = 0.8 Hz, 2 H), 6.69 (dd, *J* = 1.6 Hz, 3.6 Hz, 2 H), 4.10 (t, *J* = 7.6 Hz, 4 H), 1.72 – 1.65 (m, 4 H), 1.40 – 1.24 (m, 36 H), 0.87 (t, *J* = 6.8 Hz, 6 H). ^{13}C NMR (100 MHz, $CDCl_3$): δ (ppm) = 161.0, 145.3, 144.8, 133.8, 120.3, 113.6, 106.6, 42.6, 32.1, 30.4, 29.8, 29.7, 29.5, 29.4, 17.0, 22.8, 14.3. MALDI-TOF MS (*m/z*): calc'd for $C_{38}H_{56}N_2O_4$ [M^+] = 492.30; found 492.84.

2,5-Ditetradecyl-3,6-di(furan-2-yl)pyrrolo[3,4-c]pyrrole-1,4(2H,5H)-dione (**4-C14**).

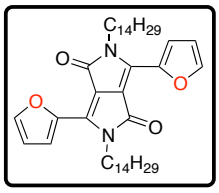

Reaction conditions were the same as for **4-2EH**, except 1-tetradecylbromide was used.

^{1}H NMR (400 MHz, $CDCl_3$): δ (ppm) = 8.35 (d, *J* = 3.2 Hz, 2 H), 7.67 (d, *J* = 1.3 Hz, 2 H), 6.74 (dd, *J* = 1.7 Hz, 3.6 Hz, 2 H), 4.20-4.09 (m, 4 H), 1.83 – 1.64 (m, 4 H), 1.53 – 1.17 (m, 44 H), 0.93 (t, *J* = 6.7 Hz, 6 H). ^{13}C NMR (100 MHz, $CDCl_3$): δ (ppm) = 160.9, 145.1, 144.7, 133.6, 120.1, 113.5, 106.4, 42.4, 29.7, 29.6, 29.4, 26.9, 22.7, 14.1. MALDI-TOF MS (*m/z*): calc'd for $C_{42}H_{64}N_2O_4$ [M^+] = 660.49; found 660.96.

2,5-Dihexadecyl-3,6-di(furan-2-yl)pyrrolo[3,4-c]pyrrole-1,4(2H,5H)-dione (**4-C16**)**.**

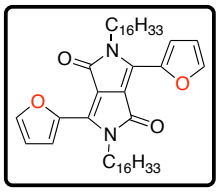

Reaction conditions were the same as for **4-2EH**, except 1-hexadecylbromide was used.

^{1}H NMR (400 MHz, $CDCl_3$): δ (ppm) = 8.35 (d, *J* = 3.4 Hz, 2 H), 7.67 (d, *J* = 1.2 Hz, 2 H), 6.74 (dd, *J* = 1.7 Hz, 3.7 Hz, 2 H), 4.20-4.09 (m, 4 H), 1.83 – 1.65 (m, 4 H), 1.50 – 1.22 (m, 52 H), 0.94 (t, *J* = 6.7 Hz, 6 H). ^{13}C NMR (100 MHz, $CDCl_3$): δ (ppm) = 160.9, 145.1, 144.7, 133.7, 120.1, 113.5, 106.5, 42.4, 29.7, 29.6, 29.4, 26.9, 22.7, 14.1. MALDI-TOF MS (*m/z*): calc'd for $C_{46}H_{72}N_2O_4$ [M^+] = 716.55; found 717.43.

3,6-Bis(5-bromofuran-2-yl)-2,5-bis(2-ethylhexyl)pyrrolo[3,4-c]pyrrole-1,4(2H,5H)-dione (**5-2EH**).

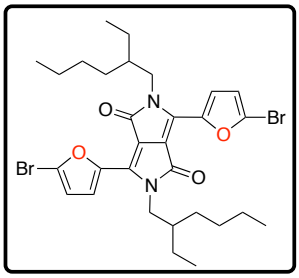

A 100-mL RBF was charged with **4-2EH** (1.01 g, 2.05 *m*mol) and 50 mL of chloroform. The mixture was cooled to 0 °C before NBS (748 mg, 4.20 *m*mol) was added in small portions. Upon the complete addition of NBS, the mixture was allowed to warm to room temperature and stirred for 2 h. The organic layer was diluted with chloroform, washed with water, dried over $MgSO_4$ and filtered. The solvent was removed under reduced pressure, and the residue was purified by flash chromatography (silica gel, chloroform) to afford 0.95 g of dark red solid (71%).

^{1}H NMR (400 MHz, $CDCl_3$): δ (ppm) = 8.30 (d, *J* = 3.7 Hz, 2 H), 6.62 (d, *J* = 3.7 Hz, 2 H), 3.99 (add, *J* = 2.7 Hz, 7.4 Hz, 4 H), 1.78 – 1.68 (m, 2 H), 1.39 – 1.24 (m, 16 H), 0.92 (t, *J* = 7.5 Hz, 6

H), 0.88 (t, J = 7.0 Hz, 6 H). ^{13}C (100 MHz, $CDCl_3$): δ (ppm) = 161.1, 146.4, 132.9, 126.4, 122.4, 115.7, 106.4, 46.4, 40.2, 30.7, 28.9, 23.9, 23.3, 14.2, 10.8. MALDI-TOF MS (*m/z*): calc'd for $C_{30}H_{38}Br_2N_2O_4$ [M^+] = 648.1; found 648.3.

3,6-Bis(5-bromofuran-2-yl)-2,5-di-(2-butyloctyl)-pyrrolo[3,4-c]pyrrole-1,4(2H,5H)-dione (**5-2BO**).

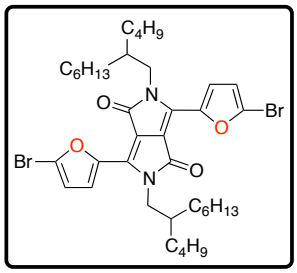

Reaction conditions were the same as for **5-2EH**, except **4-2BO** was used.

^{1}H NMR (400 MHz, $CDCl_3$): δ (ppm) = 8.34 (d, J = 3.7 Hz, 2 H), 6.67 (d, J = 3.7 Hz, 2 H), 4.04 (d, J = 7.4 Hz, 4 H), 1.89 – 1.75 (m, 2 H), 1.50 – 1.18 (m, 32 H), 0.93 (m, 12 H). ^{13}C NMR (100 MHz, $CDCl_3$): δ (ppm) = 160.9, 146.2, 145.5, 132.8, 126.3, 120.2, 115.6, 106.3, 46.6, 38.8, 31.4, 29.8, 26.5, 23.2, 22.7, 14.1. MALDI-TOF MS (*m/z*): calc'd for $C_{38}H_{54}Br_2N_2O_4$ [M^+] = 762.25; found 762.89.

3,6-Bis(5-bromofuran-2-yl)-2,5-didodecylpyrrolo[3,4-c]pyrrole-1,4(2H,5H)-dione (**5-C12**).

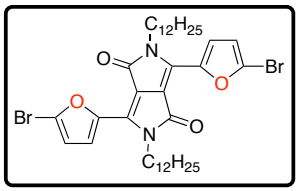

Reaction conditions were the same as for **5-2EH**, except **4-C12** was used.

^{1}H NMR (400 MHz, $CDCl_3$): δ (ppm) = 8.30 (d, J = 3.7 Hz, 2 H), 6.67 (d, J = 3.7 Hz, 2 H), 4.13-4.05 (m, 4 H), 1.80–1.66 (m, 4 H), 1.50–1.21 (m, 36 H), 0.93 (t, J = 6.7 Hz, 6 H). ^{13}C NMR (100 MHz, $CDCl_3$): δ (ppm) = 160.5, 146.2, 132.5, 126.4, 122.1, 115.5, 106.3, 42.5, 30.2, 29.6, 29.4, 26.9, 22.7, 14.1. MALDI-TOF MS (*m/z*): calc'd for $C_{38}H_{54}Br_2N_2O_4$ [M^+] = 762.25; found 762.33.

3,6-Bis(5-bromofuran-2-yl)-2,5-ditetradecyl-pyrrolo[3,4-c]pyrrole-1,4(2H,5H)-dione (**5-C14**).

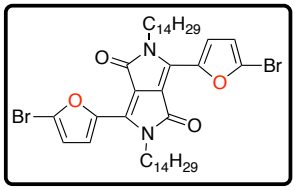

Reaction conditions were the same as for **5-2EH**, except **4-C14** was used.

^{1}H NMR (400 MHz, $CDCl_3$): δ (ppm) = 8.30 (d, J = 3.7 Hz, 2 H), 6.68 (d, J = 3.7 Hz, 2 H), 4.20-4.00 (m, 4 H), 1.80 – 1.67 (m, 4 H), 1.51 – 1.20 (m, 44 H), 0.94 (t, J = 6.6 Hz, 6 H). ^{13}C NMR (100 MHz, $CDCl_3$): δ (ppm) = 160.5, 146.2, 132.5, 126.4, 122.1, 115.5, 106.3, 42.5, 29.7, 29.6, 29.4, 26.9, 22.7, 14.1, 7.5. MALDI-TOF MS (*m/z*): calc'd for $C_{42}H_{62}Br_2N_2O_4$ [M^+] = 818.31; found 818.24.

3,6-Bis(5-bromofuran-2-yl)-2,5-dihexadecyl-pyrrolo[3,4-c]pyrrole-1,4(2H,5H)-dione **(5-C16).**

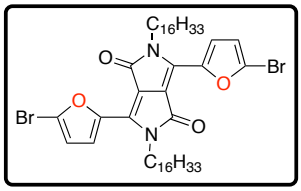

Reaction conditions were the same as for **5-2EH**, except **4-C16** was used.

^{1}H NMR (400 MHz, $CDCl_3$): δ (ppm) = 8.30 (d, J = 3.7 Hz, 2 H), 6.67 (d, J = 3.7 Hz, 2 H), 4.13-4.05 (m, 4 H), 1.78 – 1.68 (m, 4 H), 1.52 – 1.19 (m, 52 H), 0.92 (t, J = 6.6 Hz, 6 H). ^{13}C (150 MHz, $CDCl_3$, 50

°C): δ (ppm) = 160.8, 146.5, 132.8, 126.5, 122.2, 115.7, 106.7, 42.7, 32.1, 30.4, 29.9, 29.8, 29.7, 29.5, 29.4, 27.1, 22.8, 14.2. MALDI-TOF MS (*m*/*z*): calc'd for $C_{46}H_{70}Br_2N_2O_4$ [M^+] = 874.37; found 874.02.

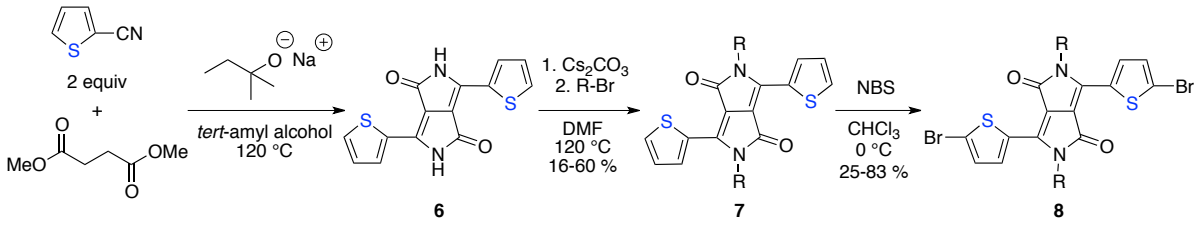

3,6-Di(thiophen-2-yl)pyrrolo[3,4-c]pyrrole-1,4(2H,5H)-dione (**6**).

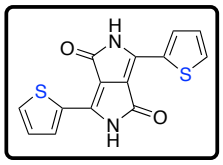

A 500 mL 3-neck flask connected to a condenser was charged with a stir bar and *tert*-amyl alcohol (250 mL). Sodium metal (2.56 g, 108 *m*mol) immersed in mineral oil was thoroughly washed with hexanes and cut into small pieces. Sodium metal pieces were slowly added to the reaction mixture over a 1.5 h period while the temperature was slowly increased to 120 °C over the same amount of time. Upon heating, the metal pieces began to bubble, and the reaction mixture turned light yellow. After all sodium metal pieces were dissolved, 2-thiophenecarbonitrile (11.9 g, 108 mmol) was added to the reaction. As dimethyl succinate (5.29 g, 36.2 *m*mol) was added dropwise to the reaction mixture over 1 h, the solution turned dark red. The reaction contents were stirred at 120 °C for 2 h, and then precipitated into acidic MeOH (400 mL MeOH and 20 mL conc. HCl). Filtration of the suspension through a Buchner funnel yielded a maroon solid (9.10 g), which was used in subsequent reactions without further purification.

2,5-Bis(2-ethylhexyl)-3,6-di(thiophen-2-yl)pyrrolo[3,4-c]pyrrole-1,4(2H,5H)-dione (**7-2EH**).

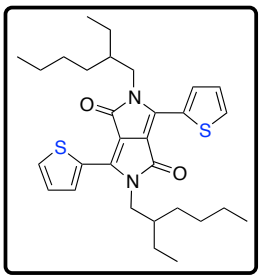

A 250 mL of round bottom flask was charged with **6** (4.50 g, 15.0 *m*mol), Cs_2CO_3 (14.60 g, 45.0 *m*mol) and dry DMF (120 mL). The reaction mixture was stirred at 120 °C for 3 h before 2-ethylhexyl bromide (7.24 g, 37.5 *m*mol) was added to the reaction. The reaction contents were heated at 140 °C for 16 h. The reaction contents were then cooled to 0 °C, filtered through a Büchner funnel and washed with chloroform. Excess DMF and chloroform were removed from the filtrate under reduced pressure with heating to 70 °C to yield a purple solid. The crude material was purified by flash chromatography (chloroform) to yield 1.24 g of purple tacky solid (16 %).

^{1}H NMR (400 MHz, $CDCl_3$, δ): 8.89 (d, *J* = 3.9 Hz, 2 H), 7.61 (d, *J* = 5.0 Hz, 2 H), 7.25 (at, *J* = 4.5 Hz, 1 H), 4.01 (m, 4 H), 1.85 (m, 2 H), 1.29 (m, 16 H), 0.85 (adt, *J* = 7.3 Hz, 8.8 Hz, 12 H). ^{13}C (100 MHz, $CDCl_3$, δ): 161.8, 140.5, 135.4, 130.6, 130.0, 128.5, 108.0, 45.9, 39.2, 30.3, 28.4, 23.6, 23.2, 14.1, 10.6. HRMS (EI, *m*/*z*) [$M]^+$ calcd for $C_{30}H_{40}N_2O_2S_2$, 524.2531; found, 524.2535. Anal. calcd for $C_{30}H_{40}N_2O_2S_2$: C, 68.66; H, 7.68; N, 5.34; found: C, 68.73; H, 7.90; N, 5.34.

2,5-Ditetradecyl-3,6-di(thiophene-2-yl)pyrrolo[3,4-c]pyrrole-1,4(2H,5H)-dione (**7-C14**).

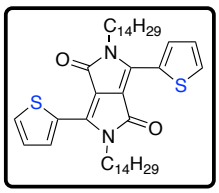

Followed the same synthetic procedure as for **7-2EH**. Instead, **6** (2.00 g, 6.66 *m*mol), Cs_2CO_3 (6.51 g, 19.98 *m*mol) and dry DMF (55 mL) were used. After the reaction mixture was heated at 130 °C for 20 h, it was precipitated into ice water. The crude materials were subsequently purified by flash chromatography ($CHCl_3$) to yield 2.07 g of purple solid (43 %).

^{1}H NMR (400 MHz, $CDCl_3$): δ (ppm) = 8.93 (d, *J* = 3.6 Hz, 2 H), 7.63 (d, *J* = 4.8 Hz, 2 H), 7.28 (dd, *J* = 4.0 Hz, 4.8 Hz, 2 H), 4.06 (t, *J* = 8.0 Hz, 4 H), 1.76–1.72 (m, 4 H), 1.45 – 1.24 (m, 44 H), 0.87 (t, *J* = 6.8 Hz, 6 H). ^{13}C NMR (100 MHz, $CDCl_3$): δ (ppm) = 161.5, 140.2, 135.4, 130.8, 129.9, 128.8, 107.8, 42.4, 32.1, 30.1, 29.8, 29.7, 29.5, 29.4, 27.0, 22.8, 14.3. MALDI-TOF MS (*m/z*): calc'd for $C_{42}H_{64}N_2O_2S_2$ [M^+] = 692.44; found 692.42.

2,5-Dihexadecyl-3,6-di(thiophene-2-yl)pyrrolo[3,4-c]pyrrole-1,4(2H,5H)-dione (**7-C16**).

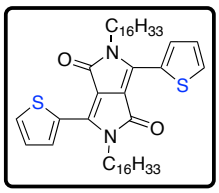

Followed the same synthetic procedure as for **7-2EH**. Instead, used **6** (2.00 g, 6.66 *m*mol), Cs_2CO_3 (6.51 g, 19.98 *m*mol), 1-bromohexadecane (5.09 g, 16.66 *m*mol) and 55 mL of dry DMF. Worked up the reaction mixture by first precipitating it into ice and water, and filtered through a Buchner funnel. Dissolved the crude materials in $CHCl_3$, precipitated the solution into methanol to remove mono-alkylated products, and filtered to 2.99 g of purple solid (60 %).

^{1}H NMR (400 MHz, $CDCl_3$): δ (ppm) = 8.93 (d, *J* = 3.6 Hz, 2 H), 7.64 (d, *J* = 5.2 Hz, 2 H), 7.28 (dd, *J* = 4.4 Hz, 4.8 Hz, 2 H), 4.07 (t, *J* = 8.0 Hz, 4 H), 1.76–1.72 (m, 4 H), 1.45–1.24 (m, 52 H), 0.87 (t, *J* = 6.8 Hz, 6 H). ^{13}C NMR (100 MHz, $CDCl_3$): δ (ppm) = 161.5, 140.2, 135.4, 130.8, 129.9, 128.8, 107.8, 42.4, 32.1, 30.1, 29.8, 29.72, 29.68, 29.5, 29.4, 27.0, 22.8, 14.3. MALDI-TOF MS (*m/z*): calc'd for $C_{46}H_{72}N_2O_2S_2$ [M^+] = 748.50; found 747.92.

3,6-Bis(5-bromothiophen-2-yl)-2,5-bis(2-ethylhexyl)pyrrolo[3,4-c]pyrrole-1,4(2H,5H)-dione (**8-2EH**).

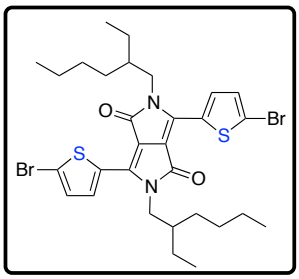

A 100 mL round bottom flask was charged with a stir bar, **7-2EH** (1.21 g, 2.31 *m*mol) and chloroform (0.1 M, 23 mL) under ambient conditions. After the reaction mixture was stirred in an ice bath at 0 °C for 20 min, NBS (821 mg, 4.61 *m*mol) was added in small portions over 30 min. After stirring for another 20 min, the reaction mixture was diluted and washed with distilled water (3×50 mL). The organic extract was dried over $MgSO_4$, and solvent was removed under reduced pressure. Purification by flash chromatography (20 % hexanes in $CHCl_3$) yielded 1.30 g of a purple solid (83 %).

^{1}H NMR (400 MHz, $CDCl_3$, δ): 8.64 (d, *J* = 4.2 Hz, 2 H), 7.22 (d, *J* = 4.2 Hz, 2 H), 3.92 (m, 4 H), 1.82 (m, 2 H), 1.26 (m, 16 H), 0.87 (aq, *J* = 7.3 Hz, 12 H). ^{13}C (100 MHz, $CDCl_3$, δ): 161.5, 139.5, 135.5, 131.6, 131.3, 119.2, 108.1, 46.1, 39.2, 30.3, 28.4, 23.7, 23.2, 14.2, 10.6. HRMS (EI, *m/z*) $[M]^+$ calcd for $C_{30}H_{38}Br_2N_2O_2S_2$, 682.0721; found, 682.0733. Anal. calcd for $C_{30}H_{38}Br_2N_2O_2S_2$: C, 52.79; H, 5.61; N, 4.10; found: C, 52.90; H, 5.52; N, 4.21.

3,6-Bis(5-bromothiophene-2-yl)-2,5-ditetradecyl-pyrrolo[3,4-c]pyrrole-1,4(2H,5H)-dione (**8-C14**).

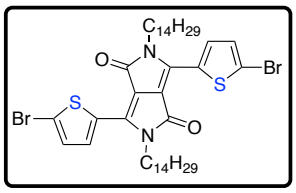

Followed the same synthetic procedure as for **8-2EH**. Instead, used **7-C12** (1.00g, 1.44 *m*mol), NBS (526 *m*g, 2.96 *m*mol) and 20 mL of $CHCl_3$ under N_2. The resulting materials were recrystallized twice in $CHCl_3$ to yield the product as a purple solid (308 *m*g, 25 %). Higher yields could have been obtained by further recrystallizing the mother liquor.

^{1}H NMR (400 MHz, $CDCl_3$): δ (ppm) = 8.68 (d, *J* = 4.0 Hz, 2 H), 7.24 (d, *J* = 4.0 Hz, 2 H), 3.98 (t, *J* = 7.6 Hz, 4 H), 1.71–1.69 (m, 4 H), 1.40–1.25 (m, 44 H), 0.87 (t, *J* = 6.4 Hz, 6 H). ^{13}C NMR (150 MHz, $CDCl_3$, 45°C): δ (ppm) = 161.3, 139.2, 135.4, 131.8, 131.4, 119.2, 108.2, 42.5, 32.1, 30.2, 29.9, 29.83, 29.81, 29.79, 29.72, 29.65, 29.5, 29.4, 27.0, 22.8, 14.2. MALDI-TOF MS (*m*/*z*): calc'd for $C_{42}H_{62}Br_2N_2O_2S_2$ [M^+] = 850.26; found 849.70.

3,6-Bis(5-bromothiophene-2-yl)-2,5-dihexadecyl-pyrrolo[3,4-c]pyrrole-1,4(2H,5H)-dione (**8-C16**).

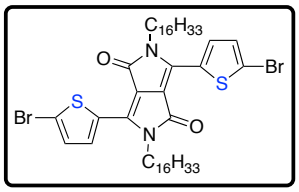

Followed the same synthetic procedure as for **8-2EH**. Instead, used **7-C14** (1.50g, 2.00 *m*mol), NBS (730 *m*g, 4.10 *m*mol) and 80 mL of $CHCl_3$ in a 250-mL RBF. The reaction mixture appeared as a purple suspension. After stirring at room temperature after 2 d under N_2, the suspension was precipitated into 50 mL of MeOH and filtered. The resulting materials were recrystallized five times in $CHCl_3$ to yield the product as a purple solid (534 *m*g, 30 %). Higher yields could have been obtained by further recrystallizing the mother liquor.

^{1}H NMR (400 MHz, $CDCl_3$): δ (ppm) = 8.68 (d, *J* = 4.0 Hz, 2 H), 7.23 (d, *J* = 4.0 Hz, 2 H), 3.98 (t, *J* = 7.6 Hz, 4 H), 1.73–1.69 (m, 4 H), 1.40–1.25 (m, 52 H), 0.88 (t, *J* = 6.4 Hz, 6 H). ^{13}C NMR (150 MHz, $CDCl_3$, 45°C): δ (ppm) = 161.3, 139.2, 135.4, 131.8, 131.4, 119.2, 108.2, 42.5, 32.1, 30.2, 29.86, 29.83, 29.82, 29.80, 29.72, 29.65, 29.5, 29.4, 27.0, 22.8, 14.2. MALDI-TOF MS (*m*/*z*): calc'd for $C_{46}H_{70}Br_2N_2O_2S_2$ [M^+] = 904.32; found 904.81.

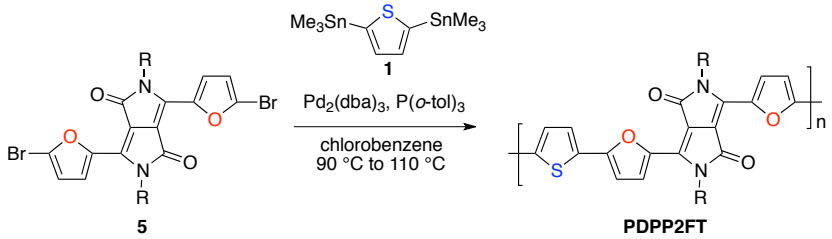

Poly(2,5-bis(2-ethylhexyl)-3-(furan-2-yl)-6-(5-(thiophen-2-yl)furan-2-yl)pyrrolo[3,4-c]pyrrole-1,4(2H,5H)-dione) (**PDPP2FT-2EH**)

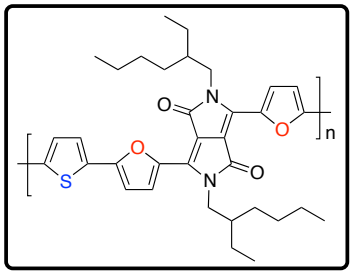

A 50-mL Schlenk tube was charged with **5-2EH** (200 *m*g, 0.307 *m*mol) and **1** (126 *m*g, 0.307 *m*mol), and the tube was evacuated and refilled with N_2 three times. Chlorobenzene (6 mL) was added, and the resulting solution was degassed by bubbling N_2 for 30 min while an oil bath was preheated to 90 °C. Upon removing the degassing needle, $Pd_2(dba)_3$ (2 mol %, 6.14 μmol, 5.62 *m*g) and P(*o*-tol)$_3$ (8 mol %, 24.56 μmol, 7.48 *m*g) were added to the solution, and the Schlenk tube was immediately heated at 90 °C. After 5 min, the mixture was stirred for additional 24 h at 110 °C. The reaction mixture was allowed to cool to 55 °C before chloroform (30 mL) and a palladium scavenger, *N,N*-diethylphenylazothioformamide (CAS# 39484-81-6, 20 mol%), were added. The resulting mixture was stirred for 3 h at 55°C and precipitated into methanol (200 mL). The precipitates were filtered through a Soxhlet thimble and purified via Soxhlet extraction. The polymer was washed for 12 h with methanol, 6 h with hexanes and 6 h in dichloromethane, and it was extracted with chloroform. The chloroform solution was then precipitated into methanol (150 mL), and the suspension was filtered through a 20 μm Nylon membrane to afford **PDPP2FT-2EH** as a dark solid (162 *m*g).

Poly(2,5-bis(2-butyloctyl)-3-(furan-2-yl)-6-(5-(thiophen-2-yl)furan-2-yl)pyrrolo[3,4-c]pyrrole-1,4(2H,5H)-dione) (**PDPP2FT-2BO**)

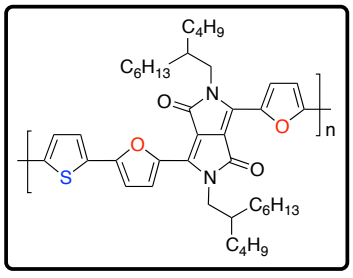

Followed the same synthetic procedure as for **PDPP2FT-2EH**. Instead, used **5-2BO** (180.0 *m*g, 0.236 *m*mol), **1** (96.71 mg, 0.236 *m*mol), $Pd_2(dba)_3$ (2 mol %, 4.72 μmol, 4.32 *m*g), P(*o*-tol)$_3$ (8 mol %, 18.88 μmol, 5.75 *m*g) and chlorobenzene (6.9 mL). The precipitates were filtered through a Soxhlet thimble and purified via Soxhlet extraction. The polymer was washed for 12 h with methanol, washed for 8 h with hexanes and extracted with chloroform. The chloroform solution was then precipitated into methanol (150 mL), and the suspension was filtered through a 20 μm Nylon membrane to afford **PDPP2FT-2BO** as a dark solid (148 *m*g).

Poly(2,5-didodecyl-3-(furan-2-yl)-6-(5-(thiophen-2-yl)furan-2-yl)pyrrolo[3,4-c]pyrrole-1,4(2H,5H)-dione) (**PDPP2FT-C12**)

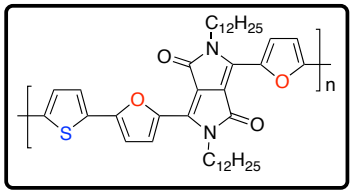

Followed the same synthetic procedure as for **PDPP2FT-2EH**. Instead, used **5-C12** (170.0 *m*g, 0.223 *m*mol), **1** (91.34 mg, 0.223 *m*mol), $Pd_2(dba)_3$ (2 mol %, 4.46 μmol, 4.08 *m*g), P(*o*-tol)$_3$ (8 mol %, 17.83 μmol, 5.43 *m*g) and chlorobenzene (6.5 mL). The precipitates were filtered through a Soxhlet thimble and purified via Soxhlet extraction. The polymer was washed for 12 h with methanol, 2 h with hexanes and 2 h in dichloromethane, and it was extracted with chloroform. The chloroform solution was then precipitated into methanol (150 mL), and the suspension was filtered through a 20 μm Nylon membrane to afford **PDPP2FT-C12** as a dark solid (40 *m*g).

Poly(2,5-ditetradecyl-3-(furan-2-yl)-6-(5-(thiophen-2-yl)furan-2-yl)pyrrolo[3,4-c]pyrrole-1,4(2H,5H)-dione) (**PDPP2FT-C14**)

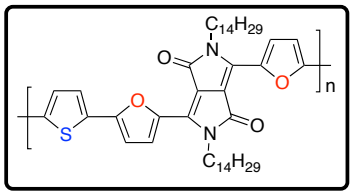

Followed the same synthetic procedure as for **PDPP2FT-2EH**. Instead, used **5-C14** (200.0 *m*g, 0.244 *m*mol), **1** (100.0 mg, 0.244 *m*mol), $Pd_2(dba)_3$ (2 mol %, 4.89 μmol, 4.47 *m*g), P(*o*-tol)$_3$ (8 mol %, 19.54 μmol, 5.95 *m*g) and chlorobenzene (7.4 mL). The precipitates were filtered through a Soxhlet thimble and purified via Soxhlet extraction. The polymer was washed for 12 h with methanol, 2 h with hexanes and 2 h in dichloromethane, and it was extracted with chloroform. The chloroform solution was then precipitated into methanol (150 mL), and the suspension was filtered through a 20 μm Nylon membrane to afford **PDPP2FT-C14** as a dark solid (169 *m*g).

Poly(2,5-dihexadecyl-3-(furan-2-yl)-6-(5-(thiophen-2-yl)furan-2-yl)pyrrolo[3,4-c]pyrrole-1,4(2H,5H)-dione) (**PDPP2FT-C16**)

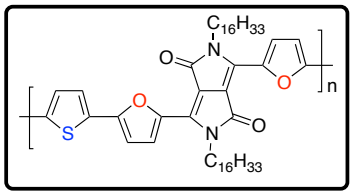

Followed the same synthetic procedure as for **PDPP2FT-2EH**. Instead, used **5-C16** (150 *m*g, 0.171 *m*mol), **1** (70.25 *m*g, 0.171 *m*mol), $Pd_2(dba)_3$ (2 mol %, 3.43 μmol, 3.14 *m*g), P(*o*-tol)$_3$ (8 mol %, 13.72 μmol, 4.17 *m*g) and chlorobenzene (5.6 mL). The precipitates were filtered through a Soxhlet thimble and purified via Soxhlet extraction. The polymer was washed for 12 h with methanol, 2 h with hexanes and 2 h in dichloromethane, and it was extracted with chloroform. The chloroform solution was then precipitated into methanol (200 mL), and the suspension was filtered through a 20 μm Nylon membrane to afford **PDPP2FT-C16** as a dark solid (123 mg).

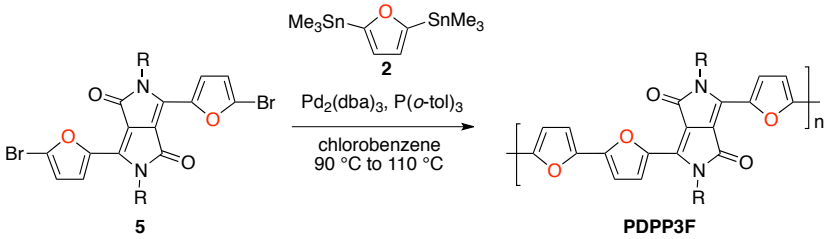

Poly(3-([2,2'-bifuran]-5-yl)-2,5-bis(2-ethylhexyl)-6-(furan-2-yl)pyrrolo[3,4-c]pyrrole-1,4(2H,5H)-dione) (**PDPP3F-2EH**)

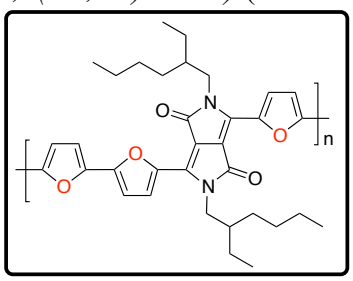

Followed the same synthetic procedure as for **PDPP2FT-2EH**. Instead, used **2** as the comonomer. The polymer was washed for 12 h with methanol, 2 h with hexanes and 2 h in dichloromethane, and it was extracted with chloroform. The chloroform solution was then precipitated into methanol (200 mL), and the suspension was filtered through a 20 μm Nylon membrane to afford **PDPP3F** as a dark purple solid (58 mg).

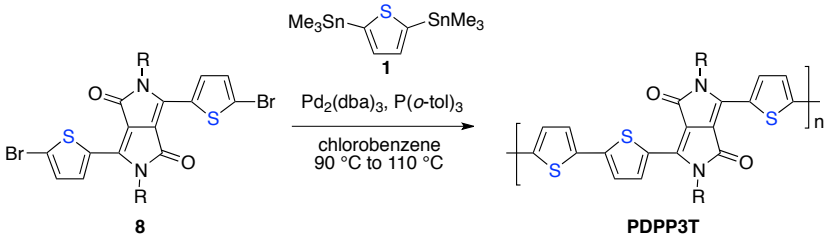

Poly(3-([2,2'-bithiophen]-5-yl)-2,5-bis(2-ethylhexyl)-6-(thiophen-2-yl)pyrrolo[3,4-c]pyrrole-1,4(2H,5H)-dione) (**PDPP3T-2EH**)

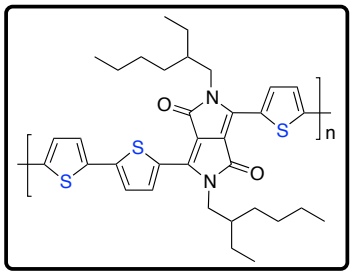

Followed the same synthetic procedure as for **PDPP2FT-2EH**. Instead, used **8-2EH** as the comonomer. The substantial solubility limitations encountered with **PDPP3T-2EH** during the purification process led us to establish the following modified protocol for the basic characterization: After 24 h of polymerization time, the reaction mixture was cooled to room temperature and aliquots were taken for SEC and CV analysis (~1 mL was extracted from the reaction mixture and precipitated into ~3 mL of methanol). The crude polymer **PDPP3T-2EH** was collected and dried under nitrogen flow before further use.

Poly(3-([2,2'-bithiophen]-5-yl)-2,5-ditetradecyl-6-(thiophen-2-yl)pyrrolo[3,4-c]pyrrole-1,4(2H,5H)-dione) (**PDPP3T-C14**)

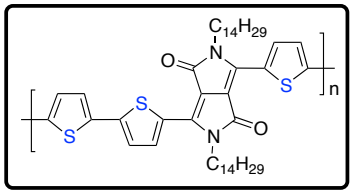

The same polymerization protocol as that described for **PDPP2FT-2EH** was followed. Instead, used **8-C14** (150 *m*g, 176 μmol), **1** (72.2 *m*g, 176 μmol), $Pd_2(dba)_3$ (3.23 *m*g, 3.53 μmol) and P(*o*-tol)$_3$ (4.29 *m*g, 14.1 μmol) in 5.3 mL of degassed chlorobenzene. After 24 h, the reaction was cooled to room temperature and aliquots were taken for SEC analysis.

Poly(3-([2,2'-bithiophen]-5-yl)-2,5-dihexadecyl-6-(thiophen-2-yl)pyrrolo[3,4-c]pyrrole-1,4(2H,5H)-dione) (**PDPP3T-C16**)

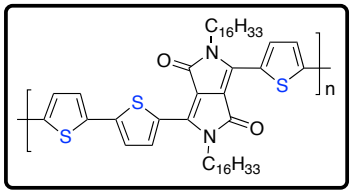

The same polymerization protocol as that described for **PDPP2FT-2EH** was followed. Instead, used **8-C16** (160 *m*g, 176 μmol), **1** (72.2 *m*g, 176 μmol), $Pd_2(dba)_3$ (3.23 *m*g, 3.53 μmol) and P(*o*-tol)$_3$ (4.29 *m*g, 14.1 μmol) in 5.5 mL of degassed chlorobenzene. The reaction mixture formed a gel-like material after 15 min of heating at 110 °C, and it was continued to be heated at 110 °C for 24 h. The reaction was then cooled to room temperature and aliquots were taken for SEC analysis.

Results of SEC analysis for all polymers are shown in Table 2-4.

Table 2-4. SEC analysis of **PDPP2FT** and **PDPP3T** derivatives.

Polymers	M_n (kDa)	M_w (kDa)	PDI
PDPP2FT-2EH	56	88	1.57
PDPP2FT-2BO	54	85	1.56
PDPP2FT-C12	46	78	1.70
PDPP2FT-C14	58	92	1.59
PDPP2FT-C16	55	87	1.60
PDPP3F-2EH	29	59	2.02
PDPP3T-2EH	2	5	2.71
PDPP3T-C14	<1	<1	--
PDPP3T-C16	0.95	1.9	1.98

2.6.2. Organic Photovoltaic Device Fabrication and Mobility Measurements

All devices were fabricated on ITO-coated glass substrates (pre-patterned, R = 20 Ω^{-1}, 150 nm, Thin Film Devices, Inc.). To clean and prepare these substrates for device fabrication, the following procedure was followed:

- Sonicate for 20 minutes in 2% Hellmanex soap water, then rinse thoroughly with deionized (DI) water
- Sonicate for 20 minutes in DI water
- Sonicate for 20 minutes in acetone
- Sonicate for 20 minutes in isopropyl alcohol, then dry under a stream of air
- UV-ozone clean for 5 minutes
- Spin-coat a thin layer (30-40 nm) of PEDOT:PSS (Clevios PVP) at 4000 RPM for 40 s, then dry in air for 10 min at 140 ^{o}C
- Transfer to glove box under N_2 for subsequent processing

Using substrates prepared as described above, the following procedure was followed to prepare solar cell devices described in **Section 2.2** with (**PDPP2FT-2EH** and **PDPP3F-2EH**):

- **PDPP2FT-2EH** solutions were prepared in chlorobenzene (CB) at a concentration of 15 mg/mL and were heated to 100 °C and stirred overnight for complete dissolution.
- **PDPP2FT-2EH** solutions were mixed with 30 mg/mL filtered $PC_{71}BM$ (Nano-C) solutions to yield blend solutions of different concentrations and weight ratios of polymer to $PC_{71}BM$.

- **PDPP3F-2EH** solutions were prepared in chloroform at a concentration of 10 mg/mL and were heated to 50 °C and stirred overnight for complete dissolution.
- **PDPP3F-2EH** solutions were mixed with 20 mg/mL filtered $PC_{71}BM$ solutions in chloroform to yield blend solutions of different concentrations and weight ratios of polymer to $PC_{71}BM$.
- Varying amounts of additive CN (v/v) were added to the blend solutions before spin coating, and the optimized amount of CN used was 9 %.
- The active layers of all devices were spin coated at 2000 RPM for 50 s on top of the PEDOT:PSS layer.
- The substrates were then placed in an evaporation chamber and pumped down to a pressure of ~ 6×10^{-7} Torr before evaporating a 1 nm LiF layer and subsequently a 100 nm Al layer through a shadow mask on top of the photoactive layer to yield devices with active areas of 0.03 cm^2.
- The mechanical removal of part of the organic layer allowed contact with the ITO and adding conductive Ag paste to the removed area to ensure electrical contact completed the device.

Using substrates prepared as described above, the following procedure was followed to prepare solar cell devices as described in **Section 2.3** with the following: **PDPP2FT-2EH, -C12, -C14 and -C16**.

- Prepare blend solution in chloroform with a polymer:$PC_{71}BM$ ratio of 1:3 by mass and a total solids concentration of 10.67 mg/mL for PDPP2FT-C12 and -C14 and 16 mg/mL for PDPP2FT-C16 and -2BO
- Add 5% by volume of high-boiling additive 1-chloronapthalene (CN)
- Spin-coat onto substrate at 2000 RPM for 40 s, followed by 4000 RPM for 5 s
- Dry under low vacuum for 20 minutes
- Thermally evaporate cathodes (1 nm LiF, 100 nm Al) under vacuum (~10^{-7} torr) through a shadow mask defining an active area of ~0.03 cm^2

Testing of the devices was performed under a nitrogen atmosphere with an Oriel Xenon arc lamp having an AM 1.5G solar filter to yield 100 mW cm^{-2} light intensity as calibrated by an NREL certified silicon photocell. Current–voltage behavior was measured with a Keithley 2400 SMU. During the device optimization process, various parameters (solution concentration, blends ratio, spin speed, additive percentage) were tested and more than 200 devices were tested and optimized conditions were repeated to ensure reproducibility.

The external quantum efficiency (EQE) was determined at zero bias by illuminating the device with monochromatic light supplied by a Xenon lamp in combination with a monochromator (Spectra Pro 150, Acton Research Corporation). The number of photons incident on the sample was calculated for each wavelength by using a Si photodiode calibrated by the manufacturer (Hamamatsu).

Using substrates prepared as described above, the following procedure was followed to prepare SCLC devices:

- Prepare polymer solution in $CHCl_3$ at a concengration of 8 mg/mL for PDPP2FT-C_{12} and -C_{14} and 10 mg/mL for PDPP2FT-C_{16} and -2BO

- Add 5% by volume of high-boiling additive CN
- Spin-coat onto substrate at either 1000 or 2000 RPM for 40 s (to vary thickness), followed by 4000 RPM for 5 s
- Dry under low vacuum for 20 minutes
- Thermally evaporate cathodes (50 nm Au) under vacuum (~10^{-7} torr) through a shadow mask defining an active area of ~0.03 cm^2
- For devices of each material, mobility values for two different film thicknesses were averaged to give the values provided.

2.6.3. Instrumentation for Characterization of Optoelectronic Properties and Active Layer Morphology

Cyclic voltammograms were collected using a Solartron 1285 potentiostat under the control of CorrWare II software. A standard three-electrode cell based on a Pt wire working electrode, a silver wire pseudo reference electrode (calibrated vs. Fc/Fc+), and a Pt wire counter electrode was purged with nitrogen and maintained under a nitrogen atmosphere during all measurements. Anhydrous acetonitrile was purchased anhydrous from Aldrich and tetrabutylammonium hexafluorophosphate (0.1 M) was used as the supporting electrolyte. Polymer films were drop cast onto a Pt wire working electrode from a chloroform, tetrahydrofuran, toluene, or chlorobenzene solution and dried under nitrogen prior to measurement.

UV-Visible absorption spectra were obtained using a Cary 5000 Conc UV-Visible spectrophotometer in transmission geometry. For thin film measurements polymers were spin coated from chlorobenzene or chloroform solutions onto cleaned glass slides. Thin-films were spin-coated from $CHCl_3$ onto untreated quartz slides, and film thickness was measured by a Veeco Dektak profilometer.

Atomic force microscopy (AFM) was performed to study the surface morphology of the polymer:PCBM blends. Topographical and phase images were obtained concurrently using a Veeco Multimode V AFM in tapping mode using RTESP tips.

Grazing-incidence x-ray scattering (GIXS) experiments were conducted at the Stanford Synchotron Radiation Lightsource on beamline 11-3. Substituting Si for ITO on glass, samples were prepared following the aforementioned procedure for SCLC devices (for neat polymer films) or for solar cell devices (for blend films). Samples were irradiated at a fixed incident angle of approximately 0.1^o and their GIXS patterns were recorded with a 2-D image detector (MAR345 image plate detector). GIXS patterns were recorded with an X-ray energy of 12.71 keV (λ = 0.975 Å). To maximize the intensity from the sample, the incident angle (~0.08^o – 0.12^o) was carefully chosen such that the X-ray beam penetrated the sample completely but did not interact significantly with the silicon substrate. Typical exposure times were 30-600 s.

2.7. References

(1) Thompson, B. C.; Fréchet, J. M. J. *Angew. Chem., Int. Ed.* **2008**, *47*, 58.
(2) Dennler, G.; Scharber, M. C.; Brabec, C. J. *Adv. Mater.* **2009**, *21*, 1323.
(3) Scharber, M. C.; Mühlbacher, D.; Koppe, M.; Denk, P.; Waldauf, C.; Heeger, A. J.; Brabec, C. J. *Adv. Mater.* **2006**, *18*, 789.
(4) Chen, J. W.; Cao, Y. *Acc. Chem. Res.* **2009**, *42*, 1709–1718.
(5) Günes, S.; Neugebauer, H.; Sariciftci, N. S. *Chem. Rev.* **2007**, *107*, 1324.
(6) Li, C.; Liu, M.; Pschirer, N. G.; Baumgarten, M.; Müllen, K. Chem. Rev. 2010, 110, 6817.
(7) Bundgaard, E.; Krebs, F. C. *Sol. Energ. Mater. Sol. Cells* **2007**, *91*, 954.
(8) Boudreault, P.-L. T.; Najari, A.; Leclerc, M. *Chem. Mater.* **2011**, *23*, 456.
(9) Li Y.; Sonar, P.; Singh, S. P.; Soh, M. S.; van Meurs, M.; Tan, J. *J. Am. Chem. Soc.* **2011**, *133*, 2198.
(10) Roncali, J. *Macromol. Rapid Commun.* **2007**, *28*, 1761.
(11) Heremans, P.; Cheyns, D.; Rand, B. P. *Acc. Chem. Res.* **2009**, *42*, 1740.
(12) Vandewal, K.; Tvingstedt, K.; Gadisa, A.; Ingana¨s, O.; Manca, J. V. *Nat. Mater.* **2009**, *8*, 904.
(13) Li, Y.; Zou, Y. *Adv. Mater.* **2008**, *20*, 2952.
(14) Hou, J.; Tan, Z. A.; Yan, Y.; He, Y.; Yang, C.; Li, Y. *J. Am. Chem. Soc.* **2006**, *128*, 4911.
(15) Varotto, A.; Treat, N. D.; Jo, J.; Shuttle, C. G.; Batara, N. A.; Brunetti, F. G.; Seo, J. H.; Chabinyc, M. L.; Hawker, C. J.; Heeger, A. J.; Wudl, F. *Angew. Chem., Int. Ed.* **2011**, *50*, 5166.
(16) Veldman, D.; Meskers, S. C. J.; Janssen, R. A. J. *Adv. Funct. Mater.* **2009**, *19*, 1939.
(17) Wienk, M. M.; Turbiez, M.; Gilot, J.; Janssen, R. A. J. *Adv. Mater.* **2008**, *20*, 2556.
(18) Chen, H.-Y.; Hou, J.; Zhang, S.; Liang, Y.; Yang, G.; Yang, Y.; Yu, L.; Wu, Y.; Li, G. *Nature Photon.* **2009**, *3*, 649.
(19) Zhou, H.; Yang, L.; Price, S. C.; Knight, K. J.; You, W. *Angew. Chem., Int. Ed.* **2010**, *49*, 7992.
(20) Blom, P. W. M.; Mihailetchi, V. D.; Koster, L. J. A.; Markov, D. E. *Adv. Mater.* **2007**, *19*, 1551.
(21) Parmer, J. E.; Mayer, A. C.; Hardin, B. E.; Scully, S. R.; McGehee, M. D.; Heeney, M.; McCulloch, I. *Appl. Phys. Lett.* **2008**, *92*, 113309.
(22) Coropceanu, V.; Cornil, J.; da Silva Filho, D. A.; Olivier, Y.; Silbey, R.; Brédas, J.-L. *Chem. Rev.* **2007**, *107*, 926.
(23) Johns, J. E.; Muller, E. A.; Frechet, J. M. J.; Harris, C. B. *J. Am. Chem. Soc.* **2010**, *132*, 15720.
(24) Peet, J.; Heeger, A. J.; Bazan, G. C. *Acc. Chem. Res.* **2009**, *42*, 1700.
(25) Di Nuzzo, D.; Aguirre, A.; Shahid, M.; Gevaerts, V. S.; Meskers, S. C. J.; Janssen, R. A. *J. Adv. Mater.* **2010**, *22*, 4321.
(26) Perez, M. D.; Borek, C.; Forrest, S. R.; Thompson, M. E. *J. Am. Chem. Soc.* **2009**, *131*, 9281.
(27) Rogers, J. T.; Schmidt, K.; Toney, M. F.; Kramer, E. J.; Bazan, G. C. *Adv. Mater.* **2011**, *23*, 2284.
(28) Salleo, A.; Kline, R. J.; DeLongchamp, D. M.; Chabinyc, M. L. *Adv. Mater.* **2010**, *22*, 3812.
(29) Piliego, C.; Holcombe, T. W.; Douglas, J. D.; Woo, C. H.; Beaujuge, P. M.; Fréchet, J. M. J. *J. Am. Chem. Soc.* **2010**, *132*, 7595.

(30) Beaujuge, P. M.; Pisula, W.; Tsao, H. N.; Ellinger, S.; Müllen, K.; Reynolds, J. R. *J. Am. Chem. Soc.* **2009**, *131*, 7514.
(31) Hou, J.; Chen, H. Y.; Zhang, S.; Li, G.; Yang, Y. *J. Am. Chem. Soc.* **2008**, *130*, 16144.
(32) Park, S. H.; Roy, A.; Beaupre, S.; Cho, S.; Coates, N.; Moon, J. S.; Moses, D.; Leclerc, M.; Lee, K.; Heeger, A. J. *Nat. Photon.* **2009**, *3*, 297.
(33) Peet, J.; Kim, J. Y.; Coates, N. E.; Ma, W. L.; Moses, D.; Heeger, A. J.; Bazan, G. C. *Nat. Mater.* **2007**, *6*, 497.
(34) Holcombe, T. W.; Woo, C. H.; Kavulak, D. F. J.; Thompson, B. C.; Fréchet, J. M. J. *J. Am. Chem. Soc.* **2009**, *131*, 14160.
(35) Woo, C. H.; Holcombe, T. W.; Unruh, D. A.; Sellinger, A.; Fréchet, J. M. J. *Chem. Mater.* **2010**, *22*, 1673.
(36) Kim, B. J.; Miyamoto, Y.; Ma, B.; Fréchet, J. M. J. *Adv. Funct. Mater.* **2009**, *19*, 2273.
(37) Woo, C. H.; Thompson, B. C.; Kim, B. J.; Toney, M. F.; Fréchet, J. M. J. *J. Am. Chem. Soc.* **2008**, *130*, 16324.
(38) Liang, Y.; Feng, D.; Wu, Y.; Tsai, S. T.; Li, G.; Ray, C.; Yu, L. *J. Am. Chem. Soc.* **2009**, *131*, 7792.
(39) Qin, R. P.; Li, W. W.; Li, C. H.; Du, C.; Veit, C.; Schleiermacher, H. F.; Andersson, M.; Bo, Z. S.; Liu, Z. P.; Ingana¨s, O.; Wuerfel, U.; Zhang, F. L. *J. Am. Chem. Soc.* **2009**, *131*, 14612.
(40) Zou, Y. P.; Najari, A.; Berrouard, P.; Beaupre, S.; Aich, B. R.; Tao, Y.; Leclerc, M. *J. Am. Chem. Soc.* **2010**, *132*, 5330.
(41) Huo, L. J.; Hou, J. H.; Zhang, S. Q.; Chen, H. Y.; Yang, Y. *Angew. Chem., Int. Ed.* **2010**, *49*, 1500.
(42) Bunz, U. H. F. *Angew. Chem., Int. Ed.* **2010**, *49*, 5037.
(43) Umeyama, T.; Takamatsu, T.; Tezuka, N.; Matano, Y.; Araki, Y.; Wada, T.; Yoshikawa, O.; Sagawa, T.; Yoshikawa, S.; Imahori, H. *J. Phys. Chem. C* **2009**, *113*, 10798.
(44) Yamamoto, T.; Zhou, Z. H.; Kanbara, T.; Shimura, M.; Kizu, K.; Maruyama, T.; Nakamura, Y.; Fukuda, T.; Lee, B. L.; Ooba, N.; Tomaru, S.; Kurihara, T.; Kaino, T.; Kubota, K.; Sasaki, S. *J. Am. Chem. Soc.* **1996**, *118*, 10389.
(45) Li, R. Z.; Lv, X. J.; Shi, D.; Zhou, D. F.; Cheng, Y. M.; Zhang, G. L.; Wang, P. *J. Phys. Chem. C* **2009**, *113*, 7469.
(46) Lin, J. T.; Chen, P. C.; Yen, Y. S.; Hsu, Y. C.; Chou, H. H.; Yeh, M. C. P. *Org. Lett.* **2009**, *11*, 97.
(47) Walker, B.; Tomayo, A. B.; Dang, X. D.; Zalar, P.; Seo, J. H.; Garcia, A.; Tantiwiwat, M.; Nguyen, T. Q. *Adv. Funct. Mater.* **2009**, *19*, 3063.
(48) Bijleveld, J. C.; Zoombelt, A. P.; Mathijssen, S. G. J.; Wienk, M. M.; Turbiez, M.; de Leeuw, D. M.; Janssen, R. A. J. *J. Am. Chem. Soc.* **2009**, *131*, 16616.
(49) Khlyabich, P. P.; Burkhart, B.; Ng, C. F.; Thompson, B. C. *Macromolecules* **2011**, *44*, 5079.
(50) Mei, J.; Graham, K. R.; Stalder, R.; Tiwari, S. P.; Cheun, H.; Shim, J.; Yoshio, M.; Nuckolls, C.; Kippelen, B.; Castellano, R. K.; Reynolds, J. R. *Chem. Mater.* **2011**, *23*, 2285.
(51) Bronstein, H.; Chen, Z.; Ashraf, R. S.; Zhang, W.; Du, J.; Durrant, J. R.; Tuladhar, P. S.; Song, K.; Watkins, S. E.; Geerts, Y.; Wienk, M. M.; Janssen, R. A. J.; Anthopoulos, T.; Sirringhaus, H.; Heeney, M.; McCulloch, I. *J. Am. Chem. Soc.* **2011**, *133*, 3272.

(52) Loser, S.; Bruns, C. J.; Miyauchi, H.; Ortiz, R. P.; Facchetti, A.; Stupp, S. I.; Marks, T. J. *J. Am. Chem. Soc.* **2011**, *133*, 8142.
(53) Sonar, P.; Singh, S. P.; Li, Y.; Soh, M. S.; Dodabalapur, A. *Adv. Mater.* **2010**, *22*, 5409.
(54) Tamayo, A. B.; Dang, X.-D.; Walker, B.; Seo, J.; Kent, T.; Nguyen, T.-Q. *Appl. Phys. Lett.* **2009**, *94*, 103301.
(55) Bijleveld, J. C.; Karsten, B. P.; Mathijssen, S. G. J.; Wienk, M. M.; de Leeuw, D. M.; Janssen, R. A. J. *J. Mater. Chem.* **2011**, *21*, 1600.
(56) Zou, Y. P.; Gendron, D.; Neagu-Plesu, R.; Leclerc, M. *Macromolecules* **2009**, *42*, 6361.
(57) Zou, Y. P.; Gendron, D.; Badrou-Aich, R.; Najari, A.; Tao, Y.; Leclerc, M. *Macromolecules* **2009**, *42*, 2891.
(58) Zou, Y.; Najari, A.; Berrouard, P.; Beaupré, S.; Aïch, B. R.; Tao, Y.; Leclerc, M. *J. Am. Chem. Soc.* **2010**, *132*, 5330.
(59) Gidron, O.; Diskin-Posner, Y.; Bendikov, M. *J. Am. Chem. Soc.* **2010**, *132*, 2148.
(60) Miyata, Y.; Nishinaga, T.; Komatsu, K. *J. Org. Chem.* **2005**, *70*, 1147.
(61) Hucke, A.; Cava, M. P. *J. Org. Chem.* **1998**, *63*, 7413.
(62) Hoven, C. V.; Dang, X.-D.; Coffin, R. C.; Peet, J.; Nguyen, T.-Q.; Bazan, G. C. *Adv. Mater.* **2010**, *22*, E63.
(63) Park, S. H.; Roy, A.; Beaupre, S.; Cho, S.; Coates, N.; Moon, J. S.; Moses, D.; Leclerc, M.; Lee, K.; Heeger, A. J. *Nature Photon.* **2009**, *3*, 297.
(64) Scharber, M. C.; Koppe, M.; Gao, J.; Cordella, F.; Loi, M. A.; Denk, P.; Morana, M.; Egelhaaf, H.-J.; Forberich, K.; Dennler, G.; Gaudiana, R.; Waller, D.; Zhu, Z.; Shi, X.; Brabec, C. J. *Adv. Mater.* **2010**, *22*, 367.
(65) Chen, H.-Y.; Hou, J.; Hayden, A. E.; Yang, H.; Houk, K. N.; Yang, Y. *Adv. Mater.* **2010**, *22*, 371.
(66) McCulloch, I.; Heeney, M.; Bailey, C.; Genevicius, K.; MacDonald, I.; Shkunov, M.; Sparrowe, D.; Tierney, S.; Wagner, R.; Zhang, W.; Chabinyc, M. L.; Kline, R. J.; McGehee, M. D.; Toney, M. F. *Nature Mater.* **2006**, *5*, 328.
(67) Wang, C.; Jimison, L. H.; Goris, L.; McCulloch, I.; Heeney, M.; Ziegler, A.; Salleo, A. *Adv. Mater.* **2010**, *22*, 697.
(68) Frisch, M. J.; Trucks, G. W.; Schlegel, H. B.; Scuseria, G. E.; Robb, M. A.; Cheeseman, J. R.; Scalmani, G.; Barone, V.; Mennucci, B.; Petersson, G. A.; Nakatsuji, H.; Caricato, M.; Li, X.; Hratchian, H. P.; Izmaylov, A. F.; Bloino, J.; Zheng, G.; Sonnenberg, J. L.; Hada, M.; Ehara, M.; Toyota, K.; Fukuda, R.; Hasegawa, J.; Ishida, M.; Nakajima, T.; Honda, Y.; Kitao, O.; Nakai, H.; Vreven, T.; Montgomery, Jr., J. A.; Peralta, J. E.; Ogliaro, F.; Bearpark, M.; Heyd, J. J.; Brothers, E.; Kudin, K. N.; Staroverov, V. N.; Kobayashi, R.; Normand, J.; Raghavachari, K.; Rendell, A.; Burant, J. C.; Iyengar, S. S.; Tomasi, J.; Cossi, M.; Rega, N.; Millam, J. M.; Klene, M.; Knox, J. E.; Cross, J. B.; Bakken, V.; Adamo, C.; Jaramillo, J.; Gomperts, R.; Stratmann, R. E.; Yazyev, O.; Austin, A. J.; Cammi, R.; Pomelli, C.; Ochterski, J. W.; Martin, R. L.; Morokuma, K.; Zakrzewski, V. G.; Voth, G. A.; Salvador, P.; Dannenberg, J. J.; Dapprich, S.; Daniels, A. D.; Farkas, Ö.; Foresman, J. B.; Ortiz, J. V.; Cioslowski, J.; Fox, D. J. *Gaussian 09 Revision C.01*.
(69) Rieger, R.; Beckmann, D.; Mavrinskiy, A.; Pisula, W.; Kastler, M.; Müllen, K. *Chem Mater*. **2010**, *22*, 5314.
(70) Lee, J. K.; Ma, W. L.; Brabec, C. J.; Yuen, J.; Moon, J. S.; Kim, J. Y.; Lee, K.; Bazan, G. C.; Heeger, A. J. J. Am. Chem. Soc. 2008, 130, 3619.
(71) Yu, G.; Heeger, A. J. J. Appl. Phys. 1995, 78, 4510.

(72) Halls, J. J. M.; Walsh, C. A.; Greenham, N. C.; Marseglia, E. A.; Friend, R. H.; Moratti, S. C.; Holmes, A. B. Nature 1995, 376, 498.
(73) Guo, J.; Liang, Y.; Szarko, J.; Lee, B.; Son, H. J.; Rolczynski, B. S.; Yu, L.; Chen, L. X. J. Phys. Chem. B 2009, 114, 742.
(74) Beiley, Z. M.; Hoke, E. T.; Noriega, R.; Dacuña, J.; Burkhard, G. F.; Bartelt, J. A.; Salleo, A.; Toney, M. F.; McGehee, M. D. *Adv. Energ. Mater.* **2011**, *1*, 954.
(75) Street, R. A.; Northrup, J. E.; Salleo, A. *Phys. Rev. B* **2005**, *71*, 165202.
(76) Kim, Y.; Cook, S.; Tuladhar, S. M.; Choulis, S. A.; Nelson, J.; Durrant, J. R.; Bradley, D. D. C.; Giles, M.; McCulloch, I.; Ha, C.-S.; Ree, M. *Nature Mater.* **2006**, *5*, 197.
(77) Warren, B. E. X-Ray Diffraction; Addison-Wesley: Reading, MA, 1969.
(78) Rivnay, J.; Noriega, R.; Northrup, J. E.; Kline, R. J.; Toney, M. F.; Salleo, A. *Phys. Rev. B* **2011**, *83*, 121306.

Chapter III

Enhancing Intermolecular Connectivity of Conjugated Small Molecules via Pyrene-Directed Self-Assembly

3.1. Introduction: Improving Interconnectivity of Conjugated Small Molecules

Organic photovoltaics (OPVs) are a promising technology for cost-effective and scalable production of renewable energy.[1–3] Current research in OPV materials focuses primarily on the design and synthesis of semiconducting polymers capable of both light absorption and charge transport. In OPV cells utilizing a bulk-heterojunction (BHJ) architecture, conjugated polymers have demonstrated promising device efficiency; however, they can suffer from drawbacks such as batch-to-batch variation and chain-end contamination, which can reduce overall performance and device consistency.[4,5]

In order to develop OPV materials that exhibit not only favorable electronic properties but also batch-to-batch consistency, electroactive small molecules have recently received attention as alternatives to polymers.[4,6–9] While small molecules can be synthesized and solution-processed into devices just like polymers, they do not suffer from the inherent polydispersity of polymeric materials. They can be synthesized and purified as single molecular entities, thus eliminating the sort of device variability that can arise from material inhomogeneity. Despite these potential advantages, current data shows that the photovoltaic efficiencies of small molecules lag behind those of the highest-performing polymers.[5,10,11]

The relatively low performance of small molecules may be attributed to their limited interconnectivity through the active layer, resulting in low device fill factors. Earlier studies[12–15] have shown that polymers with higher molecular weight (M_n) perform better in BHJ solar cells than lower M_n polymers. In low M_n polymers, charge transport is limited by the short chain length.[12] By extension, as small molecules represent the lower limit of M_n, their device performance can suffer from inadequate interconnectivity and inefficient charge extraction. Herein, we demonstrate that the interconnectivity of small molecule semiconductors can be greatly improved by directed molecular self-assembly. Small molecules designed with this principle are shown to form highly ordered and interconnected domains and exhibit large fill factors and efficiencies in OPV devices.

3.2. Molecular Design: End-Group-Facilitated Self-Assembly via π-π Interactions

We postulated that the introduction of π-stacking moieties onto the ends of small molecules would facilitate favorable end-to-end π-π interactions, leading to enhanced charge transport between adjacent molecules. To investigate this approach, a series of small molecules was synthesized, each with different electron-rich end-groups (Figure 3-1). End-groups were selected for their varying degrees of planarity, which can affect their tendency to π-stack. Triphenylamine (TPA) has a non-planar structure with its phenyl groups twisting into a propeller motif.[16] Benzo[1,2-*b*;4,5- *b*′]dithiophene (BDT) contains a planar fused ring but has non-coplanar alkoxy substituents. Pyrene is a completely planar moiety and has a strong propensity to π -stack. In addition, the regio-connectivity between pyrene and the chromophoric core was varied in order to study the effect of end-group symmetry.

As a platform for investigating the effects of these end-groups, diketopyrrolopyrrole (DPP) was chosen to be the electron-deficient core, since this moiety allows for control of small molecule solution-processability and solid-state molecular ordering through modulation of the *N*-alkyl substituents.[17] The DPP core has also demonstrated promising optical properties, charge carrier mobility, and photovoltaic performance in numerous small molecule and polymeric materials;[5,18–29] in particular, Nguyen *et al.* have reported a DPP-containing small molecule donor that achieved 4.4% efficiency with phenyl-C_{71}-butyric acid methyl ester ($PC_{71}BM$) in BHJ devices.[5]

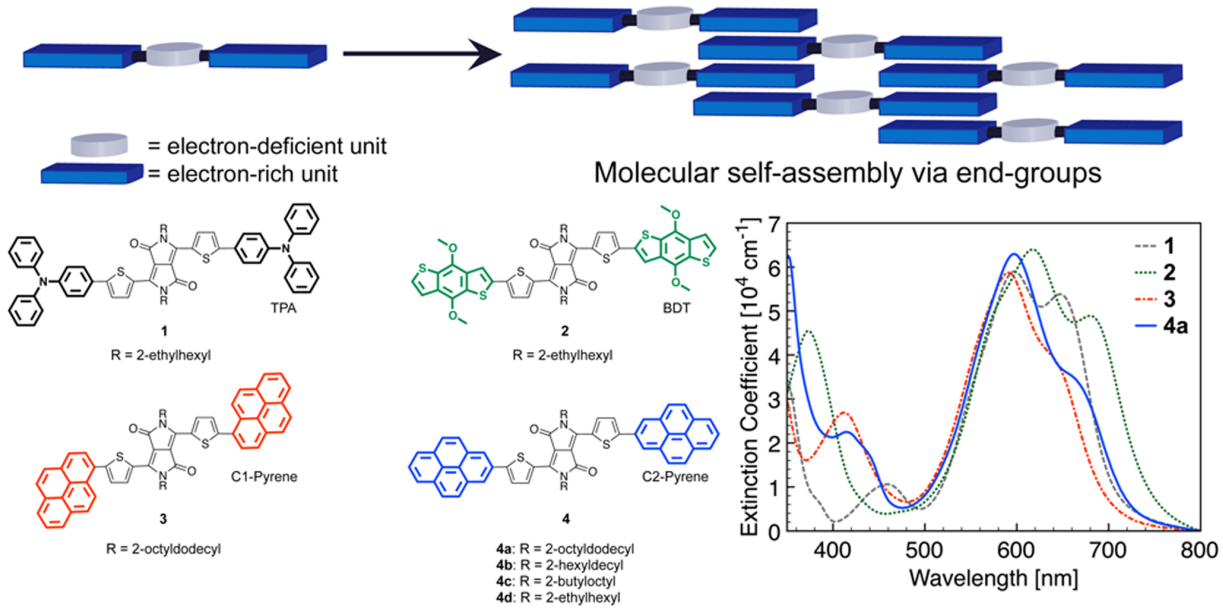

Figure 3-1. Donor-acceptor small molecules are designed to self-assemble through the electron-rich π -stacking units (top). Molecules **1**, **2**, **3** and **4** are based on a DPP core moiety flanked by electron-rich end-groups (bottom left). The UV-vis absorption spectra of **1**, **2**, **3** and **4a** were obtained as thin films (bottom right).

3.3. Results and Discussion

3.3.1. Synthesis and Optoelectronic Properties

As shown in Scheme 3-1, synthesis of the electron-deficient DPP core **5** was achieved via condensation between 2-thiophenecarbonitrile and dimethyl succinate in the presence of *tert*-amyl alkoxide, which was generated *in situ*.[30] Deprotonation of **5** followed by an S_N2 reaction with branched alkyl halides allowed for functionalization of side chains.[31] To fine-tune the solubility and processability of the target molecules, the DPP core was substituted with alkyl groups of various sizes and bulk, namely 2-octyldodecyl (**a**), 2-hexyldecyl (**b**), 2-butyloctyl (**c**), and 2-ethylhexyl (**d**) groups Bromination of the thiophene units in **6a-d** using two equivalents of *N*-bromosuccinimide (NBS) yielded **7a-d**.

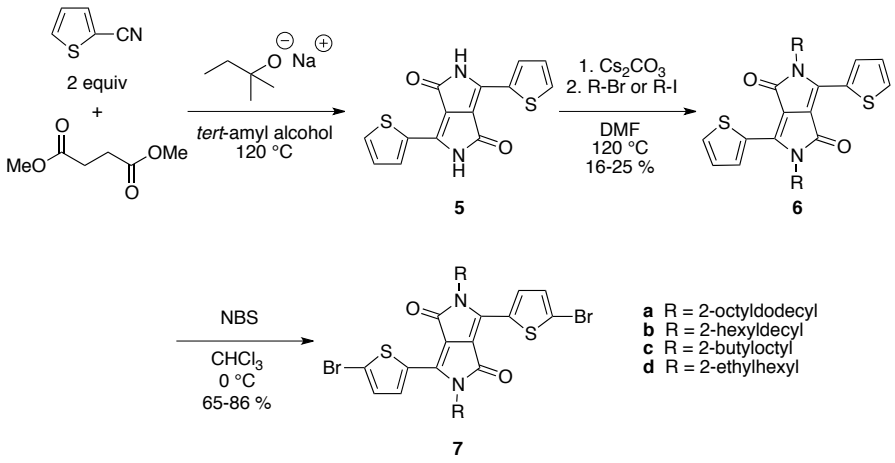

Scheme 3-1. Synthesis of the electron-deficient dibromo-DPP coupling partners **7a-d**.

To enable cross-coupling with the dibrominated DPP-core, the electron-rich end-groups were either borylated or stannylated (Scheme 3-2). TPA was functionalized with the boronic acid pinacol ester via Pd-catalyzed Miyaura borylation of 4-bromotriphenylamine. To synthesize the BDT end group, benzo[1,2-*b*:4,5-*b'*]dithiophene-4,8-dione was first reduced and aromatized to hydroquinone with zinc and then methylated to yield **9**. Subsequent lithiation with 1 equivalent of *n*-butyllithium followed by stannylation afforded the product as a mixture of **9** and monostannyl BDT **10**.[32] While pyrene-1-boronic acid was commercially available, the C2-pyrene boronate ester **11** was obtained by Hartwig Ir(I)-catalyzed C-H functionalization.[33] The bulky active catalyst [Ir(bpy)(Bpin)$_3$] selectively borylates at the C2 position rather than at the more sterically hindered C1 position.[34] The yield of this reaction was only 24 % because the diborylated species was a major byproduct, and it can be improved upon using an excess of pyrene such that bis(pinacolato)diboron becomes the limiting reagent.

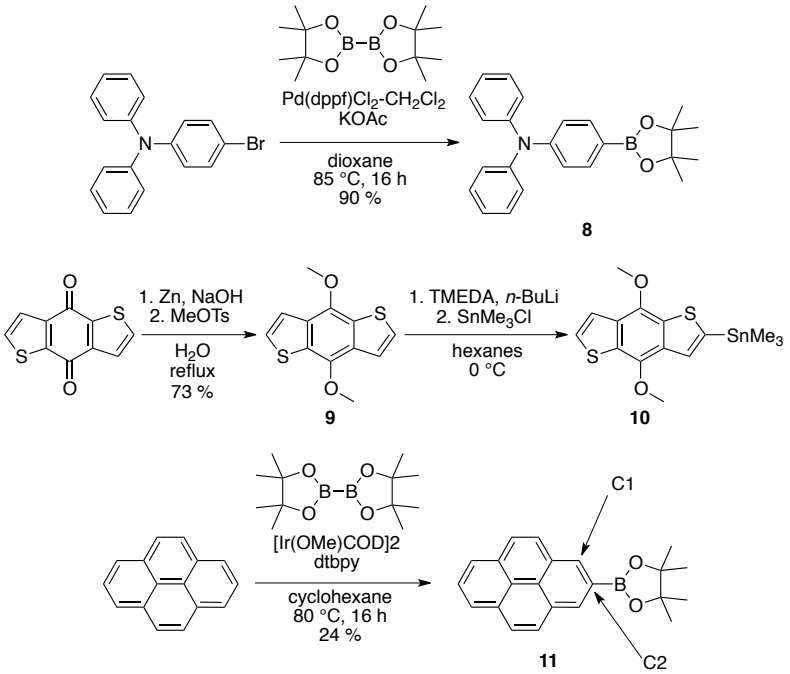

Scheme 3-2. Borylation and stannylation of the electron-rich coupling partners that will become the small molecule end-groups.

Syntheses of the small molecules **1**, **3** and **4a**-**d** were achieved through Pd(0)-catalyzed Suzuki cross-coupling reactions of the TPA or pyrene end-groups with the dibrominated DPP-core in moderate to high yields except for **4d**, which exhibits low solubility. Stille cross-coupling reaction between BDT **10** to DPP **7a** affords small molecule **2**. (Scheme 3-3). All four molecules were characterized by UV-visible spectroscopy in films. They exhibit strong absorption in the visible range with optical band gaps ranging from 1.7-1.8 eV (Figure 3-1 bottom right). They also show comparable absorption profiles relative to one another. The energy levels of all the small molecules were determined by both photoelectron spectroscopy in air (PESA) and cyclic voltammetry (CV), and these values are summarized in Table 3-1. Comparing the energy levels of the small molecules, it appears that the end-group substitution affects the LUMO levels more significantly than it does to the HOMO levels; in particular, molecule **2**, which is flanked with BDT end groups, shows the lowest LUMO level. All four small molecules exhibit optical and electronic properties that are suitable for OPV applications.

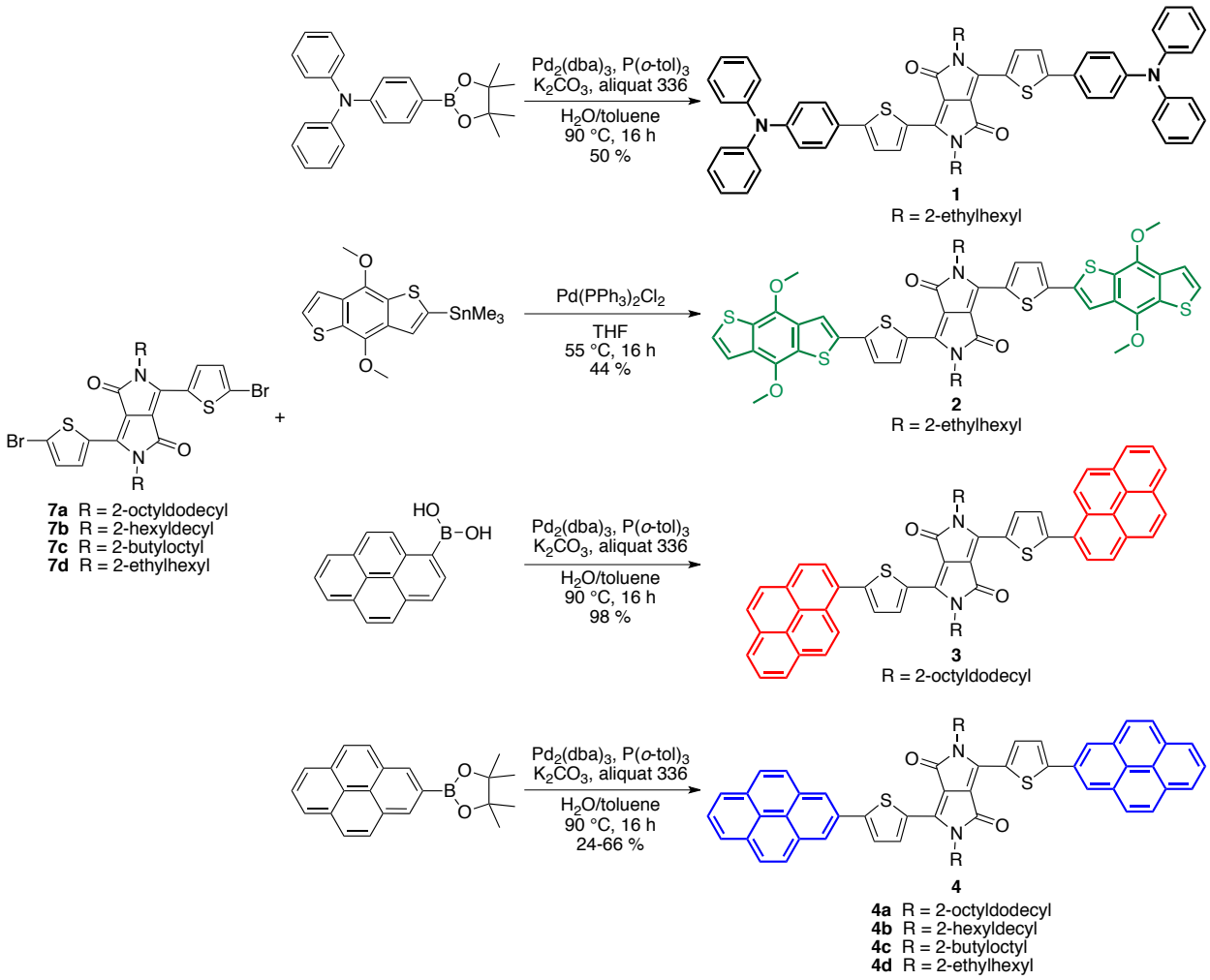

Scheme 3-3. Pd-catalyzed Suzuki or Stille cross-coupling reactions yield the final four small molecules.

Table 3-1. Optical and electrochemical properties of **1**-**4a** in thin films.

	Extinction Coefficient[a] [cm^{-1}]	Optical band gap[b] [eV]	HOMO (PESA[c]) [eV]	HOMO (CV[d]) [eV]	LUMO (CV[d]) [eV]
1	5.9×10^4	1.76	5.2	5.5	3.7
2	6.4×10^4	1.66	5.1	5.5	3.8
3	6.4×10^4	1.81	5.1	5.6	3.5
4a	6.3×10^4	1.70	5.1	5.6	3.5

[a]Measured at λ_{max}. [b]Based on absorption onsets. [c]Photoelectron spectroscopy in air (PESA) measurements. [d]Cyclic voltammetry (CV) measurements, vs. (Fc/Fc^+).

3.3.2. Photovoltaic Performance and Mobility Measurements

To determine the OPV performance of the small molecule materials, thin-film BHJ devices were prepared with the following architecture: ITO/PEDOT:PSS/small molecule:$PC_{71}BM$/Al. Upon extensive device optimization, small molecule **4a** exhibits a notable maximum power conversion efficiency (PCE) of 2.7%, whereas **1** , **2** and **3** exhibit lower device PCEs of 1.3%, 1.7% and 0.7%, respectively (Table 3-2, Figure 3-2). While **1**, **2** and **4a** possess similar

optoelectronic properties, their varying device performances suggest that PCE is highly dependent on end-group planarity. However, end-group planarity alone does not ensure high device efficiency, as demonstrated by the low PCE of **3**. Changing the site of pyrene substitution from C1 (**3**) to C2 (**4a**) led to an enhancement of device performance, indicating that end-group symmetry can also have a dramatic influence on PCE.

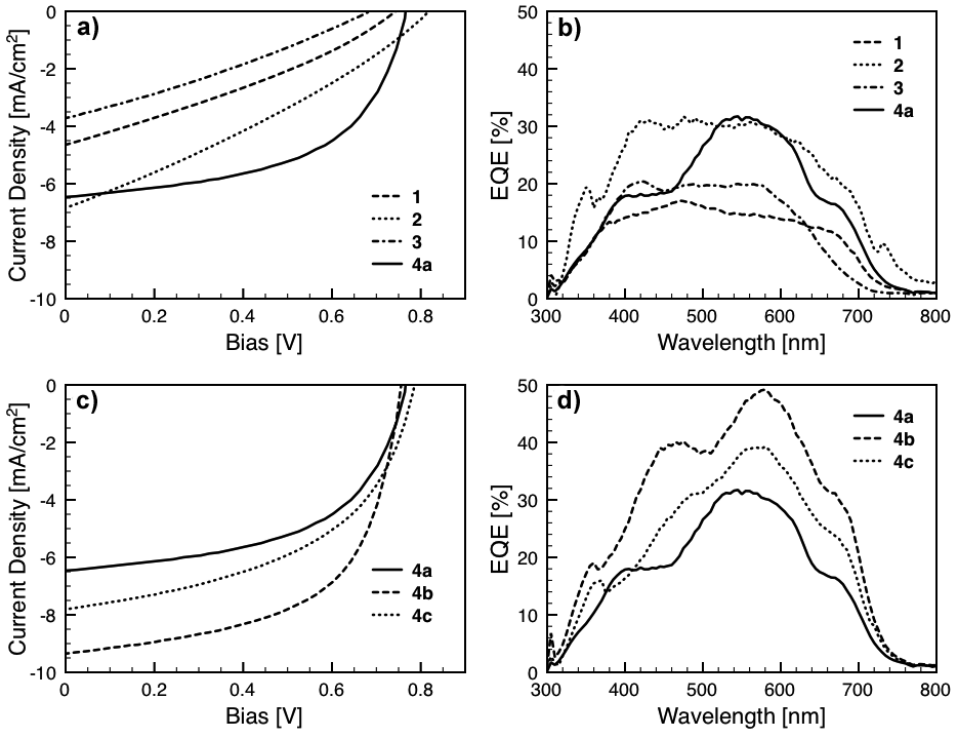

Figure 3-2. Characteristic *J-V* curves of solar cells fabricated from (a) **1-4a**, and (c) **4a-4c**, illuminated under AM 1.5G, 100 mW/cm^2. External quantum efficiency (EQE) spectra of devices based on (b) **1-4a** and (d) **4a-4c**.

Table 3-2. Average PV performance of 1-4 blended with $PC_{71}BM$.

	Blend Ratio[a]	J_{SC}[e] [mA cm^{-2}]	V_{OC}[f] [V]	FF[g]	PCE [%]	Max. PCE [%]
1	1:4[b]	-4.3	0.73	0.31	1.0	1.3
2	1:4[c]	-6.2	0.81	0.30	1.3	1.7
3	1:4[b]	-3.2	0.73	0.29	0.7	0.7
4a	2:1[b]	-5.7	0.77	0.55	2.4	2.7
4b	2:1[b]	-8.3	0.76	0.58	3.7	4.1
4c	2:1[d]	-6.6	0.78	0.48	2.4	3.0

[a]Mass ratio of small molecule donor to $PC_{71}BM$. [b]Devices prepared from solution in chloroform. [c,d]Devices prepared from solution in mixed solvent: chlorobenzene/1,2-dichlorobenzene ([c]66.7/33.3 v/v; [d]75/25 v/v). [e]J_{sc} = short-circuit current density. [f]V_{oc} = open-circuit voltage. [g]FF = fill factor.

Further structural optimization of the C2-pyrene-based molecules was achieved by varying the *N*-alkyl solubilizing side-chains on the core moiety. Previous studies[35,36] have shown that side-chains can affect crystallinity, intermolecular spacing, and OPV device performance. To determine whether shorter alkyl chains could tighten molecular packing and improve OPV

performance, the 2-octyldodecyl groups on **4a** were replaced with 2-hexyldecyl (**4b**), 2-butyloctyl (**4c**), and 2-ethylhexyl (**4d**) groups. Molecule **4b** exhibits the highest PCE (4.1% max.) in this series and has the one of the highest fill factors (0.58) for a solution-processed small molecule OPV system.[37–40] Further decreasing the size of the alkyl groups resulted in limited solubility and processing challenges, giving **4c** a lower device performance than **4b**. Molecule **4d** lacked sufficient solubility to be processed into a functional device.

As shown in Table 3-2 and Figure 3-2, the high device PCE of C2-pyrene-based molecules can be mainly attributed to their high fill factors (FFs). FF is known to depend mainly on carrier mobility, charge recombination, current leakage, and balanced transport of holes and electrons through the device active layer.[1,37,41–43] Molecules **4a** and **4b** exhibit device FFs of 0.55 and 0.58, whereas molecules **1**, **2** and **3** exhibit FFs of 0.29, 0.30 and 0.31, respectively. The high FFs are unique to **4a** – **4c**, even at different donor:$PC_{71}BM$ ratios (Figure 3-3b). Devices fabricated with **1**, **2** and **3** were optimized at a 1:4 donor:$PC_{71}BM$ ratio; further increasing the donor content reduced device FF and PCE even though the hole mobility of these devices increased (Figure 3-3). In contrast, for molecules containing C2-pyrene end-groups (**4a** – **4c**), increasing the donor content enhanced both FF and hole mobility, contributing to the high device efficiency at the optimized ratio of 2:1 donor:$PC_{71}BM$ ratio. These results suggest that, relative to the other end-groups studied, the C2-pyrene end-group affects intermolecular interactions which may promote molecular packing and active layer morphology favorable for high device PCE.

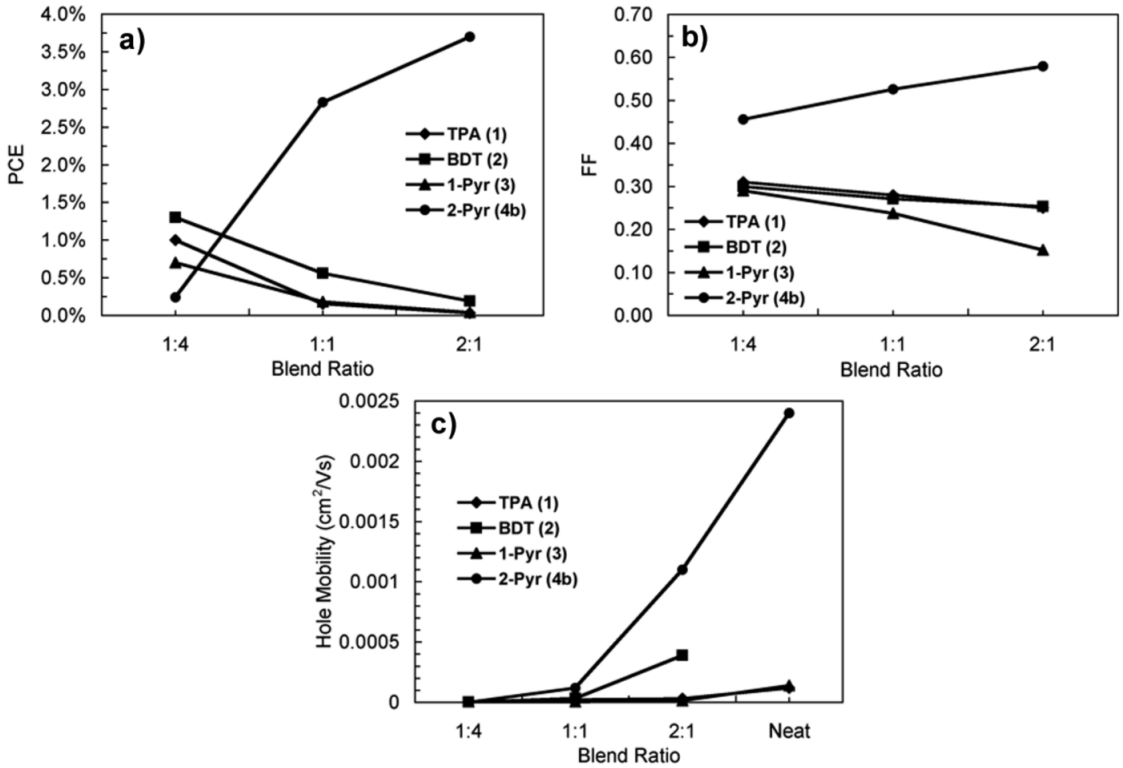

Figure 3-3. Effects of different blend ratios (small molecule:$PC_{71}BM$) on (a) PCE, (b) FF, and (c) space-charge-limited current (SCLC) hole mobility of the devices fabricated from molecules **1** , **2** , **3** and **4b**. As donor content increases, the FF and PCE are enhanced only in molecules with C2-pyreneend-groups.

3.3.3. Active Layer Morphology

To provide insight into how the C2-pyrene end-group can promote molecular assembly, the nanoscale film morphology and solid-state packing of DPP-C2-pyrene were investigated by atomic force microscopy (AFM) and X-ray diffraction. By AFM characterization, the active layers of the thin-film devices fabricated from **1** and **3** appear smooth and relatively amorphous, while the device active layer of **2** exhibits domains approaching the 1-μm length scale. In contrast, the device active layers of **4a** and **4b** display a network of highly crystalline features sized ~ 10–30 nm (Figures 3-4 and 3-5).

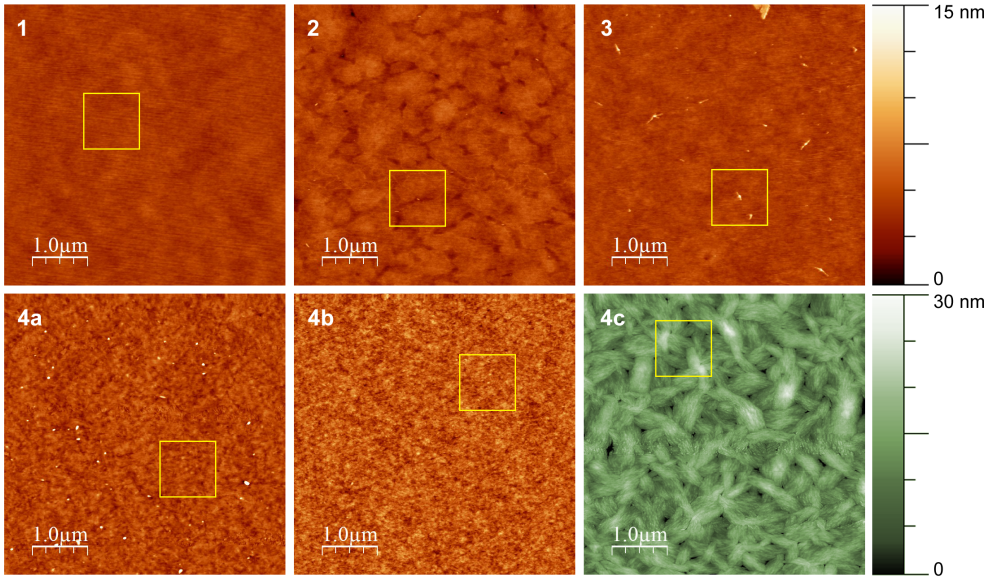

Figure 3-4. Tapping-mode AFM height images of the active layers of devices made using **1-4c**. Yellow boxes indicate the magnified portions shown in Figure 3-5. Note the unique height scale of **4c**.

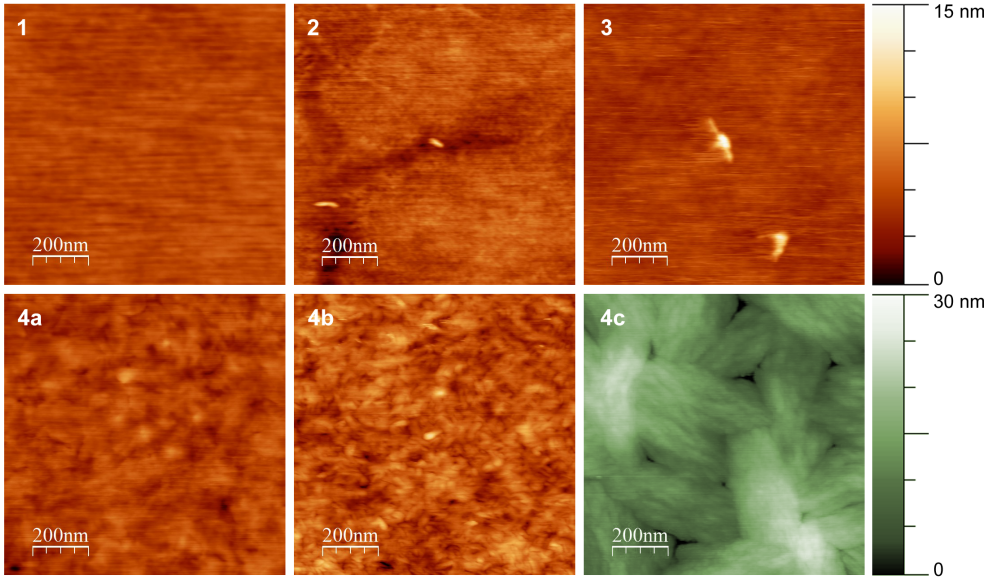

Figure 3-5. Magnified tapping-mode AFM height images, covering the corresponding regions outlined in yellow in Figure 3-4. Note the unique height scale of **4c**.

Grazing-incidence X-ray scattering (GIXS) pattern of a thin-film BHJ of **4b** and $PC_{71}BM$ shows sharply defined rings and peaks, suggesting that the packing of **4b** is both more crystalline and more aligned than that of **1**, **2** and **3**, whose scattering patterns indicate relatively amorphous films (Figure 3-6).

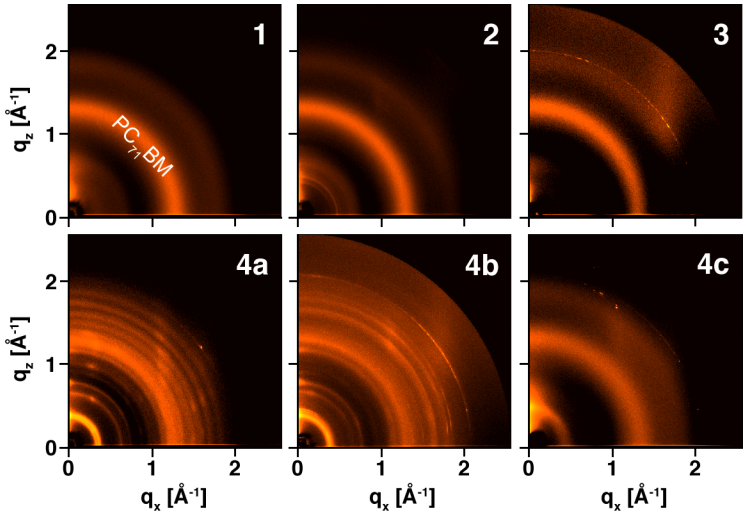

Figure 3-6. 2-D GIXS patterns of thin films of **1-4c** blended with $PC_{71}BM$, prepared under the same conditions as for optimized device fabrication.

3.3.4. Effect of Thermal Annealing on the Solar Cell Performance of DPP-C2-Pyrene

During the optimization of solar cell performance with the four small molecules, it was found that thermal annealing had a dramatic impact on devices fabricated with DPP-C2-pyrene molecules (**4a-c**). As shown in Figure 3-7, films cast from a blend of **4b** and $PC_{71}BM$ performs poorly at about 0.3 %; upon heating the devices at 130 °C for 35 min, the PCE improves due to increases in both current and FF. The significant improvements of current and FF suggest that thermal treatment of **4b** may enhance charge transport as a result of enhanced molecular ordering.

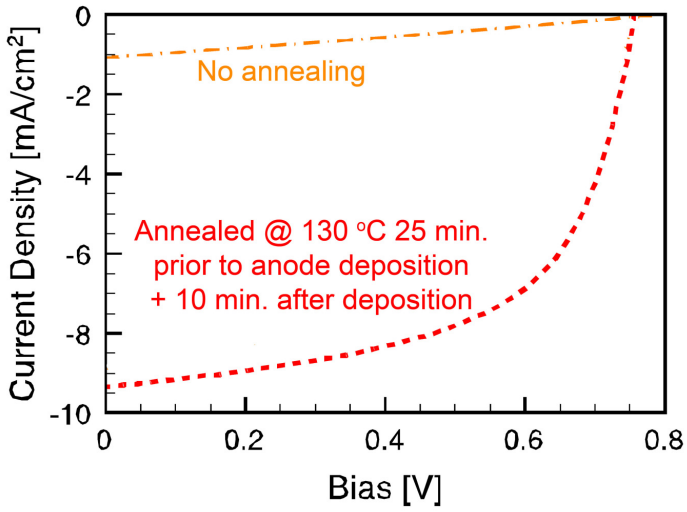

Figure 3-7. OPV devices fabricated with as cast blends of **4b** and $PC_{71}BM$ show very poor performance; however, upon annealing the devices at 130 °C, both the current and fill factor improve dramatically.

GIXS patterns were recorded for films **4b**:$PC_{71}BM$ blends determine the effect of various post-processing thermal treatments on molecular ordering (Figure 3-8). The as-cast film appears relatively amorphous, and the only visible ring belongs to the scattering of $PC_{71}BM$ domains (Figure 3-8(a)). The development of several peaks and rings in the film annealed at 130 °C for 15 min indicate that the molecules become more crystalline and aligned than the as-cast film. For the film annealed for 5 h, the scattering features do not change but appear to be more defined than in the pattern shown in Figure 3-8(b).

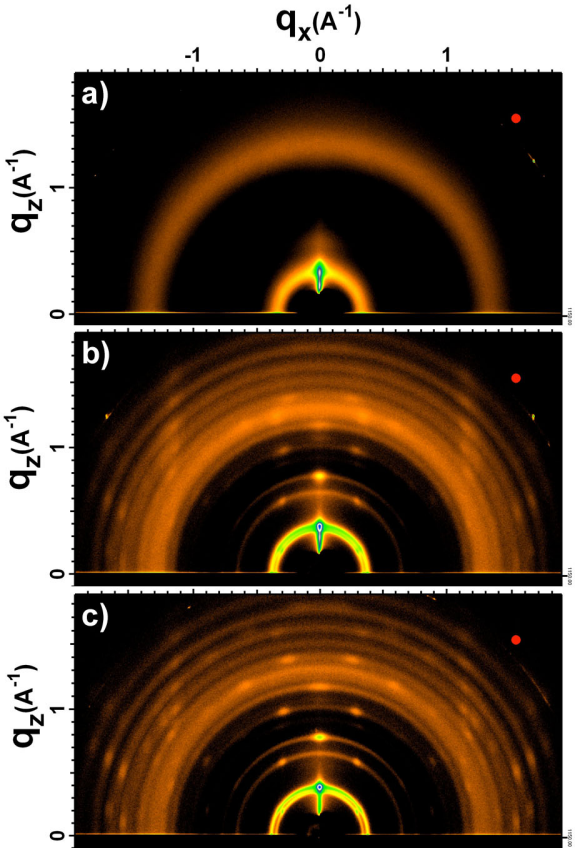

Figure 3-8. 2-D GIXS patterns of thin films of **4a** blended with $PC_{71}BM$. Films were prepared under the same conditions as for optimized device fabrication, with the exception of annealing: a) as-cast, b) annealed 15 minutes at 130 ^{o}C, and c) annealed 5 hours at 130 ^{o}C.

3.4. Determination of Small Molecule Packing by Single Crystal X-ray Diffraction

In order to elucidate how DPP-C2-pyrene molecules may pack in the solid-state, single crystals of **4a** were obtained by vapor diffusing isopropanol into a toluene solution of **4a**. Single crystal X-ray analysis of **4a** shows a closely-packed, interdigitated crystal structure with extensive overlap of C2-pyrene moieties (Figure 3-9). The interplanar distance between two pyrene units is 3.50 Å, confirming strong face-to-face π-π interaction between molecules. With this packing configuration, charges can move both parallel (*c* direction) and perpendicular (*b* direction) to the long-axis of the molecule, which accounts for the high hole mobilities measured for **4b**.

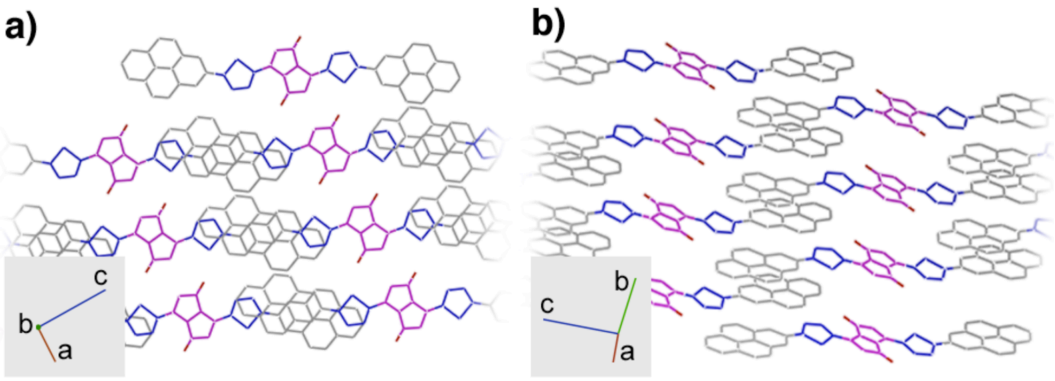

Figure 3-9. (a) View down the *b* -axis and (b) an angle view of the single crystal structure of **4a**, as determined by X-ray crystallography. Alkyl side chains are omitted for clarity. The pyrene-pyrene interplanar distance is ~ 3.50 Å, confirming close π – π stacking between pyrene moieties.

3.5. Conclusion

We demonstrate that efficient OPV materials can be constructed by the attachment of completely planar, symmetric end-groups to electroactive small molecules. Appending C2-pyrene as the small molecule end-group results in materials with tight, aligned crystal packing and favorable morphology dictated by π-π interactions. The intermolecular connectivity promoted by C2-pyrene allows devices containing blends of **4b** and $PC_{71}BM$ to reach a maximum PCE above 4% with a FF approaching 0.6. This device FF is one of the highest values reported to date in high-performing small molecule BHJ OPVs. The use of end-groups to direct molecular self-assembly represents an effective strategy for designing high-performance small molecule OPV devices.

3.6. Experimental

3.6.1. Synthetic Details

All commercially available reagents obtained from suppliers were used without further purification. Unless otherwise noted, all reactions were carried out under nitrogen with standard Schlenk techniques, and all glassware used in dry reactions were flame dried under high-vacuum prior to use. All organic extracts were dried over magnesium sulfate ($MgSO_4$) powder, and solvents were removed under reduced pressure with a rotary evaporator. Toluene, tetrahydrofuran (THF) and dimethylformamide (DMF) were purified and dried by passing through two columns of neutral alumina under nitrogen prior to use. All solvents used in Pd-catalyzed cross-coupling reactions were degassed by freeze-pump-thaw prior to use. Flash chromatography was performed using Silicycle SiliaFlash ® P60 (particle size 40-63 μm, 230-400 mesh) silica gel.

All ^{1}H and ^{13}C NMR spectra were obtained in chloroform-*d*, unless otherwise noted, with a Bruker AVQ-400, AVB-400, DRX-500, AV-500 or AV-600 instrument. ^{13}C spectra were measured with a proton-decoupling pulse program. All chemical shifts (ppm) were calibrated to the residual peak of the deuterated solvent. Matrix-assisted laser desorption/ionization-time of flight mass spectrometry (MALDI-TOF MS) was performed on a PerSeptive Biosystems Voyager-DE using 2,2':5',2"-terthiophene as the matrix. Samples were prepared by diluting the monomers in chloroform with the matrix. Data from high-resolution mass spectrometry

(HRMS) using electron impact (EI) were obtained by the UC Berkeley mass spectrometry facility. Elemental analysis (CHN) was performed by the UC Berkeley microanalysis laboratory. Melting points were measured on an Electrothermal Melt-Temp apparatus.

3,6-Di(thiophen-2-yl)pyrrolo[3,4-c]pyrrole-1,4(2H,5H)-dione (**5**).

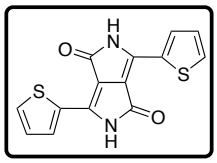

A 500 mL 3-neck flask connected to a condenser was charged with a stir bar and *tert*-amyl alcohol (250 mL). Sodium metal (2.56 g, 108 *m*mol) immersed in mineral oil was thoroughly washed with hexanes and cut into small pieces. Sodium metal pieces were slowly added to the reaction mixture over a 1.5 h period while the temperature was slowly increased to 120 °C over the same amount of time. Upon heating, the metal pieces began to bubble, and the reaction mixture turned light yellow. After all sodium metal pieces were dissolved, 2-thiophenecarbonitrile (11.9 g, 108 mmol) was added to the reaction. As dimethyl succinate (5.29 g, 36.2 *m*mol) was added dropwise to the reaction mixture over 1 h, the solution turned dark red. The reaction contents were stirred at 120 °C for 2 h, and then precipitated into acidic MeOH (400 mL MeOH and 20 mL conc. HCl). Filtration of the suspension through a Buchner funnel yielded a maroon solid (9.10 g), which was used in subsequent reactions without further purification.

2,5-Bis(2-octyldodecyl)-3,6-di(thiophen-2-yl)pyrrolo[3,4-c]pyrrole-1,4(2H,5H)-dione (**6a**).

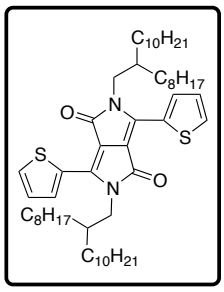

A 250 mL of round bottom flask was charged with **5** (3.50 g, 11.7 *m*mol), Cs_2CO_3 (11.4 g, 35.0 *m*mol) and dry DMF (120 mL). The reaction mixture was stirred at 120 °C for 3 h before 2-octyldodecyl iodide (11.9 g, 29.1 *m*mol) was added to the reaction. The reaction contents were heated at 140 °C for 16 h. The reaction contents were then cooled to 0 °C, filtered through a Büchner funnel and washed with chloroform. Excess DMF and chloroform were removed from the filtrate under reduced pressure with heating to 70 °C to yield a purple solid. The crude material was purified by flash chromatography (loaded crude materials with chloroform and eluted with 40 % hexanes in toluene) to yield 2.41 g of purple tacky solid (24 %).

Mp: 76.0 – 77.8 °C. ^{1}H NMR (600 MHz, $CDCl_3$, δ): 8.88 (d, *J* = 3.9 Hz, 2 H), 7.62 (d, *J* = 5.0 Hz, 2 H), 7.27 (dd, *J* = 3.9 Hz, 5.0 Hz, 2 H), 4.02 (d, *J* = 7.75 Hz, 4 H), 1.91 (m, 2 H), 1.25 (m, 64 H), 0.86 (adt, *J* = 7.1 Hz, 9.2 Hz, 12 H). ^{13}C (150 MHz, $CDCl_3$, δ): 161.9, 140.6, 135.3, 130.6, 130.0, 128.5, 108.1, 46.2, 37.7, 31.9, 31.8, 31.1, 30.0, 29.6, 29.54, 29.48, 29.34, 29.28, 26.2, 22.67, 22.65, 14.1. MALDI-TOF MS (*m/z*): $[M]^+$ calcd for $C_{54}H_{88}N_2O_2S_2$, 860.6; found, 861.1. Anal. calcd for $C_{54}H_{88}N_2O_2S_2$: C, 75.29; H, 10.30; N, 3.25; found: C, 75.41; H, 10.50; N, 3.17.

2,5-Bis(2-hexyldecyl)-3,6-di(thiophen-2-yl)pyrrolo[3,4-c]pyrrole-1,4(2H,5H)-dione (**6b**).

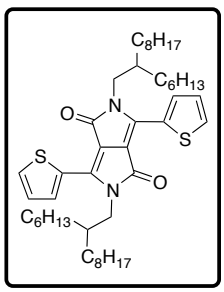

Reaction conditions were the same as for **6a**, except **5** (4.50 g, 15.0 *m*mol), Cs_2CO_3 (14.60 g, 45.0 *m*mol), 2-hexyldecyl iodide [1] (7.24 g, 37.5 *m*mol) were used. Purification of the crude material through flash chromatography (loaded crude materials with chloroform and eluted with 15 % hexanes in toluene) yielded 1.89 g of maroon tacky solid (17 %).

^{1}H NMR (400 MHz, $CDCl_3$, δ): 8.89 (d, *J* = 3.9 Hz, 2 H), 7.61 (d, *J* = 5.0 Hz, 2 H), 7.26 (dd, *J* = 4.0 Hz, 4.9 Hz, 1 H), 4.02 (m, 4 H), 1.91 (m, 2 H), 1.26

(m, 48 H), 0.85 (aq, J = 7.3 Hz, 8.8 Hz, 12 H). ^{13}C (100 MHz, $CDCl_3$, δ): 161.8, 140.5, 135.4, 130.6, 130.0, 129.1, 128.5, 128.3, 108.0, 46.3, 37.8, 32.0, 31.9, 31.3, 30.1, 29.8, 29.6, 29.4, 26.3, 22.80, 22.76, 14.3, 14.2. MALDI-TOF MS (*m/z*) $[M]^+$ calcd for $C_{46}H_{72}N_2O_2S_2$, 748.5; found: 748.7.

2,5-Bis(2-butyloctyl)-3,6-di(thiophen-2-yl)pyrrolo[3,4-c]pyrrole-1,4(2H,5H)-dione (**6c**).

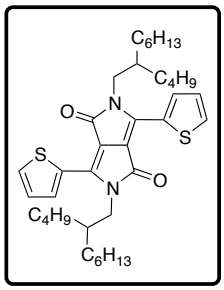

Reaction conditions were the same as for **6a**, except 2-butyloctyl iodide (8.63 g, 37.5 *m*mol) and dry DMF (120 mL) were used. Purification of the crude material through flash chromatography (loaded crude materials with chloroform and eluted with increasing gradient from 25 % to 0 % hexanes in toluene) yielded 1.87 g of purple tacky solid (25 %).

Mp: 108.8–110.7 °C. ^{1}H NMR (400 MHz, $CDCl_3$, δ): 8.86 (d, J = 3.9 Hz, 2 H), 7.62 (d, J = 5.0 Hz, 2 H), 7.25 (dd, J = 4.0 Hz, 4.5 Hz, 1 H), 4.02 (d, J = 7.7 Hz, 4 H), 1.90 (m, 2 H), 1.24 (m, 32 H), 0.84 (adt, J = 2.6 Hz, 6.7 Hz, 12 H). ^{13}C (150 MHz, $CDCl_3$, δ): = 161.7, 140.4, 135.1, 130.4, 129.8, 128.4, 108.0, 46.2, 37.7, 31.7, 31.2, 30.9, 29.7, 28.4, 26.2, 23.0, 22.6, 14.03, 13.97. MALDI-TOF MS (EI, *m/z*) $[M]^+$ calc'd for $C_{38}H_{56}N_2O_2S_2$, 636.4; found, 636.9. Anal. calcd for $C_{38}H_{56}N_2O_2S_2$: C, 71.65; H, 8.86; N, 4.40; found: C, 72.02; H, 8.92; N, 4.29.

2,5-Bis(2-ethylhexyl)-3,6-di(thiophen-2-yl)pyrrolo[3,4-c]pyrrole-1,4(2H,5H)-dione (**6d**).

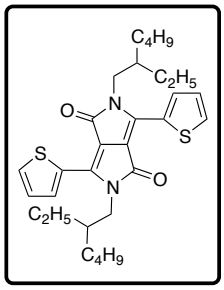

Reaction conditions were the same as for **6a**, except **5** (4.50 g, 15.0 *m*mol), Cs_2CO_3 (14.60 g, 45.0 *m*mol), 2-ethylhexyl bromide (7.24 g, 37.5 *m*mol) and dry DMF (120 mL) were used. Purification of the crude material through flash chromatography ($CHCl_3$) yielded 1.24 g of purple tacky solid (16 %).

^{1}H NMR (400 MHz, $CDCl_3$, δ): 8.89 (d, J = 3.9 Hz, 2 H), 7.61 (d, J = 5.0 Hz, 2 H), 7.25 (at, J = 4.5 Hz, 1 H), 4.01 (m, 4 H), 1.85 (m, 2 H), 1.29 (m, 16 H), 0.85 (adt, J = 7.3 Hz, 8.8 Hz, 12 H). ^{13}C (100 MHz, $CDCl_3$, δ): 161.8, 140.5, 135.4, 130.6, 130.0, 128.5, 108.0, 45.9, 39.2, 30.3, 28.4, 23.6, 23.2, 14.1, 10.6. HRMS (EI, *m/z*) $[M]^+$ calcd for $C_{30}H_{40}N_2O_2S_2$, 524.2531; found, 524.2535. Anal. calcd for $C_{30}H_{40}N_2O_2S_2$: C, 68.66; H, 7.68; N, 5.34; found: C, 68.73; H, 7.90; N, 5.34.

3,6-Bis(5-bromothiophen-2-yl)-2,5-bis(2-octyldodecyl)pyrrolo[3,4-c]pyrrole-1,4(2H,5H)-dione (**7a**).

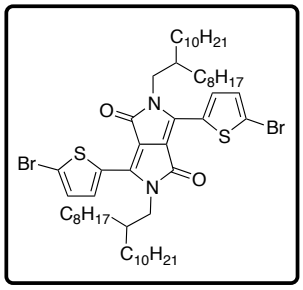

A 100 mL round bottom flask was charged with a stir bar, **6a** (1.20 g, 1.39 *m*mol) and chloroform (0.1 m, 14 mL) under ambient conditions. After the reaction mixture was stirred in an ice bath at 0 °C for 20 min, *N*-bromosuccinimide (NBS) (508 mg, 2.86 *m*mol) was added in small portions over 30 min. After stirring for another 20 min, the reaction was washed with distilled water (3×50 mL). The organic extract was dried over $MgSO_4$, and solvent was removed under reduced pressure. Purification by flash chromatography (40 % hexanes in toluene) yielded 929 mg of a purple solid (65 %).

Mp 95.0 – 96.9 °C. ^{1}H NMR (400 MHz, $CDCl_3$, δ): 8.63 (d, J = 4.2 Hz, 2 H), 7.21 (d, J = 4.2 Hz, 2 H), 3.91 (d, J = 7.7 Hz, 4 H), 1.87 (m, 2 H), 1.25 (m, 64 H), 0.86 (adt, J = 5.3 Hz, 6.9 Hz,

12 H). ^{13}C (125 MHz, $CDCl_3$, δ): 161.4, 139.4, 135.3, 131.4, 131.2, 118.9, 108.0, 46.3, 37.7, 31.91, 31.87, 31.20, 30.0, 29.63, 29.55, 29.5, 29.4, 29.3, 26.2, 22.68, 22.66, 14.11. MALDI-TOF MS (*m/z*) $[M]^+$ calcd for $C_{54}H_{86}Br_2N_2O_2S_2$, 1018.5; found, 1018.3. Anal. calcd for $C_{54}H_{86}Br_2N_2O_2S_2$: C, 63.64; H, 8.50; N, 2.75; found: C, 63.73; H, 8.71; N, 2.73.

3,6-Bis(5-bromothiophen-2-yl)-2,5-bis(2-hexyldecyl)pyrrolo[3,4-c]pyrrole-1,4(2H,5H)-dione (**7b**).

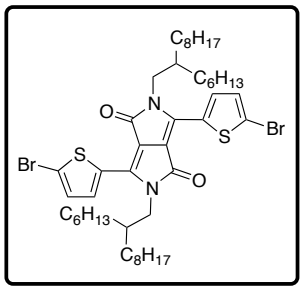

Reaction conditions and workup were the same as for **7a**, except **6b** (1.02 g, 1.36 *m*mol) and NBS (497 mg, 2.79 *m*mol) were used. Purification by flash chromatography (25 % hexanes in toluene) yielded 1.06 g of a purple solid (86 %).

Mp 114.5 – 116.0 °C. ^{1}H NMR (400 MHz, $CDCl_3$, δ): 8.62 (d, *J* = 4.2 Hz, 2 H), 7.21 (d, *J* = 4.2 Hz, 2 H), 3.92 (d, *J* = 7.8 Hz, 4 H), 1.88 (m, 2 H), 1.26 (m, 48 H), 0.85 (m, 12 H). ^{13}C (100 MHz, $CDCl_3$, δ): 161.1, 139.4, 135.3, 131.4, 131.2, 118.9, 108.1, 46.4, 37.8, 31.9, 31.7, 31.2, 30.0, 29.6, 29.5, 29.3, 26.2, 26.1, 22.7, 22.6, 14.09, 14.06. MALDI-TOF MS (*m/z*) $[M]^+$ calcd for $C_{46}H_{70}Br_2N_2O_2S_2$, 904.3; found, 904.2. Anal. calcd for $C_{46}H_{70}Br_2N_2O_2S_2$: C, 60.91; H, 7.78; N, 3.09; found: C, 60.99; H, 7.93; N, 3.10.

3,6-Bis(5-bromothiophen-2-yl)-2,5-bis(2-butyloctyl)pyrrolo[3,4-c]pyrrole-1,4(2H,5H)-dione (**7c**).

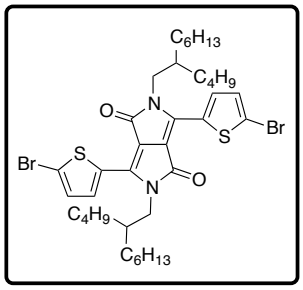

Reaction conditions and workup were the same as for **7a**, except **6c** (1.00 g, 1.57 *m*mol) and NBS (573 mg, 3.22 *m*mol) were used. Purification by flash chromatography (35 % hexanes in $CHCl_3$) yielded 1.07 g of a purple solid (85 %).

Mp 151.2 – 153.7 °C. ^{1}H NMR (400 MHz, $CDCl_3$, δ): 8.61 (d, *J* = 4.2 Hz, 2 H), 7.22 (d, *J* = 4.2 Hz, 2 H), 3.92 (m, 4 H), 1.87 (m, 2 H), 1.25 (m, 32 H), 0.85 (adt, *J* = 3.4 Hz, 6.7 Hz, 12 H). ^{13}C (100 MHz, $CDCl_3$, δ): 161.4, 139.4, 135.2, 131.4, 131.2, 118.9, 108.1, 46.3, 37.7, 31.7, 31.1, 30.9, 29.6, 28.4, 26.1, 23.0, 22.6, 14.1, 14.0. MALDI-TOF MS (*m/z*) $[M]^+$ calcd for $C_{38}H_{54}Br_2N_2O_2S_2$, 792.2; found, 792.2. Anal. calcd for $C_{38}H_{54}Br_2N_2O_2S_2$: C, 57.43; H, 6.85; N, 3.52; found: C, 57.63; H, 6.96; N, 3.48.

3,6-Bis(5-bromothiophen-2-yl)-2,5-bis(2-ethylhexyl)pyrrolo[3,4-c]pyrrole-1,4(2H,5H)-dione (**7d**).

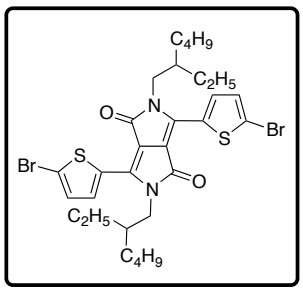

Reaction conditions and workup were the same as for **7a**, except **6d** (1.21 g, 2.31 *m*mol) and NBS (821 mg, 4.61 *m*mol) were used. Purification by flash chromatography (20 % hexanes in $CHCl_3$) yielded 1.30 g of a purple solid (83 %).

^{1}H NMR (400 MHz, $CDCl_3$, δ): 8.64 (d, *J* = 4.2 Hz, 2 H), 7.22 (d, *J* = 4.2 Hz, 2 H), 3.92 (m, 4 H), 1.82 (m, 2 H), 1.26 (m, 16 H), 0.87 (aq, *J* = 7.3 Hz, 12 H). ^{13}C (100 MHz, $CDCl_3$, δ): 161.5, 139.5, 135.5, 131.6, 131.3, 119.2, 108.1, 46.1, 39.2, 30.3, 28.4, 23.7, 23.2, 14.2, 10.6.

HRMS (EI, *m/z*) $[M]^+$ calcd for $C_{30}H_{38}Br_2N_2O_2S_2$, 682.0721; found, 682.0733. Anal. calcd for $C_{30}H_{38}Br_2N_2O_2S_2$: C, 52.79; H, 5.61; N, 4.10; found: C, 52.90; H, 5.52; N, 4.21.

N,N-Diphenyl-4-(4,4,5,5-tetramethyl-1,3,2-dioxaborolan-2-yl)aniline (**8**).

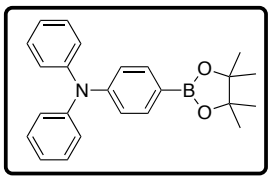

A 3-neck 250-mL round bottom flask was charged with a stir bar, 4-bromotriphenylamine (4.00 g, 12.4 *m*mol), *bis*(pinacolato)diboron (B_2pin_2) (3.29 g, 13.0 *m*mol), dichloro[1,1'-bis(diphenylphosphino)-ferrocene]palladium(II) dichloromethane adduct ($Pd(dppf)Cl_2 \cdot CH_2Cl_2$) (271 mg, 0.332 *m*mol), anhydrous potassium acetate (KOAc) (3.31 g, 33.6 *m*mol) and degassed dioxane (120 mL). After the reaction mixture was heated at 85 °C for 16 h, it was extracted with diethyl ether and washed with distilled water. The organic extract was dried over $MgSO_4$, and solvent was removal under reduced pressure yielded a brown viscous oil. Purification with flash chromatography (25 % hexanes in CH_2Cl_2) yielded 4.30 g of tacky off-white solid (95 %).

^{1}H NMR (600 MHz, $CDCl_3$, δ): 7.67 (d, *J* = 8.5 Hz, 2 H), 7.26 (t, *J* = 7.9 Hz, 4 H), 7.11 (d, *J* = 7.6 Hz, 4 H), 7.04 (m, 4 H), 1.34 (s, 12 H). ^{13}C (150 MHz, $CDCl_3$, δ): 150.7, 147.5, 136.0, 129.43, 125.1, 123.5, 121.9, 83.7, 25.0. HRMS (EI, *m/z*) $[M]^+$ calcd for $C_{24}H_{26}BNO_2$, 371.2057; found, 371.2068. Anal. calcd for $C_{24}H_{26}BNO_2$: C, 77.64; H, 7.06; N, 3.77; found: C, 77.61; H, 7.04; N, 3.93.

4,8-Dimethoxybenzo[1,2-b:4,5-b']dithiophene (**9**).

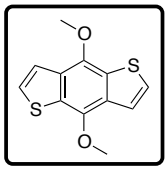

Benzo[1,2-*b*:4,5-*b'*]dithiophene-4,8-dione (2.00 g, 9.08 *m*mol), zinc powder (2.08 g, 31.8 *m*mol) and water (50 mL) were combined in a 100 mL flask, followed by sodium hydroxide (5.48 g, 137 *m*mol). The mixture was heated at reflux for 2 h, until the reaction contents turned bright yellow. The reaction mixture was then cooled to room temperature, methyl tosylate (6.76 g, 36.3 *m*mol) was added to the mixture, and the reaction contents were heated at 50 °C for 12 h. The reaction mixture was cooled to room temperature and quenched with water. The mixture was extracted with diethyl ether (3 x 50 mL), dried and volatile solvents were evaporated. The organic extract was purified by column chromatography on silica gel with a mixed mobile phase of chloroform and hexanes (90:10) to yield compound **3** as a colorless solid (1.65 g, 73 %).

^{1}H NMR (400 MHz, $CDCl_3$, δ): 7.51 (d, *J* = 5.54 Hz, 2H), 7.40 (d, *J* = 5.53 Hz, 2H), 4.14 (s, 6H). ^{13}C NMR (100 MHz, $CDCl_3$, δ): 145.47, 131.40, 129.92, 126.41, 120.22, 61.14. HRMS (EI, *m/z*) $[M]^+$ calcd for $C_{12}H_{10}O_2S_2$, 250.0122; found, 250.0128. Anal. calcd for $C_{12}H_{10}O_2S_2$: C, 57.57; H, 4.03; found: C, 57.31; H, 3.90.

2-Trimethyltin-4,8-dimethoxybenzo[1,2-b:4,5-b']dithiophene (**10**).

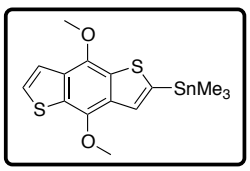

Compound **9** (2.02 g, 8.07 *m*mol), tetramethylethylenediamine (dried over CaH_2 and vacuum distilled, 1.80 mL, 12.2 *m*mol) and dry THF (50 mL) were combined in a dry 100 mL flask. The reaction contents were cooled to 0 °C and n-butyllithium (3.39 mL, 2.50 M, 8.48 *m*mol) was added to the flask via syringe. After stirring for 2 h at room temperature, the reaction mixture was cooled back to 0 °C and trimethyltin chloride (2.57 g, 12.9 *m*mol) was added. After stirring for 8 h at room temperature, the reaction contents were quenched with water. The mixture was extracted with diethyl ether (3 x 50 mL), dried and volatile solvents were

evaporated. To remove the distanylated byproduct, the organic extract was purified by column chromatography on silica gel with a mixed mobile phase of 75% chloroform in hexanes to yield the mixed mono- and non-stanylated products. The mixture of products was used in the subsequent reaction without further purification.

4,4,5,5-Tetramethyl-2-(pyren-2-yl)-1,3,2-dioxaborolane (**11**).

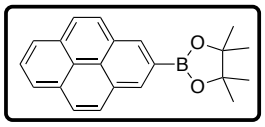

A 50 mL round bottom flask was charged with a stir bar, pyrene (809 mg, 4.00 *m*mol), bis(pinacolato)diboron (B_2pin_2) (1.12 g, 4.40 *m*mol), di-μ-methoxobis(1,5-cyclooctadiene)diiridium(I) ([Ir(OMe)COD]$_2$) (5 mol%, 132 mg, 0.200 *m*mol), 4,4'-di-*tert*-butyl-2,2'-bipyridine (dtbpy) (10 mol%, 107 mg, 0.400 *m*mol), and cyclohexane (15 mL). After the reaction mixture was heated at 80 °C for 20 h, solvent was removed with rotary evaporator to yield a brown solid. The crude product was purified by flash chromatography (50 % hexanes in CH_2Cl_2), and solvent removal from the combined fractions yielded an off-white solid (320 mg, 24 %).

^{1}H NMR (400 MHz, $CDCl_3$, δ): 8.64 (s, 2 H), 8.17 (d, J = 7.6 Hz, 2 H), 8.11 (d, J = 9.0 Hz, 2 H), 8.06 (d, J = 9.0 Hz, 2 H), 8.02 (t, J = 7.6 Hz, 1 H), 1.47 (s, 12 H). ^{13}C (100 MHz, $CDCl_3$, δ): 131.8, 131.5, 130.6, 127.9, 127.4, 126.5, 125.0, 84.3, 25.6. HRMS (EI, *m/z*) $[M]^+$ calcd for $C_{22}H_{21}BO_2$, 328.1635; found, 328.1647. Anal. calcd for $C_{22}H_{21}BO_2$: C, 80.51; H, 6.45; found: C, 80.63; H, 6.55.

3,6-Bis(5-(4-(diphenylamino)phenyl)thiophen-2-yl)-2,5-bis(2-ethylhexyl)pyrrolo[3,4-c]pyrrole-1,4(2H,5H)-dione (**1**).

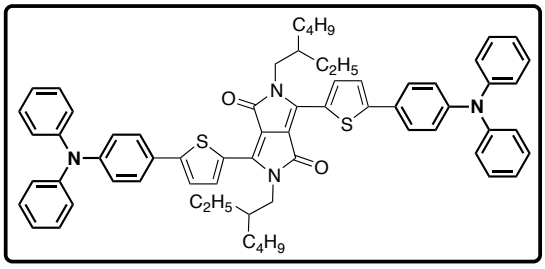

A 50 mL Schlenk tube was charged with the following materials: a stir bar, **6d** (841 mg, 1.23 *m*mol), **8** (1.01 g, 2.71 *m*mol), bis(dibenzylideneacetone)palladium (0) ($Pd_2(dba)_3$) (22.6 mg, 24.6 μmol), tri-*o*-tolylphosphine (P(*o*-tol)$_3$) (30.1 mg, 98.6 μmol), anhydrous K_2CO_3 (1.60 g, 11.6 mmol), 2 drops of aliquat 336, freeze-pump-thawed toluene (23.2 mL) and freeze-pump-thawed distilled water (5.8 mL). The reaction mixture was heated at 90 °C for 16 h before being precipitated into 250 mL of MeOH. The precipitates were filtered through a 20 μm nylon membrane. Purification by flash chromatography (10 % hexanes in chloroform) yielded 703 mg of the desired product as a metallic purple solid (56 %).

^{1}H NMR (500 MHz, $CDCl_3$, δ): 8.53-9.75 (s, 1 H), 7.5-7.8 (s, 2 H), 7.41 (s, 1H), 7.35 (t, J = 7.8 Hz, 4 H), 7.19 (d, J = 7.7 Hz, 4 H), 7.13 (d, J = 8.6 Hz, 4 H), 4.12 (s, 2 H), 2.01 (m, 1 H), 1.43 (m, 5 H), 1.32 (m, 3 H), 0.96 (t, J = 7.4 Hz, 3H), 0.91 (t, J = 7.0 Hz, 3 H). HRMS (FAB, *m/z*) $[M]^+$ calcd for $C_{66}H_{66}N_4O_2S_2$, 1010.4627; found, 1010.4653. Anal. calcd for $C_{66}H_{66}N_4O_2S_2$: C, 78.38; H, 6.58; N, 5.54; found: C, 78.12; H, 6.20; N, 5.62.

3,6-Bis(5-(4,8-dimethoxybenzo[1,2-b:4,5-b']dithiophen-2-yl)thiophen-2-yl)-2,5-bis(2-ethylhexyl)pyrrolo[3,4-c]pyrrole-1,4(2H,5H)-dione (**2**).

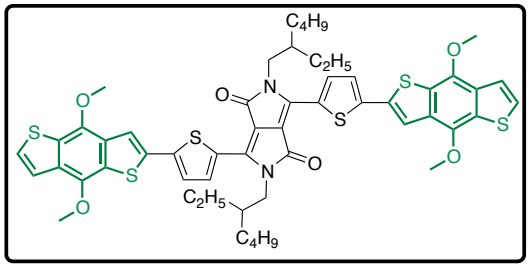

A 50 mL Schlenk tube was charged with **7d** (401 mg, 0.586 *m*mol), **10** (731 mg, 1.77 *m*mol), $Pd(PPh_3)_2Cl_2$ (20.6 mg, 29.3 μmol) and freeze-pump-thawed THF (24 mL). As mentioned previously, **S9** contained a mixture of non- and mono-stannylated compounds; the calculation was done assuming that the materials contained only the mono-stannylated product, and an excess of **S9** (3 equiv.) was used in this reaction. The reaction mixture was stirred at 55 °C for 3 h and then at 60 °C for 16 h. After cooling the reaction contents to room temperature, the crude mixture was precipitated into 200 mL of MeOH and filtered through a 20 µm nylon membrane. Purification by flash chromatography ($CHCl_3$) yielded 264 mg of a metallic purple solid (44 %).

^{1}H NMR (500 MHz, $CDCl_3$, δ): 8.97 (d, *J* = 3.10 Hz, 2 H), 7.68 (s, 2 H), 7.48 (d, *J* = 5.48 Hz, 2 H), 7.44 (d, *J* = 4.07 Hz, 2 H), 7.41 (d, *J* = 5.38 Hz, 2 H), 4.18 (s, 6 H), 4.14 (s, 6 H), 4.08 (m, 4 H), 1.96 (m, 2 H), 1.39 (m, 16 H), 0.93 (m, 12 H). HRMS (FAB, *m/z*) $[M]^+$ calcd for $C_{54}H_{56}N_2O_6S_6$, 1020.2463; found, 1020.2477. Anal. calcd for $C_{54}H_{56}N_2O_6S_6$: C, 63.50; H, 5.53; N, 2.74; found: C, 63.38; H, 5.26; N, 2.88.

2,5-Bis(2-octyldodecyl)-3,6-bis(5-(pyren-1-yl)thiophen-2-yl)pyrrolo[3,4-c]pyrrole-1,4(2H,5H)-dione (**3**).

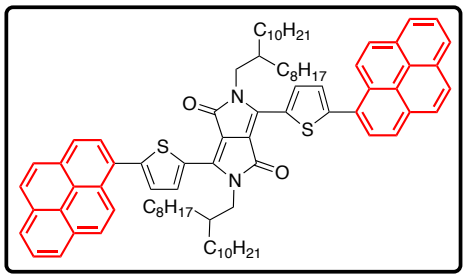

A 50 mL Schlenk tube was charged with the following materials: a stir bar, **7a** (292 mg, 0.286 *m*mol), pyrene-1-boronic acid (256 mg, 0.630 *m*mol), $Pd_2(dba)_3$ (5.24 mg, 5.73 μmol), P(*o*-tol)$_3$ (6.97 mg, 22.9 μmol), anhydrous K_2CO_3 (316 mg, 2.29 *m*mol), 1 drop of aliquat 336, freeze-pump-thawed toluene (5.7 mL) and freeze-pump-thawed distilled water (1.1 mL). The reaction mixture was heated at 90 °C for 16 h before being precipitated into 200 mL of MeOH. The precipitates were filtered through a 20.0 µm nylon membrane. Purification by flash chromatography twice (40 % hexanes in chloroform, and then 100 % chloroform) yielded 353 mg of the desired product as a tacky metallic purple solid (98 %).

Mp 127.1 – 129.2 °C. ^{1}H NMR (500 MHz, $CDCl_3$, δ): 9.17 (s, 2 H), 8.57 (d, *J* = 9.3, 2H), 8.24 (m, 6H), 8.15 (m, 6 H), 8.11 (d, *J* = 8.9 Hz, 2 H), 8.06 (t, *J* = 7.6 Hz, 2 H), 7.6 (d, *J* = 3.9 Hz, 2 H), 4.16 (d, *J* = 7.7 Hz, 4H), 2.11 (m, 2 H), 1.45 – 1.10 (m, 64 H), 0.81 (aq, *J* = 7.0 Hz, 12 H). MALDI-TOF MS (*m/z*) $[M]^+$ calcd for $C_{86}H_{104}N_2O_2S_2$, 1260.8; found, 1260.9. Anal. calcd for $C_{86}H_{104}N_2O_2S_2$: C, 81.86; H, 8.31; N, 2.22; found: C, 81.47; H, 8.50; N, 2.14.

2,5-Bis(2-octyldodecyl)-3,6-bis(5-(pyren-2-yl)thiophen-2-yl)pyrrolo[3,4-c]pyrrole-1,4(2H,5H)-dione (**4a**).

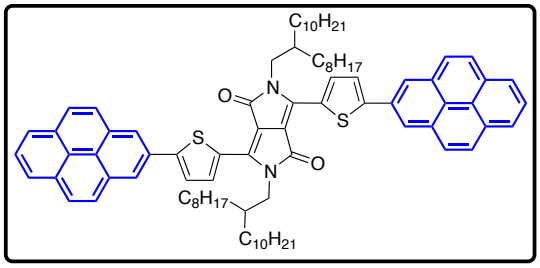

A 50 mL Schlenk tube was charged with the following materials: a stir bar, **7a** (278 mg, 0.272 *m*mol), **11** (197 mg, 0.598 *m*mol), $Pd_2(dba)_3$ (4.99 mg, 5.45 μmol), P(*o*-tol)$_3$ (6.63 mg, 21.8 *μ*mol), anhydrous K_2CO_3 (354 mg, 2.0 *m*mol/mL H_2O), 1 drop of aliquat 336, freeze-pump-thawed toluene (5.1 mL) and freeze-pump-thawed distilled water (1.3 mL). The reaction mixture was heated at 90 °C for 16 h before being precipitated into 200 mL of MeOH. The precipitates were filtered through a 20.0 μm nylon membrane. Purification by flash chromatography twice (40 % hexanes in chloroform, and then 100 % chloroform) yielded 228 mg of the desired product as a metallic, dark purple solid (66 %).

^{1}H NMR (500 MHz, $CDCl_3$, δ): 9.06 (d, *J* = 4.1 Hz, 2 H), 8.43 (s, 4H), 8.19 (d, *J* = 7.6 Hz, 4H), 8.10 (m, 8 H), 8.01 (at, *J* = 7.6 Hz, 2 H), 7.77 (d, *J* = 4.1 Hz, 2 H), 4.18 (d, *J* = 7.7 Hz, 4 H), 2.08 (m, 2 H), 1.27 (m, 64 H), 0.79 (add, *J* = 6.4 Hz, 7.5 Hz, 12 H). HRMS (FAB, *m/z*) $[M]^+$ calcd for $C_{86}H_{104}N_2O_2S_2$, 1260.7539; found, 1260.7560. Anal. calcd for $C_{86}H_{104}N_2O_2S_2$: C, 81.86; H, 8.31; N, 2.22; found: C, 81.56, H, 8.48; N, 2.46.

2,5-Bis(2-hexyldecyl)-3,6-bis(5-(pyren-2-yl)thiophen-2-yl)pyrrolo[3,4-c]pyrrole-1,4(2H,5H)-dione (**4b**).

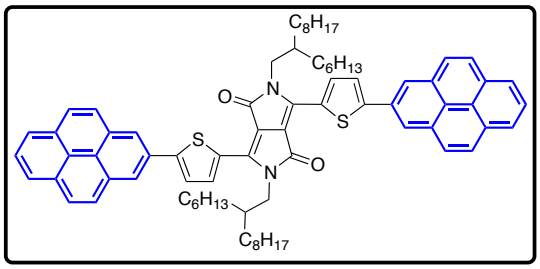

Reaction conditions and workup were the same as for **4a**, except **7b** (300 mg, 0.331 *m*mol), **11** (179 mg, 0.728 *m*mol), $Pd_2(dba)_3$ (6.01 mg, 6.62 *μ*mol), P(*o*-tol)$_3$ (8.05 mg, 26.4 *μ*mol), anhydrous K_2CO_3 (366 mg, 2.0 *m*mol/mL H_2O), 1 drop of aliquat 336, freeze-pump-thawed toluene (6.6 mL) and freeze-pump-thawed distilled water (1.3 mL) were used. Purification by flash chromatography (loaded crude materials in $CHCl_3$, and eluted with increasing gradient from 50 % to 80 % $CHCl_3$ in hexanes) yielded 182 mg of a metallic, dark purple solid (48 %).

Mp 261.2 – 262.4 °C. ^{1}H NMR (500 MHz, $CDCl_3$, δ): 9.04 (d, *J* = 4.0 Hz, 2 H), 8.30 (s, 4H), 8.10 (d, *J* = 7.6 Hz, 4H), 8.00 (q, *J* = 8.9 Hz, 8 H), 7.92 (t, *J* = 7.6 Hz, 2 H), 7.68 (d, *J* = 4.1 Hz, 2 H), 4.13 (d, *J* = 7.7 Hz, 4 H), 2.05 (m, 2 H), 1.45 – 1.18 (m, 48 H), 0.84 (t, *J* = 6.8 Hz, 6 H), 0.80 (t, *J* = 6.7 Hz, 6 H). MALDI-TOF MS (*m/z*) $[M]^+$ calcd for $C_{78}H_{88}N_2O_2S_2$, 1148.6; found, 1146.2. Anal. calcd for $C_{78}H_{88}N_2O_2S_2$: C, 81.49; H, 7.72; N, 2.44; found: C, 81.19, H, 7.70; N, 2.41.

2,5-Bis(2-butyloctyl)-3,6-bis(5-(pyren-2-yl)thiophen-2-yl)pyrrolo[3,4-c]pyrrole-1,4(2H,5H)-dione (**4c**).

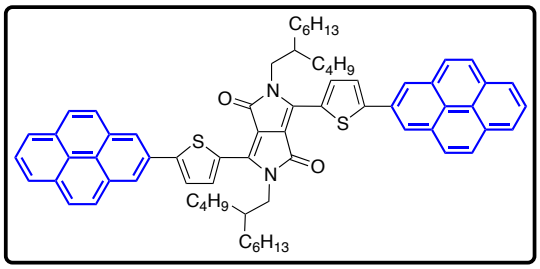

Reaction conditions and workup were the same as for **4a**, except **7c** (300 mg, 0.338 *m*mol), **11** (204 mg, 0.624 *m*mol), $Pd_2(dba)_3$ (6.91 mg, 7.55 μmol), P(*o*-tol)$_3$ (9.19 mg, 30.2 *μ*mol), anhydrous K_2CO_3 (417 mg, 2.0 *m*mol/mL H_2O), 1 drop of aliquat 336, freeze-pump-thawed toluene (7.5 mL) and freeze-pump-thawed distilled water (1.5 mL) were used. Purification by flash chromatography (loaded crude materials in $CHCl_3$, and eluted with increasing gradient from 40 % to 85 % $CHCl_3$ in hexanes) yielded 185 mg of a metallic, dark purple solid (47 %).

Mp 268.1 – 271.3 °C. ^{1}H NMR (500 MHz, $CDCl_3$, δ): 9.06 (d, *J* = 4.1 Hz, 2 H), 8.46 (s, 4H), 8.20 (d, *J* = 7.6 Hz, 4H), 8.12 (m, 8 H), 8.01 (at, *J* = 7.6 Hz, 2 H), 7.79 (d, *J* = 4.1 Hz, 2 H), 4.19 (d, *J* = 7.8 Hz, 4 H), 2.07 (m, 2 H), 1.50 – 1.25 (m, 32 H), 0.91 (t, *J* = 7.1 Hz, 6 H), 0.83 (t, *J* = 6.9 Hz, 6 H). MALDI-TOF MS (*m/z*) $[M]^+$ calcd for $C_{70}H_{72}N_2O_2S_2$, 1036.5; found, 1036.9. Anal. calcd for $C_{70}H_{72}N_2O_2S_2$: C, 81.04; H, 7.00; N, 2.70; found: C, 80.67, H, 6.95; N, 2.65.

2,5-Bis(2-ethylhexyl)-3,6-bis(5-(pyren-2-yl)thiophen-2-yl)pyrrolo[3,4-c]pyrrole-1,4(2H,5H)-dione (**4d**).

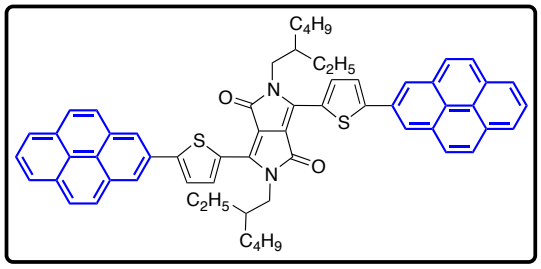

Reaction conditions and workup were the same as for **4a**, except **7d** (290 mg, 0.425 *m*mol), **11** (307 mg, 0.935 *m*mol), $Pd_2(dba)_3$ (8.52 mg, 9.3 *μ*mol), P(*o*-tol)$_3$ (11.4 mg, 37.4 *μ*mol), anhydrous K_2CO_3 (553 mg, 2.0 *m*mol/mL H_2O), 1 drop of aliquat 336, freeze-pump-thawed toluene (8.0 mL) and freeze-pump-thawed distilled water (2.0 mL) were used. Purification by flash chromatography with $CHCl_3$ yielded 95 mg of a metallic, dark purple solid (24 %).

^{1}H NMR (400 MHz, $CDCl_3$): due to the low solubility of **4d**, the sample concentration was below the NMR detection limit. MALDI-TOF MS (*m/z*) $[M]^+$ calcd for $C_{62}H_{56}N_2O_2S_2$, 924.4; found, 924.6.

3.6.2. UV-visible Absorption and Cyclic Voltammetry

UV-vis spectral data were measured with Varian Cary 50 spectrophotometer. Thin film measurements were collected by spin-casting thin-films onto untreated quartz slides. For extinction coefficient measurements, films of varying thicknesses were obtained by spin-casting from a series of increasingly dilute solutions, starting with the same solutions used for SCLC device preparation (see above for details).

Cyclic voltammograms were collected using a Solartron 1285 potentiostat under the control of CorrWare II software. A standard three electrode cell based on a Pt wire working electrode, a silver wire pseudo reference electrode (calibrated vs. Fc/Fc^+, which is assumed to have an absolute energy level of -5.13 eV to vacuum),[44] and a Pt wire counter electrode was purged with nitrogen and maintained under a nitrogen atmosphere during all measurements. Acetonitrile was purchased anhydrous from Aldrich and tetrabutylammonium hexafluorophosphate (0.1 M) was

used as the supporting electrolyte. Small molecule films were drop cast onto a Pt wire working electrode from a 1% (w/w) chloroform solution and dried under nitrogen prior to measurement.

3.6.3. Organic Solar Cell Fabrication, Performance Testing and Mobility Measurements

All devices were fabricated on ITO-coated glass substrates (pre-patterned, R = 20 Ω^{-1}, Thin Film Devices, Inc.). The substrates were sonicated for 20 minutes in 2% Helmanex soap water and rinsed extensively with deionized (DI) water. They were then sonicated for 20 minutes in DI water, 20 minutes in acetone, and 20 minutes in isopropyl alcohol, followed by drying under a stream of air. The substrates were then UV-ozone cleaned for 5 minutes. A thin layer (30-40 nm) of PEDOT:PSS (Clevios PH) was spin-coated onto each substrate at 4000 RPM for 40 s, followed by 10 minutes of drying at 140 ^{o}C in air. The samples were then transferred to a glovebox under N_2, where the active layers were spin-coated at 2000 RPM for 40 s. The cathode was thermally evaporated under vacuum (~10^{-7} torr) through a shadow mask that defines an active area of ~0.03 cm^2. Some of the samples were then thermally annealed by placing them substrate-side down (active layer facing up) on a hot plate. Details of the solution concentrations, cathode deposition, and annealing steps for each molecule are shown in **Table 3-3**. Current-voltage (*J-V*) curves were measured using a Keithley 2400 source-measure unit under AM 1.5 G solar illumination at 100 mW cm^{-2} (1 sun) using a Thermal-Oriel 150 W solar simulator.

Table 3-3. Optimized spin-coating, solution, cathode, and annealing parameters for device fabrication from each of the small molecules.

	Solution Concentration [mg/mL]		Solvent	Cathode	Annealing
	Donor	$PC_{71}BM$			
1	5	20	$CHCl_3$	Al (100 nm)	110 ^{o}C, 10 min
2	5	20	2:1 CB:DCB	Al (100 nm)	110 ^{o}C, 10 min
3	4	16	CB	Al (100 nm)	100 ^{o}C, 10 min
4a	15	7.5	$CHCl_3$	Al (100 nm)	130 ^{o}C, 25 min† 130 ^{o}C, 10 min
4b	15	7.5	$CHCl_3$	Al (100 nm)	130 ^{o}C, 25 min † 130 ^{o}C, 10 min
4c	15	7.5	CB	Al (100 nm)	130 ^{o}C, 1 min † 130 ^{o}C, 1 min

† = annealed prior to cathode deposition
CB = chlorobenzene
DCB = 1,2-dichlorobenzene

SCLC devices for **1**, **2**, **3**, and **4b** were fabricated following the same substrate preparation, spin-coating parameters, and annealing conditions as for the respective solar cell devices. Neat donor small molecule films were spin-cast from solutions of: 15 mg/mL in $CHCl_3$ for **1**, 15 mg/mL in CB for **2**, 20 mg/mL in CB for **3**, and 20 mg/mL in $CHCl_3$ for **4b**. Blend films were spin-cast from these same solutions mixed with solutions of $PC_{71}BM$: 30 mg/mL in $CHCl_3$ for **1**, 30 mg/mL in CB and DCB (mixed to obtain 2:1 overall CB:DCB) for **2**, 20 mg/mL in CB for **3**, and 30 mg/mL in $CHCl_3$ for **4b**. For each molecule and blend ratio, two different film thicknesses were prepared to provide a more accurate measurement. Gold was used as the cathode material rather than Al in order to promote hole-only transport. Dark current *J-V*

characteristics were measured using the same setup used for testing solar cell devices. Voltage was corrected for the built-in voltage and the voltage drop from series resistance. Hole mobility was obtained by fitting *J-V* data to the Mott-Gurney Law.

3.6.4. Morphology and Crystal Packing by AFM, GIXS and Single-Crystal X-Ray Diffraction

Height profiles of the active layers of devices made using **1-4c** were imaged using a Veeco Multimode V Atomic Force Microscope (AFM) operated in tapping mode.

X-ray crystal packing structure of **4a** was determined by Dr. Antonio DiPasquale at the UC Berkeley College of Chemistry X-Ray Crystallography Facility. Molecule **4a** was recrystallized from toluene (solvent) and isopropanol (precipitant) by vapor diffusion over a two-week period to yield red rods. A red rod 0.10 x 0.10 x 0.04 mm in size was mounted on a Cryoloop with Paratone oil. Data were collected in a nitrogen gas stream at 100(2) K using phi and omega scans. Crystal-to-detector distance was 60 mm and exposure time was 10 seconds per frame using a scan width of 1.0°. Data collection was 96.0% complete to 50.00° in q. A total of 8622 reflections were collected covering the indices, -6<=*h*<=7, -15<=*k*<=15, -16<=*l*<=16. 3547 reflections were found to be symmetry independent, with an R_{int} of 0.0411. Indexing and unit cell refinement indicated a primitive, triclinic lattice. The space group was found to be P-1 (No. 2). The data were integrated using the Bruker SAINT software program and scaled using the SADABS software program. Solution by direct methods (SIR-2008) produced a complete heavy-atom phasing model consistent with the proposed structure. All non-hydrogen atoms were refined anisotropically by full-matrix least-squares (SHELXL-97). All hydrogen atoms were placed using a riding model. Their positions were constrained relative to their parent atom using the appropriate HFIX command in SHELXL-97. CCDC 831594 contains the crystallographic data which can be obtained free of charge from The Cambridge Crystallographic Data Centre via www.ccdc.cam.ac.uk/data_request/cif.

Grazing-incidence X-ray scattering (GIXS) experiments were conducted at the Stanford Synchotron Radiation Laboratory on beamline 11-3. Samples were irradiated at a fixed incident angle on the order of 0.1° and their GIXS patterns were recorded with a 2-D image detector (MAR345 image plate detector). GIXS patterns were recorded with an X-ray energy of 12.71 keV (λ = 0.975 Å). To maximize the intensity from the sample, the incident angle (~0.1°– 0.12°) was carefully chosen such that the X-ray beam penetrated the sample completely but did not interact with the silicon substrate. Typical exposure times were 30-600 s. To ensure that surface conditions matched those used for device fabrication, a thin layer (~40 nm) of PEDOT:PSS was spin-coated onto silicon substrates that were pretreated with UV-ozone for 5 min. Then the GIXS samples were prepared by spin-coating the same solutions used for device fabrication at 2000 rpm for 40 s.

3.7. References

(1) Hains, A. W.;Liang, Z.; Woodhouse, M. A.; Gregg, B. A. *Chem. Rev.* **2010**, *110*, 6689.
(2) Arias, A. C.; MacKenzie, J. D.; McCulloch, I; Rivnay, J.; Salleo, A. *Chem. Rev.* **2010**, *110*, 3.
(3) Thompson, B.C.; Fréchet, J. M. J. *Angew. Chem. Int. Ed.* **2008**, *47*, 58.
(4) Roncali, J. *Acc. Chem. Res.* **2009**, *42*, 1719.
(5) Walker, B.; Tamayo, A. B.; Dang, X.-D.; Zalar, P.; Seo, J. H.; Garcia, A.; Tantiwiwat, M.; Nguyen, T.-Q. *Adv. Funct. Mater.* **2009**, *19*, 3063.

(6) Bürckstümmer, H.; Kronenberg, N. M.; Gsänger, M.; Stolte, M.; Meerholz, K. *J. Mater. Chem.* **2010**, *20*, 240.
(7) Walker, B.; Kim, C.; Nguyen, T.-Q.; *Chem. Mater.* **2011**, *23*, 470.
(8) Shin, R. Y. C.; Sonar, P.; Siew, P. S.; Chen, Z.-K.; Sellinger, A. *J. Org. Chem.* **2009**, *74*, 3293.
(9) Palilis, L. C.; Lane, P. A.; Kushto, G. P.; Purushothaman, B.; Anthony, J. E.; Kafafi, Z. H. *Org. Electron.* **2008**, *9*, 747 .
(10) Liang, Y.; Yu, L. *Acc. Chem. Res.* **2010**, *43*, 1227.
(11) Liang, Y.; Xu, Z.; Xia, J.; Tsai, S.; Wu, Y.; Li, G.; Ray, C.; Yu, L. *Adv. Mater.* **2010**, *22*, E135.
(12) Kline, R. J.; McGehee, M. D.; Kadnikova, E. N.; Liu, J.; Fréchet, J. M. J.; Toney, M. F. *Macromolecules* **2005**, *38*, 3312.
(13) Zen, A.; Pfl aum, J.; Hirschmann, S.; Zhuang, W.; Jaiser, F.; Asawapirom, U.; Rabe, J. P.; Scherf, U.; Neher, D. *Adv. Funct. Mater.* **2004**, *14*, 757.
(14) Tong, A. M.; Cho, S.; Rogers, J. T.; Schmidt, K.; Hsu, B. B. Y.; Moses, D.; Coffin, R. C.; Kramer, E. J.; Bazan, G. C.; Heeger, A. J. *Adv. Funct. Mater.* **2010**, *20*, 3959.
(15) Müller, C.; Wang, E.; Andersson, L. M.; Tvingstedt, K.; Zhou, Y.; Andersson, M. R.; Inganäs, O. *Adv. Funct. Mater.* **2010**, *20*, 2124.
(16) Tang, W.; Hai, J.; Dai, Y.; Huang, Z.; Lu, B.; Yuan, F.; Tang, J.; Zhang, R. *Sol. Energ. Mat. Sol. C* **2010**, *94*, 1963.
(17) Tamayo, A. B.; Tantiwiwat, M.; Walker, B.; Nguyen, T.-Q. *J . Phys. Chem. C* **2008**, *112*, 15543.
(18) Loser, S.; Bruns, C. J.; Miyauchi, H.; Ortiz, R. P.; Facchetti, A.; Stupp, S. I.; Marks, T. J. *J. Am. Chem. Soc.* **2011**, *133*, 8142.
(19) Bijleveld, J. C.; Gevaerts, V. X.; Nuzzo, D. D.; Turbiez, M.; Mathijssen, S. G. J.; de Leeuw, D. M.; Wienk, M. M.; Janssen, R. A. J. *Adv. Mater.* **2010**, *22*, E242.
(20) Zhou, E.; Yamakawa, S.; Tajima, K.; Yang, C.; Hashimoto, K. *Chem. Mater.* **2009**, *21*, 4055.
(21) Tamayo, A. B.; Dang, X.-D.; Walker, B.; Seo, J.; Kent, T.; Nguyen, T.-Q. *Appl. Phys. Lett.* **2009**, *94*, 103301.
(22) Bijleveld, J. C.; Zoombelt, A. P.; Mathijssen, S. G. J.; Wienk, M. M.; Turbiez, M.; de Leeuw, D. M.; Janssen, R. A. J. *J. Am. Chem. Soc.* **2009**, *131*, 16616.
(23) Wink, M. M.; Turbiez, M.; Gilot, J.; Janssen, R. A. J. *Adv. Mater.* **2008**, *20*, 2556.
(24) Bronstein, H.; Chen, Z.; Ashraf, R. S.; Zhang, W.; Du, J.; Durrant, J. R.; Tuladhar, P. S.; Song, K.; Watkins, S. E.; Geerts, Y.; Wienk, M. M.; Janssen, R. A. J.; Anthopoulos, T.; Sirringhaus, H.; Heeney, M.; McCulloch, I. *J. Am. Chem. Soc.* **2011**, *133*, 3272.
(25) Li, Y.; Sonar, P.; Singh, S. P.; Soh, M. S.; van Meurs, M.; Tan, J. *J. Am. Chem. Soc.* **2011**, *133*, 2198.
(26) Sonar, P.; Singh, S.; Li, Y.; Soh, M.; Dodabalapur, A. *Adv. Mater.* **2010**, *22*, 5409.
(27) Nelson, T. L.; Young, T. M.; Liu, J.; Mishra, S. P.; Belot, J. A.; Balliet, C. L.; Javier, A. E.; Kowalewski, T.; McCullough, R. D. *Adv. Mater.* **2010**, *22*, 4617.
(28) Bürgi, L.; Turbiez, M.; Pfeiffer, R.; Bienewald, F.; Kirner, H. J.; Winnewisser, C. *Adv. Mater.* **2008**, *20*, 2217.
(29) Tantiwiwat, M.; Tamayo, A. B.; Luu, N.; Dung, X.-D.; Nguyen, T.-Q. *J. Phys. Chem. C* **2008**, *112*, 17402.

(30) Morton, C. J. H.; Riggs, R. L.; Smith, D. M.; Westwood, N. J.; Lightfoot, P.; Slawin, A. M. E. *Tetrahedron* **2005**, *61*, 727.
(31) Letizia, J. A.; Salata, M. R.; Tribout, C. M.; Facchetti, A.; Ratner, M. A.; Marks, T. J. *J. Am. Chem. Soc.* **2008**, *130*, 9679.
(32) Hou, J.; Park, M.-H.; Zhang, S.; Yao, Y.; Chen, L.-M.; Li, J.-H.; Yang, Y. *Macromolecules* **2008**, *41*, 6012.
(33) Mkhalid, I.; Barnard, J.; Marder, T.; Murphy, J.; Hartwig, J. *Chem. Rev.* **2009**, *110*, 890.
(34) Coventry, D. N.; Batsanov, A. S.; Goeta, A. E.; Howard, J. A. K.; Marder, T. B.; Perutz, R. N. *Chem. Commun.* **2005**, 2172.
(35) Piliego, C.; Holcombe, T. W.; Douglas, J. D.; Woo, C. H.; Beaujuge, P. M.; Fréchet, J. M. J. *J. Am. Chem. Soc.* **2010**, *132*, 7595.
(36) Szarko, J. M.; Guo, J.; Liang, Y.; Lee, B.; Rolczynski, B. S.; Strzalka, J.; Xu, T.; Loser, S.; Marks, T. J.; Yu, L.; Chen, L. X. *Adv. Mater.* **2010**, *22*, 5468.
(37) Wong, W. W. H.; Singh, T. B.; Vak, D.; Pisula, W.; Yan, C.; Feng, X.; Williams, E. L.; Chan, K. L.; Mao, Q.; Jones, D. J.; Ma, C.; Müllen, K. ; Bäuerle, P.; Holmes, A. B. *Adv. Funct. Mater.* **2010**, *20*, 927.
(38) Shang, H.; Fan, H.; Liu, Y.; Hu, W.; Li, Y.; Zhan, X. *Adv. Mater.* **2011**, *23*, 1554.
(39) Mei, J.; Graham, K. R.; Stalder, R.; Tiwari, S. P.; Cheun, H.; Shim, J.; Yoshio, M.; Nuckolls, C.; Kippelen, B.; Castellano, R. K.; Reynolds, J. R. *Chem. Mater.* **2011**, *23*, 2285.
(40) Schubert, M.; Yin, C.; Castellani, M.; Bange, S.; Tam, T. L.; Sellinger, A.; Hörhold, H.-H.; Kietzke, T.; Neher, D. *J. Chem. Phys.* **2009**, *130*, 094703.
(41) Kim, M.; Kim, B.; Kim, J. *ACS Appl. Mater. Interfaces* **2009**, *1*, 1264.
(42) Kagayama, H.; Ohishi, H.; Tanaka, M.; Ohmori, Y.; Shirota, Y. *Adv. Funct. Mater.* **2009**, *19*, 3948.
(43) Wagner, J.; Gruber, M.; Hinderhofer, A.; Wilke, A.; Bröker, B.; Frisch, J.; Amsalem, P.; Vollmer, A.; Opitz, A.; Koch, N.; Schreiber, F.; Brütting, W. *Adv. Funct. Mater.* **2010**, *20*, 4295.
(44) Cardona, C. M.; Li, W.; Kaifer, A. E.; Stockdale, D.; Bazan, G. C. *Adv. Mater.* **2011**, *23*, 2367.

Chapter IV

Antiaromatic Pentalenes in Conjugated Small Molecules

4.1. Introduction: Tuning Band Gaps of Conjugate Materials via Antiaromaticity

Conjugated materials have raised significant attention due to their potential applications in organic electronic devices, such as solar cells,[1–3] field-effect transistors,[4–7] sensors,[8] and artificial photosynthetic systems.[9,10] In many of these applications, the material of interest often requires a small energy gap between its highest-occupied molecular orbital (HOMO) and lowest-unoccupied molecular orbital (LUMO) levels.[11,12] This narrow band gap can be achieved with materials that exhibit significant quinoidal character, which manifests in decreased bond-length alternation and substantial electron delocalization through the conjugated system.[13–16]

To increase the contribution of the quinoidal resonance form, two major strategies include the donor-acceptor (D-A) approach and the competing aromaticity approach.[16–31] In the D-A approach, an electron-rich (donor) moiety is covalently linked to an electron-deficient (acceptor) moiety, resulting in the "push-pull" effect and the delocalization of the rehybridized orbitals (Figure 4-1a). In order to tune the energy levels of these coupling partners, the acceptors are typically functionalized with electron-withdrawing groups (EWGs) while the donors tend to bear electron-donating groups (EDGs). The effect of competing aromaticity on energy levels can be exemplified by comparing the band gaps of polythiophene (2.0 eV) and poly(isothianaphthene) (1.0 eV).[15,19] The repeat unit of poly(isothianaphthene) consists of a thiophene ring with benzene fused to its C_3-C_4 bond, and because benzene has a greater aromatic stabilization energy than thiophene, the quinoidal form of the polymer is favored (Figure 4-1b). As a consequence, polyisothianaphthene exhibits reduced bond-length alternation and a narrow band gap.

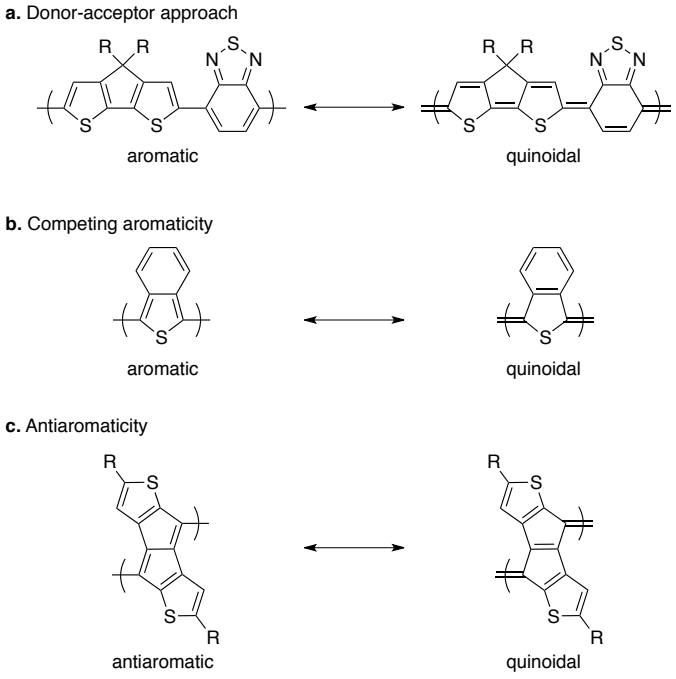

Figure 4-1. Synthetic strategies for increased quinoidal character (decreasing bond-length alternation) and narrow band gaps. (a) Covalent linkages between electron-rich and electron-poor units enhance electron delocalization via push-pull effect. (b) Polyisothianapthenes exhibit smaller band gaps than do polythiophenes due to the competing aromaticity between the benzene and thiophene of the fused system. (c) This work proposes the use of antiaromatic unit to favor the quinoidal resonance form, thereby increasing electron-delocalization.

Inspired by the competing aromaticity strategy, we hypothesized that a moiety with a formally antiaromatic core should favor the quinoidal resonance form, subsequently reducing band gaps of conjugated materials (Figure 4-1c). To test our hypothesis, we chose to incorporate pentalenes into donor-acceptor small molecules because pentalenes are formally antiaromatic by containing 4*n*π-electrons. Furthermore, their derivatives,[20–31] such as pentalenodithiophenes and dibenzopentalenes, offer improved thermal stability and synthetically accessibility due to the electronic stabilization provide by the fused aromatic systems. While dinaphthopentalene molecules have been investigated as acene analogues for applications in both organic photovoltaics and organic field effect transistors,[31] diarylpentalenes have not yet been incorporated into solution-processable, low band gap materials. In this report, we describe the syntheses of three low-band-gap, conjugated molecules that each contains a pentaleno[2,1-*b*:5,4-*b*′]dithiophene (PDT) core, which is accessed via modified Pd-catalyzed annulation based on the procedures reported by Levi and Tilley.[20,21] We also investigate the effect of two different end-groups—benzothiophehe and carbazole—on their optical and electronic properties by UV-vis spectroscopy and cyclic voltammetry. While the small molecules bear no electron-withdrawing functionalities, the resulting material still show optical band gaps of ~1.8 eV.

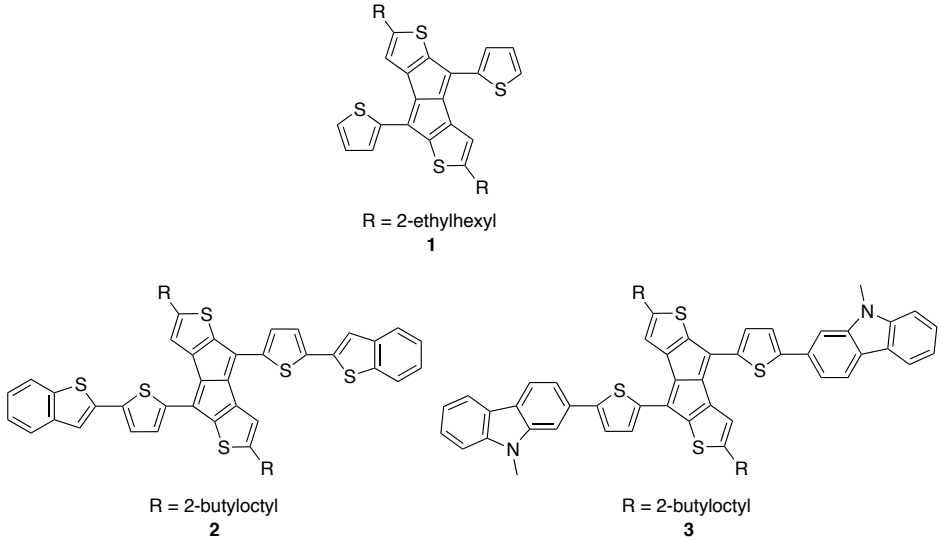

Figure 4-2. Structures of pentalenodithiophene and pentalene-based target small molecules.

4.2. Synthesis and Characterization of Pentalenodithiophene

4.2.1. Design and Theoretical Calculations of Pentalenodithiophene Small Molecules

Based on literature reports, the absorption onsets of diarylpentalene molecules ranges from 550-600 nm.[22,27] To further redshift the absorption of these materials, we extended conjugation of the small molecules by appending a thiophene π-bridge followed by an electron-rich moiety at each end of the pentalene core (Figure 4-2). Compared to previously reported dibenzopentalenes or pentalenodithiophenes functionalized with benzene rings, the thiophene bridge should minimize the torsional strain between the pentalene core and the end-groups as planarity is one of the important criteria in designing functional conjugated materials. To evaluate the planarity of the proposed small molecules, we performed density functional theory (DFT) calculations using the B3LYP functionals and 6-31G(d,p) basis set.[32] We determined that there is only a small twist between the pentalene core and the thiophene π-bridge. Visualization of the frontier

molecular orbitals shows that the HOMOs localize on the pentalene cores while the LUMOs delocalize through the π-bridge into the end-groups (Figures 4-3, 4-4, and 4-5).

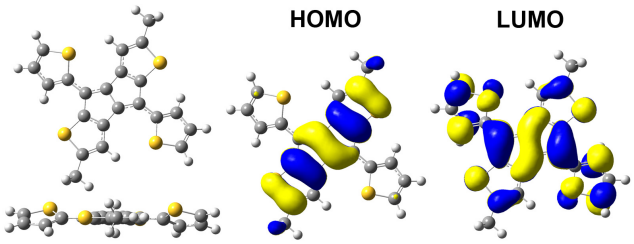

Figure 4-3. Top and side views of the optimized geometries of **1** and visualization of its HOMO and LUMO based on DFT calculations using B3LYP functional and 6-31G(d,p) basis set.

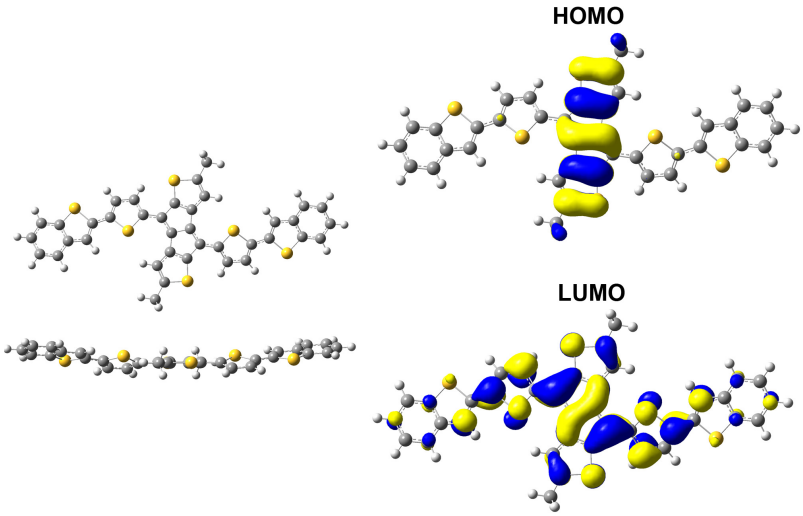

Figure 4-4. Top and side views of the optimized geometries of **2** and visualization of its HOMO and LUMO based on DFT calculations using B3LYP functional and 6-31G(d,p) basis set.

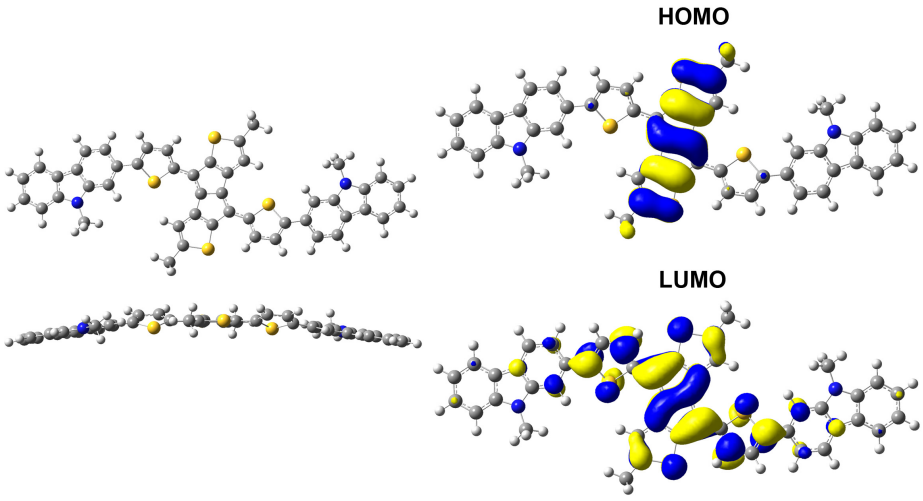

Figure 4-5. Top and side views of the optimized geometries of **3** and visualization of its HOMO and LUMO based on DFT calculations using B3LYP functional and 6-31G(d,p) basis set.

4.2.2. Synthesis of Pentalenodithiophene Small Molecules

To investigate the feasibility of synthesizing the target molecules, we first set out to synthesize the dialkyl-di(thiophen-2-yl)pentalenodithiophene (PDT) **1**. As shown in Scheme 4-1, lithiation of thiophene followed by alkylation yielded **4a**, which was then brominated at the C5-position with *N*-bromosuccinimide (NBS). Lithium diisopropylamide (LDA)-promoted "halogen dance"[33,34] rearrangement allowed **5a** to isomerize and form the 2,4-disubstituted thiophene **6a**. The alkyne linker was installed via Sonogashira corss-coupling between trimethylsilylacetylene to yield **7a**. Subsequent cleavage of the TMS group followed by monobromination with NBS yielded substrate **10** for the screening of Pd-catalyzed annulation. A more convergent synthetic approach was not taken because 2-bromo-5-ethynylthiophene was expected to be volatile and difficult to work with.

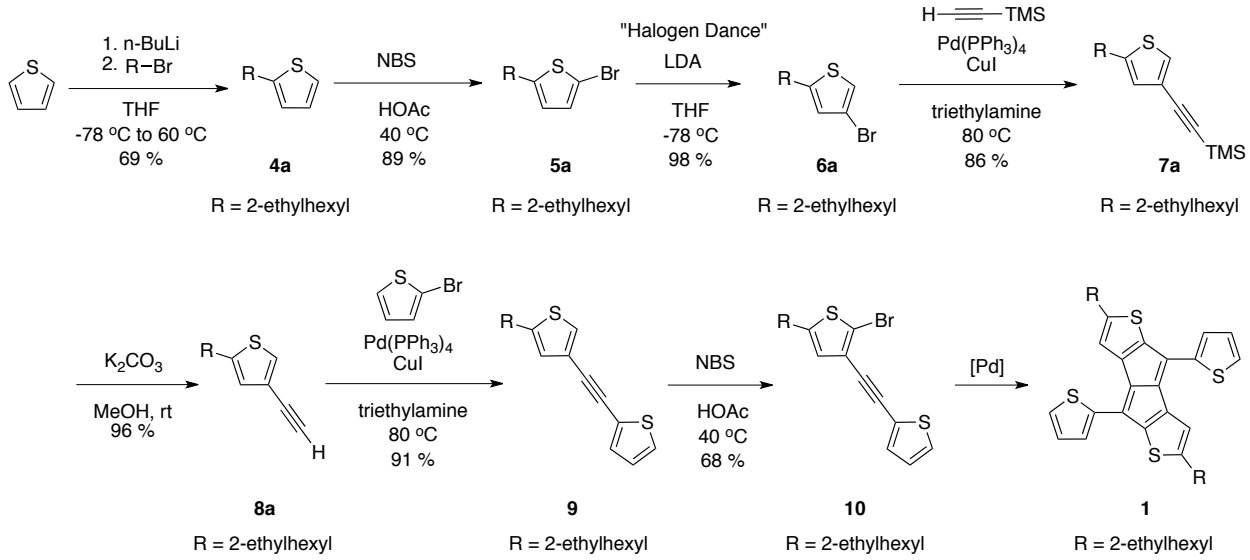

Scheme 4-1. Synthesis of the pentalenodithiophene core.

The Pd-catalyzed cyclization of **10** only led to 5.6% of PDT **1** using the reported catalytic system with $Pd_2(dba)_3/P^tBu_3$ and synthetic procedures. This yield is very poor compared to the reported 55% for the benzene-substituted analogue. Optimization of this reaction with **10** was carried out by screening of several ligands, bases and solvent compositions. Electron-rich aryl phosphine ligands led to a decrease in yields, and the starting material was completely recovered with electron-rich biaryl phosphine ligands. However, the yield more than doubled when P(2-furyl)$_3$ was used. Upon optimization, it was found that including a source of fluoride in the reaction mixture suppressed product formation while using K_3PO_4 as the base, sodium ascorbate as the reductant and a mixture of dioxane and water as the solvent improved the yield of the annulation to 25 % (Table 4-1). While we were able to arrive at the pentalene core, subsequent bromination or borylation of the core did not yield the desired coupling partners for subsequent cross coupling with the end-groups for the small molecule synthesis.

The pentalene molecule **1** synthesized under the optimized condition was fully characterized by NMR spectroscopy, elemental analysis and mass spectrometry; however, these characterization methods could not distinguish between isomers that show similar NMR shifts and splitting patterns. Thus, to confirm the absolute configuration of the synthesized PDT,

single crystals were obtained for **1** by vapor diffusion (isopropanol into a toluene solution), and the ORTEP view of **1** is displayed in Figure 4-6.

Table 4-1. Optimization of the palladium catalyzed cyclization.

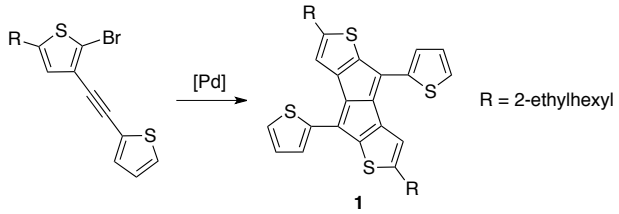

Entry	Pd	Ligand	Base	F^-	Reductant	Solvent	Yield (%)
Equiv.	3.0 mol%[a]	6 mol%	2.0	2.2	2.0	0.15 M	-
1	$Pd_2(dba)_3$	P^tBu_3	Cs_2CO_3	CsF	hydroquinone	dioxane	5.6
2	$Pd_2(dba)_3$	P(*o*-tolyl)$_3$	Cs_2CO_3	CsF	hydroquinone	dioxane	2.0
3	$Pd_2(dba)_3$	X-Phos	Cs_2CO_3	CsF	hydroquinone	dioxane	0
4	$Pd_2(dba)_3$	S-Phos	Cs_2CO_3	CsF	hydroquinone	dioxane	0
5	$Pd_2(dba)_3$	P(2-furyl)$_3$	Cs_2CO_3	CsF	hydroquinone	dioxane	12.9
6	$Pd_2(dba)_3$	P(2-furyl)$_3$	Cs_2CO_3	CsF	hydroquinone	dioxane:H_2O (5:1)	9.2
7	$Pd_2(dba)_3$	P(2-furyl)$_3$	Cs_2CO_3	--	hydroquinone	dioxane:H_2O (5:1)	17.5
8	$Pd_2(dba)_3$	P(2-furyl)$_3$	K_3PO_4	--	hydroquinone	dioxane	5.7
9	$Pd_2(dba)_3$	P(2-furyl)$_3$	K_3PO_4	--	hydroquinone	dioxane:H_2O (5:1)	18.5
10	$Pd_2(dba)_3$	P(2-furyl)$_3$	K_3PO_4	--	hydroquinone	toluene:H_2O (5:1)	16.1
11	$Pd_2(dba)_3$	P(2-furyl)$_3$	K_2CO_3	--	hydroquinone	toluene:H_2O (5:1)	5.3
12	$Pd_2(dba)_3$	P(2-furyl)$_3$	KOAc	--	hydroquinone	toluene:H_2O (5:1)	7.8
13	$Pd_2(dba)_3$	P(2-furyl)$_3$	Et_3N	--	hydroquinone	toluene:H_2O (5:1)	9.8
14	$Pd_2(dba)_3$	P(2-furyl)$_3$	K_3PO_4	--	Na-ascorbate	toluene:H_2O (5:1)	18.2
15	$Pd_2(dba)_3$	P(2-furyl)$_3$	K_3PO_4	--	Na-ascorbate	dioxane:H_2O (5:1)	25.7

[a]Used 1.5 mol% of $Pd_2(dba)_3$, which is 3 mol% loading of Pd(0).

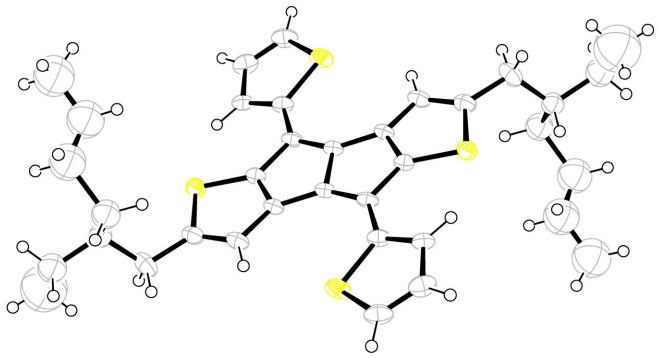

Figure 4-6. ORTEP diagram of **1** with thermal ellipsoids at 50% probability.

In addition, attempts have been made to synthesize the analogous pentaleno[1,2-*b*:4,5-*b'*]dithiophene with a different route as outlined in Scheme 4-2. 2-Thiopheneacetic acid was first esterified under acidic condition in methanol to yield **11**. The methyl ester **11** was then acylated via Friedel-Crafts aceylation with Sn(IV)Cl_4 to afford ketone **12**,[35] whose side chain was reduced to the alkane with triethylsilane in trifluoroacetic acid to complete the side-chain functionalization (**13**). However, subsequent oxidative dimerization of the methyl ester or the corresponding acid yielded no desired product. While the thiophene-substituted

dibenzopentalene can be synthesized through this route,[36] the analogous pentalenodithiophene core can only be accessed through the Pd- and Ni-catalyzed cyclizations reported here and previously published results.[20–22,27]

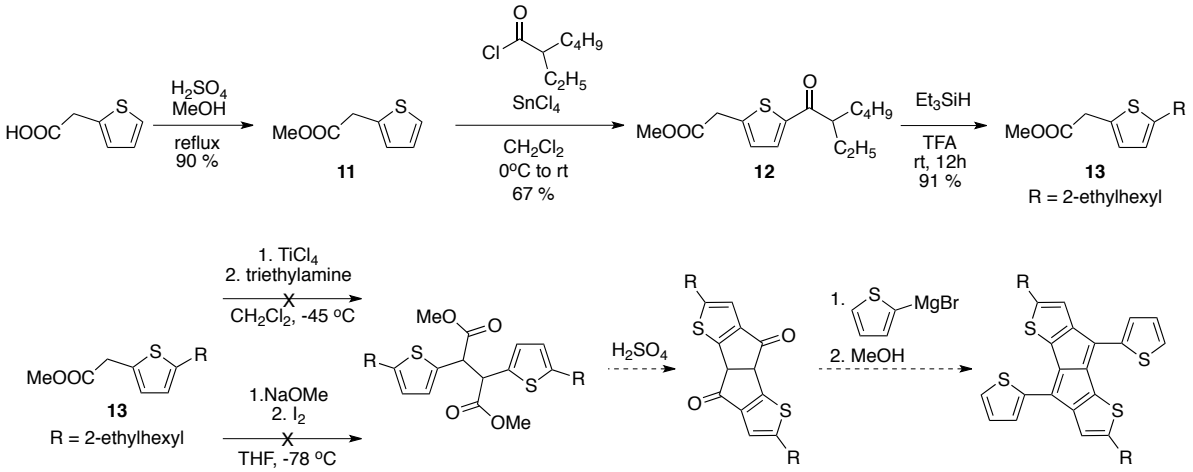

Scheme 4-2. Attempted synthesis of pentaleno[1,2-*b*:4,5-*b′*]dithiophene via oxidative coupling and cyclization.

For synthesizing the end groups of molecules **2** and **3** (Scheme 4-3), benzothiophene boronic acid was commercially available while carbazole borylate **15** was achieved by alkylation of 9H-carbazol-2-yl trifluoromethanesulfonate followed by Pd-catalyzed Miyaura borylation. Since the two target molecules are more extensively conjugated than **1**, they are expected to be less soluble, requiring the use of a bulkier side chain than the 2-ethylhexyl group. Thus, molecule **8b** bearing a 2-butyloctyl solubilizing group was be synthesized following a similar synthetic route to Scheme 4-1. The end-groups were coupled to molecule **8b** via Suzuki cross-coupling reactions. Subsequent bromination of **18** and **19** was achieved with lithiation followed by CBr_4 addition at –78 °C to install the bromide at the desired position (**20** and **21**). Note that the **18** and **19** both degraded when NBS was used as the brominating reagent, and no products were observed. Finally, Pd-catalyzed annulation of **20** and **21** under the optimized conditions afforded pentalenodithiophene small molecules **2** and **3**, respectively, with yields ranging from 28-29 %. While attempts had been made to grow single crystals of **2** and **3**, both molecules formed very thin, small needles was not suitable for X-ray characterization.

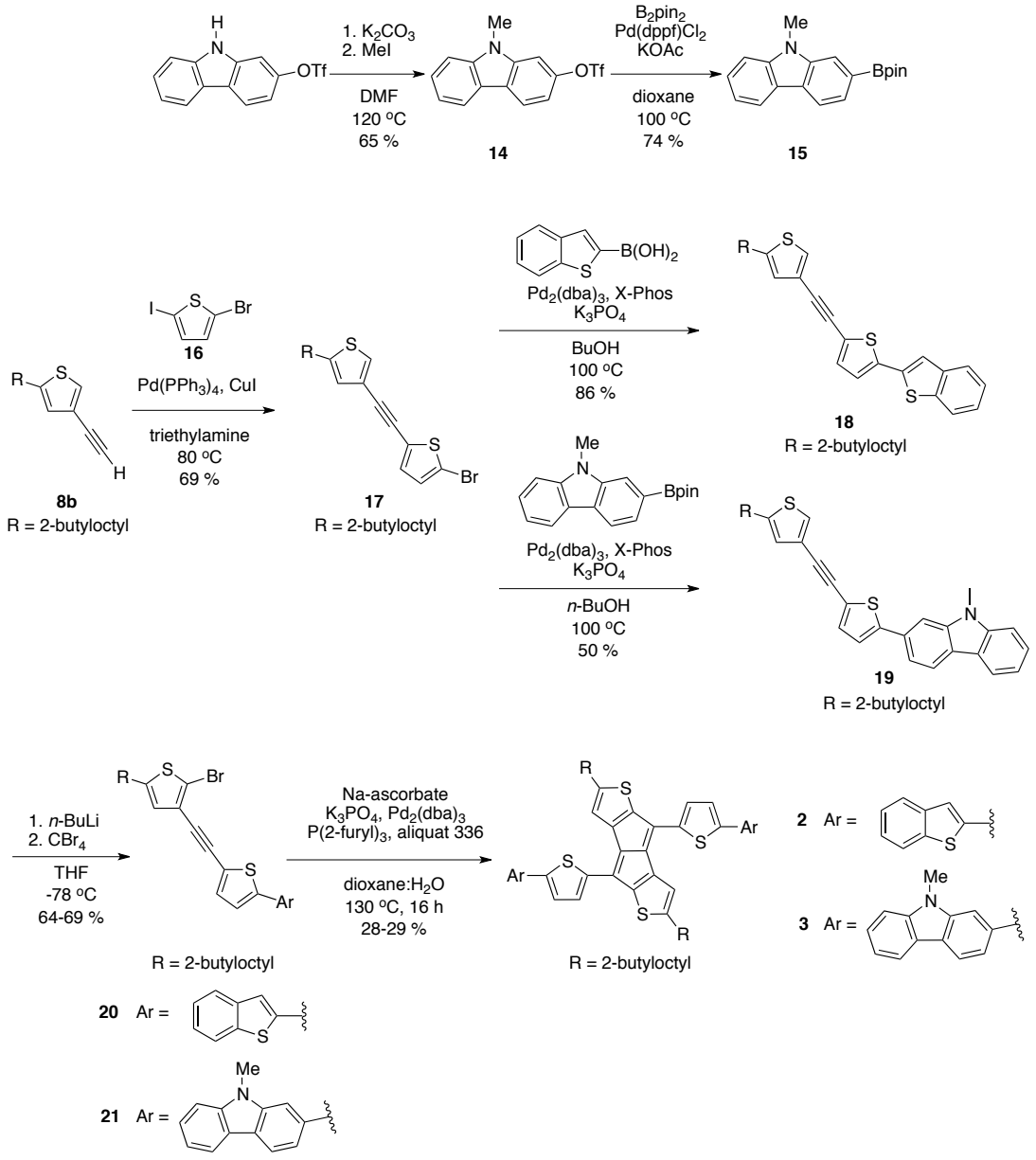

Scheme 4-3. Synthesis of the target small molecule with benzothiophene and carbazole using the optimized cyclization method.

4.2.3. Optical and Electrochemical Properties of Pentalenodithiophene

UV-visible spectroscopy was used to characterize the absorption profiles of the small molecules in chloroform solutions (Figure 4-7). The optical band gaps of these materials were calculated from wavelengths of absorption onset (1.87–2.13 eV), and the molar extinction coefficients of these materials were also determined at λ_{max}. With extinction coefficients on the order of 10^4, these materials also show relatively even absorption across the visible spectrum while typical donor-acceptor, low band gap materials tend to exhibit attenuated absorption in the 400-500 nm region.[18,37] Based on cyclic voltammetry measurements, the HOMO levels are –5.5 eV for both small molecules while LUMO energy levels are -4.0 eV and -3.4 eV for molecules **2** and **3**, respectively. The band gaps determined by CV correlate well with the optical

band gaps. Table 4-2 summarizes both optical and electrochemical parameters determined for all three pentalenodithiophene molecules.

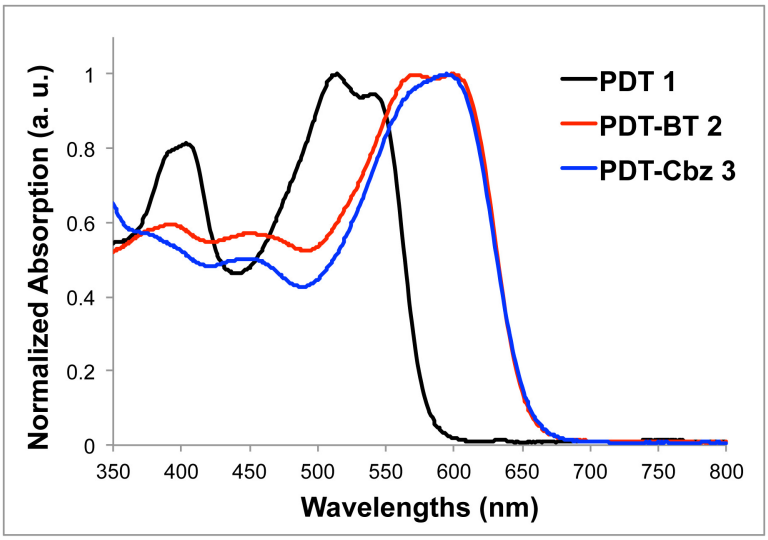

Figure 4-7. UV-vis absorption spectra in chloroform.

Table 4-2. Optical and electronic band gaps of pentalenodithiophene

	λ_{onset} (nm)	E_g (eV)	λ_{max} (nm)	ε ($M^{-1}cm^{-1}$)	HOMO (eV)	LUMO (eV)	CV band gap (eV)
PDT (**1**)	583	2.13	513	1.63×10^4	--	--	--
PDT-BT (**2**)	662	1.87	599	2.92×10^4	-5.5	-3.9	1.6
PDT-Cbz (**3**)	663	1.87	595	3.52×10^4	-5.5	-3.4	2.1

4.3. Conclusion

Three different pentalenodithiophene small molecules have been successfully synthesized with an optimized Pd-catalyzed annulation. The structure of PDT **1** was confirmed with single-crystal X-ray diffraction. UV-vis absorption profiles of the pentalene molecules show red-shifted absorption onset and even coverage of a significant portion of the visible spectrum. These pentalene molecules **1**–**3** also display extinction coefficients on the order of 10^4 $M^{-1}cm^{-1}$, and CV measurements of these materials corroborate the trends observed in the UV-vis. Based on these optoelectronic characteristics, molecules based on pentalenodithiophene show great promise as electroactive materials for potential applications in organic electronic devices. With this work, we demonstrate that introducing antiaromaticity into conjugated backbones is an effective strategy for designing materials with low band gaps. As a future direction, functionalizing the antiaromatic core with a bromide, boronate or stannane handle will allow for the syntheses of alternating copolymers with appropriate viscosity for solution-processable organic electronic devices.

4.4. Experimental

4.4.1. Synthetic Details

All commercially available reagents obtained from suppliers were used without further purification. Unless otherwise noted, all reactions were carried out under nitrogen with standard Schlenk techniques, and all glassware used in dry reactions were flame dried under high-vacuum prior to use. All organic extracts were dried over magnesium sulfate ($MgSO_4$) powder, and solvents were removed under reduced pressure with a rotary evaporator. Toluene, tetrahydrofuran (THF) and dimethylformamide (DMF) were purified and dried by passing through two columns of neutral alumina under nitrogen prior to use. All solvents used in Pd-catalyzed cross-coupling reactions were degassed by freeze-pump-thaw prior to use. Flash chromatography was performed using Silicycle SiliaFlash ® P60 (particle size 40-63 μm, 230-400 mesh) silica gel.

All ^{1}H and ^{13}C NMR spectra were obtained in chloroform-*d*, unless otherwise noted, with a Bruker AVQ-400, AVB-400, DRX-500, AV-500 or AV-600 instrument. ^{13}C spectra were measured with a proton-decoupling pulse program. All chemical shifts (ppm) were calibrated to the residual peak of the deuterated solvent. Matrix-assisted laser desorption/ionization-time of flight mass spectrometry (MALDI-TOF MS) was performed on a PerSeptive Biosystems Voyager-DE using 2,2':5',2''-terthiophene as the matrix. Samples were prepared by diluting the monomers in chloroform with the matrix. Elemental analysis (CHN) was performed by the UC Berkeley microanalysis laboratory.

2-(2-Ethylhexyl)thiophene (**4a**).

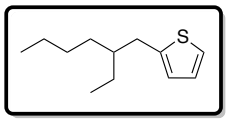

A 250-mL 3-neck flask connected to a condenser was charged with thiophene (6.54 g, 3.0 equiv., 77.7 *m*mol) and dry THF (43 mL) under N_2 atmosphere. The solution was cooled to -78 °C for 30 min in a CO_2/isopropanol (IPA) bath, followed by dropwise addition *n*-BuLi (1.6 M in hexanes, 21 mL, 1.3 equiv., 33.7 *m*mol) at -78 °C. The reaction mixture was stirred at -78 °C before 2-ethylhexylbromide (5.00 g, 1.00 equiv. 25.9 *m*mol) was added in one portion, and it was heated at 60 °C for 20 h. Upon cooling the reaction contents, all THF was removed under reduced pressure by rotary evaporation. The residue was extracted with hexanes three times; the organic layer was dried over $MgSO_4$ and filtered, and the solvent was removed by rotary evaporation to yield a brown oil. Purification by flash chromatography (silica gel, hexanes) afforded 3.49 g of product (colorless oil, 69 %). (Chem Mater. 2007, 19, 1070)

^{1}H NMR (400 MHz, $CDCl_3$, δ): 7.11 (d, J = 5.1 Hz, 1 H), 6.92 (dd, J = 3.3, 5.1 Hz, 1 H), 6.76 (d, J = 3.3 Hz, 1 H), 2.77 (d, J = 6.7 Hz, 2 H), 1.58 (m, 1 H), 1.37–1.25 (m, 8 H), 0.89 (at, J = 7.4 Hz, 6 H). ^{13}C (100 MHz, $CDCl_3$, δ): 144.5, 126.7, 125.1, 123.1, 41.6, 34.0, 32.5, 29.0, 25.6, 23.2, 14.3, 11.0. GC-MS (EI, *m/z*) $[M]^+$ calcd for $C_{12}H_{20}S$, 196.13; found, 196.1.

2-(2-Butyloctyl)thiophene (**4b**)

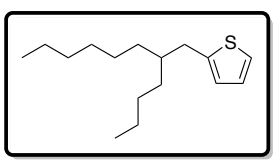

Reaction conditions were the same as for **4a**, except thiophene (2.56 g, 3.0 equiv., 30.4 *m*mol), *n*-BuLi (2.5 M in hexanes, 5.5 mL, 1.3 equiv., 13.2 *m*mol), 2-butyloctyliodide (3.0 g, 1.0 equiv., 10.1 *m*mol) and dry THF (17 mL) were used. Purification by flash chromatography (silica gel, hexanes) afforded 1.79 g of product (colorless oil, 70 %). (Cite butyloctyliodide synthesis)

^{1}H NMR (600 MHz, $CDCl_3$, δ): 7.12 (d, *J* = 5.1 Hz, 1 H), 6.92 (dd, *J* = 3.6, 5.0 Hz, 1 H), 6.76 (d, *J* = 3.4 Hz, 1 H), 2.77 (d, *J* = 6.7 Hz, 2 H), 1.63 (m, 1 H), 1.33–1.25 (m, 16 H), 0.94–0.85 (m, 6 H). ^{13}C (150 MHz, $CDCl_3$, δ): 144.5, 126.7, 125.1, 123.0, 40.1, 34.4, 33.3, 33.3, 33.0, 32.0, 29.8, 29.0, 26.7, 23.2, 22.84, 22.83, 14.29, 14.27, 14.26. GC-MS (EI, *m/z*) $[M]^+$ calcd for $C_{16}H_{28}S$, 252.19; found, 252.2.

2-Bromo-5-(2-ethylhexyl)thiophene (**5a**)

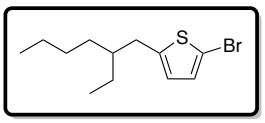

Under ambient conditions, a 250-mL, round-bottom flask was charged with **4a** (4.08 g, 1.0 equiv., 20.8 *m*mol), NBS (3.70 g, 1.05 equiv., 20.8 *m*mol) and glacial acetic acid (21 mL). The reaction mixture was stirred at 40 °C for 1.5 h before being neutralized with $NaHCO_3$, washed with water twice, extracted with hexanes three times. The organic layer was dried over $MgSO_4$ and filtered, and the solvent was removed by rotary evaporation to yield a yellow oil. The crude product was passed through a pad of silica gel with hexanes as an eluent, and removing solvent from the filtrate afforded 5.09 g of product (colorless oil, 89 %).

^{1}H NMR (400 MHz, $CDCl_3$, δ): 6.89 (d, *J* = 3.6 Hz, 1 H), 6.56 (d, *J* = 3.6 Hz, 1 H), 2.73 (d, *J* = 6.8 Hz, 2 H), 1.55 (m, 1 H), 1.42–1.29 (m, 8 H), 0.97–0.91 (m, 6 H). ^{13}C (100 MHz, $CDCl_3$, δ): ^{13}C NMR (100 MHz, $CDCl_3$, δ): 146.3, 129.5, 125.5, 108.8, 41.4, 34.4, 32.4, 29.0, 25.6, 23.1, 14.3, 10.9. GC-MS (EI, *m/z*) $[M]^+$ calcd for $C_{12}H_{19}BrS$, 276.04; found, 276.0.

2-Bromo-5-(2-butyloctyl)thiophene (**5b**)

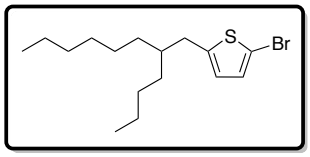

Under ambient conditions, a 50-mL, round-bottom flask was charged with **4b** (1.63 g, 1.0 equiv., 6.45 *m*mol), NBS (1.21 g, 1.05 equiv., 6.78 *m*mol) and glacial acetic acid (6.5 mL). The reaction mixture was stirred at room temperature for 16 h before being neutralized with $NaHCO_3$. The organic layer was washed with saturated $NaHCO_3$ solution twice and with water twice, dried over $MgSO_4$ and filtered. The solvent was removed by rotary evaporation to yield a yellow oil. The crude product was passed through a pad of silica gel with hexanes as an eluent, and removing solvent from the filtrate afforded 2.01 g of product (colorless oil, 94 %)

^{1}H NMR (600 MHz, $CDCl_3$, δ): 6.89 (d, *J* = 3.7 Hz, 1 H), 6.56 (d, *J* = 3.7 Hz, 1 H), 2.73 (d, *J* = 6.7 Hz, 2 H), 1.57 (m, 1 H), 1.41–1.30 (m, 16 H), 0.96–0.91 (m, 6 H). ^{13}C NMR (150 MHz, $CDCl_3$, δ): 146.3, 129.5, 125.6, 108.8, 39.9, 34.9, 33.2, 32.9, 32.0, 29.7, 29.0, 26.7, 23.1, 22.8, 14.3. GC-MS (EI, *m/z*) $[M]^+$ calcd for $C_{16}H_{27}BrS$, 332.10; found, 332.0.

4-Bromo-2-(2-ethylhexyl)thiophene (**6a**).

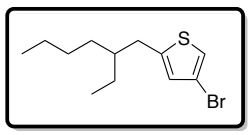

"Halogen Dance." In a 25-mL flask, diisopropylamine (1.5 mL, d = 0.717 g/mL, 1.15 equiv., 10.5 *m*mol) was dissolved in dry THF (7 mL) under N_2 atmosphere, and the solution was to 0 °C. *n*-BuLi (1.6 M in hexanes, 7 mL, 1.2 equiv. 10.9 *m*mol) was added to the flask dropwise, and the lithium diisopropylamide (LDA) solution was stirred at 0 °C for 20 min before warming up to room temperature for 2 h. A separate 50-mL, 3-neck flask was charged with **5a** (2.50 g, 1.0 equiv., 9.08 *m*mol) and dry THF (9 mL), and the solution cooled to -78 °C. The LDA solution was then added to the bromothiophene solution in small portions over 2 h, and the reaction mixture was stirred for another 30 min at -78 °C. Methanol (2 mL) was added to flask to quench the reaction,

and the mixture was warmed up to room temperature. The resulting light yellow suspension was diluted with hexanes and washed with water three times. The organic layer was dried over $MgSO_4$ and filtered, and the solvent was removed by rotary evaporation to yield an orange oil. The crude product was passed through a pad of silica gel with hexanes as an eluent, and subsequent removal of solvent from the filtrate afforded 2.46 g of product (colorless oil, 98 %, containing 99% of the desired 2,4-disubstituted isomer).

^{1}H NMR (400 MHz, $CDCl_3$, δ): 7.01 (s, 1 H), 6.68 (s, 1 H), 2.73 (d, J = 6.7 Hz, 2 H), 1.57 (m, 1 H), 1.41–1.30 (m, 8 H), 0.96–0.91 (m, 6 H). ^{13}C (100 MHz, $CDCl_3$, δ): 150.0, 127.7, 120.4, 108.9, 41.3, 34.0, 32.4, 28.9, 25.5, 23.1, 14.3, 10.9. GC-MS (EI, *m/z*) $[M]^+$ calcd for $C_{12}H_{19}BrS$, 276.04; found, 276.1.

4-Bromo-2-(2-butyloctyl)thiophene (**6b**).

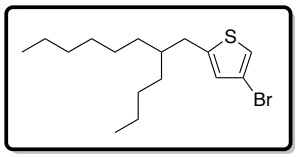

Reaction conditions were the same as for **6a**, except diisopropylamine (990 μL, d = 0.717 g/mL, 1.15 equiv., 6.98 *m*mol) in 4.5 mL dry THF, *n*-BuLi (2.5 M in hexanes, 2.9 mL, 1.2 equiv. 7.28 *m*mol) and **5b** (2.00 g, 1.0 equiv., 6.07 *m*mol) in dry THF (6 mL) were used. Purification by passing the crude material through a pad of silica gel (hexanes) afforded 1.88g of product (colorless oil, 91%).

^{1}H NMR (600 MHz, $CDCl_3$, δ): 7.01 (s, 1 H), 6.67 (s, 1 H), 2.71 (d, J = 6.7 Hz, 2 H), 1.59 (m, 1 H), 1.30–1.24 (m, 16 H), 0.89 (adt, J = 2.6, 7.3 Hz, 6 H). ^{13}C (150 MHz, $CDCl_3$, δ): 146.0, 127.7, 120.4, 109.0, 39.9, 34.5, 33.2, 32.9, 32.0, 29.7, 28.9, 26.7, 23.1, 22.8, 14.3. GC-MS (EI, *m/z*) $[M]^+$ calcd for $C_{16}H_{27}BrS$, 332.10; found, 332.0.

((5-(2-Ethylhexyl)thiophen-3-yl)ethynyl)trimethylsilane (**7a**).

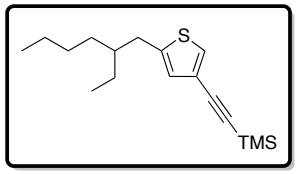

A 100-mL, 3-neck flask attached to a condenser was charged with **6a** (2.46 g, 1.0 equiv., 8.93 *m*mol) and evacuated/refilled with N_2 three times; in the meantime, an oil bath was preheated to 60 °C. Triethylamine (36 mL) and 0.5 mL of trimethylsilylacetylene (2.6 mL, d = 0.695 g/mL, 2.0 equiv., 17.9 *m*mol) was added to the flask. The reaction mixture was heated at 60 °C immediately upon the addition of tetrakis(triphenylphosphine)palladium(0) ($Pd(PPh_3)_4$, 51.6 mg, 0.5 mol%, 44.6 μmol) and copper(I) iodide (17.0 mg, 1 mol%, 89.3 μmol). The remaining trimethylsilylacetylene was added in small portions over 2 h. The reaction mixture was stirred at 60 °C for 16 h before being diluted with hexanes. The organic layer was washed with saturated NH_4Cl solution twice and with water twice, dried over $MgSO_4$ and filtered, and the solvent was removed by rotary evaporation to yield a brown oil. Purification by flash chromatography (silica gel, hexanes) afforded 2.26 g of product (light yellow oil, 86 %).

^{1}H NMR (400 MHz, $CDCl_3$, δ): 7.27 (s, 1 H), 6.78 (s, 1 H), 2.68 (d, J = 6.8 Hz, 2 H), 1.56 (m, 1 H), 1.39–1.25 (m, 8 H), 0.96–0.85 (m, 6 H), 0.23 (s, 9 H). ^{13}C (MHz, $CDCl_3$, δ): = 144.4, 127.9, 121.7, 100.7, 93.1, 41.4, 33.9, 32.4, 31.7, 29.0, 25.5, 23.1, 14.3, 10.9, 0.14. GC-MS (EI, *m/z*) $[M]^+$ calcd for $C_{17}H_{28}SSi$, 292.17; found, 292.2.

((5-(2-Butyloctyl)thiophen-3-yl)ethynyl)trimethylsilane (**7b**).

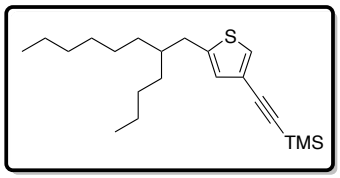

Reaction conditions were the same as for **7a**, except **6b** (1.88 g, 1.0 equiv., 5.67 *m*mol), trimethylsilylacetylene (1.6 mL, d = 0.695 g/mL, 2.0 equiv., 11.3 *m*mol), $Pd(PPh_3)_4$ (32.7 mg, 0.5 mol%, 28.3 μmol), copper(I) iodide (10.7 mg, 1 mol%, 56.7 μmol), triethylamine (23 mL) were used, and the reaction mixture was heated at 75 °C. Purification by flash chromatography (silica gel, hexanes) afforded 1.71 g of product (colorless oil, 87%).

^{1}H NMR (400 MHz, $CDCl_3$, δ): 7.27 (s, 1 H), 6.77 (s, 1 H), 2.68 (d, J = 6.8 Hz, 2 H), 1.58 (m, 1 H), 1.29–1.24 (m, 16 H), 0.89 (m, 6 H), 0.23 (s, 9 H). ^{13}C (100 MHz, $CDCl_3$, δ): = 144.r, 127.94, 127.92, 121.6, 100.7, 93.1, 40.0, 34.3, 33.2, 32.9, 32.0, 29.7, 29.0, 26.7, 23.1, 22.8, 14.3 0.15. GC-MS (EI, *m/z*) $[M]^+$ calcd for $C_{21}H_{36}SSi$, 348.23; found, 348.3.

2-(2-Ethylhexyl)-4-ethynylthiophene (**8a**).

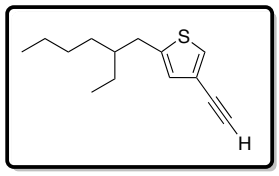

Under ambient conditions, 250-mL RBF was charged with **7a** (2.26 g, 1.0 equiv., 7.71 *m*mol), K_2CO_3 (964 mg, 0.9 equiv., 6.97 *m*mol) and methanol (39 mL), and the reaction mixture was allowed to stir for 16 h at room temperature. The reaction mixture was extracted with hexanes twice, and the organic layer was dried over $MgSO_4$ and filtered. The solvent was then removed by rotary evaporation to yield 1.63 g of product (light yellow oil, 96 %).

^{1}H NMR (400 MHz, $CDCl_3$, δ): 7.31 (s, 1 H), 6.80 (s, 1 H), 2.99 (s, 1 H), 2.70 (d, J = 6.8 Hz, 2 H), 1.56 (m, 1 H), 1.38–1.24 (m, 8 H), 0.92–0.84 (m, 6 H). ^{13}C (100 MHz, $CDCl_3$, δ): = 144.6, 128.3, 127.9, 79.6, 76.3, 41.4, 33.8, 32.4, 29.0, 25.5, 23.1, 14.3, 10.9. GC-MS (EI, *m/z*) $[M]^+$ calcd for $C_{14}H_{20}S$, 220.13; found, 220.1.

2-(2-Butyloctyl)-4-ethynylthiophene (**8b**). OL406.

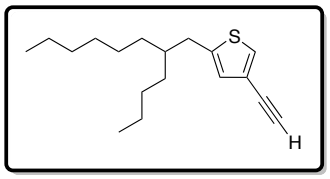

Reaction conditions were the same as for **8a**, except **7b** (1.71 g, 1.0 equiv., 4.90 *m*mol), K_2CO_3 (613 mg, 0.9 equiv., 4.44 *m*mol) and methanol (24.5 mL) were used, and 1.25 g of product was obtained (light yellow oil, 92 %).

^{1}H NMR (400 MHz, $CDCl_3$, δ): 7.31 (s, 1 H), 6.79 (s, 1 H), 2.99 (s, 1 H), 2.70 (d, J = 6.7 Hz, 2 H), 1.60 (m, 1 H), 1.32–1.26 (m, 16 H), 0.94–0.87 (m, 6 H). ^{13}C (100 MHz, $CDCl_3$, δ): = 144.6, 128.e, 127.9, 120.5, 79.6, 76.3, 40.0, 34.3, 33.2, 32.9, 32.0, 29.74, 29.0, 26.7, 23.1, 22.8, 14.3. GC-MS (EI, *m/z*) $[M]^+$ calcd for $C_{18}H_{28}S$, 276.19; found, 276.1.

2-(2-Ethylhexyl)-4-(thiophen-2-ylethynyl)thiophene (**9**).

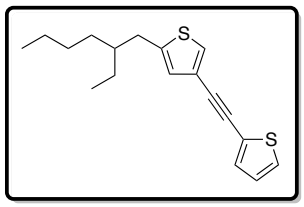

A 100-mL, 3-neck flask attached to a condenser was charged with 2-bromothiophene (1.81 g, 1.5 equiv., 11.1 *m*mol) and evacuated/refilled with N_2 three times before adding triethylamine (30 mL); in the meantime, an oil bath was preheated to 60 °C in the meantime. In a separate 10-mL flask, **8a** (1.63 g, 1.0 equiv., 7.40 *m*mol) was dissolved in triethylamine (3 mL) under N_2, and 1 mL of this solution was added to the reaction flask. The reaction mixture was heated at 60 °C

immediately upon the addition of $Pd(PPh_3)_4$ (42.8 mg, 0.5 mol%, 37.0 μmol) and copper(I) iodide (14.1 mg, 1 mol%, 74.0 μmol). The remaining triethylamine solution of **8a** was added in small portions over 1 h. The reaction mixture was stirred at 60 °C for 16 h before being diluted with hexanes. The organic layer was washed with saturated NH_4Cl solution twice and with water twice, dried over $MgSO_4$ and filtered, and the solvent was removed by rotary evaporation to yield a brown oil. Purification by flash chromatography (silica gel, hexanes) afforded 2.05 g of product (yellow oil, 91 %).

^{1}H NMR (MHz, $CDCl_3$, δ): 7.32 (s, 1 H), 7.27 (d, J = 5.4 Hz, 1 H), 7.25 (d, J = 3.7 Hz, 1 H), 7.00 (dd, J = 3.6, 5.2 Hz, 1 H), 6.84 (s, 1 H), 2.72 (d, J = 6.8 Hz, 2 H), 1.57 (m, 1 H), 1.38–1.26 (m, 8 H), 0.93–0.86 (m, 6 H). ^{13}C (100 MHz, $CDCl_3$, δ): = 144.7, 131.8, 127.5, 127.18, 127.15, 127.10, 123.6, 121.3, 89.0, 81.5, 41.4, 33.9, 32.4, 29.0, 25.5, 23.1, 14.3, 10.9. GC-MS (EI, *m/z*) $[M]^+$ calcd for $C_{18}H_{22}S_2$, 302.12; found, 302.1.

2-Bromo-5-(2-ethylhexyl)-3-(thiophen-2-ylethynyl)thiophene (**10**).

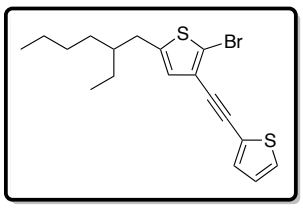

In a 50-mL RBF, **9** (2.03 g, 1.0 equiv., 6.71 *m*mol) was dissolved in a 1:1 mixture of chloroform (6.7 mL) and glacial acetic acid (6.7 mL), and the solution was cooled to 0 °C. NBS (1.25 g, 1.05 equiv., 7.05 *m*mol) was added to the flask in one shot. The reaction mixture was warmed to room temperature over 30 min, and it was stirred at room temperature for 16 h before being diluted with hexanes. The organic layer was neutralized with saturated $NaHCO_3$ solution three times, washed with water twice, dried over $MgSO_4$ and filtered. The solvent was removed by rotary evaporation to yield a dark green oil. Purification by flash chromatography (silica gel, hexanes) afforded 1.74 g product (yellow oil, 68 %).

^{1}H NMR (400 MHz, $CDCl_3$, δ): 7.30 (m, 2 H), 7.00 (dd, J = 3.8, 5.0 Hz, 1 H), 6.69 (s, 1 H), 2.66 (d, J = 6.7 Hz, 2 H), 1.54 (m, 1 H), 1.37–1.26 (m, 8 H), 0.91–0.86 (m, 6 H). ^{13}C (100 MHz, $CDCl_3$, δ): = 145.0, 132.3, 127.7, 127.4, 127.3, 123.5, 123.1, 114.0, 87.4, 85.6, 41.2, 34.4, 32.4, 29.0, 25.5, 23.1, 14.3, 10.9. GC-MS (EI, *m/z*) $[M]^+$ calcd for $C_{18}H_{21}BrS_2$, 382.02; found, 382.0.

2,6-Bis(2-ethylhexyl)-4,8-di(thiophen-2-yl)pentaleno[2,1-b:5,4-b']dithiophene (**1**).

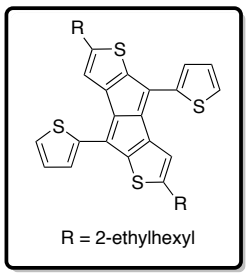

A 15-mL pressure tube was charged with sodium ascorbate (51.9 mg, 2.0 equiv., 0.262 *m*mol), K_3PO_4 (55.6 mg, 2.0 equiv., 0.262 *m*mol), $Pd_2(dba)_3$ (1.80 mg, 1.5 mol%, 1.97 μmol), tri(2-furyl)phosphine ($P(2\text{-furyl})_3$, 1.83 mg, 6.0 mol%, 7.87 μmol) and aliquat 336 (1 drop), and it was capped with a inverted septum. The tube was evacuated and refilled with N_2 three times while an oil bath was preheated to 130 °C. In a separate flask, **10** (50 mg, 1.0 equiv., 0.131 *m*mol) was dissolved in dioxane (freeze-pump-thawed, 874 μL) under N_2 atmosphere. Upon addition of the dioxane solution and distilled water (freeze-pump-thawed, 175 μL, dioxane:water = 5:1), the pressure tube was tightly sealed with an o-ring-lined Teflon® cap and immediately inserted into the preheated oil bath. The reaction mixture turned red within 5 min of heating and was stirred at 130 °C for 16 h. After the reaction vessel was cooled to room temperature completely, the reaction mixture was diluted with chloroform and filtered through a pad of celite 545 topped with a thin layer of $MgSO_4$. Removal of solvent by rotary evaporation yielded a brown solid. The crude mixture was purified by flash chromatography (silica gel, eluted with increasing

gradient from hexanes to 10 % chloroform in hexanes) and then recrystallization (layered methanol on a chloroform solution of the product). The crystal suspension was filtered through a 0.22 μm Nylon membrane and washed with methanol to afford 10.1 mg of dark purple fluffy needles (25.6 %).

^{1}H NMR (MHz, $CDCl_3$, δ): 7.43 (d, *J* = 5.1, 2 H), 7.33 (d, *J* = 3.7, 2 H), 7.09 (dd, *J* = 3.8, 5.1 Hz, 2 H), 6.62 (s, 2 H), 2.57 (d, *J* = 6.7 Hz, 4 H), 1.51 (m, 2 H), 1.42–1.23 (m, 16 H), 0.91–0.87 (m, 12 H). GC-MS (MALDI-TOF, *m/z*) $[M]^+$ calcd for $C_{36}H_{42}S_4$, 602.22; found, 603.14.

9-Methyl-9H-carbazol-2-yl trifluoromethanesulfonate (**14**).

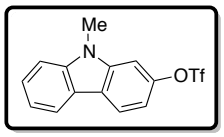

A 50-mL, 3-neck flask attached to a condenser was charged with 9H-carbazol-2-yl trifluoromethanesulfonate (500 mg, 1.0 equiv., 1.59 *m*mol) and K_2CO_3 (438 mg, 2.0 equiv., 3.17 *m*mol), and the flask was evacuated and refilled with N_2 three times. Dry DMF (15 mL) was transferred to the flask, and the reaction mixture was heated at 120 °C for 40 min before methyl iodide (250 μL, d = 2.28 g/mL, 2.5 equiv., 3.97 *m*mol) was added. After 16 h, the reaction mixture was cooled to room temperature and diluted with diethyl ether. The organic layer was washed with water three times, dried over $MgSO_4$ and filtered, and the solvent was removed by rotary evaporation to yield an orange solid. Purification by flash chromatography (silica gel, 30 % chloroform in hexanes) afforded 342 mg of product (white, crystalline solid, 65%).

^{1}H NMR (600 MHz, $CDCl_3$, δ): 8.09 (dd, *J* = 6.8, 8.1 Hz, 2 H), 7.53 (dd, *J* = 7.1, 8.3 Hz, 1 H), 7.44 (d, *J* = 8.2 Hz, 1 H), 7.30 (m, 2 H), 7.13 (dd, *J* = 2.2, 8.5 Hz, 1 H), 3.87 (s, 3 H). ^{13}C (150 MHz, $CDCl_3$, δ): = 149.0, 142.1, 141.1, 126.8, 122.8, 122.0, 121.4, 120.7, 120.0, 112.0, 109.0, 102.0, 29.5. GC-MS (EI, *m/z*) $[M]^+$ calcd for $C_{14}H_{10}F_3NO_3S$, 329.03; found, 329.0.

9-Methyl-2-(4,4,5,5-tetramethyl-1,3,2-dioxaborolan-2-yl)-9H-carbazole (**15**).

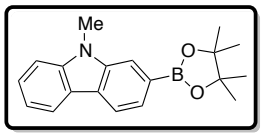

A 50-mL, 3-neck flask attached to a condenser was charged with **14** (342 mg, 1.0 equiv., 1.04 *m*mol), bis(pinacolato)diboron (527 mg, 2.0 equiv., 2.07 *m*mol), potassium acetate (305 mg, 3.0 equiv., 3.11 *m*mol), [1,1′-Bis(diphenylphosphino)ferrocene]dichloropalladium(II) methylene chloride adduct ($Pd(dppf)Cl_2$-CH_2Cl_2, 42.3 mg, 5 mol%, 51.9 μmol). The reaction flask was evacuated and refilled with N_2 three times while an oil bath was preheated to 100 °C. Upon addition of anhydrous dioxane (10 mL), the reaction mixture was immediately heated at 100 °C. After 16 h, the reaction mixture was cooled to room temperature and extracted with diethyl ether twice. The organic layer was washed with brine three times, dried over $MgSO_4$ and filtered, and the solvent was removed by rotary evaporation to yield a light brown oil. Purification of the crude material by flash chromatography (silica gel, 75 % chloroform in hexanes) afforded 236 mg of product (yellow oil, 74 %)

^{1}H NMR (400 MHz, $CDCl_3$, δ): 8.15 (d, *J* = 7.8 Hz, 2 H), 7.94 (s, 1 H), 7.75 (d, *J* = 7.8 Hz, 1 H), 7.53 (dd, *J* = 7.1, 8.3 Hz, 1 H), 7.42 (d, *J* = 8.2 Hz, 1 H), 7.29 (t, *J* = 7.0 Hz, 1 H), 3.90 (s, 3 H), 1.44 (s, 12 H). ^{13}C (100 MHz, $CDCl_3$, δ): = 141.6, 140.66, 126.4, 125.4, 125.1, 122.6, 120.9, 119.7, 118.9, 115.1, 108.7, 83.9, 29.2, 25.1. GC-MS (EI, *m/z*) $[M]^+$ calcd for $C_{19}H_{22}BNO_2$, 307.17; found, 307.2.

2-Bromo-5-iodothiophene (**16**).

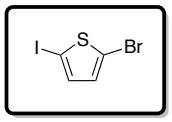

Under ambient condition, a 25-mL flask was charged with 2-bromothiophene (1.00 g, 1.0 equiv., 6.13 *m*mol) and chloroform (6 mL), and the solution was cooled to 0 °C. Iodine (934 mg, 0.6 equiv., 3.68 *m*mol) and (diacetoxyiodo)benzene ($PhI(OAc)_2$, 1.00 g, 0.51 equiv., 3.14 *m*mol) were added to the reaction mixture, which was stirred at 0 °C before warming up to room temperature. After 12 h, the reaction mixture was quenched with saturated sodium thiosulfate ($Na_2S_2O_3$) solution and diluted with chloroform. The organic later was washed with saturated $Na_2S_2O_3$ solution twice, washed with water twiced, dried over $MgSO_4$ and filtered, and the solvent was removed by rotary evaporation to yield a brown oil. Iodobenzene was distilled away (bp 34-36 °C at 800 *m*Torr) from the crude material, which was then passed through a pad of silica gel with hexanes as the eluent. Removal of the volatiles afforded 1.32 g of the product (light yellow oil, 75 %).

^{1}H NMR (600 MHz, $CDCl_3$, δ): 7.04 (d, J = 4.2 Hz, 1 H), 7.75 (d, J = 4.2 Hz, 1 H). ^{13}C (150 MHz, $CDCl_3$, δ): = 138.9, 137.6, 131.8, 115.3. GC-MS (EI, *m/z*) $[M]^+$ calcd for $C_{44}H_2BrIS$, 289.81; found, 289.9.

4-((5-Bromothiophen-2-yl)ethynyl)-2-(2-butyloctyl)thiophene (**17**).

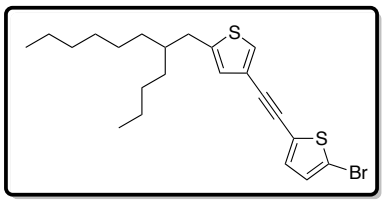

A 50-mL, 3-neck flask attached to a condenser was charged with **16** (1.32 g, 1.01 equiv., 4.57 *m*mol) and evacuated/refilled with N_2 three times before the addition of triethylamine (17 mL). In the meantime, an oil bath was preheated to 60 °C in the meantime. In a separate 10-mL flask, **8b** (1.25 g, 1.0 equiv., 4.52 *m*mol) was dissolved in triethylamine (5 mL) under N_2, and 0.5 mL of this solution was added to the reaction flask. The reaction mixture was heated at 60 °C immediately upon the addition of $Pd(PPh_3)_4$ (24.9 mg, 0.5 mol%, 21.5 μmol) and copper(I) iodide (8.2 mg, 1 mol%, 43.0 μmol). The remaining triethylamine solution of OL252 was added in small portions over 1.5 h. The reaction mixture was stirred at 60 °C for 16 h before being diluted with diethyl ether. The organic layer was washed with saturated NH_4Cl solution twice and with water twice, dried over $MgSO_4$ and filtered, and the solvent was removed by rotary evaporation to yield a brown oil. Purification by flash chromatography (silica gel, hexanes) afforded 1.37 g of product (colorless oil, 69 %).

^{1}H NMR (600 MHz, $CDCl_3$, δ): 7.32 (s, 1 H), 6.98 (d, J = 3.9 Hz, 1 H), 6.94 (d, J = 3.9 Hz, 1 H), 6.81 (s, 1 H), 2.71 (d, J = 6.8 Hz, 2 H), 1.61 (m, 1 H), 1.34–1.25 (m, 16 H), 0.90–0.87 (m, 6 H). ^{13}C (150 MHz, $CDCl_3$, δ): = 144.9, 132.0, 130.2, 127.5, 127.4, 125.4, 120.9, 112.9, 90.0, 80.6, 40.0, 34.4, 33.3, 33.0, 32.0, 30.0, 29.0, 26.7, 23.1, 22.8, 14.26, 14.25. GC-MS (EI, *m/z*) $[M]^+$ calcd for $C_{22}H_{29}BrS_2$, 438.09; found, 438.1.

2-(5-((5-(2-Butyloctyl)thiophen-3-yl)ethynyl)thiophen-2-yl)benzo[b]thiophene (**18**).

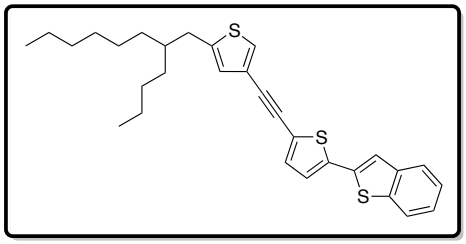

A 25-mL, 3-neck flask attached to a condenser was charged with **17** (450 mg, 1.0 equiv., 1.19 *m*mol), thianaphthene-2-boronic acid (220 mg, 1.2 equiv., 1.23 *m*mol), K_3PO_4 (437 mg, 2.0 equiv., 2.06 *m*mol), $Pd_2(dba)_3$ (9.42 mg, 1.0 mol%, 10.3 μmol) and X-Phos (9.81 mg, 2.0 mol%, 20.6 μmol). The flask was evacuated and refilled with N_2 three times while an oil bath was

preheated to 100 °C. Upon transferring *n*-BuOH (freeze-pump-thawed, 5 mL) to the flask, the reaction mixture was heated at 100 °C for 20 h. After cooling to room temperature, the dark brown reaction mixture was diluted with diethyl ether. The organic layer was washed with saturated NH_4Cl solution twice and water twice, dried over $MgSO_4$ and filtered, and the solvent was removed by rotary evaporation to yield a thick, brown oil. Purification by flash chromatography (silica gel, 5 % chloroform in hexanes) afforded 436 mg of product (yellow solid, 86%).

^{1}H NMR (400 MHz, $CDCl_3$, δ): 7.78 (d, J = 7.6 Hz, 1 H), 7.74 (d, J = 7.6 Hz, 1 H), 7.40 (s, 1 H), 7.34 (m, 3 H), 7.18 (s, 2 H), 6.85 (s, 1 H), 2.73 (d, J = 6.7 Hz, 2 H), 1.62 (m, 1 H), 1.33–1.25 (m, 16 H), 0.95–0.87 (m, 6 H). ^{13}C (100 MHz, $CDCl_3$, δ): = 144.8, 140.4, 139.3, 138.6, 136.7, 132.7, 127.5, 127.4, 125.0, 124.93, 124.90, 123.7, 123.5, 122.3, 121.1, 120.3, 90.6, 81.5, 40.0, 34.4, 33.3, 32.9, 32.0, 31.7, 29.8, 29.0, 26.7, 23.1, 22.8, 14.3. MALDI-TOF (*m/z*) $[M]^+$ calcd for $C_{30}H_{34}S_3$, 490.18; found, 491.37.

2-(5-((5-(2-Butyloctyl)thiophen-3-yl)ethynyl)thiophen-2-yl)-9-methyl-9H-carbazole (**19**).

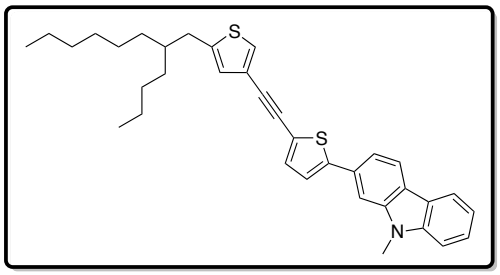

Reaction conditions were the same as for **18**, except **17** (310 mg, 1.0 equiv., 0.709 *m*mol), **15** (236 mg, 1.08 equiv., 0.768 *m*mol), K_3PO_4 (296 mg, 2.0 equiv., 1.40 *m*mol), $Pd_2(dba)_3$ (6.39 mg, 1.0 mol%, 6.98 μmol) and X-Phos (6.66 mg, 2.0 mol%, 14.0 μmol) and *n*BuOH (3.5 mL) were used. In the workup, diethyl ether was used instead of chloroform for the saturated NH_4Cl solution and water washes. Purification by flash chromatography (silica gel, 20 % chloroform in hexanes) afforded 191 mg of product (yellow solid, 50%).

^{1}H NMR (600 MHz, $CDCl_3$, δ): 8.07 (d, J = 7.9 Hz, 1 H), 8.05 (d, J = 8.1 Hz, 1 H), 7.55 (s, 1 H), 7.48 (m, 2 H), 7.39 (d, J = 8.1 Hz, 1 H), 7.35 (s, 1 H), 7.30 (d, J = 3.8 Hz, 1 H), 7.26 (m, 2 H), 6.88 (s, 1 H), 3.85 (s, 3 H), 2.74 (d, J = 6.7 Hz, 2 H), 1.64 (m, 1 H), 1.32–1.28 (m, 16 H), 0.93–0.87 (m, 6 H). ^{13}C (150 MHz, $CDCl_3$, δ): = 147.1, 144.7, 141.8, 141.5, 133.0, 131.5, 127.6, 127.0, 126.1, 123.1, 122.8, 122.7, 122.4, 121.4, 120.8, 120.5, 119.4, 117.5, 108.6, 105.8, 89.8, 82.0, 40.0, 34.8, 34.4, 33.3, 33.0, 32.0, 31.7, 29.8, 29.2, 29.0, 26.7, 25.4, 23.1, 22.8, 14.3.

2-(5-((2-Bromo-5-(2-butyloctyl)thiophen-3-yl)ethynyl)thiophen-2-yl)benzo[b]thiophene (**20**).

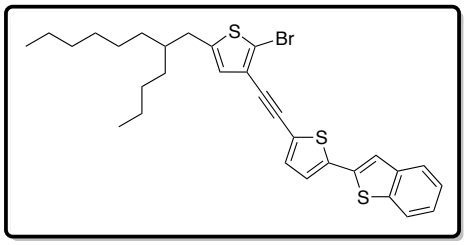

A 25-mL, 3-neck flask was charged with **18** (436 mg, 1.0 equiv., 0.889 *m*mol). The flask was evacuated and refilled with N_2 three times before dry THF (9 mL) was added, and the solution was cooled to -78 °C. *n*-BuLi (2.5 M in hexanes, 373 μL, 1.05 equiv., 0.933 *m*mol) was added dropwise to the reaction mixture, which was then stirred at -78 °C for 1.5 h. A dry THF (1.0 mL) solution of CBr_4 (354 mg, 1.2 equiv., 1.07 *m*mol) was then added to the reaction mixture over 15 min at -78 °C. The reaction mixture was then stirred at room temperature for 16 h before being diluted with diethyl ether. The organic layer was washed with brine twice, dried over $MgSO_4$ and filtered, and the solvent was removed by rotary evaporation to yield a brown oil. Purification by flash

chromatography (silica gel, 5 % chloroform in hexanes) afforded 322 mg of product (yellow solid, 64 %).

^{1}H NMR (400 MHz, $CDCl_3$, δ): 7.78 (d, *J* = 7.6 Hz, 1 H), 7.74 (d, *J* = 7.2 Hz, 1 H), 7.41 (s, 1 H), 7.35 (m, 2 H), 7.23 (d, *J* = 3.9 Hz, 1 H), 7.18 (d, *J* = 3.8 Hz, 1 H), 2.67 (d, *J* = 6.7 Hz, 2 H), 1.62 (m, 1 H), 1.37–1.22 (m, 16 H), 0.93–0.87 (m, 6 H). ^{13}C (100 MHz, $CDCl_3$, δ): = 145.1, 140.3, 139.3, 139.1, 136.5, 133.1, 127.3, 125.0, 125.0, 123.7, 123.3, 122.9, 122.3, 120.4, 114.4, 89.0, 85.5, 39.8, 34.8, 33.2, 32.9, 32.0, 29.7, 29.0, 26.7, 23.1, 22.8, 14.3. MALDI-TOF (*m/z*) $[M]^+$ calcd for $C_{30}H_{33}BrS_3$, 570.09; found, 569.06.

2-(5-((2-Bromo-5-(2-butyloctyl)thiophen-3-yl)ethynyl)thiophen-2-yl)-9-methyl-9H-carbazole (**21**).

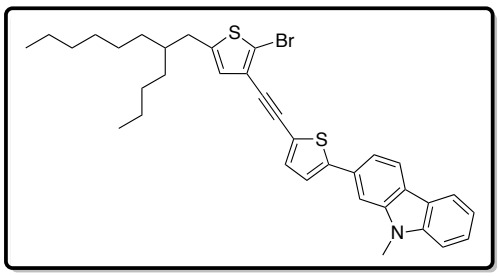

Reaction conditions were the same as for **18**, except **19** (190 mg, 1.0 equiv., 0.353 *m*mol), *n*-BuLi (2.5 M in hexanes, 155 μL, 1.1 equiv., 0.389 *m*mol), CBr_4 (140 mg, 1.2 equiv., 0.424 *m*mol) in 0.5 mL THF and THF (3.5 mL) were used. For the workup, the reaction mixture was diluted with diethyl ether instead of chloroform, and the organic layer was washed with brine twice. Purification by flash chromatography (silica gel, 20 % chloroform in hexanes) afforded 150 mg of product (light brown solid, 69 %).

^{1}H NMR (600 MHz, $CDCl_3$, δ): 8.07 (t, *J* = 8.7 Hz, 2 H), 7.57 (s, 1 H), 7.49 (m, 2 H), 7.40 (d, *J* = 8.1 Hz, 1 H), 7.31 (q, *J* = 3.8 Hz, 2 H), 7.26 (t, *J* = 7.4 Hz, 1 H), 6.71 (s, 1 H), 3.87 (s, 3 H), 2.68 (d, *J* = 6.7 Hz, 2 H), 1.60 (m, 1 H), 1.31–1.28 (m, 16 H), 0.95–0.88 (m, 6 H). ^{13}C (150 MHz, $CDCl_3$, δ): = 147.7, 145.1, 141.8, 141.5, 133.5, 131.5, 127.4, 126.2, 123.6, 123.1, 123.0, 122.7, 121.9, 120.9, 120.5, 119.4, 117.6, 114.0, 108.7, 105.8, 88.2, 86.1, 39.8, 34.9, 33.2, 32.9, 32.0, 29.7, 29.2, 29.0, 26.7, 23.1, 22.8, 14.3.

4,8-Bis(5-(benzo[b]thiophen-2-yl)thiophen-2-yl)-2,6-bis(2-butyloctyl)pentaleno[2,1-b:5,4-b']dithiophene (**2**).

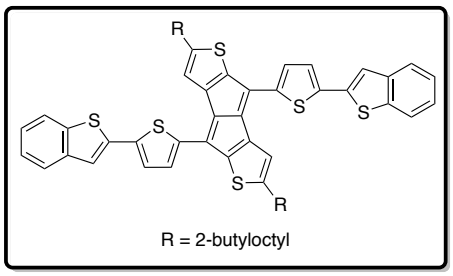

A 30-mL pressure tube was charged with **20** (75 mg, 1.0 equiv., 0.132 *m*mol), sodium ascorbate (52 mg, 2.0 equiv., 0.263 *m*mol), K_3PO_4 (56 mg, 2.0 equiv., 0.263 *m*mol), $Pd_2(dba)_3$ (1.81 mg, 1.5 mol%, 1.98 μmol), P(2-furyl)$_3$ (1.83 mg, 6.0 mol%, 7.90 μmol) and aliquat 336 (1 drop), and it was capped with a inverted septum. The tube was evacuated and refilled with N_2 three times while an oil bath was preheated to 130 °C. Upon addition of dioxane (freeze-pump-thawed, 1.3 mL) and distilled water (freeze-pump-thawed, 263 μL, dioxane:water = 5:1), the pressure tube was tightly sealed with an o-ring-lined Teflon® cap and immediately inserted into the preheated oil bath. The reaction mixture turned brown within 5 min of heating and was stirred at 130 °C for 16 h. After the reaction vessel was cooled to room temperature completely, the reaction mixture was diluted with chloroform. The organic layer was washed with water three times to remove all the salts, dried over $MgSO_4$ and filtered, and the solvent was removed by rotary evaporation to yield a black solid. The crude mixture was passed through a pad of neutral alumina topped with a layer of celite 545 to remove

any residual palladium (eluent: chloroform). The filtrate was concentrated, precipitated into hexanes and then filtered by vacuum filtration. The solid was purified by recrystallization (layered methanol on a chloroform solution of the solid), and the crystal suspension was filtered through a 0.22 μm Nylon membrane and washed with methanol to afford 19 mg of dark purple solid (29 %).

^{1}H NMR (600 MHz, $CDCl_3$, δ): 7.79 (d, J = 7.9 Hz, 2 H), 7.75 (d, J = 7.7 Hz, 2 H), 7.47 (s, 2 H), 7.36 (t, J = 7.1 Hz, 2 H), 7.33 (t, J = 7.0 Hz, 2 H), 7.28 (q, J = 4.1 Hz, 4 H), 6.63 (s, 2 H), 2.62 (d, J = 6.7 Hz, 4 H), 1.60 (m, 2 H), 1.33–1.25 (m, 32 H), 0.97–0.85 (m, 12 H). Anal. calcd for $C_{60}H_{66}S_6$: C, 73.57; H, 6.79; found: C, 73.33; H, 7.0.

2,2'-(5,5'-(2,6-Bis(2-butyloctyl)pentaleno[2,1-b:5,4-b']dithiophene-4,8-diyl)bis(thiophene-5,2-diyl))bis(9-methyl-9H-carbazole) (**3**). OL420.

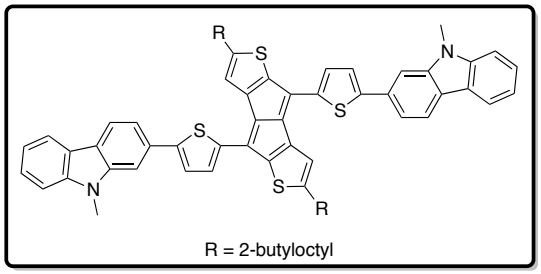

A 15-mL pressure tube was charged with **21** (150 mg, 1.0 equiv., 0.243 *m*mol), sodium ascorbate (96.3 mg, 2.0 equiv., 0.486 *m*mol), K_3PO_4 (103 mg, 2.0 equiv., 0.486 *m*mol), $Pd_2(dba)_3$ (3.34 mg, 1.5 mol%, 3.65 μmol), P(2-furyl)$_3$ (3.39 mg, 6.0 mol%, 14.6 μmol) and aliquat 336 (2 drops), and it was capped with a inverted septum. The tube was evacuated and refilled with N_2 three times while an oil bath was preheated to 130 °C. Upon addition of dioxane (freeze-pump-thawed, 2.4 mL) and distilled water (freeze-pump-thawed, 490 μL, dioxane:water = 5:1), the pressure tube was tightly sealed with an o-ring-lined Teflon® cap and immediately inserted into the preheated oil bath. The reaction mixture turned brown within 5 min of heating and was stirred at 130 °C for 16 h. After the reaction vessel was cooled to room temperature completely, the reaction mixture was diluted with chloroform. The organic layer was washed with water three times to remove all the salts, dried over $MgSO_4$ and filtered, and the solvent was removed by rotary evaporation to yield a black solid. The crude mixture was passed through a pad of neutral alumina topped with a layer of celite 545 to remove any residual palladium (eluent: chloroform). The filtrate was concentrated, precipitated into hexanes and then filtered by vacuum filtration. The solid was purified by recrystallization (layered methanol on a chloroform solution of the solid), and the crystal suspension was filtered through a 0.22 μm Nylon membrane and washed with methanol to afford 36 mg of dark purple solid (28 %).

^{1}H NMR (MHz, $CDCl_3$, δ): 8.09 (d, J = 8.0 Hz, 4 H), 7.62 (s, 2 H), 7.53 (d, J = 8.1 Hz, 2 H), 7.5 (m, 2 H), 7.42 (m, 4 H), 7.38 (d, J = 3.9 Hz, 2 H), 7.26 (m, 2 H), 6.71 (s, 2 H), 3.91 (s, 6 H), 2.63 (d, J = 6.7 Hz, 4 H), 1.62 (m, 2 H), 1.39–1.28 (m, 16 H), 0.91 (t, J = 6.4 Hz, 6 H), 0.86 (t, J = 6.4 Hz, 6 H).

Methyl 2-(5-(2-ethylhexanoyl)thiophen-2-yl)acetate (**12**). NB.

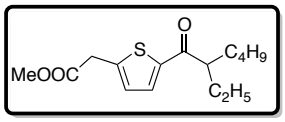

A 250-mL 3-neck flask was charged with **11** (2.90 g, 1.0 equiv., 18.57 *m*mol) and 2-ethylhexanoyl chloride (2.87 g, 0.95 equiv., 17.64 *m*mol), and the flask was evacuated and refilled with N_2 three times before 62 mL dry dichloromethane (DCM) was added. The solution of **11** was cooled to 0 °C, at which Sn(IV)Cl_4 (6.52 mL, 14.51 g, 3.0 equiv., 55.70 *m*mol) was added slowly to the reaction mixture over 10 min. Upon complete addition, the reaction mixture was warmed

to room temperature and stirred for another 2 h, after which 2 M HCl solution was added to quench the reaction. DCM was removed under reduced pressure, and the residue was redissolved in diethyl ether and washed with brine. The organic layer was isolated, dried over $MgSO_4$, and filtered. Upon removal of solvent, the remaining orange oil was purified by flash chromatography (silica gel, 1:1 chloroform:hexanes) to afford 3.83 g of light yellow oil (72.9 %).

^{1}H NMR (400 MHz, $CDCl_3$, δ): 7.57 (d, *J* = 4.9 Hz, 1 H), 6.97 (d, *J* = 4.0 Hz, 1 H), 3.85 (s, 2 H), 3.73 (s, 3 H), 3.07 (m, 1 H), 1.73 (m, 2 H), 1.52 (m, 2 H), 1.24 (m, 4 H), 0.84 (m, 6 H). ^{13}C (100 MHz, $CDCl_3$, δ): = 197.4, 170.1, 145.1, 144.1, 131.6, 128.2, 52.6, 49.7, 35.9, 32.3, 29.9, 26.0, 23.0, 14.0, 12.2. GC-MS (EI, *m/z*) $[M]^+$ calcd for $C_{15}H_{22}O_3S$, 282.13; found, 282.1.

Methyl 2-(5-(2-ethylhexyl)thiophen-2-yl)acetate (**13**). NB.

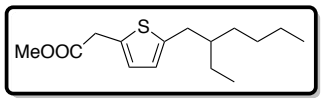

In a 100-mL RBF, **12** (3.83 g, 1.0 equiv., 13.5 *m*mol) was dissolved in 54 mL of trifluoroacetic acid. Under N_2 atmosphere, triethylsilane (4.32 mL, 3.15 g, 2.0 equiv., 27.09 *m*mol) was added to the solution over 5 min, and the reaction mixture turned yellow and cloudy. After 1.5 h, another 2 equiv. of triethylsilane was added because there was still residual starting material present, and the mixture was stirred at rt for 20 h. The reaction mixture was diluted with diethyl ether and neutralized carefully with $NaHCO_3$ solution. The organic layer was washed with distilled water twice, dried over $MgSO_4$, and filtered. Crude material was obtained upon removal of solvent, and subsequent purification by flash chromatography (silica gel, 10 % ethyl acetate in hexanes) afforded the desired product as 3.28 g of colorless oil (91 %)

^{1}H NMR (400 MHz, $CDCl_3$, δ): 6.72 (d, *J* = 3.6 Hz, 1 H), 6.59 (d, *J* = 3.2 Hz, 1 H), 3.77 (s, 2 H), 3.72 (s, 3 H), 2.69 (d, *J* = 6.8 Hz, 2 H), 1.54 (m, 1 H), 1.48–1.25 (m, 8 H), 0.89 (m, 6 H). ^{13}C (100 MHz, $CDCl_3$, δ): = 171.3, 144.4, 132.6, 126.5, 124.8, 52.3, 41.4, 35.6, 34.2, 32.5, 29.0, 25.6, 32.1, 14.3, 10.9. GC-MS (EI, *m/z*) $[M]^+$ calcd for $C_{15}H_{24}O_2S$, 268.15; found, 268.2.

4.4.2. Optical and Electrochemical Characterization

UV-vis spectral data were measured with Varian Cary 50 spectrophotometer. For extinction coefficient measurements, a stock solution of pentalene in chloroform was serially diluted, and spectra were collected from solutions of varying concentration in a quartz cuvette with a path-length of 1 cm. Since the concentration of each dilution is known, the extinction coefficient can be calculated based on Beer's Law.

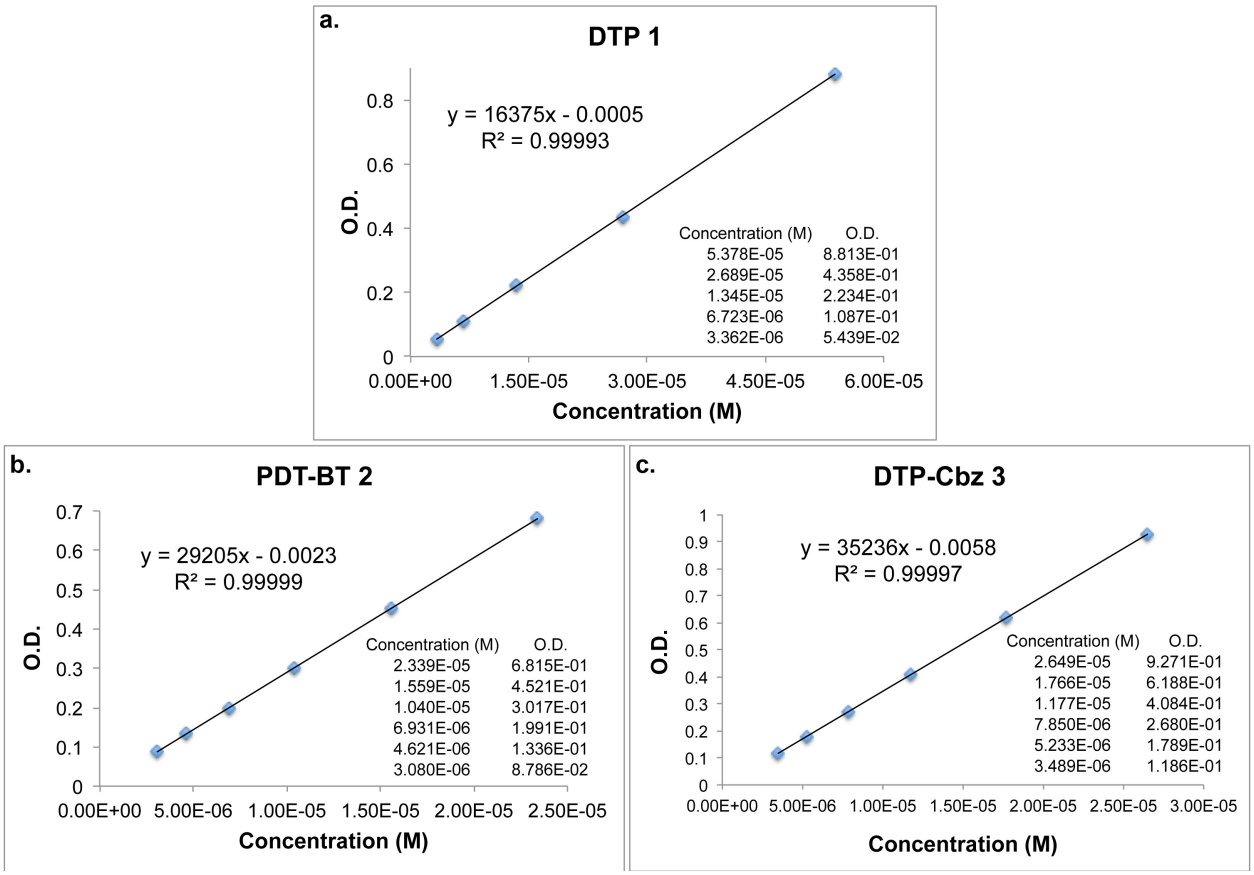

Figure 4-9. Extinction coefficient calculations and fits for (a) PDT **1**, (b) PDT-BT **2**, and (c) PDT-Cbz **3**.

Cyclic voltammograms were collected using a Solartron 1285 potentiostat under the control of CorrWare II software. A standard three electrode cell based on a Pt wire working electrode, a silver wire pseudo reference electrode (calibrated vs. Fc/Fc^{+}, which is assumed to have an absolute energy level of -5.13 eV to vacuum),[44] and a Pt wire counter electrode was purged with nitrogen and maintained under a nitrogen atmosphere during all measurements. Acetonitrile was purchased anhydrous from Aldrich and tetrabutylammonium hexafluorophosphate (0.1 M) was used as the supporting electrolyte. Small molecule films were drop cast onto a Pt wire working electrode from a 1% (w/w) chloroform solution and dried under nitrogen prior to measurement.

4.4.2. Acquisition and Analysis of Single-Crystal X-Ray Diffraction

A red needle 0.100 x 0.030 x 0.020 mm in size was mounted on a Cryoloop with Paratone oil. Data were collected in a nitrogen gas stream at 100(2) K using phi and omega scans. Crystal-to-detector distance was 60 mm and exposure time was 20 seconds per frame using a scan width of 1.0°. Data collection was 99.8% complete to 67.000° in θ. A total of 21074 reflections were

collected covering the indices, -41<=*h*<=41, -13<=*k*<=13, -9<=*l*<=7. 2891 reflections were found to be symmetry independent, with an R_{int} of 0.0659. Indexing and unit cell refinement indicated a C-centered, monoclinic lattice. The space group was found to be C 2/c (No. 15). The data were integrated using the Bruker SAINT software program and scaled using the SADABS software program. Solution by iterative methods (SHELXT) produced a complete heavy-atom phasing model consistent with the proposed structure. All non-hydrogen atoms were refined anisotropically by full-matrix least-squares (SHELXL-2013). All hydrogen atoms were placed using a riding model. Their positions were constrained relative to their parent atom using the appropriate HFIX command in SHELXL-2013.

Table 4-3. Crystal data and structure refinement for PDT **1**.

X-ray ID	PDT **1**	
Empirical formula	C36 H42 S4	
Formula weight	602.93	
Temperature	100(2) K	
Wavelength	1.54178 Å	
Crystal system	Monoclinic	
Space group	C 2/c	
Unit cell dimensions	a = 34.7631(11) Å	α= 90°.
	b = 11.4946(4) Å	β= 100.101(2)°.
	c = 8.0333(3) Å	γ = 90°.
Volume	3160.25(19) $Å^3$	
Z	4	
Density (calculated)	1.267 Mg/m^3	
Absorption coefficient	2.929 mm^{-1}	
F(000)	1288	
Crystal size	0.100 x 0.030 x 0.020 mm^3	
Crystal color/habit	red needle	
Theta range for data collection	2.582 to 68.504°.	
Index ranges	-41<=h<=41, -13<=k<=13, -9<=l<=7	
Reflections collected	21074	
Independent reflections	2891 [R(int) = 0.0659]	
Completeness to theta = 67.000°	99.8 %	
Absorption correction	Semi-empirical from equivalents	
Max. and min. transmission	0.929 and 0.735	
Refinement method	Full-matrix least-squares on F^2	
Data / restraints / parameters	2891 / 0 / 175	
Goodness-of-fit on F^2	1.044	
Final R indices [I>2sigma(I)]	R1 = 0.0637, wR2 = 0.1625	
R indices (all data)	R1 = 0.0886, wR2 = 0.1808	
Extinction coefficient	n/a	
Largest diff. peak and hole	0.474 and -0.453 e.$Å^{-3}$	

Table 4-4. Atomic coordinates (x 10^4) and equivalent isotropic displacement parameters ($Å^2$x 10^3) for PDT **1**. U(eq) is defined as one third of the trace of the orthogonalized U^{ij} tensor.

	x	y	z	U(eq)
C(1)	4481(1)	-4381(3)	8223(6)	41(1)
C(2)	4239(1)	-3828(3)	6985(5)	38(1)
C(3)	4284(1)	-2597(3)	7048(5)	28(1)
C(4)	4575(1)	-2248(3)	8393(5)	27(1)
C(5)	4696(1)	-1068(3)	8856(4)	24(1)
C(6)	5001(1)	-639(3)	10012(4)	23(1)
C(7)	4488(1)	-34(3)	8065(4)	25(1)
C(8)	4662(1)	986(3)	8730(4)	24(1)
C(9)	4453(1)	1985(3)	8047(5)	30(1)
C(10)	4127(1)	1718(3)	6901(5)	32(1)
C(11)	3834(1)	2533(4)	5904(6)	44(1)
C(12)	3424(2)	2415(7)	6182(9)	40(2)
C(13)	3139(3)	3148(9)	4899(13)	63(3)
C(14)	3140(6)	2923(18)	3180(20)	169(8)
C(15)	3393(3)	2739(10)	7995(12)	60(2)
C(16)	2997(4)	2027(13)	8440(20)	97(4)
C(17)	3042(4)	903(12)	8870(20)	104(4)
C(18)	2713(5)	264(14)	9170(20)	122(5)
C(12A)	3530(5)	2995(16)	6870(20)	84(5)
C(13A)	3196(7)	3720(20)	5780(30)	139(9)
C(14A)	3256(5)	4400(16)	4730(20)	94(5)
C(15A)	3355(4)	2132(15)	8039(19)	68(4)
C(16A)	3089(9)	2580(30)	8960(40)	162(11)
C(17A)	3011(7)	1540(20)	10310(30)	122(8)
C(18A)	2772(16)	900(50)	10660(80)	360(30)
S(1)	4776(1)	-3446(1)	9520(1)	36(1)
S(2)	4069(1)	226(1)	6649(1)	31(1)

Table 4-5. Bond lengths [Å] and angles [°] for PDT **1**

C(1)-C(2)	1.346(6)	C(14A)-H(14E)	0.9800
C(1)-S(1)	1.708(4)	C(14A)-H(14F)	0.9800
C(1)-H(1)	0.9500	C(15A)-C(16A)	1.38(3)
C(2)-C(3)	1.424(5)	C(15A)-H(15C)	0.9900
C(2)-H(2)	0.9500	C(15A)-H(15D)	0.9900
C(3)-C(4)	1.403(5)	C(16A)-C(17A)	1.66(3)
C(3)-H(3)	0.9500	C(16A)-H(16C)	0.9900
C(4)-C(5)	1.449(4)	C(16A)-H(16D)	0.9900
C(4)-S(1)	1.727(4)	C(17A)-C(18A)	1.18(6)
C(5)-C(6)	1.372(5)	C(17A)-H(17C)	0.9900
C(5)-C(7)	1.475(4)	C(17A)-H(17D)	0.9900
C(6)-C(8)#1	1.463(5)	C(18A)-H(18D)	0.9800
C(6)-C(6)#1	1.469(6)	C(18A)-H(18E)	0.9800
C(7)-C(8)	1.383(5)	C(18A)-H(18F)	0.9800
C(7)-S(2)	1.710(4)	C(2)-C(1)-S(1)	112.6(3)
C(8)-C(9)	1.416(5)	C(2)-C(1)-H(1)	123.7
C(8)-C(6)#1	1.463(5)	S(1)-C(1)-H(1)	123.7
C(9)-C(10)	1.366(5)	C(1)-C(2)-C(3)	113.1(4)
C(9)-H(9)	0.9500	C(1)-C(2)-H(2)	123.4
C(10)-C(11)	1.505(5)	C(3)-C(2)-H(2)	123.4
C(10)-S(2)	1.735(4)	C(4)-C(3)-C(2)	111.8(3)
C(11)-C(12)	1.487(8)	C(4)-C(3)-H(3)	124.1
C(11)-C(12A)	1.518(17)	C(2)-C(3)-H(3)	124.1
C(11)-H(11A)	0.9900	C(3)-C(4)-C(5)	127.1(3)
C(11)-H(11B)	0.9900	C(3)-C(4)-S(1)	110.3(2)
C(12)-C(15)	1.526(13)	C(5)-C(4)-S(1)	122.6(3)
C(12)-C(13)	1.548(12)	C(6)-C(5)-C(4)	131.7(3)
C(12)-H(12)	1.0000	C(6)-C(5)-C(7)	105.3(3)
C(13)-C(14)	1.40(2)	C(4)-C(5)-C(7)	123.0(3)
C(13)-H(13A)	0.9900	C(5)-C(6)-C(8)#1	143.1(3)
C(13)-H(13B)	0.9900	C(5)-C(6)-C(6)#1	110.5(4)
C(14)-H(14A)	0.9800	C(8)#1-C(6)-C(6)#1	106.4(4)
C(14)-H(14B)	0.9800	C(8)-C(7)-C(5)	111.7(3)
C(14)-H(14C)	0.9800	C(8)-C(7)-S(2)	111.8(2)
C(15)-C(16)	1.694(18)	C(5)-C(7)-S(2)	136.3(3)
C(15)-H(15A)	0.9900	C(7)-C(8)-C(9)	112.3(3)
C(15)-H(15B)	0.9900	C(7)-C(8)-C(6)#1	106.1(3)
C(16)-C(17)	1.340(18)	C(9)-C(8)-C(6)#1	141.5(3)
C(16)-H(16A)	0.9900	C(10)-C(9)-C(8)	112.8(3)
C(16)-H(16B)	0.9900	C(10)-C(9)-H(9)	123.6
C(17)-C(18)	1.414(18)	C(8)-C(9)-H(9)	123.6
C(17)-H(17A)	0.9900	C(9)-C(10)-C(11)	128.5(4)
C(17)-H(17B)	0.9900	C(9)-C(10)-S(2)	111.4(3)
C(18)-H(18A)	0.9800	C(11)-C(10)-S(2)	120.0(3)
C(18)-H(18B)	0.9800	C(12)-C(11)-C(10)	116.0(4)
C(18)-H(18C)	0.9800	C(10)-C(11)-C(12A)	114.3(7)
C(12A)-C(15A)	1.56(2)	C(12)-C(11)-H(11A)	108.3
C(12A)-C(13A)	1.57(3)	C(10)-C(11)-H(11A)	108.3
C(12A)-H(12A)	1.0000	C(12)-C(11)-H(11B)	108.3
C(13A)-C(14A)	1.20(3)	C(10)-C(11)-H(11B)	108.3
C(13A)-H(13C)	0.9900	H(11A)-C(11)-H(11B)	107.4
C(13A)-H(13D)	0.9900		
C(14A)-H(14D)	0.9800		

C(11)-C(12)-C(15)	110.6(6)	C(15A)-C(12A)-C(13A)	110.4(15)
C(11)-C(12)-C(13)	111.7(6)	C(11)-C(12A)-H(12A)	104.2
C(15)-C(12)-C(13)	111.0(7)	C(15A)-C(12A)-H(12A)	104.2
C(11)-C(12)-H(12)	107.8	C(13A)-C(12A)-H(12A)	104.2
C(15)-C(12)-H(12)	107.8	C(14A)-C(13A)-C(12A)	123(2)
C(13)-C(12)-H(12)	107.8	C(14A)-C(13A)-H(13C)	106.7
C(14)-C(13)-C(12)	116.2(11)	C(12A)-C(13A)-H(13C)	106.7
C(14)-C(13)-H(13A)	108.2	C(14A)-C(13A)-H(13D)	106.7
C(12)-C(13)-H(13A)	108.2	C(12A)-C(13A)-H(13D)	106.7
C(14)-C(13)-H(13B)	108.2	H(13C)-C(13A)-H(13D)	106.6
C(12)-C(13)-H(13B)	108.2	C(13A)-C(14A)-H(14D)	109.5
H(13A)-C(13)-H(13B)	107.4	C(13A)-C(14A)-H(14E)	109.5
C(13)-C(14)-H(14A)	109.5	H(14D)-C(14A)-H(14E)	109.5
C(13)-C(14)-H(14B)	109.5	C(13A)-C(14A)-H(14F)	109.5
H(14A)-C(14)-H(14B)	109.5	H(14D)-C(14A)-H(14F)	109.5
C(13)-C(14)-H(14C)	109.5	H(14E)-C(14A)-H(14F)	109.5
H(14A)-C(14)-H(14C)	109.5	C(16A)-C(15A)-C(12A)	117.1(19)
H(14B)-C(14)-H(14C)	109.5	C(16A)-C(15A)-H(15C)	108.0
C(12)-C(15)-C(16)	106.3(9)	C(12A)-C(15A)-H(15C)	108.0
C(12)-C(15)-H(15A)	110.5	C(16A)-C(15A)-H(15D)	108.0
C(16)-C(15)-H(15A)	110.5	C(12A)-C(15A)-H(15D)	108.0
C(12)-C(15)-H(15B)	110.5	H(15C)-C(15A)-H(15D)	107.3
C(16)-C(15)-H(15B)	110.5	C(15A)-C(16A)-C(17A)	107(2)
H(15A)-C(15)-H(15B)	108.7	C(15A)-C(16A)-H(16C)	110.4
C(17)-C(16)-C(15)	117.2(12)	C(17A)-C(16A)-H(16C)	110.4
C(17)-C(16)-H(16A)	108.0	C(15A)-C(16A)-H(16D)	110.4
C(15)-C(16)-H(16A)	108.0	C(17A)-C(16A)-H(16D)	110.4
C(17)-C(16)-H(16B)	108.0	H(16C)-C(16A)-H(16D)	108.6
C(15)-C(16)-H(16B)	108.0	C(18A)-C(17A)-C(16A)	143(4)
H(16A)-C(16)-H(16B)	107.2	C(18A)-C(17A)-H(17C)	101.1
C(16)-C(17)-C(18)	118.8(14)	C(16A)-C(17A)-H(17C)	101.1
C(16)-C(17)-H(17A)	107.6	C(18A)-C(17A)-H(17D)	101.1
C(18)-C(17)-H(17A)	107.6	C(16A)-C(17A)-H(17D)	101.1
C(16)-C(17)-H(17B)	107.6	H(17C)-C(17A)-H(17D)	104.5
C(18)-C(17)-H(17B)	107.6	C(17A)-C(18A)-H(18D)	109.5
H(17A)-C(17)-H(17B)	107.0	C(17A)-C(18A)-H(18E)	109.5
C(17)-C(18)-H(18A)	109.5	H(18D)-C(18A)-H(18E)	109.5
C(17)-C(18)-H(18B)	109.5	C(17A)-C(18A)-H(18F)	109.5
H(18A)-C(18)-H(18B)	109.5	H(18D)-C(18A)-H(18F)	109.5
C(17)-C(18)-H(18C)	109.5	H(18E)-C(18A)-H(18F)	109.5
H(18A)-C(18)-H(18C)	109.5	C(1)-S(1)-C(4)	92.19(19)
H(18B)-C(18)-H(18C)	109.5	C(7)-S(2)-C(10)	91.62(17)
C(11)-C(12A)-C(15A)	117.8(13)		
C(11)-C(12A)-C(13A)	114.4(15)		

Symmetry transformations used to generate equivalent atoms:
#1 -x+1,-y,-z+2

Table 4-6. Anisotropic displacement parameters ($Å^2 x\ 10^3$) for PDT **1**. The anisotropic displacement factor exponent takes the form: $-2\pi^2[\ h^2\ a^{*2}U^{11} + ...\ + 2\ h\ k\ a^*\ b^*\ U^{12}\ ]$

	U^{11}	U^{22}	U^{33}	U^{23}	U^{13}	U^{12}
C(1)	58(3)	18(2)	50(3)	-2(2)	15(2)	-6(2)
C(2)	51(2)	27(2)	38(2)	-11(2)	12(2)	-11(2)
C(3)	37(2)	21(2)	28(2)	0(1)	10(2)	-5(1)
C(4)	38(2)	20(2)	27(2)	-2(1)	11(2)	-1(1)
C(5)	37(2)	16(2)	23(2)	1(1)	12(1)	1(1)
C(6)	32(2)	18(2)	21(2)	1(1)	9(1)	0(1)
C(7)	31(2)	23(2)	23(2)	1(1)	7(1)	-1(1)
C(8)	32(2)	19(2)	23(2)	3(1)	8(1)	3(1)
C(9)	42(2)	21(2)	29(2)	4(2)	11(2)	5(2)
C(10)	38(2)	27(2)	34(2)	6(2)	13(2)	6(2)
C(11)	49(2)	38(2)	43(3)	9(2)	5(2)	17(2)
S(1)	48(1)	18(1)	42(1)	0(1)	6(1)	0(1)
S(2)	32(1)	30(1)	30(1)	3(1)	5(1)	1(1)

Table 4-7. Hydrogen coordinates (x 10^4) and isotropic displacement parameters ($Å^2$x 10^3) for PDT **1**.

	x	y	z	U(eq)
H(1)	4488	-5202	8361	50
H(2)	4056	-4219	6153	46
H(3)	4135	-2075	6273	34
H(9)	4532	2758	8355	36
H(11A)	3921	3341	6181	53
H(11B)	3838	2411	4686	53
H(12)	3348	1580	6008	48
H(13A)	2871	3019	5119	75
H(13B)	3202	3980	5116	75
H(14A)	2948	3424	2488	253
H(14B)	3073	2106	2939	253
H(14C)	3400	3082	2929	253
H(15A)	3361	3590	8099	72
H(15B)	3632	2496	8782	72
H(16A)	2905	2443	9376	117
H(16B)	2787	2083	7438	117
H(17A)	3243	857	9908	125
H(17B)	3150	501	7964	125
H(18A)	2793	-532	9502	184
H(18B)	2517	244	8130	184
H(18C)	2602	637	10071	184
H(12A)	3675	3577	7673	101
H(13C)	3003	3154	5202	167
H(13D)	3064	4158	6579	167
H(14D)	3007	4694	4109	141
H(14E)	3399	4012	3934	141
H(14F)	3412	5050	5270	141
H(15C)	3227	1492	7327	82
H(15D)	3574	1788	8842	82
H(16C)	2842	2784	8205	194
H(16D)	3195	3283	9584	194
H(17C)	3225	993	10212	147
H(17D)	3096	1937	11407	147
H(18D)	2869	541	11756	537
H(18E)	2718	293	9790	537
H(18F)	2532	1333	10709	537

4.5. References

(1) Hains, A. W.; Liang, Z.; Woodhouse, M. A.; Gregg, B. A. *Chem. Rev.* **2010**, 110, 6689.
(2) Grätzel, M.; Janssen, R. A. J.; Mitzi, D. B.; Sargent, E. H. *Nature* **2012**, *488*, 304.
(3) Cheng, Y.-J.; Yang, S.-H.; Hsu, C.-S. *Chem. Rev.* **2009**, *109*, 5868.
(4) Wang, C.; Dong, H.; Hu, W.; Liu, Y.; Zhu, D. *Chem. Rev.* **2011**, *111*, 3358.
(5) Murphy, A. R.; Fréchet, J. M. J. *Chem. Rev.* **2007**, *107*, 1066.
(6) Bendikov, M.; Wudl, F.; Perepichka, D. F. *Chem. Rev.* **2004,** *104*, 4891.
(7) Huitema, H. E. A.; Gelinck, G. H.; van der Putten, J. B. P. H.; Kuijk, K. E.; Hart, C. M.; Cantatore, E.; Herwig, P. T.; van Breemen, A. J. J. M.; de Leeuw, D. M. *Nature* **2001**, *414*, 599.
(8) Hatchett, D. W.; Josowicz, M. *Chem. Rev.* **2008,** *108*, 746.

(9) Aratani, N.; Kim, D.; Osuka, A. *Acc. Chem. Res.* **2009**, *42*, 1922.
(10) Fukuzumi, S. *Phys. Chem. Chem. Phys.* **2008**, *10*, 2283.
(11) Gettinger, C. L.; Heeger, A. J.; Drake, J. M.; Pine, D. J. *J. Chem. Phys.* **1994**, *101*, 1673.
(12) Lowe, J. P.; Kafafi, S. A. *J. Am. Chem. Soc.* **1984**, *106*, 5837.
(13) Brédas, J.-L. *J. Phys. Chem.* **1985**, *82*, 3808.
(14) Hoffman, R. *Angew. Chem. Int. Ed. Engl.* **1987**, *26*, 846.
(15) Kertesz, M.; Choi, C. H.; Yang, S. *Chem. Rev.* **2005,** *105*, 3448.
(16) Roncali, J. *Macromol. Rapid Commun.* **2007**, *28*, 1761.
(17) Gompper, R.; Wagner, H.-U. *Angew. Chem. Int. Ed. Engl.* **1988**, *27*, 1437.
(18) Walker, B.; Kim, C.; Nguyen, T.-Q. *Chem. Mater.* **2011**, *23*, 470.
(19) Brédas, J.-L.; Heeger, A. J.; Wudl, F. *J. Chem. Phys.* **1986**, *85*, 4673.
(20) Levi, Z. U.; Tilley, T. D. *J. Am. Chem. Soc.* **2009**, *131*, 2796.
(21) Levi, Z. U.; Tilley, T. D. *J. Am. Chem. Soc.* **2010**, *132*, 11012.
(22) Kawase, T.; Konishi, A.; Hirao, Y.; Matsumoto, K.; Kurata, H.; Kubo, T. *Chem. Eur. J.* **2009**, *15*, 2653.
(23) Zhang, H.; Karasawa, T.; Yamada, H.; Wakamiya, A.; Yamaguchi, S. *Org. Lett.* **2009**, *11*, 3076.
(24) Saito, M. *Symmetry* **2010**, *2*, 950.
(25) Wang, D.; Michinobu, T. *J. Polym. Sci. A: Polym. Chem.* **2011**, *49*, 72.
(26) Xu, F.; Peng, L.; Orita, A.; Otera, J. *Org. Lett.* **2012**, *14*, 3970.
(27) Konishi, A.; Fujiwara, T.; Ogawa, N.; Hirao, Y.; Matsumoto, K.; Kurata, H.; Kubo, T.; Kitamura, C.; Kawase, T. *Chem. Lett.* **2010**, *39*, 300.
(28) Yin, X.; Li, Y.; Zhu, Y.; Kan, Y.; Li, Y.; Zhu, D. *Org. Lett.* **2011**, *13*, 1520.
(29) Chakraborty, M.; Tessier, C. A.; Youngs, W. J. *J. Org. Chem.* **1999**, *64*, 2947.
(30) Willner, I.; Rabinovitz, M. *J. Am. Chem. Soc.* **1978**, *100*, 337.
(31) Kawase, T.; Fujiwara, T.; Kitamura, C.; Konishi, A.; Hirao, Y.; Matsumoto, K.; Kurata, H.; Kubo, T.; Shinamura, S.; Mori, H.; Miyazaki, E.; Takimiya, K. *Angew. Chem. Int. Ed.* **2010**, *49*, 7728.
(32) Frisch, M. J.; Trucks, G. W.; Schlegel, H. B.; Scuseria, G. E.; Robb, M. A.; Cheeseman, J. R.; Scalmani, G.; Barone, V.; Mennucci, B.; Petersson, G. A.; Nakatsuji, H.; Caricato, M.; Li, X.; Hratchian, H. P.; Izmaylov, A. F.; Bloino, J.; Zheng, G.; Sonnenberg, J. L.; Hada, M.; Ehara, M.; Toyota, K.; Fukuda, R.; Hasegawa, J.; Ishida, M.; Nakajima, T.; Honda, Y.; Kitao, O.; Nakai, H.; Vreven, T.; Montgomery, Jr., J. A.; Peralta, J. E.; Ogliaro, F.; Bearpark, M.; Heyd, J. J.; Brothers, E.; Kudin, K. N.; Staroverov, V. N.; Kobayashi, R.; Normand, J.; Raghavachari, K.; Rendell, A.; Burant, J. C.; Iyengar, S. S.; Tomasi, J.; Cossi, M.; Rega, N.; Millam, J. M.; Klene, M.; Knox, J. E.; Cross, J. B.; Bakken, V.; Adamo, C.; Jaramillo, J.; Gomperts, R.; Stratmann, R. E.; Yazyev, O.; Austin, A. J.; Cammi, R.; Pomelli, C.; Ochterski, J. W.; Martin, R. L.; Morokuma, K.; Zakrzewski, V. G.; Voth, G. A.; Salvador, P.; Dannenberg, J. J.; Dapprich, S.; Daniels, A. D.; Farkas, Ö.; Foresman, J. B.; Ortiz, J. V.; Cioslowski, J.; Fox, D. J. Gaussian 09, Revision C.01.
(33) Schnürch, M.; Spina, M.; Khan, A. F.; Mihovilovic, M. D.; Stanetty, P. *Chem. Soc. Rev.* **2007**, *36*, 1046.
(34) Bossi, M.; Belov, V.; Polyakova, S.; Hell, S. W. *Angew. Chem. Int. Ed.* **2006**, *45*, 7462.
(35) Hedenström, E.; Nguyen, B.-V.; Silks, L. A. *Tetrahedron: Asymmetry* **2002**, *13*, 835.
(36) Yang, J.; Lakshmikantham, M. V.; Cava, M. P. *J. Org. Chem.* **2000**, *65*, 6739.
(37) Thompson, B. C.; Fréchet, J. M. J. *Angew. Chem. Int. Ed.* **2008**, *47*, 58.

Chapter V

Ester-Functionalized Oxadiazolopyridine (ODP) as an Electron-Deficient Comonomer in Semiconducting Polymers for Efficient Organic Solar Cells

5.1. Introduction: Development of New Building Blocks via Atomic Substitution

Organic photovoltaics (OPVs) have emerged as an alternative technology to current silicon-based systems for harvesting solar energy.[1,2] The solution-processability of conjugated materials offers the potential for scalable, low-cost production of lightweight, flexible OPV devices.[3–5] In particular, high-performing organic solar cells consist of a bulk-heterojunction (BHJ) architecture, where p- and n-type materials form an interpenetrating network within the device active layer. Since the first report of BHJ solar cells in 1995,[6,7] the power conversion efficiencies of OPVs have recently surpassed 8% due to the development of active layer material, use of novel interlayers, and alteration of device configuration.[8–15]

In terms of molecular design requirements, an ideal polymer for OPVs should display high extinction coefficients in the visible region while having energy levels aligned with those of the n-type materials, typically fullerene derivatives. Strong absorption with redshifted onset (i.e. narrow band gap) optimizes the solar flux harvested, and a 0.3 eV energy level offset with fullerenes ensures sufficient driving force for excitons dissociation.[1,2] Both of these characteristics contribute to the short-circuit current density (J_{SC}) of a solar cell. Furthermore, achieving a high device open-circuit voltage (V_{OC}) requires a large energetic difference between the polymer's HOMO and the fullerene's LUMO. These optical and electronic properties can be controlled and tuned by functionalizing the conjugated polymer backbone with electron-donating and -withdrawing groups.[16,17] In addition, the processability, solubility, and solid-state packing are typically modulated by the design of alkyl substituents. The length and steric bulk of side-chains can significantly influence the backbone π-π stacking distances and correlation lengths, both of which are important metrics for efficient carrier transport.[18–21]

It has been demonstrated by several groups that simple atomic substitution (carbon vs. silicon vs. germanium; oxygen vs. sulfur vs. selenium) in conjugated building blocks can dramatically affect solubility and packing of the resulting conjugated polymers or small molecules.[22–26] Recently, our group has investigated the effect of substituting furan for thiophene on the intrinsic properties of the conjugated polymers and its impact on OPV device performance.[27] We discovered that this substitution dramatically alters the solubility of the resulting polymers but has little effect on their electronics. In contrast, replacing sulfur with oxygen in benzothiadiazole, an electron-poor comonomer, has shown to lower the frontier molecular orbital (FMO) energy levels of several low band gap polymers due to the greater electronegativity of oxygen.[28]

Surveying the structures of high-performing materials shows that both benzothiadiazole and its derivative thiadiazolopyridine are promising electron-deficient building blocks. Specifically, thiadiazolopyridine has been incorporated into polymers with PCEs above 6% and small molecules with PCEs reaching 6.7%.[29,30] Due to the electron-deficient nature of pyridine, materials containing thiadiazolopyridine are expected to exhibit energy levels lower than those of benzothiadiazole-based materials and perform with an imrpoved device V_{OC}. Leclerc and coworkers first investigated these effects in polymers containing 2,7-carbazole as the donor comonomer, and they correlated the atomic substitution to the polymer electronic properties and subsequently to device performance.[28] While these electron-poor monomers show great promise, they bear no solubilizing groups, thereby hindering the synthesis of high-M_n polymers and limiting the processability of these materials. In order to ensure the synthesis of solution-processable, high-molecular-weight polymers, the electron-donating monomer must then be functionalized with large bulky solubilizing groups. Thus, we designed an ester-functionalized oxadiazolopyridine (R-ODP) as the acceptor monomer for our polymers. The ester functionality

is electron withdrawing, allows for simple, modular installation of solubilizing groups, and has shown to be an effective substitution in other high-performing materials such as PBDTTT.[31,32]

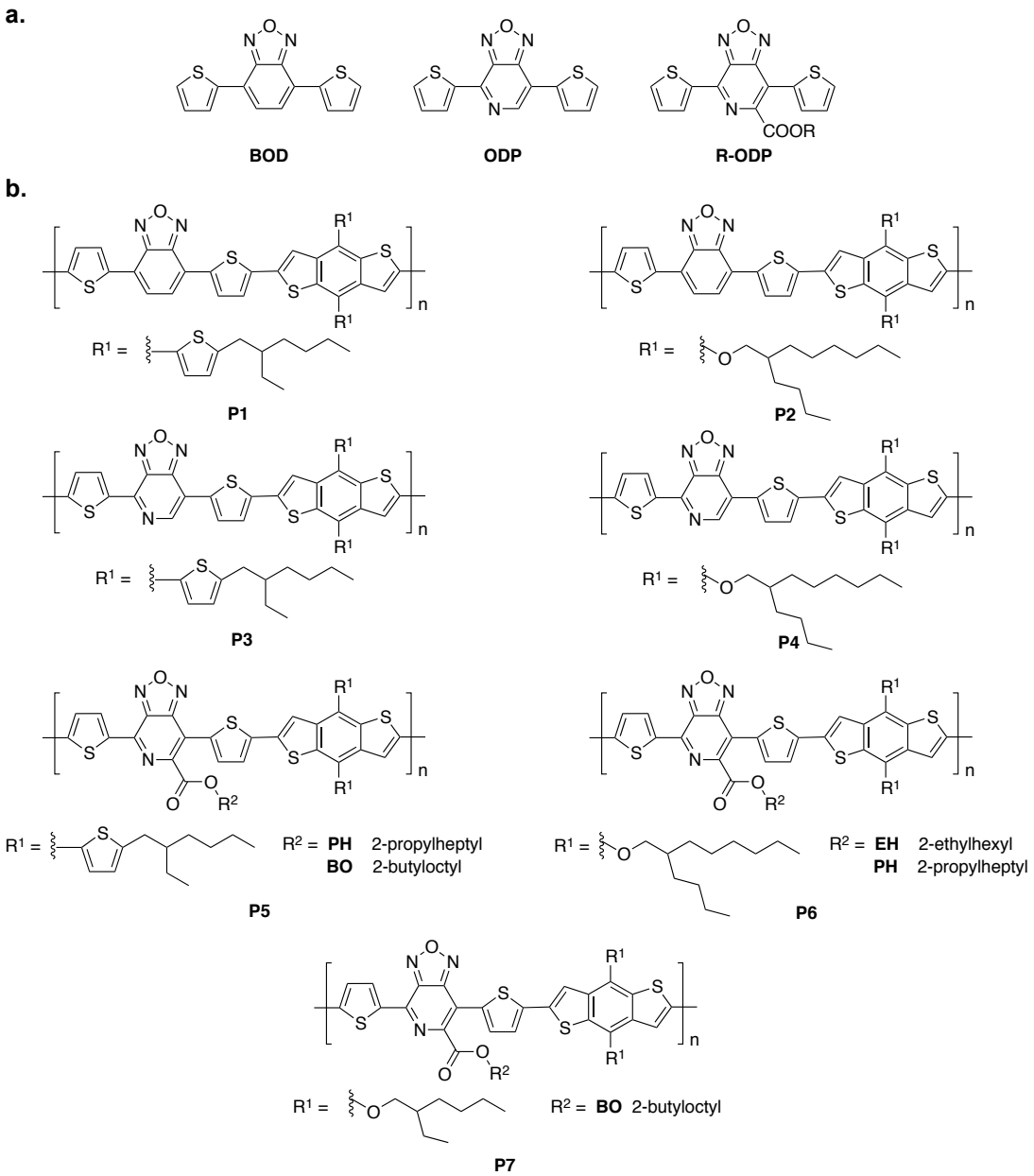

Figure 5-1. (a) Structures of benzooxadiazole (BOD), oxadiazolopyridine (ODP), and ester-functionalized ODP (R-ODP), where R can be hexadecyl (C16), 2-ethylhexyl (EH), 2-propylheptyl (PH) or 2-butyloctyl (BO). (b) Structures of the polymer series synthesized in this work. (b) Structures of polymers synthesized in this work.

Herein, we report the synthesis, characterization, and solar cell performance of conjugated polymers containing benzodithiophene (BDT) as the donor monomer and either benzooxadiazole (BOD) or oxadiazolopyridine (ODP) as the acceptor monomer (Figure 5-1). The ODP monomer is also functionalized with various solubilizing ester functional groups to impart sufficient solubility to the final copolymers. The planarity and relative energy levels of the copolymers were estimated by density functional theory (DFT) calculations. Geometry optimization of the

representative polymer trimers reveals that the ester group causes the backbone to twist in **P5**–**P7** while **P1**–**P4** are expected to be completely planar. Characterization of the copolymers by ultraviolet-visible (UV-vis) spectroscopy and cyclic voltammetry (CV) shows that changing the acceptor comonomer from BOD to ODP leads to a reduction of the HOMO energy level and decrease in the band gap. In solar cells, **P2** exhibits low device PCE, and **P1**, **P3**, and **P4** do not possess sufficient solubility for functional devices. However, the solubility of **P5**–**P7** can be tuned by the size of the ester group, and OPV devices containing these copolymers show moderate to high performance. In particular, copolymer **P5-BO** was able to achieve a PCE of 8% with $PC_{71}BM$ in regular BHJ device architecture after side-chain optimization of both the BDT and ODP monomers. In addition, gold and silver nanoparticles were embedded in the hole-transporting interlayer, PEDOT:PSS, to enhance light absorption *via* surface plasmon resonance as an attempt to further improve OPV device performance.

5.2. Molecular Designs, Synthesis and Optoelectronic Characterization

5.2.1. Choice of Electron-Rich Comonomer and Material Synthesis

For copolymerization with our acceptor monomers, BDT was selected because the fused benzene ring can increase aromatic stabilization and lower the HOMO energy level. Several reports have demonstrated that copolymers containing BDT often show high device V_{OC}, some of which approach 1 eV.[11,33–36] Due to the large, planar structure of BDT, many of BDT-based materials exhibit face-on packing in thin films where the π-π stacking direction orients out of plane relative to the substrate, favoring charge transport in OPV devices. In this work, we investigated for BDT substituted with either alkoxy or alkylthienyl groups as side chains.[37]

The syntheses of unfunctionalized BOD and ODP comonomers have been reported;[28] by modifying the published procedure, the R-ODP monomer can be synthesized in a straightforward, scalable, modular fashion (Scheme 5-1).[38] Briefly, 2-acetylthiophene was oxidatively dimerized in acidic conditions to yield *N*-oxide **1**, which was subsequently reduced by zinc to **2**. A condensation between **2** and ethyl glycinate enabled the cyclization to form the pyridine ring in **3**, and the reaction was performed with a large excess of the glycinate over 4 days to ensure complete consumption of **2**. In the penultimate step, **3** was be functionalized with various alkyl alcohols through acid catalyzed transesterification, and subsequent bromination of **5** with *N*-bromosuccinimide (NBS) afforded the desired monomer **6**. The advantage of this procedure is that the transesterification step not only allows for a variety of alcohol to be installed in the late stage of the synthesis but also enables the substitution of other functional groups such as amide groups. Note that the bromination step can be switched with esterification to further improve the modularity of this route, though the yield for brominating the ethyl ester **3** is relatively low.

Using $Pd_2(dba)_3$/P(*o*-tol)$_3$ as the catalytic system, Stille polycondensation between **6** and distannylated BDT in chlorobenzene afforded copolymers **P1**–**P7**. Note that all polymers were synthesized with an imbalanced comonomer ratio, where 0.97 equivalent of the stannylated BDT was used (**6** : BDT = 1.0 : 0.97) in order to achieve polymers with high molecular weights. Size-exclusion chromatography (SEC, eluent: chloroform), was performed to determine the molecular weight (M_n and M_w) and polydispersity index (PDI) of each material. Copolymers **P1**–**P4** exhibited very limited solubility in chloroform and could not be characterized; the data acquired for **P5**–**P7** are listed in Table 5-1.

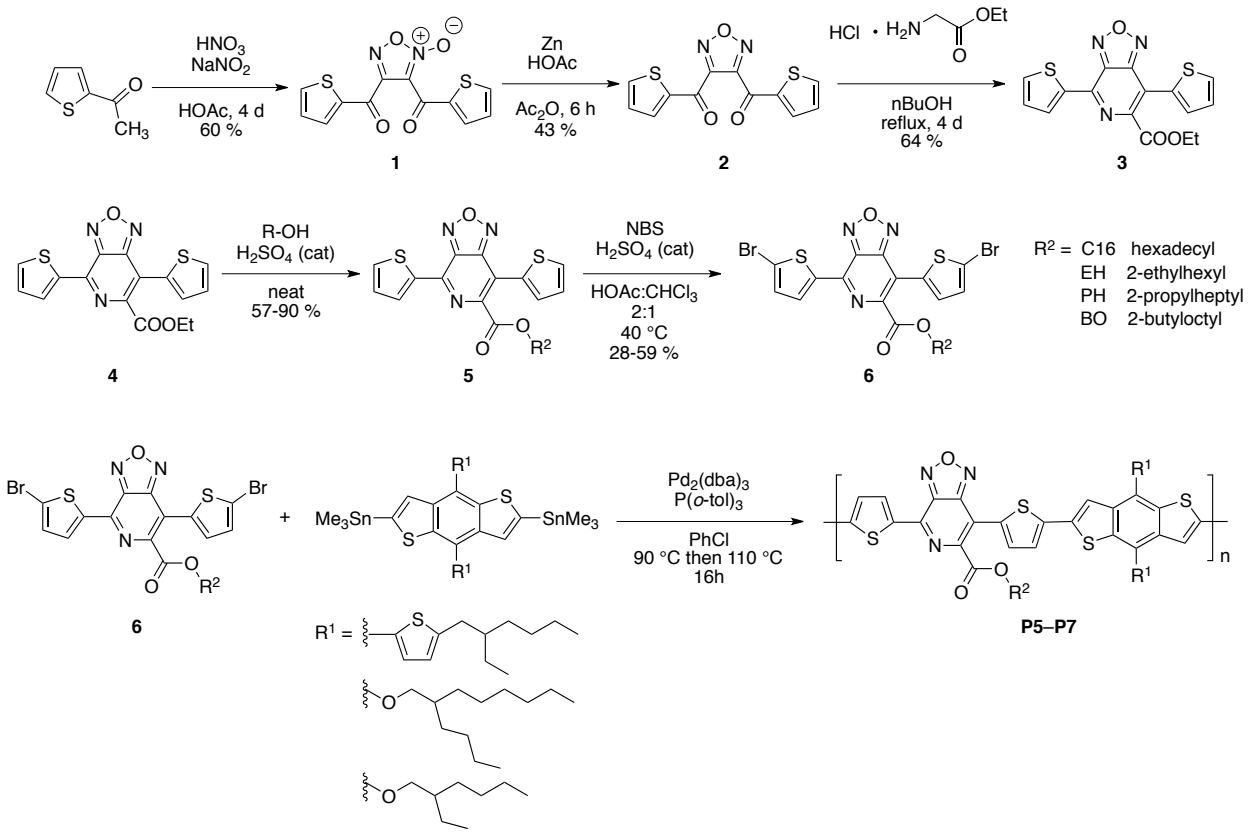

Scheme 5-1. (a) Structures of the electron-deficient monomers investigated in this work: benzooxadiazole (BOD), oxadiazolopyridine (ODP), and ester-functionalized ODP (R-ODP). (b) Route for the synthesis of R-ODP monomers and polymerization conditions.

Table 5-1. Chloroform SEC determined molecular weights of **P5**–**P7**.

polymer[a]	M_n (kDa)	M_w (kDa)	PDI
P5-PH	61.6	132.8	2.16
P5-BO	61.3	183.2	2.99
P6-EH	112.2	258.6	2.30
P6-PH	94.7	198.2	2.09
P7-BO	85.4	235.6	2.76

[a]Molecular weights of polymers **P1**–**P4** do not exhibit sufficient solubility for measurements by SEC.

5.2.2. Assessment of Molecular Geometry by DFT Calculations

Density functional theory (DFT) calculations were used to assess the planarity of each polymer backbone, and geometry optimization was performed on the representative trimers of **P1**–**P6** (**P7** has the same backbone and BDT substitution pattern as **P6**) using the B3LYP hybrid functionals and the 6-31G(d,p) basis set.[39] Table 5-2 lists the dihedral angles between each ring as shown; because the ODP portion of the monomer is asymmetric, the dihedral angle about the bond at the pyridine C2 (a) is listed separately from the angle about the bond at the pyridine C5 position (a'). The trimer backbones of **P1**–**P4** are nearly coplanar between the acceptor monomer and the thiophene π-bridge with dihedral angles < 0.6° (a and a') while there is a slight twist between the π-bridge and the BDT moiety (< 5 °). In contrast, **P5** and **P6**/**P7** show increase

backbone twisting about all of the bonds, and the dihedral angle a' is the largest (> 23°). This result suggests that steric interactions between the ester group and the adjacent thiophene cause the backbone to rotate out of plane. While deviation from planarity may reduce the extent of orbital overlap along the conjugated system and strong intermolecular interactions, the backbone twisting, along with the ester substituents, is likely to impart additional solubility to the polymers.

Table 5-2. Inter-ring dihedral angle based on DFT calculations using B3LYP/6-31G (d,p). Note that a and a' are structurally identical in each of P1 and P2 trimers because BOD is symmetrical.

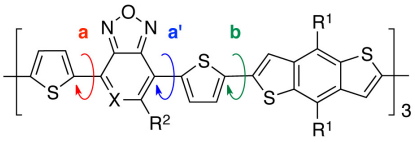

P1 trimer R^1 = 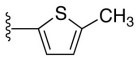 R^2 = H X = C

P2 trimer R^1 =  R^2 = H X = C

P3 trimer R^1 = 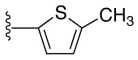 R^2 = H X = N

P4 trimer R^1 =  R^2 = H X = N

P5 trimer R^1 = 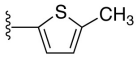 R^2 = COOMe X = N

P6/P7 trimer R^1 =  R^2 = COOMe X = N

trimer	dihedral angles around inter-ring bonds (°)			energy levels (eV)		
	a/a'		b	HOMO	LUMO	band gap
P1	0.357		3.064	-2.98	-4.93	1.95
P2	0.570		1.183	-3.04	-5.01	1.97
	a	a'	b			
P3	0.205	0.091	4.445	-3.20	-5.01	1.81
P4	0.137	0.530	1.543	-3.27	-5.10	1.83
P5	0.595	23.858	6.330	-3.33	-5.07	1.74
P6/P7	0.651	23.060	8.589	-3.39	-5.15	1.76

The frontier molecular orbital (FMO) energy levels of the trimers were also estimated by DFT caculations, with B3LYP/6-31G(d,p) parameters, to provide insight into the effect of nitrogen substitution and ester functionalization on the electronics of trimers. As expected, replacing the fused benzene with pyridine lowers both HOMO and LUMO energy levels (**P1** vs. **P3**, **P2** vs. **P4**) since pyridine is more electronegative than benzene. Moreover, this atomic substitution shows a greater influence on the LUMO levels than on the HOMO levels because the LUMOs in donor-acceptor materials tend to localize on the electron-poor moieties. The attachment of an ester group to the ODP monomer further lowers the FMO energy levels due to the electron-withdrawing nature of C=O by resonance (**P3** vs. **P5**, **P4** vs. **P6**/**P7**). Since the LUMO energy levels decrease faster than HOMO levels with increasingly electron-deficient monomers, the band gap of the trimer become narrower from BOD to ODP then to R-ODP. In addition, two polymers with the same acceptor unit shows a difference in the FMO levels because of the substituents on the BDT momnomer, and upon comparison, trimers functionalized with methylthienyl groups exhibit higher energy levels than those substituted with alkoxy groups (**P1** vs. **P2**, **P3** vs. **P4**, **P5** vs. **P6**/**P7**). These tends will be experimentally evaluated by electrochemical characterization.

5.2.3. Electrochemical and Optical Characterization

Cyclic voltammetry was performed to determine the HOMO and LUMO energy levels of **P1**–**P7**. As predicted by DFT calculations, replacing benzene with pyridine slightly lowers the HOMO level and significantly reduces the LUMO level, and the band gaps decrease by 0.24 eV from **P1** to **P3** and by 0.15 eV from **P2** to **P4**. Attachment of an ester to the ODP monomer also leads to a decrease in the LUMO energy levels of the polymers, except for those substituted with 2-butyloctyl esters. Compared to **P3** and **P4**, the ester-bearing derivatives **P5** and **P6**/**P7** also show reduced band gaps, respectively. One interesting observation is that substituting 2-propylheptyl (PH) ester with 2-butyloctyl (BO) ester leads to an increase in the LUMO energy level by > 0.1 eV. It has been shown by the You group that side-modulations can influence intermolecular interactions in films and subsequently alter the energy levels of bulk materials.[40] Thus, these differences between the LUMOs of PH- and BO-substituted polymers may indicate a change in the solid-state packing of the polymers.

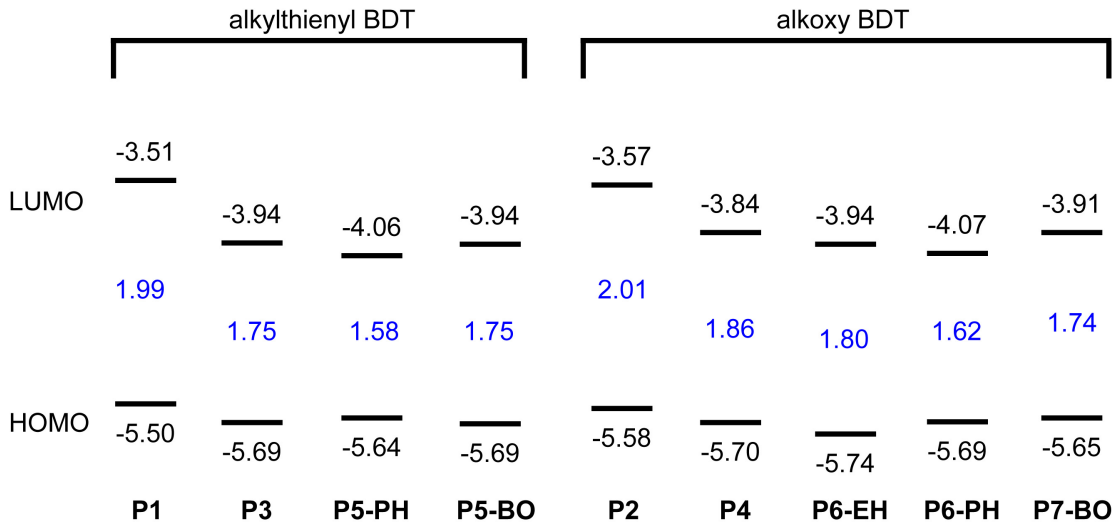

Figure 5-3. HOMO and LUMO energy level diagram of **P1**–**P7** in the unit of eV, and the electrochemical band gap of each polymer is listed (blue text) between the two energy levels in eV. All values were determined by cyclic voltammetry (CV).

To determine the absorption range of **P1**–**P7**, the polymers were characterized by solution and solid-state UV-visble (UV-vis) spectroscopy (Figure 5-4). All of the polymers exhibit broad absorption that covers a large portion the visible spectrum, ensuring effective collection of the solar flux. The absorption onsets of the polymers do not change much from solution to thin films, suggesting the formation of polymer aggregates in chloroform; thus, these spectra are obtained from polymer suspensions instead of solutions. Note that all polymer suspension in chloroform were filtered through a 0.45 μm PTFE syringe filter prior to measurement, except for **P2** in chloroform, which formed aggregates larger than 450 nm and could not be filtered.

The effects of atomic substitution and ester-functionalization on polymer absorption are more evident in Figure 5-4 b and d. In agreement with CV measurements, replacement of the BOD moiety with ODP moiety redshifts the polymer absorption onsets, indicating a decrease in the band gaps. However, spectrum of **P4** shows an energy onset lower than those of **P6-EH**, **P6-PH** and **P7-BO**, all three of which show similar absorption profiles. Compared to **P6** and **P7**, the electron-deficient ODP moiety in **P4** bears no solubilizing groups that can prevent strong

intermolecular interactions in aggregates or films; moreover, the backbone of **P4** is much more planar than the twisted backbones of **P6** and **P7**, as determined from the DFT calculations. This difference in planarity can lead to significant overlap between the π-systems of P4, and the absorption redshift can be due to intermolecular electronic transitions.

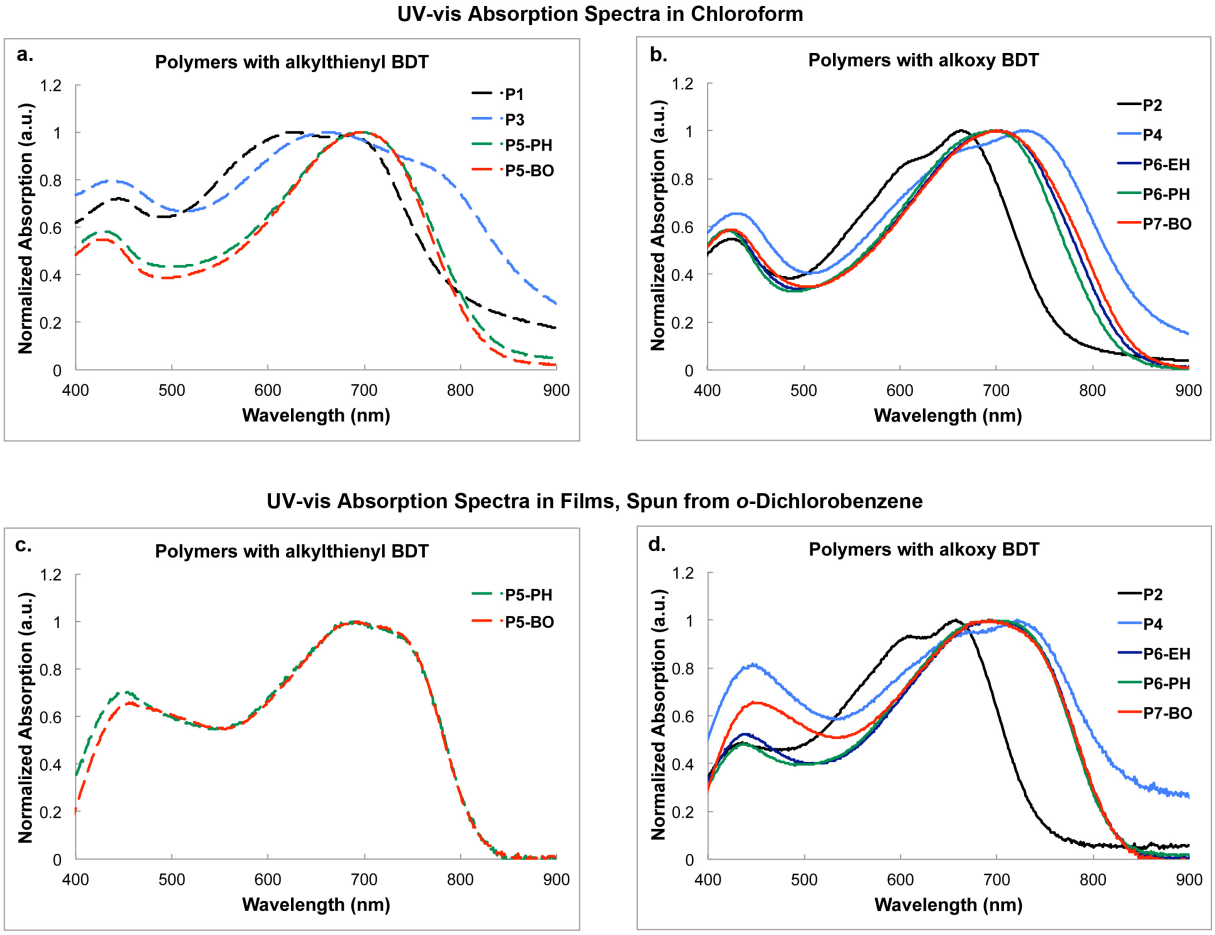

Figure 5-4. UV-visible absorption profiles of **P1**–**P7** in chloroform (top) and in thin films (bottom). For clarity, spectra presented in (a) and (c) are for polymers containing 2-ethylhexylthienyl-BDT as the donor monomer, and spectra present in (b) and (d) are for polymers containing alkoxy-BDT as the donor monomer. Note that thin-film spectra of **P1** and **P3** are not shown due to their low solubility in *o*-dichlorobenzene, and the resulting films were too thin for absorption measurements.

5.3. Solar Cell Performance

Organic solar cells were fabricated from **P2** and **P5**–**P7** with regular bulk-heterojucntion device architecture: ITO/PEDOT:PSS/polymer:$PC_{71}BM$/Al, where a LiF interlayer was inserted between the active layer and Al electrode for some of the polymers. Polymers **P1**, **P3** and **P4** could not be processed into functional OPV devices due to their limited solubility in *o*-dichlorobenzene at 180 °C. Representative current-voltage (*J*-*V*) plots of the best performing devices are shown in Figure 5-5, and Table 5-3 summarizes the processing and performance parameters for optimized devices.

Table 5-3. Device processing[a] and performance parameters of optimized devices.

Polymer	p-:n-types[b]	electrode	additive (% v/v)	V_{OC} (V)	J_{SC} (mA/cm^2)	FF	PCE_{avg} (%)	PCE_{max} (%)
P2	1:2	LiF/Al	none	0.60	-5.59	0.42	1.4	1.4
P5-PH	1:3.5	LiF/Al	none	0.86	-12.71	0.56	6.2	6.3
P5-BO	1:3.5	LiF/Al	none	0.90	-13.61	0.58	7.1	8.0
P6-EH	1.2	Al	none	0.75	-11.56	0.37	3.2	4.2
P6-PH	1:3	LiF/Al	0.3% ODT[d]	0.83	-9.49	0.61	4.8	5.3
P7-BO[c]	1:2	Al	none	0.85	-9.39	0.53	4.3	5.0

[a]Details about the specific processing concentrations for each material can be found in the Experimental section. [b]polymer:$PC_{71}BM$ ratio in the blend solution. [c]Devices were annealed at 180 °C in the glovebox for 5 min after the Al electrode deposition. [d]ODT = 1,8-octanedithiol.

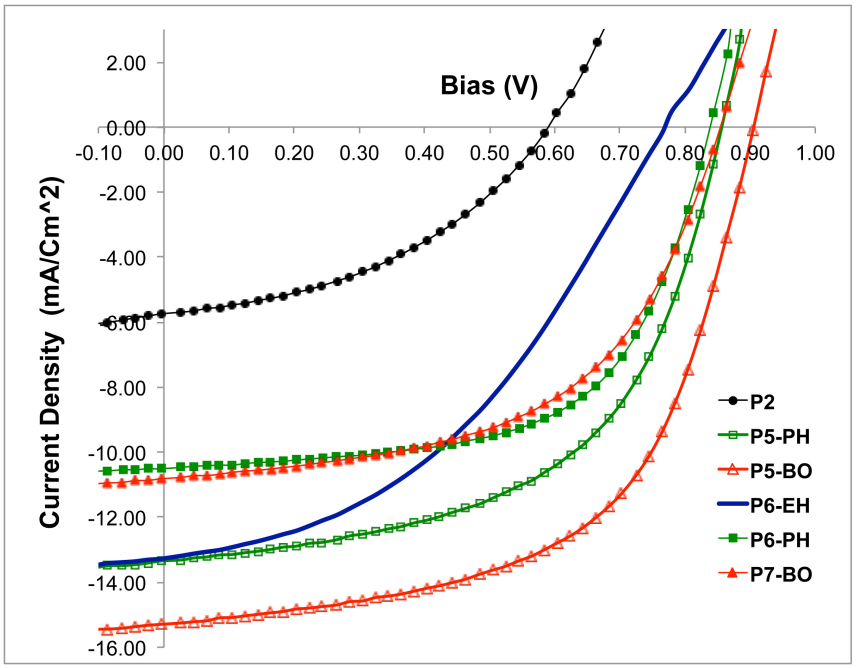

Figure 5-5. Representative J-V plots of **P2**, **P5-PH**, **P5-BO**, **P6-EH**, **P6-PH**, and **P7-BO**.

OPV devices frabricated from **P5-BO** perform the best, demonstrating V_{OC}, J_{SC}, and PCE of 0.90 V, -13.61 mA/cm^2, and 8.0% (average 7.1%), respectively. In contrast, solar cells containing **P2** show the lowest current density and efficiency, which may be partly attributed to its limited and processability; films spun from **P2** tend to be very thin, which is unfavorable for light absorption. **P2** also shows a much lower V_{OC} value than all of the other ODP polymers (0.6 V vs. 0.75–0.90 V). This low V_{OC} is expected because the HOMO energy level of **P2** is at -5.58 eV, which is the highest in the series.

For all R-ODP-based polymers, the electronegative nitrogen atom in the pyridine ring not only lowers their HOMO levels but also significantly stabilizes their LUMOs, allowing for redshifted absorption spectra strong light absorption by the active layer. As a result, all of these solar cells exhibit J_{SC} values above 10 mA/cm^2. Furthermore, since **P5**–**P7** exhibit similar absorption spectra, any difference in the measured current densities may be attributed to the nanostructural order and intrinsic hole mobility of the active layer.

In addition to J_{SC}, the extent of intermolecular interactions may also affect the device V_{OC} of **P5**–**P7** even though they bear the same conjugated backbone. With the same donor monomer,

P5-BO exhibits higher V_{OC} than **P5-PH**, and **P6-PH** shows higher V_{OC} than **P6-EH**. It has been demonstrated that strong intermolecular interactions between polymer backbones can lead to reduced V_{OC} by increasing the rate of charge recombination at the polymer-fullerene interface.[40–42] It has also been shown that large, bulky side chains disrupt π-π interactions between polymers.[20,36] Since 2-butyloctyl group is more sterically demanding than 2-propylheptyl group, we hypothesize that the backbone of **P5-BO** interact with each other more weakly than do the backbone of **P5-PH**, thereby limiting intermolecular interactions and enhancing device V_{OC}. Morphology characterization, including atomic force microscopy and grazing-incidence X-ray diffraction, will be performed in the near future to elucidate the origin of this V_{OC} difference.

Close examination of the device performance parameters also reveals that solar cells fabricated from **P5**–**P7** seem to exhibit relatively low fill-factors (FFs) when compared to other high-performing polymers. Sources that limit FF include imbalanced charge transport, high charge recombination, and inefficient charge extraction at the electrodes.[43–48] During device optimization, it was found that the use of LiF interlayer dramatically improves the device performance of **P5-BO**, **P5-PH**, and **P6-PH** by raising the fill factors. This observation suggests that electron injection into the cathode is inefficient with Al alone as the electrode. For the fabrication of **P5-BO**-based solar cells, it was found that adding a small amount (0.3% v/v) of 1,8-octanedithiol (ODT) in the polymer:$PC_{71}BM$ blend solution also yielded devices with high efficiency, where V_{OC} = 0.87 V, J_{SC} = -14.48 mA/cm^2, FF = 0.64, and PCE = 7.2 % (8.0 % max).

5.4. Plasmon-Enhanced OPV Device Performance—Preliminary Results

Recently, localized surface plamon resonance (LSPR) has been exploited to improve the efficiency of OPV device light absorption.[8,12,13,49] By embedding plasmonic nanostructures into the PEDOT:PSS layer, OPV devices were shown to achieve PCEs well above 8% due to enhanced J_{SC} and FF. Inspired by these reports, we incorporated gold and silver nanoparticles (NPs), each with two different sizes (40 nm and 50 nm), into solar cells fabricated with our champion polymer **P5-BO** under the optimized processing condition. Preliminary results are summarized in Table 5-4, and representative *J-V* curve of the best-performing devices under each condition is shown in Figure 5-6.

Table 5-4. Plasmon-enhanced OPV devices fabricated from **P5-BO**.

Particle	size (nm)	conc. (μg/mL)	V_{OC} (V)	J_{SC} (mA/cm^2)	FF	PCE_{avg} (%)	PCE_{max} (%)
none[a] (control)	--	--	0.90	-12.4	0.59	6.6	6.7
gold	40	10	0.90	-13.0	0.62	7.2	8.4
gold	50	30	0.90	-12.6	0.61	6.7	7.6
silver	40	10	0.90	-12.0	0.61	6.6	7.1
silver	50	10	0.90	-12.6	0.60	6.9	7.2
none (record)	--	--	0.90	-13.6	0.58	7.1	8.0

[a]These devices were fabricated along with the rest of the NP-containing solar cells so that the effect of plasmonic enhancement can be determined. [b]Performance of the best-performing devices are shown here for reference.

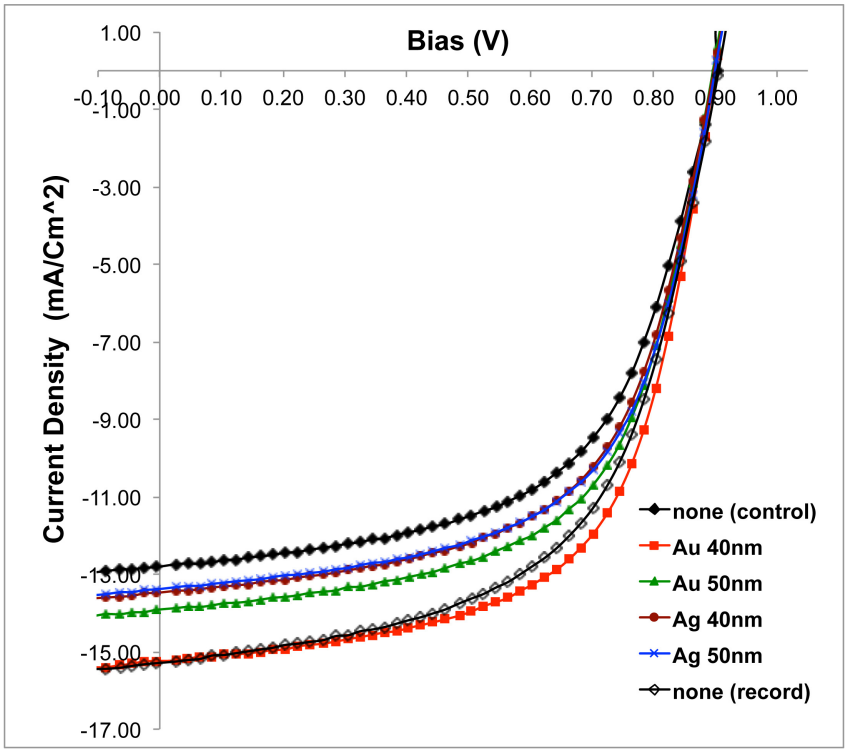

Figure 5-6. Representative J-V plots of plasmonic-enhanced **P5-BO**-containing solar cells.

Within the device series fabricated at the same time (first 5 entries in Table 5-4), solar cells with PEDOT:PSS:Au/Ag layers all performed at higher efficiencies than the control cells as a result of increased J_{SC} and FF. The improvement of current density is expected because of LSPR from the nanoparticles, and the enhanced FF can be attributed a decrease in the series resistance in the solar cells.[12] External quantum efficiency (EQE) spectra of these devices will be obtained in the future to show the spectral regions with increased absorption due to plasmonic resonance.

5.5. Conclusion

In summary, we have developed ester-functionalized oxadiazolopyridine (R-ODP) as an acceptor monomer for conjugated polymers with high OPV performance. Compared to the analogous benzooxadiazole, the replacement of benzene with pyridine significantly stabilizes the frontier molecular orbital energy levels. Furthermore, the attachment of an ester group can impart solubility by providing alkyl side chains and by slightly twisting the polymer backbone out of plane. The efficient, scalable synthetic route also enables modular functionalization of alkyl esters with various lengths and bulk. Copolymerization of benzodithiophene and R-ODP yields solution-processable polymers with high OPV performance. In particular, BHJ solar cells fabricated with **P5-BO** and $PC_{71}BM$ achieved a maximum PCE of 8.0%. We further demonstrate that the OPV performance of **P5-BO** can be improved to 8.4% efficiency by incorporating it in devices where plasmonic nanoparticles are embedded in the PEDOT:PSS layer. The localized surface plasmon resonance of gold and silver nanoparticles induces a local field enhancement that improves device light absorption, subsequently raising J_{SC}, FF, and PCE.

Immediate future work for this project includes morphology characterization of the active layer by AFM and GIXS, along with EQE measurements to determine the effect of plasmonic

enhancement provided by the incorporation of Au and Ag nanoparticles. Other future projects can explore the effects of various functionalities attached to the ODP monomer since side chains can be appended to ODP at late stage of the monomer synthesis via transeserification. Potential functionalities include alkene-, bromide-, or CF_3-terminated alcohols. Substitution of ester with amide may also influence the electronics and OPV device performance of ODP-containing copolymers.

5.6. Experimental

5.6.1. Synthetic Materials and Methods

All commercially available reagents obtained from suppliers were used without further purification. Unless otherwise noted, all reactions were carried out under nitrogen with standard Schlenk techniques, and all glassware used in dry reactions were flame dried under high-vacuum prior to use. All organic extracts were dried over magnesium sulfate ($MgSO_4$) powder, and solvents were removed under reduced pressure with a rotary evaporator. *N*-Bromosuccinimide (NBS) was recrystallized in distilled water before use. Bezodithiphene comonomers, (4,8-bis(5-(2-ethylhexyl)thiophen-2-yl)benzo[1,2-*b*:4,5-*b′*]dithiophene-2,6-diyl)bis(trimethylstannane) (**EHTBDT**) and (4,8-bis((2-ethylhexyl)oxy)benzo[1,2-*b*:4,5-*b′*]dithiophene-2,6-diyl)bis(trimethylstannane) (**EHOBDT**), were purchased from SunaTech Inc and used without further purification. Flash chromatography was performed using Silicycle SiliaFlash ® P60 (particle size 40-63 μm, 230-400 mesh) silica gel.

All ^1H and ^{13}C NMR spectra were obtained in chloroform-*d*, unless otherwise noted, with a Bruker AV-600 instrument. ^{13}C spectra were measured with a proton-decoupling pulse program. All chemical shifts (ppm) were calibrated to the residual peak of the deuterated solvent. Matrix-assisted laser desorption/ionization-time of flight mass spectrometry (MALDI-TOF MS) was performed on a Applied Biosystems Voyager-DE BioSpectrometry Workstation using 2,2':5',2''-terthiophene as the matrix. Samples were prepared by diluting the monomers in chloroform with the matrix. Elemental analysis (CHN) was performed by the UC Berkeley microanalysis laboratory.

5.6.2. Monomer Syntheses and Characterization

(4,8-Bis((2-butyloctyl)oxy)benzo[1,2-b:4,5-b']dithiophene-2,6-diyl)bis(trimethylstannane) (**BOOBDT**).

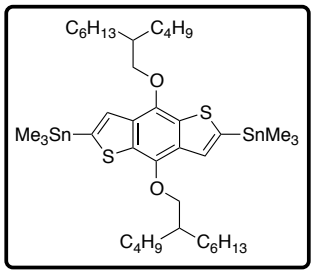

Synthesized following the procedures reported in reference 50.

Ethyl 4,7-di(thiophen-2-yl)-[1,2,5]oxadiazolo[3,4-c]pyridine-6-carboxylate (**4**).

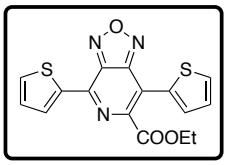

Synthesized following the procedures reported in reference 38.

Dodecyl 4,7-di(thiophen-2-yl)-[1,2,5]oxadiazolo[3,4-c]pyridine-6-carboxylate (**5-C12**).

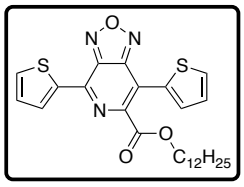

A 25-mL RBF attached to a condenser was charged with ester **4** (198 mg, 1.0 equiv., 0.560 *m*mol), dodecanol (5.6 mL, 0.1 M) and 5 drops of conc. H_2SO_4. The reaction mixture was heated at 120 °C for 16 h before being neutralized with saturated $NaHCO_{3(aq)}$. Brine was added to the crude materials and extracted with chloroform 3 times. The organic layer was dried over $MgSO_4$ and filtered, and the solvent was removed under reduced pressure by rotary evaporation. The orange residue was purified by flash chromatography (silica gel, 60 % chloroform in hexanes), and removal of solvent from the product fractions yielded orange oil containing residual dodecanol. Product was recrystallized from ethanol to afford 210 mg of orange solid (76 %).

^{1}H NMR (MHz, $CDCl_3$, δ): 8.57 (d, *J* = 3.8 Hz, 1 H), 7.71 (m, 2 H), 7.59 (d, *J* = 5.1 Hz, 1 H), 7.29 (dd, *J* = 3.8, 5.0 Hz, 1 H), 7.20 (dd, *J* = 3.7, 5.1 Hz, 1 H), 4.36 (t, *J* = 6.6 Hz, 2 H), 1.66 (m, 2 H), 1.30-1.23 (m, 18 H), 0.88 (t, *J* = 7.0 Hz, 3 H). ^{13}C (150 MHz, $CDCl_3$, δ): 166.8, 150.6, 145.7, 143.8, 140.0, 133.8, 133.3, 132.7, 130.7, 129.5, 129.3, 128.1, 113.2, 66.8, 32.1, 29.82, 29.78, 29.72, 29.65, 29.5, 29.4, 28.4, 25.9, 22.8, 14.3. MALDI-TOF MS (*m/z*): $[M]^-$ calcd for $C_{26}H_{31}N_3O_3S_2$, 497.18; found, 497.26. Anal. calcd for $C_{26}H_{31}N_3O_3S_2$: C, 62.75; H, 6.28; N, 8.44; found: C, 62.98; H, 6.36; N, 8.26.

Hexadecyl 4,7-di(thiophen-2-yl)-[1,2,5]oxadiazolo[3,4-c]pyridine-6-carboxylate (**5-C16**).

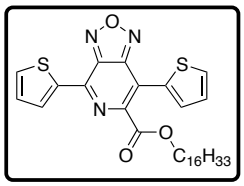

A 25-mL RBF attached to a condenser was charged with ester **4** (250 mg, 1.0 equiv., 0.699 *m*mol) and 1-hexadecanol (2.8g, *d* = 0.811 g/mL, 0.1 M), and the mixture was heated at 80 °C. When all hexadecanol melted, 5 drops of conc. H_2SO_4 were added to the solution. The reaction mixture was heated at 120 °C for 16 h before cooled down to room temperature. The solidified reaction mixture was dissolved in chloroform with gentle heating and loaded directly onto a column; the crude material was purified by flash chromatography (silica gel, 50 % chloroform in hexanes). Removal of solvent and subsequent recrystallization (ethanol) afforded 222 mg of orange solid (57 %).

^{1}H NMR (MHz, $CDCl_3$, δ): 8.57 (d, *J* = 3.9 Hz, 1 H), 7.71 (m, 2 H), 7.59 (d, *J* = 5.1 Hz, 1 H), 7.29 (dd, *J* = 3.8, 5.0 Hz, 1 H), 7.20 (dd, *J* = 3.7, 5.1 Hz, 1 H), 4.36 (t, *J* = 6.6 Hz, 2 H), 1.65 (m, 2 H), 1.30-1.23 (m, 26 H), 0.88 (t, *J* = 7.0 Hz, 3 H). ^{13}C (150 MHz, $CDCl_3$, δ): 166.6, 150.4, 145.5, 143.54, 143.53, 139.7, 133.6, 133.1, 132.5, 130.5, 129.3, 129.1, 127.9, 113.0, 66.6, 36.3, 31.89, 29.7, 29.64, 29.63, 29.61, 29.53, 29.46, 29.3, 29.2, 28.2, 25.7, 22.7, 14.1. MALDI-TOF MS (*m/z*): $[M]^-$ calcd for $C_{30}H_{39}N_3O_3S_2$, 553.24; found, . Anal. calcd for $C_{30}H_{39}N_3O_3S_2$: C, 65.07; H, 7.10; N, 7.59; found: C, 65.00; H, 7.13; N, 7.46.

2-Ethylhexyl 4,7-di(thiophen-2-yl)-[1,2,5]oxadiazolo[3,4-c]pyridine-6-carboxylate (**5-EH**).

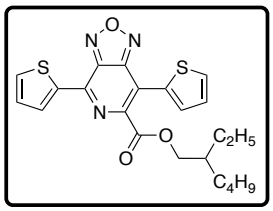

A 25-mL RBF attached to a condenser was charged with ester **4** (400 mg, 1.0 equiv., 1.12 *m*mol), 2-ethyl-1-hexanol (5.6 mL, 0.2 M) and 10 drops of conc. H_2SO_4. The reaction mixture was heated at 100 °C for 16 h before being diluted with chloroform and neutralized with saturated $NaHCO_{3(aq)}$. The organic layer was washed with saturated $NaHCO_{3(aq)}$ twice, washed with brine 3 times, dried over $MgSO_4$ and filtered. The solvent was removed under reduced pressure by rotary evaporation. The orange residue was purified by flash chromatography (silica gel, 50 % chloroform in hexanes), and removal of solvent afforded 444 mg of orange oil that subsequently crystallized into a solid (90 %).

^{1}H NMR (600 MHz, $CDCl_3$, δ): 8.56 (d, J = 3.8 Hz, 1 H), 7.70 (m, 2 H), 7.58 (d, J = 5.0 Hz, 1 H), 7.28 (dd, J = 3.8, 5.0 Hz, 1 H), 7.20 (d, J = 3.7, 5.1 Hz, 1 H), 4.27 (at, J = 6.05 Hz, 2 H), 1.60 (m, 1 H), 1.32-1.24 (m, 8 H), 0.87 (m, 6 H). ^{13}C (150 MHz, $CDCl_3$, δ): 167.0, 150.6, 145.6, 143.7, 140.0, 133.7, 133.3, 132.7, 130.6, 129.5, 129.3, 128.1, 113.2, 69.0, 38.7, 30.3, 29.0, 23.7, 23.1, 14.2, 11.1. MALDI-TOF MS (*m/z*): $[M]^-$ calcd for $C_{22}H_{23}N_3O_3S_2$, 441.12; found, 441.15. Anal. calcd for $C_{22}H_{23}N_3O_3S_2$: C, 59.84; H, 5.25; N, 9.52; found: C, 59.98; H, 5.46; N, 9.45.

2-Propylheptyl 4,7-di(thiophen-2-yl)-[1,2,5]oxadiazolo[3,4-c]pyridine-6-carboxylate (**5-PH**).

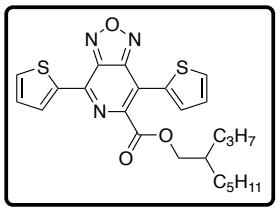

A 25-mL RBF attached to a condenser was charged with ester **4** (600 mg, 1.0 equiv., 1.68 *m*mol), 2-propyl-1-heptanol (6 mL) and 5 drops of conc. H_2SO_4. The reaction mixture was heated at 120 °C for 16 h. Upon cooling to room temperature, the reaction mixture was loaded directly onto a column; the crude material was purified by flash chromatography (silica gel, 50 % chloroform in hexanes). Removal of solvent and subsequent recrystallization (ethanol) afforded 763 mg of orange solid (97%).

^{1}H NMR (600 MHz, $CDCl_3$, δ): 8.55 (d, J = 3.7 Hz, 1 H), 7.70 (m, 2 H), 7.58 (d, J = 5.0 Hz, 1 H), 7.27 (dd, J = 4.0, 4.8 Hz, 1 H), 7.20 (d, J = 3.7, 5.1 Hz, 1 H), 4.26 (d, J = 5.7 Hz, 2 H), 1.68 (m, 1 H), 1.29-1.24 (m, 12 H), 0.87 (m, 6 H). ^{13}C (150 MHz, $CDCl_3$, δ): 166.96, 150.58, 145.59, 143.69, 143.67, 139.94, 133.68, 133.24, 132.71, 130.58, 129.47, 129.30, 128.07, 113.17, 69.37, 37.10, 33.39, 32.25, 31.05, 26.47, 22.74, 19.95, 14.52, 14.24. MALDI-TOF MS (*m/z*): $[M]^-$ calcd for $C_{24}H_{27}N_3O_3S_2$, 469.15; found, 469.6. Anal. calcd for $C_{24}H_{27}N_3O_3S_2$: C, 61.38; H, 5.79; N, 8.95; found: C, 61.29; H, 5.94; N, 8.62.

2-Butyloctyl 4,7-di(thiophen-2-yl)-[1,2,5]oxadiazolo[3,4-c]pyridine-6-carboxylate (**5-BO**).

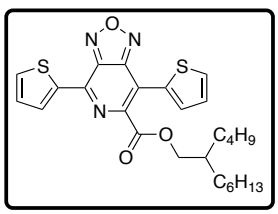

A 25-mL RBF attached to a condenser was charged with ester **4** (800 mg, 1.0 equiv., 2.24 *m*mol), 2-butyl-1-octanol (10 mL) and 5 drops of conc. H_2SO_4. The reaction mixture was heated at 120 °C for 16 h. Upon cooling to room temperature, the reaction mixture was loaded directly onto a column; the crude material was purified by flash chromatography (silica gel, 50 % chloroform in hexanes). Removal of solvent and subsequent recrystallization (ethanol) afforded 772 mg of orange solid (69 %).

^{1}H NMR (600 MHz, $CDCl_3$, δ): 8.55 (d, J = 3.7 Hz, 1 H), 7.70 (m, 2 H), 7.58 (d, J = 4.9 Hz, 1 H), 7.27 (dd, J = 4.1, 5.0 Hz, 1 H), 7.20 (d, J = 3.8, 4.0 Hz, 1 H), 4.27 (d, J = 5.8 Hz, 2 H), 1.67

(m, 1 H), 1.30-1.24 (m, 16 H), 0.87 (m, 6 H). ^{13}C (150 MHz, $CDCl_3$, δ): 166.96, 150.56, 145.56, 143.67, 143.66, 139.93, 133.66, 133.22, 132.71, 130.58, 129.46, 129.29, 128.06, 113.14, 69.36, 37.30, 31.94, 31.10, 30.77, 29.73, 28.98, 26.77, 23.09, 22.80, 14.23, 14.21. MALDI-TOF MS (*m/z*): $[M]^-$ calcd for $C_{26}H_{31}N_3O_3S_2$, 497.18; found, 497.7. Anal. calcd for $C_{26}H_{31}N_3O_3S_2$: C, 62.75; H, 6.28; N, 8.44; found: C, 60.96; H, 6.05; N, 7.69.

Dodecyl 4,7-bis(5-bromothiophen-2-yl)-[1,2,5]oxadiazolo[3,4-c]pyridine-6-carboxylate (**6-C12**).

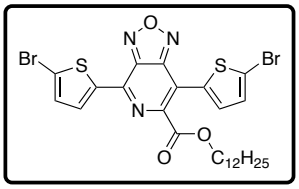

A 25-mL RBF attached to a condenser was charged with ester **5-C12** (170 mg, 1.0 equiv., 0.342 *m*mol), NBS (152 mg, 2.5 equiv., 0.854 *m*mol), 2:1 acetic acid (2.4 mL):chloroform (1.2 mL) mixture and 5 drops of conc. H_2SO_4. The reaction mixture turned dark red and was heated at 40 °C for 16 h before it was diluted with chloroform. The organic layer was washed with saturated $NaHCO_{3(aq)}$ 3 times, washed with water twice, dried over $MgSO_4$ and filtered. Solvent was removed under reduced pressure by rotary evaporation to yield an orange residue, which was then purified by flash chromatography (silica gel, 50 % chloroform in hexanes). Removal of solvent and subsequent recrystallization (ethanol:chloroform) afforded 123 mg of orange solid (55 %). Note that the workup/extraction step may be skipped; see synthesis for **6-PH** or **6-BO**.

^{1}H NMR (600 MHz, $CDCl_3$, δ): 8.29 (d, *J* = 4.1 Hz, 1 H), 7.48 (d, *J* = 4.0 Hz, 1 H), 7.25 (d, *J* = 4.2 Hz, 1 H), 7.16 (d, *J* = 4.0 Hz, 1 H), 4.38 (t, *J* = 6.5 Hz, 2 H), 1.70 (m, 2 H), 1.31-1.26 (m, 18 H), 0.87 (t, *J* = 7.0 Hz, 3 H). ^{13}C (150 MHz, $CDCl_3$, δ): 166.37, 150.29, 144.66, 143.50, 143.31, 141.20, 134.12, 134.04, 132.52, 131.20, 131.00, 122.68, 117.41, 112.49, 67.01, 32.07, 29.82, 29.79, 29.75, 29.71, 29.51, 29.39, 28.47, 25.96, 22.84, 14.27. MALDI-TOF MS (*m/z*): $[M]^-$ calcd for $C_{26}H_{29}Br_2N_3O_3S_2$, 655.00; found, 655.4. Anal. calcd for $C_{26}H_{29}Br_2N_3O_3S_2$: C, 47.64; H, 4.46; N, 6.41; found: C, 47.26; H, 4.44; N, 6.18.

Hexadecyl 4,7-bis(5-bromothiophen-2-yl)-[1,2,5]oxadiazolo[3,4-c]pyridine-6-carboxylate (**6-C16**).

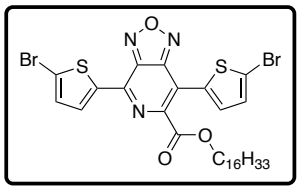

A 25-mL RBF attached to a condenser was charged with ester **5-C16** (200 mg, 1.0 equiv., 0.361 *m*mol), NBS (161 mg, 2.5 equiv., 0.903 *m*mol), 2:1 acetic acid (2.4 mL):chloroform (1.2 mL) mixture and 5 drops of conc. H_2SO_4. The reaction mixture turned dark red and was heated at 40 °C for 16 h before it was diluted with chloroform. The organic layer was washed with saturated $NaHCO_{3(aq)}$ 3 times, washed with water twice, dried over $MgSO_4$ and filtered. Solvent was removed under reduced pressure by rotary evaporation to yield an orange residue, which was then purified by flash chromatography (silica gel, 50 % chloroform in hexanes). Removal of solvent and subsequent recrystallization (ethanol:chloroform) afforded 151 mg of orange solid (59 %). Note that the workup/extraction step may be skipped; see synthesis for **6-PH** or **6-BO**.

^{1}H NMR (MHz, $CDCl_3$, δ): 8.29 (d, *J* = 4.1 Hz, 1 H), 7.48 (d, *J* = 4.0 Hz, 1 H), 7.25 (d, *J* = 4.1 Hz, 1 H), 7.16 (d, *J* = 4.0 Hz, 1 H), 4.38 (t, *J* = 6.5 Hz, 2 H), 1.70 (m, 2 H), 1.27-1.25 (m, 26 H), 0.88 (t, *J* = 7.0 Hz, 3 H). ^{13}C (150 MHz, $CDCl_3$, δ): 166.37, 150.28, 144.65, 143.49, 143.31, 141.20, 134.12, 134.04, 132.52, 131.20, 131.00, 122.68, 117.41, 112.49, 67.01, 32.07, 29.85, 29.84, 29.83, 29.81, 29.76, 29.72, 29.51, 29.40, 28.48, 25.97, 22.84, 14.27. MALDI-TOF MS

(*m/z*): $[M]^-$ calcd for $C_{30}H_{37}Br_2N_3O_3S_2$, 711.06; found, 711.8. Anal. calcd for $C_{30}H_{37}Br_2N_3O_3S_2$: C, 50.64; H, 5.24; N, 5.91; found: C, 50.80; H, 5.35; N, 5.70.

2-Ethylhexyl 4,7-bis(5-bromothiophen-2-yl)-[1,2,5]oxadiazolo[3,4-c]pyridine-6-carboxylate (**6-EH**).

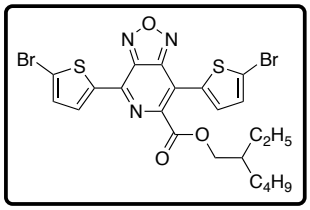

A 25-mL RBF attached to a condenser was charged with ester **5-EH** (442 mg, 1.0 equiv., 1.00 *m*mol), NBS (445 mg, 2.5 equiv., 2.5 *m*mol), 2:1 acetic acid (6.7 mL):chloroform (3.3 mL) mixture and 5 drops of conc. H_2SO_4. The reaction mixture turned dark red and was heated at 40 °C for 16 h before it was diluted with chloroform. The organic layer was washed with saturated $NaHCO_{3(aq)}$ 3 times, washed with water twice, dried over $MgSO_4$ and filtered. Solvent was removed under reduced pressure by rotary evaporation to yield an orange residue, which was then purified by flash chromatography (silica gel, 40 % chloroform in hexanes). Removal of solvent and subsequent recrystallization (ethanol) afforded 165 mg of orange solid (27 %). Note that the workup/extraction step may be skipped; see synthesis for **6-PH** or **6-BO**.

^{1}H NMR (MHz, $CDCl_3$, δ): 8.29 (d, *J* = 4.1 Hz, 1 H), 7.47 (d, *J* = 4.0 Hz, 1 H), 7.25 (d, *J* = 4.2 Hz, 1 H), 7.16 (d, *J* = 3.9 Hz, 1 H), 4.29 (d, *J* = 5.8 Hz, 2 H), 1.64 (m, 1 H), 1.37-1.28 (m, 8 H), 0.90 (at, *J* = 7.5 Hz, 6 H). ^{13}C (150 MHz, $CDCl_3$, δ): 166.51, 150.33, 144.66, 143.54, 143.32, 141.26, 134.11, 134.07, 132.51, 131.17, 131.03, 122.67, 117.40, 112.52, 69.21, 38.82, 30.39, 29.06, 23.70, 23.14, 14.25, 11.15. MALDI-TOF MS (*m/z*): $[M]^-$ calcd for $C_{22}H_{21}Br_2N_3O_3S_2$, 598.94; found, 599.4. Anal. calcd for $C_{22}H_{21}Br_2N_3O_3S_2$: C, 44.09; H, 3.53; N, 7.01; found: C, 43.99; H, 3.55; N, 7.03.

2-Propylheptyl 4,7-bis(5-bromothiophen-2-yl)-[1,2,5]oxadiazolo[3,4-c]pyridine-6-carboxylate (**6-PH**).

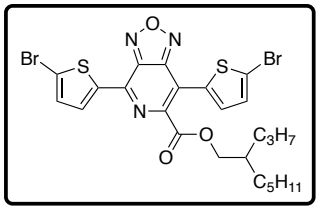

A 25-mL RBF attached to a condenser was charged with ester **5-PH** (723 mg, 1.0 equiv., 1.54 *m*mol), NBS (603 mg, 2.2 equiv., 3.38 *m*mol), 2:1 acetic acid (8 mL):chloroform (4 mL) mixture and 5 drops of conc. H_2SO_4. The reaction mixture turned dark red and was heated at 40 °C for 16 h. Upon cooling to room temperature, the reaction mixture was loaded directly onto a column; the crude material was purified by flash chromatography (silica gel, 50 % chloroform in hexanes). Removal of solvent and subsequent recrystallization (ethanol) afforded 329 mg of orange solid (34 %).

^{1}H NMR (MHz, $CDCl_3$, δ): 8.29 (d, *J* = 4.1 Hz, 1 H), 7.47 (d, *J* = 3.9 Hz, 1 H), 7.25 (d, *J* = 4.1 Hz, 1 H), 7.15 (d, *J* = 4.0 Hz, 1 H), 4.28 (d, *J* = 5.7 Hz, 2 H), 1.71 (m, 1 H), 1.33-1.25 (m, 12 H), 0.89 (aq, *J* = 6.9 Hz, 6 H). ^{13}C (150 MHz, $CDCl_3$, δ): 166.53, 150.33, 144.64, 143.50, 143.33, 141.27, 134.10, 134.08, 132.51, 131.16, 131.03, 122.66, 117.43, 112.54, 69.62, 37.21, 33.45, 32.33, 31.13, 26.55, 22.81, 20.03, 14.55, 14.28. MALDI-TOF MS (*m/z*): $[M]^-$ calcd for $C_{24}H_{25}Br_2N_3O_3S_2$, 626.97; found, 627.8. Anal. calcd for $C_{24}H_{25}Br_2N_3O_3S_2$: C, 45.94; H, 4.02; N, 6.70; found: C, 45.75; H, 4.15; N, 6.60.

2-Butyloctyl 4,7-bis(5-bromothiophen-2-yl)-[1,2,5]oxadiazolo[3,4-c]pyridine-6-carboxylate (**6-BO**).

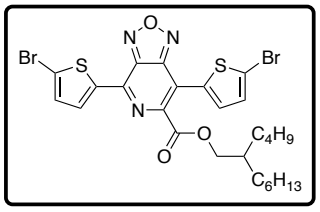

A 25-mL RBF attached to a condenser was charged with ester **5-BO** (543 mg, 1.0 equiv., 1.09 *m*mol), NBS (428mg, 2.2 equiv., 2.40 *m*mol), 2:1 acetic acid (7 mL):chloroform (3.5 mL) mixture and 5 drops of conc. H_2SO_4. The reaction mixture turned dark red was heated at 40 °C for 16 h. Upon cooling to room temperature, the reaction mixture was loaded directly onto a column; the crude material was purified by flash chromatography (silica gel, 50 % chloroform in hexanes). Removal of solvent and subsequent recrystallization (ethanol) afforded 311 mg of orange solid (44 %).

^{1}H NMR (MHz, $CDCl_3$, δ): 8.29 (d, *J* = 4.1 Hz, 1 H), 7.48 (d, *J* = 4.0 Hz, 1 H), 7.25 (d, *J* = 4.2 Hz, 1 H), 7.15 (d, *J* = 4.0 Hz, 1 H), 4.28 (d, *J* = 5.8 Hz, 2 H), 1.70 (m, 1 H), 1.30-1.26 (m, 16 H), 0.89 (m, 6 H). ^{13}C (150 MHz, $CDCl_3$, δ): 166.53, 150.32, 144.63, 143.48, 143.33, 141.27, 134.09, 134.07, 132.51, 131.17, 131.02, 122.65, 117.43, 112.52, 69.62, 37.42, 32.00, 31.19, 30.85, 29.81, 29.06, 26.85, 23.15, 22.85, 14.27, 14.26. MALDI-TOF MS (*m/z*): $[M]^-$ calcd for $C_{26}H_{29}Br_2N_3O_3S_2$, 655.00; found, 655.9. Anal. calcd for $C_{54}H_{88}N_2O_2S_2$: C, 47.64; H, 4.46; N, 6.41; found: C, 47.25; H, 4.31; N, 6.19.

5.6.3. Polymer Syntheses

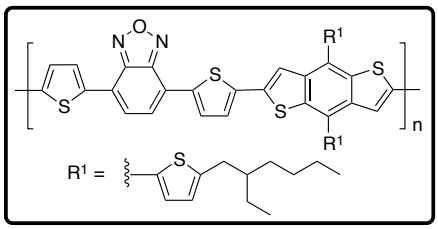

P1

A 25-mL Schlenk tube was charged with 4,7-bis(5-bromothiophen-2-yl)benzo[*c*][1,2,5]oxadiazole (75.2 *m*g, 1.0 equiv., 0.170 *m*mol) and **EHTBDT** (149.23 *m*g, 0.97 equiv., 0.165 *m*mol), and the tube was evacuated and refilled with N_2 three times. Chlorobenzene (7 mL) was added, and the resulting solution was degassed by bubbling N_2 for 30 min while an oil bath was preheated to 90 °C. Upon removing the degassing needle, $Pd_2(dba)_3$ (2 mol %, 3.4 μmol, 3.11 *m*g) and P(*o*-tol)$_3$ (8 mol %, 13.6 μmol, 4.14 *m*g) were added to the solution, and the Schlenk tube was immediately heated at 90 °C. After 5 min, the mixture was stirred for additional 16 h at 110 °C. Overnight, the reaction mixture became a gel (jelly-like). The reaction mixture was allowed to cool to 55 °C before chloroform (30 mL) and a palladium scavenger, *N,N*-diethylphenylazothioformamide (CAS# 39484-81-6, 20 mol%), were added. The resulting mixture was stirred for 3 h at 55°C and precipitated into methanol (150 mL). The precipitates were filtered through a Soxhlet thimble and purified via Soxhlet extraction. The polymer was washed with methanol, hexanes, dichloromethane, and chlorobenzene, and it was extracted with 1,1,2,2-tetrachloroethane (TCE). The TCE solution was then precipitated into methanol (100 mL), and the suspension was filtered through a 0.45 μm Nylon membrane to afford **P1** as a dark solid.

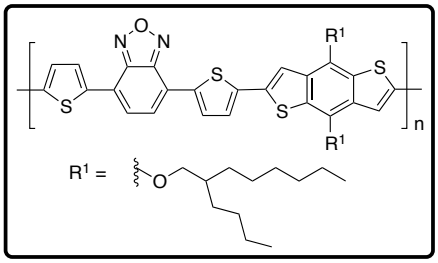

P2

Followed the same synthetic procedure as for **P1**. Used 4,7-bis(5-bromothiophen-2-yl)benzo[*c*][1,2,5]oxadiazole (83.7 *m*g, 1.0 equiv., 0.189 *m*mol), **BOOBDT** (162.4 mg, 0.97 equiv., 0.184 *m*mol), $Pd_2(dba)_3$ (2 mol %, 3.78 μmol, 3.46 *m*g), P(*o*-tol)$_3$ (8 mol %, 15.12 μmol, 4.60 *m*g) and chlorobenzene (7 mL). The precipitates were filtered through a Soxhlet thimble and purified via Soxhlet extraction. The polymer was washed with methanol and hexanes, and it was extracted with chlorobenzene followed by TCE. Both the chlorobezene and TCE fractions were precipitated separately into methanol (100 mL), and the suspension was filtered through a 0.45 μm Nylon membrane to afford **P2** as a dark solid (chlorobenzene = 51.5 mg, TCE = 41.7 mg).

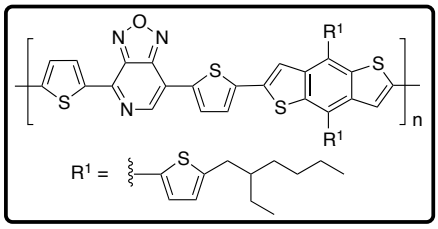

P3

Followed the same synthetic procedure as for **P1**. Used 4,7-4,7-bis(5-bromothiophen-2-yl)-[1,2,5]oxadiazolo[3,4-*c*]pyridine (60.0 *m*g, 1.0 equiv., 0.135 *m*mol), **BOOBDT** (118.8 mg, 0.97 equiv., 0.131 *m*mol), $Pd_2(dba)_3$ (2 mol %, 2.71 μmol, 2.48 *m*g), P(*o*-tol)$_3$ (8 mol %, 10.83 μmol, 3.30 *m*g) and chlorobenzene (5.6 mL). The precipitates were filtered through a Soxhlet thimble and purified via Soxhlet extraction. The precipitates were filtered through a Soxhlet thimble and purified via Soxhlet extraction. The polymer was washed with methanol, hexanes, and chlorobenzene, and it was extracted with TCE. The TCE solution was then precipitated into methanol (100 mL), and the suspension was filtered through a 0.45 μm Nylon membrane to afford **P3** as a dark solid (< 5 mg).

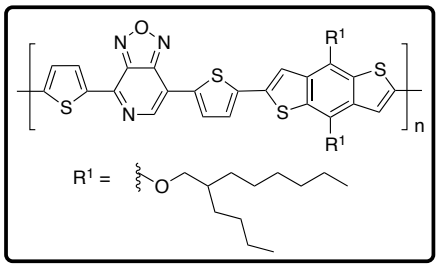

P4

Followed the same synthetic procedure as for **P1**. Used 4,7-4,7-bis(5-bromothiophen-2-yl)-[1,2,5]oxadiazolo[3,4-*c*]pyridine (75.0 *m*g, 1.0 equiv., 0.169 *m*mol), **BOOBDT** (145.2 mg, 0.97 equiv., 0.164 *m*mol), $Pd_2(dba)_3$ (2 mol %, 3.39 μmol, 3.10 *m*g), P(*o*-tol)$_3$ (8 mol %, 13.54 μmol, 4.12 *m*g) and chlorobenzene (5.6 mL). The precipitates were filtered through a Soxhlet thimble and purified via Soxhlet extraction. The polymer was washed with methanol, hexanes, and chlorobenzene, and it was extracted with TCE. The TCE solution was then precipitated into methanol (100 mL), and the suspension was filtered through a 0.45 μm Nylon membrane to afford **P4** as a dark solid (7 mg)

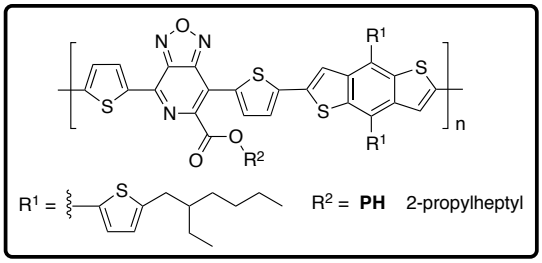

P5-PH

Followed the same synthetic procedure as for **P1**. Used **6-PH** (101.0 *m*g, 1.0 equiv., 0.161 *m*mol), **EHTBDT** (141.25 mg, 0.97 equiv., 0.156 *m*mol), $Pd_2(dba)_3$ (2 mol %, 3 μmol, 2.95 *m*g), P(*o*-tol)$_3$ (8 mol %, 13 μmol, 3.92 *m*g) and chlorobenzene (6 mL). The precipitates were filtered through a Soxhlet thimble and purified via Soxhlet extraction. The polymer was washed with methanol, hexanes, dichloromethane, and chlorobenzene, and it was extracted with TCE. The TCE solution was then precipitated into methanol (100 mL), and the suspension was filtered through a 0.45 μm Nylon membrane to afford **P5-PH** as a dark solid (149.0 mg).

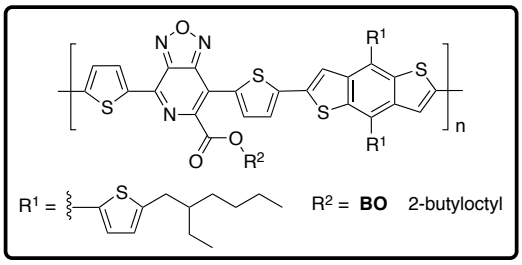

P5-BO

Followed the same synthetic procedure as for **P1**. Used **6-BO** (118.0 *m*g, 1.0 equiv., 0.180 *m*mol), **EHTBDT** (158.0 mg, 0.97 equiv., 0.175 *m*mol), $Pd_2(dba)_3$ (2 mol %, 3..60 μmol, 3.30 *m*g), P(*o*-tol)$_3$ (8 mol %, 14.4 μmol, 4.38 *m*g) and chlorobenzene (6 mL). The precipitates were filtered through a Soxhlet thimble and purified via Soxhlet extraction. The polymer was washed with methanol, hexanes, dichloromethane, and chlorobenzene, and it was extracted with TCE. The TCE solution was then precipitated into methanol (100 mL), and the suspension was filtered through a 0.45 μm Nylon membrane to afford **P5-BO** as a dark solid (153.8 mg)

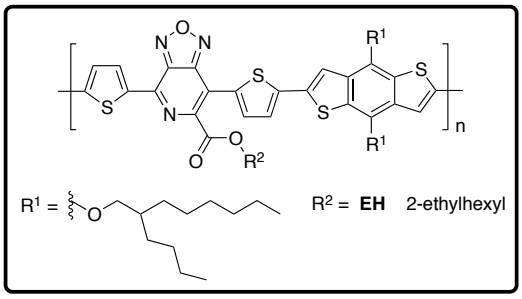

P6-EH

Followed the same synthetic procedure as for **P1**. Used **6-EH** (100.0 *m*g, 1.0 equiv., 0.167 *m*mol), **BOOBDT** (143.2 mg, 0.97 equiv., 0.162 *m*mol), $Pd_2(dba)_3$ (2 mol %, 3.34 μmol, 3.05 *m*g), P(*o*-tol)$_3$ (8 mol %, 13.35 μmol, 4.06 *m*g) and chlorobenzene (5.6 mL). The precipitates were filtered through a Soxhlet thimble and purified via Soxhlet extraction. The polymer was washed with methanol, hexanes, and dichloromethane, and it was extracted with chlorobenzene. The chlorobenzene solution was then precipitated into methanol (150 mL), and the suspension was filtered through a 0.45 μm Nylon membrane to afford **P3** as a dark solid (113 mg)

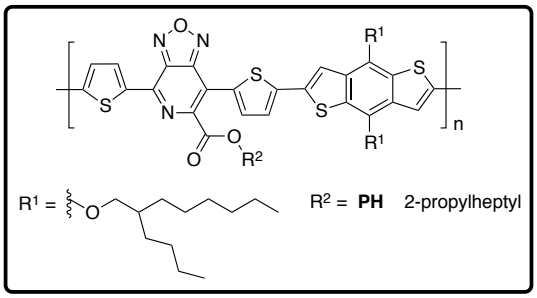

P6-PH

Followed the same synthetic procedure as for **P1**. Used **6-PH** (91.0 *m*g, 1.0 equiv., 0.145 *m*mol), **BOOBDT** (124.44 mg, 0.97 equiv., 0.141 *m*mol), $Pd_2(dba)_3$ (2 mol %, 2.9 μmol, 2.7 *m*g), P(*o*-tol)$_3$ (8 mol %, 11.6 μmol, 3.5 *m*g) and chlorobenzene (5.6 mL). The precipitates were filtered through a Soxhlet thimble and purified via Soxhlet extraction. The polymer was washed with methanol, hexanes, and dichloromethane, and and it was extracted with chlrobenzene. The chlorobenzene solution was then precipitated into methanol (100 mL), and the suspension was filtered through a 0.45 μm Nylon membrane to afford **P6-PH** as a dark solid (71.0 mg).

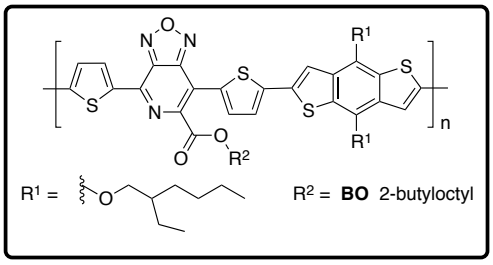

P7-BO

Followed the same synthetic procedure as for **P1**. Used **6-BO** (118.0 *m*g, 1.0 equiv., 0.180 *m*mol), **EHOBDT** (134.9 mg, 0.97 equiv., 0.175 *m*mol), $Pd_2(dba)_3$ (2 mol %, 3.60 μmol, 3.30 *m*g), P(*o*-tol)$_3$ (8 mol %, 14.4 μmol, 4.38 *m*g) and chlorobenzene (6 mL). The precipitates were filtered through a Soxhlet thimble and purified via Soxhlet extraction. The polymer was washed with methanol, hexanes, dichloromethane, and chlorobenzene, and it was extracted with TCE. The TCE solution was then precipitated into methanol (100 mL), and the suspension was filtered through a 0.45 μm Nylon membrane to afford **P3** as a dark solid (94.6 mg)

5.6.4. OPV Device Fabrication

All devices were fabricated on ITO-coated glass substrates (pre-patterned, R = 20 Ω^{-1}, Thin Film Devices, Inc.). The substrates were sonicated for 20 minutes in 2% Helmanex soap water and rinsed extensively with deionized (DI) water. They were then sonicated for 20 minutes in DI water, 20 minutes in acetone, and 20 minutes in isopropyl alcohol, followed by drying under a stream of air. The substrates were then UV-ozone cleaned for 5 minutes.

For the devices described in Section 5.3, thin layer (30-40 nm) of PEDOT:PSS (Clevios PH, passed through a 0.45 PVDF syringe filter prior to use) was spin-coated onto each substrate at 4000 RPM for 40 s, followed by 10 minutes of drying at 150 °C in air. For plasmon-enhanced devices, colloidal suspension samples of Au (40 nm and 50 nm) and Ag (40 nm and 50 nm) nanoparticles in nanopure water were purchased from NanoCS. The desired amounts of NP solutions were transferred to Eppendorf tubes, and the aliquots were centrifuged at 10,000 rpm for 10 min. The supernatant for each sample was removed, and the pellet was resuspended in 200 μm of filtered PEDOT:PSS. The blend solutions were spin-coated onto each substrate at 4000 RPM for 40 s, followed by 30 minutes of drying at 100 °C in air.

All samples were then transferred to a glovebox under N_2, where the active layers were spin-coated at 2000 RPM for 40 s. The cathode (1 nm LiF and/or 100 nm Al) was thermally evaporated under vacuum (~10^{-7} torr) through a shadow mask that defines an active area of ~0.03 cm^2. Some of the samples were then thermally annealed by placing them substrate-side down (active layer facing up) on a hot plate. All active layers were processed from *o*-dichlorobenzene solutions of the polymers and $PC_{71}BM$ Details of the solution concentrations,

blend ratio, spin-speed, cathode deposition, use of additive, and annealing steps for each molecule are shown in **Table 5-6**. Current-voltage (*J-V*) curves were measured using a Keithley 2400 source-measure unit under AM 1.5 G solar illumination at 100 mW cm^{-2} (1 sun) using a Thermal-Oriel 150 W solar simulator.

Table 5-4. Optimized solution concentrations, blend ratio, spin-speed, cathode deposition, use of additive, and annealing for device fabrication from each of the processable polymer.

	concentration (mg/mL)		D:A	spin-speed (rpm)	cathode	additive (v/v)	annealing
	polymer	$PC_{71}BM$					
P2	10	30	1:2	@1000, 30 s @4000, 15 s	LiF/Al	none	--
P5-PH	7.5	20	1:35	@1000, 30 s @4000, 15 s	LiF/Al	none	--
P5-BO	7.5	25	1:3	@1000, 30 s @4000, 15 s	LiF/Al	none	--
P6-EH	15	20	1:4	@800, 30 s @4000, 10 s	Al	none	--
P6-PH	10	20	1:3	@1000, 30 s @4000, 15 s	LiF/Al	0.3 % ODT	--
P7-BO	8	20	1:2	@1200, 30 s @4000, 10 s	Al	none	@180 °C 5 min

ODT = 1,8-octanedithiol

5.6.5. Characterization by UV-vis spectroscopy and Cyclic Voltammetry

UV-Vis spectral data were measured at room temperature with a Varian Cary 50 Conc spectrophotometer. Thin film measurements were collected by spin-coating a chloroform solution of the sample onto ITO-coated glass substrates. The thickness of the thin films was measured by profilometry (Veeco Dektat 150) and determined to be 80±10 nm. A blank ITO-coated glass substrate was used as reference.

Cyclic voltammograms were collected using a Solartron 1285 potentiostat under the control of CorrWare II software. A standard three electrode cell based on a Pt wire working electrode, a silver wire pseudo-reference electrode (calibrated vs. Fc/Fc^{+}), and a Pt wire counter electrode was purged with nitrogen and maintained under a nitrogen atmosphere during all measurements. Acetonitrile was purchased anhydrous from Aldrich and tetrabutylammonium hexafluorophosphate (0.1 M) was used as the supporting electrolyte. Polymer films were drop cast onto a Pt wire working electrode from a 1% (w/w) chloroform solution and dried under nitrogen prior to measurement.

5.7. References

(1) Thompson, B. C.; Fréchet, J. M. J. *Angew. Chem. Int. Ed.* **2008**, *47*, 58.
(2) Günes, S.; Neugebauer, H.; Sariciftci, N. S. *Chem. Rev.* **2007**, *107*, 1324.
(3) Tumbleston, J. R.; Liu, Y.; Samulski, E. T.; Lopez, R. *Adv. Energ. Mater.* **2012**, *2*, 477.
(4) Cheng, Y.-J.; Yang, S.-H.; Hsu, C.-S. *Chem. Rev.* **2009**, *109*, 5868.
(5) Krebs, F. C. *Sol. Eng. Mater. Sol. Cells* **2009**, 93, 394.
(6) Yu, G.; Gao, J.; Hummelen, J. C.; Wudl, F.; Heeger, A. J. *Science* **1995**, *270*, 1789.
(7) Halls, J. J. M.; Walsh, C. A.; Greenham, N. C.; Marseglia, E. A.; Friend, R. H.; Moratti, S. C.; Holmes, A. B. *Nature* **1995**, *376*, 498.

(8) Li, X.; Choy, W. C. H.; Huo, L.; Xie, F.; Sha, W. E. I.; Ding, B.; Guo, X.; Li, Y.; Hou, J.; You, J.; Yang, Y. *Adv. Mater.* **2012**, *24*, 3046.
(9) He, Z.; Zhong, C.; Huang, X.; Wong, W.-Y.; Wu, H.; Chen, L.; Su, S.; Cao, Y. *Adv. Mater.* **2011**, *23*, 4636.
(10) Chen, H.-C.; Chen, Y.-H.; Liu, C.-C.; Chien, Y.-C.; Chou, S.-W.; Chou, P. T. *Chem. Mater.* **2012**, *24*, 4766.
(11) Cabanetos, C.; El Labban, A.; Bartelt, J. A.; Douglas, J. D.; Mateker, W. R.; Fréchet, J. M. J.; McGehee, M. D.; Beaujuge, P. M. B. *J. Am. Chem. Soc.* **2013**, *135*, 4656.
(12) Lu, L.; Luo, Z.; Xu, T.; Yu, L. *Nano Lett.* **2013**, *13*, 59.
(13) Choi, H.; Lee, J.-P.; Ko, S.-J.; Jung, J.-W.; Park, H.; Yoo, S.; Park, O.; Jeong, J.-R.; Park, S.; Kim, J. Y. *Nano Lett.* **2013**, *13*, 2204.
(14) He, Z.; Zhong, C.; Su, S.; Xu, M.; Wu, H.; Cao, Y. *Nature Photon.* **2012**, *6*, 591.
(15) Small, C. E.; Chen, S.; Subbiah, J.; Amb, C. M.; Tsang, S. W.; Lai, T. H.; Reynolds, J. R.; So, F. *Nature Photon.* **2012**, *6*, 115.
(16) Zhou, H.; Yang, L.; You, W. *Macromolecules* **2012**, *45*, 607.
(17) Henson, Z. B.; Müllen, K.; Bazan, G. C. *Nature Chem.* **2012**, *4*, 699.
(18) Li, Z.; Zhang, Y.; Tsang, S.-W.; Du, X.; Zhou, J.; Tao, Y.; Ding, J. *J. Phys. Chem. C* **2011**, *115*, 18002.
(19) Chu, T.-Y.; Lu, J.; Beaupré, S.; Zhang, Y.; Pouliot, J.-R.; Zhou, J.; Najari, A.; Leclerc, M.; Tao, Y. *Adv. Funct. Mater.* **2012**, *22*, 2345.
(20) Yiu, A. T.; Beaujuge, P. M.; Lee, O. P.; Woo, C. H.; Toney, M. F.; Fréchet, J. M. J. *J. Am. Chem. Soc.* **2012**, *134*, 2180.
(21) Mei, J.; Kim, D. H.; Ayzner, A. L.; Toney, M. F.; Bao, Z. *J. Am. Chem. Soc.* **2011**, *133*, 20130.
(22) Amb, C. M.; Chen, S.; Graham, K. R.; Subbiah, J.; Small, C. E.; So, F.; Reynolds, J. R. *J. Am. Chem. Soc.* **2011**, *133*, 10062.
(23) Beaupré, S.; Boudreault, P.-L. T.; Leclerc, M. *Adv. Mater.* **2010**, *22*, E6.
(24) Cheng, Y.-J.; Chen, C.-H.; Ho, Y.-J.; Chang, S.-W.; Witek, H. A.; Hsu, C.-S. *Org. Lett.*, **2011**, *13*, 5484.
(25) Lee, J.; Han, A.-R.; Kim, J.; Kim, Y.; Oh, J. H.; Yang, C. *J. Am. Chem. Soc.* **2012**, *134*, 20713.
(26) Chen, C.-H.; Hsieh, C.-H.; Dubosc, M.; Cheng, Y.-J.; Hsu, C.-S. *Macromolecules* **2010**, *43*, 697.
(27) Woo, C. H.; Beaujuge, P. M.; Holcombe, T. W.; Lee, O. P.; Fréchet, J. M. J. *J. Am. Chem. Soc.* **2010**, *132*, 15547.
(28) Blouin, N.; Michaud, A.; Gendron, D.; Wakim, S.; Blair, E.; Neagu-Plesu, R.; Bellete, M.; Tao, Y.; Leclerc, M. *J. Am. Chem. Soc.* **2008**, *130*, 732.
(29) Zhou, H.; Yang, L.; Price, S. C.; Knight, K. J.; You, W. *Angew. Chem. Int. Ed.* **2010**, *49*, 7992.
(30) van der Poll, T. S.; Love, J. A.; Nguyen, T.-Q.; Bazan, G. C. *Adv. Mater.* **2012**, *24*, 3646.
(31) Liang, Y.; Feng, D.; Wu, Y.; Tsai, S.-T.; Li, G.; Ray, C.; Yu, L. *J. Am. Chem. Soc.*, **2009**, *131*, 7792.
(32) Chen, H.-Y.; Hou, J.; Zhang, S.; Liang, Y.; Yang, G.; Yang, Y.; Yu, L.; Wu, Y.; Li, G. *Nature Photon.* **2009**, *3*, 649.
(33) Hou, J.; Park, M.-H.; Zhang, S.; Yao, Y.; Chen, L.-M.; Li, J.-H.; Yang, Y. *Macromolecules* **2008**, *41*, 6012.

(34) Li, Y. *Acc. Chem. Res.* **2012**, *45*, 723.
(35) Liang, Y.; Yu, L. *Acc. Chem. Res.*, **2010**, *43*, 1227.
(36) Piliego, C.; Holcombe, T. W.; Douglas, J. D.; Woo, C. H.; Beaujuge, P. M.; Fréchet, J. M. J. *J. Am. Chem. Soc.* **2010**, *132*, 7595.
(37) Huo, L.; Zhang, S.; Guo, X.; Xu, F.; Li, Y.; Hou, J. *Angew. Chem. Int. Ed.* **2011**, *50*, 9697.
(38) Gorohmaru, H.; Thiemann, T.; Sawada, T.; Takahashi, K.; Nishi-i, K.; Ochi, N.; Kosugi, Y.; Mataka, S. *Heterocycles* **2002**, *56*, 421-431.
(39) Frisch, M. J.; Trucks, G. W.; Schlegel, H. B.; Scuseria, G. E.; Robb, M. A.; Cheeseman, J. R.; Scalmani, G.; Barone, V.; Mennucci, B.; Petersson, G. A.; Nakatsuji, H.; Caricato, M.; Li, X.; Hratchian, H. P.; Izmaylov, A. F.; Bloino, J.; Zheng, G.; Sonnenberg, J. L.; Hada, M.; Ehara, M.; Toyota, K.; Fukuda, R.; Hasegawa, J.; Ishida, M.; Nakajima, T.; Honda, Y.; Kitao, O.; Nakai, H.; Vreven, T.; Montgomery, Jr., J. A.; Peralta, J. E.; Ogliaro, F.; Bearpark, M.; Heyd, J. J.; Brothers, E.; Kudin, K. N.; Staroverov, V. N.; Kobayashi, R.; Normand, J.; Raghavachari, K.; Rendell, A.; Burant, J. C.; Iyengar, S. S.; Tomasi, J.; Cossi, M.; Rega, N.; Millam, J. M.; Klene, M.; Knox, J. E.; Cross, J. B.; Bakken, V.; Adamo, C.; Jaramillo, J.; Gomperts, R.; Stratmann, R. E.; Yazyev, O.; Austin, A. J.; Cammi, R.; Pomelli, C.; Ochterski, J. W.; Martin, R. L.; Morokuma, K.; Zakrzewski, V. G.; Voth, G. A.; Salvador, P.; Dannenberg, J. J.; Dapprich, S.; Daniels, A. D.; Farkas, Ö.; Foresman, J. B.; Ortiz, J. V.; Cioslowski, J.; Fox, D. J. Gaussian 09, Revision C.01.
(40) Yang, L.; Zhou, H.; You, W. *J. Phys. Chem. C* **2010**, *114*, 16793.
(41) Perez, M. D.; Borek, C.; Forrest, S. R.; Thompson, M. E. *J. Am. Chem. Soc.* **2009**, *131*, 9281.
(42) Beate Burkhart, Petr P. Khlyabich, and Barry C. Thompson *Macromolecules*, **2012**, *45* (9), pp 3740
(43) Yang, L.; Zhou, H., You, W. *J. Phys. Chem. C* **2010**, *114*, 16793.
(44) Wong, W. W. H.; Singh, T. B.; Vak, D.; Pisula, W.; Yan, C.; Feng, X.; Williams, E. L.; Chan, K. L.; Mao, Q.; Jones, D. J.; Ma, C.; Müllen, K.; Bäuerle, P.; Holmes, A. B. *Adv. Funct. Mater.* **2010**, *20*, 927
(45) J. Peet, L. Wen, P. Byrne, S. Rodman, K. Forberich, Y. Shao, N. Drolet, R. Gaudiana, G. Dennler, and D. Waller Appl. Phys. Lett. 98, 043301 −20H——
(46) Fabiano, S.; Chen, Z.; Vahedi, S.; Facchetti, A.; Pignataroc, B.; Loi, M. A. *J. Mater. Chem.* **2011**, *21*, 5891.
(47) Schubert, M.; Yin, C.; Castellani, M.; Bange, S.; Tam, T. L.; Sellinger, A.; Hörhold, H.-H.; Kietzke, T.; Neher, D. *J. Chem. Phys.* **2009**, *130*, 094703.
(48) Zhang, Y.; Dang, X. D.; Kim, C.; Nguyen, T.-Q. *Adv. Energy Mater.* **2011**, *1*, 610.
(49) Gan, Q.; Bartoli, F. J.; Kafafi, Z. H. *Adv. Mater.* **2013**, *25*, 2385.
(50) Subramaniyan, S.; Xin, H.; Kim, F. S.; Jenekhe, S. A. *Macromolecules* **2011**, *44*, 6245.

Chapter VI

Electron Transfer Dynamics of Triphenylamine Dyes Bound to TiO_2 Nanoparticles from Femtosecond Stimulated Raman Spectroscopy (FSRS)

6.1. Introduction: Photoexcited Electron Transfer at the Organic/Inorganic Interface

Photoexcited electron transfer across an organic/inorganic interface is a crucial, efficiency-determining step in many important processes such as photocatalytic water splitting[1] and dye-sensitized photocurrent generation.[2] In all cases, a light-absorbing dye is used to "sensitize" an inexpensive semiconductor such as titanium dioxide. This strategy allows for the generation of reactive conduction band electrons with visible light, thereby exploiting a significant part of the solar spectrum. These processes for generating reactive electrons have been intensely studied with particular attention to both photochemical pathways and material properties that lead to efficient photoexcited electron transfer. To date, there are several key aspects of these processes that remain unknown. For example, the rate and yield of the direct recombination of photogenerated electrons and molecular cations at the interface are unclear, and the effects of the dye binding modality and conjugation length on charge separation are poorly understood.

If the energy level alignment between the dye and TiO_2 is appropriate, population of the S1 state of the dye via photoexcitation will lead to subsequent electron injection, presumably into the conduction band of the TiO_2, though it has been suggested that surface trap states could also be involved.[3] Electrons in the conduction band are then available for further reactions or, in the case of dye-sensitized solar cells (DSSCs), collection at an electrode. Two criteria must be met to maximize the yield of the downstream reactions: first, injection efficiency must be maximal, and second, the lifetime of injected electrons in the conduction band must be as long as possible, which means that the efficiency of the reverse reaction (i.e., recombination)[4] must be minimal. In order to design systems that meet both of these criteria, a mechanistic understanding of both electron injection and recombination is necessary.

In general, electron injection occurs on the ultrafast time scale, while recombination can occur on a multitude of time scales ranging from picoseconds to microseconds. In the case of ruthenium and other metal-containing dyes, injection from the singlet state occurs in ~100 fs and injection from the triplet state is on the order of picoseconds.[5] On the other hand, for metal-free dyes, the injection step is on the order of 10 fs or less and has nearly 100% transfer efficiency.[6–9] Thus, most studies of metal-free systems have focused on the recombination of the injected electrons and molecular cations.

Transient absorption (TA) spectroscopy[5,8–15] has been the method of choice for measuring ultrafast kinetics of photoexcited interfacial electron transfer (ET). Most,[9–13] but not all,[8] reports have concluded that the multiexponential (picoseconds−microseconds) decay observed in the TA is due to the recombination of electrons and holes, meaning that the recombination rate, and therefore the overall efficiency of charge separation, can be predicted. To obtain less ambiguous information on ruthenium- and iron-based dyes, the Lian group has performed a series of studies combining visible and, more species-specific, mid-IR TA.[5,15,16] However, experiments probing both the photoexcited electronic and structural dynamics have yet to be conducted on systems with metal-free dyes.

Organic dyes often contain linked donor and acceptor moieties to broaden their absorption in the visible region, and they are bound to the semiconductor surface through coordinating, acidic functional groups. Of all the dyes synthesized thus far, those containing triphenylamine (TPA) have been the most promising, achieving up to 8% power conversion efficiency in photovoltaics.[17] However, the effect that dye structure has on ET is still not fully understood. It is hypothesized that placing the hole localizing TPA moiety farther from the semiconductor surface may help keep charge carriers separate, thereby slowing down recombination. Additionally, the binding group can influence electron injection and recombination; She et al.[15]

found that ruthenium dyes using phosphonic acid binding groups to bind to TiO_2 displayed slower injection than those bound through carboxylic acids.

To interrogate the interfacial ET in TPA-dye-sensitized particles with structural specificity, we use femtosecond stimulated Raman spectroscopy (FSRS) in conjunction with concurrent NIR (830−940 nm) TA.[18] FSRS has the unique ability to provide Raman vibrational spectra with femtosecond time resolution over a broad bandwidth. For example, FSRS has been used to probe the multidimensional reaction coordinate of green fluorescent protein[19] and to elucidate the ultrafast structural mechanisms of isomerization in azobenzene[20] and stilbene.[21] More recently, FSRS was used to study charge transfer between coumarin 343 and TiO_2[22] and within donor-acceptor molecules.[23,24]

In this report, we use FSRS to study the dye/semiconductor interface exploring the effect of different binding moieties and conjugation lengths on interfacial ET and the internal relaxation processes of both the dye and the nanoparticle. Discrepancies between the TA kinetics and the vibrational dynamics of the dye cation suggest that an alternative interpretation of the TA decays of these systems is necessary. Furthermore, the observed excited state structures for extended conjugation systems reveal an unexpected loss mechanism via photoisomerization of the dye.

6.2. Design and Synthesis of Metal-Free Organic Dyes and Dye-TiO_2 Conjugates

The metal-free organic molecules used in this study are designed based on high-performing dyes in DSSCs. These dyes typically contain a hole-localization moiety, an optional π-bridge, an electron-deficient unit and an anchoring group (Figure 6-1). The anchoring group should bind strongly to an inorganic surface. Carboxylic acid is the most common binding moiety for attachment to titania and other metal oxides; other groups such as phosphonic acid can also be used. To facilitate exciton dissociation and efficient electron injection into the conduction band of TiO_2, the electron-deficient unit is functionalized with the binding group such that the LUMO of the dye physically locates near the surface of the inorganic particle, allowing for extensive orbital overlap. In contrast, the electron-rich moiety should locate away from the inorganic particle in order to minimize back electron transfer, and the installment of a π-bridge may further decrease the probability of a charge recombination event by increasing the distance between the positions of the HOMO and LUMO.

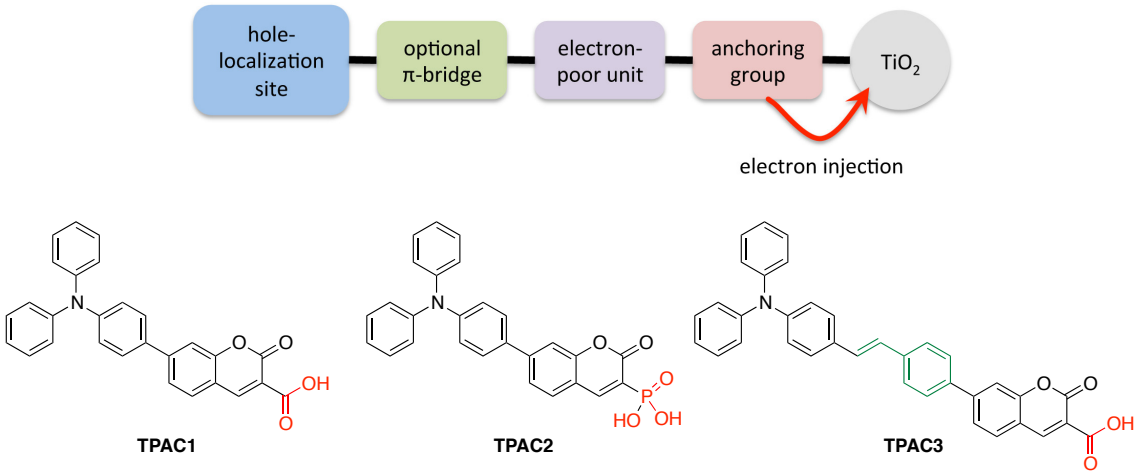

Figure 6-1. (Top) General design scheme for a metal-free dye that exhibits low band gap. (Bottom) The metal-free, triphenylamine-coumarin (TPAC) dyes used in this work: TPAC1, TPAC2 and TPAC3.

This work investigates the effects of binding groups and π-bridge on the charge transfer dynamics at the dye/TiO_2 interface with transient absorption and FSRS. In terms of dye design, triphenylamine is selected to be the electron-rich moiety for reasons mentioned previously; coumarin is chosen to be the electron-deficient unit because it allows for facile functionalization of the anchoring groups: carboxylic acid (**TPAC1**) and phosphonic acid (**TPAC2**). Furthermore, since many metal-free organic dyes contain vinyl groups as part of their π-bridges, **TPAC3** is designed to investigate whether the incorporation of a vinylphenyl linker leads to decreased charge recombination rates.

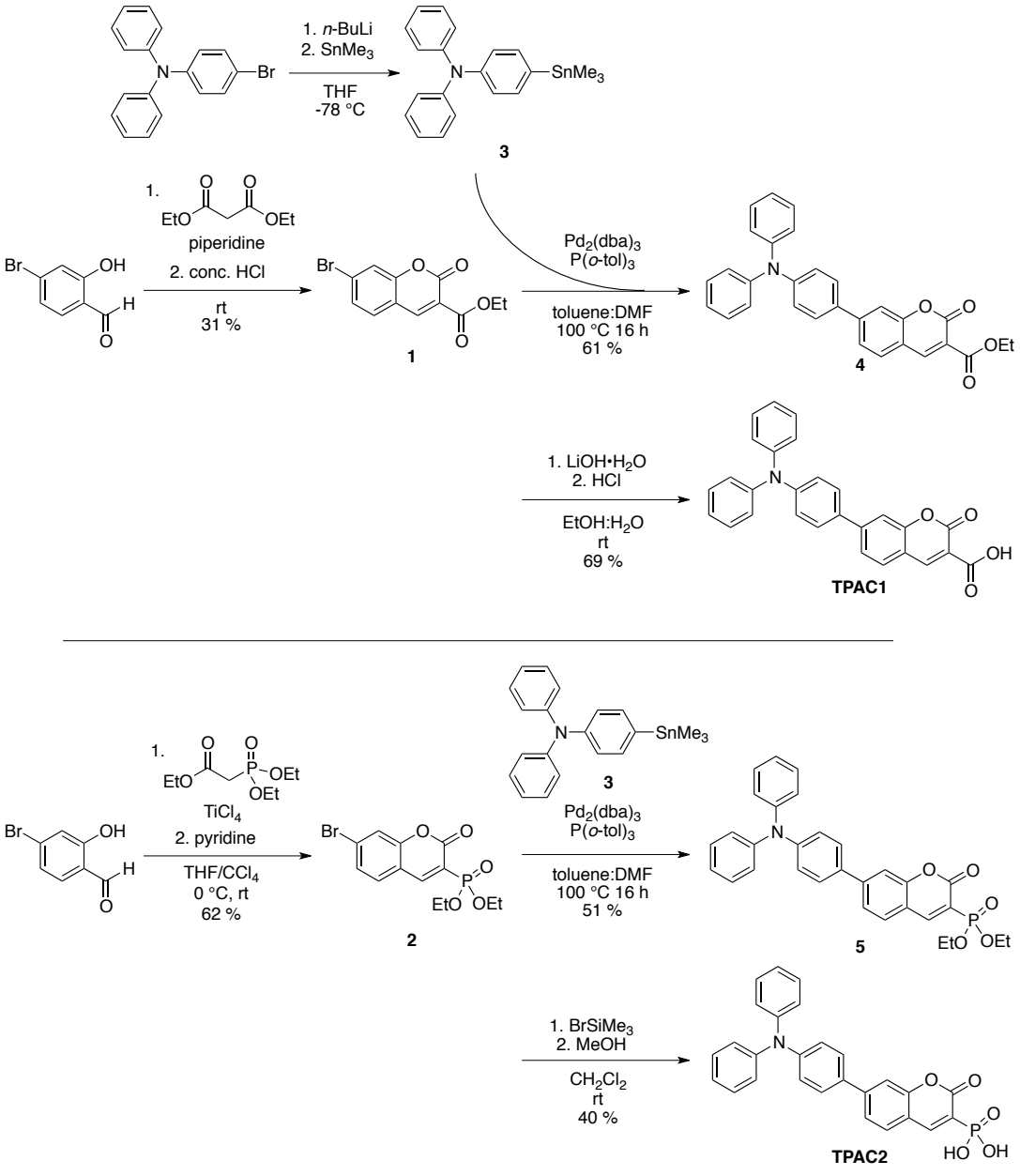

Scheme 6-1. Routes for the syntheses of TPAC1 and TPAC2.

The syntheses of the TPAC dyes are summarized here. The coumarin portion of the TPACs was synthesized from 4-bromosalicylaldehyde and diethylmalonate or triethyl phosphonoacetate

via the Perkin reaction for **TPAC1**/**3** (**1**) and **TPAC2** (**2**), respectively. The triphenylamine was stannylated (**3**) to enable subsequent Pd-catalyzed Stille cross-coupling with the bromofunctionalized coumarin fragments to provide the ester-protected **4** and **5** (Scheme 6-1). For **TPAC3**, the vinylphenyl linker was added to the triphenylamine using a previously reported Wittig olefination procedure (**6**).[25] The ester-protected **8** was synthesized in a similar manner to TPAC1 and TPAC2 via Stille cross-coupling of the stannylated triphenylamine vinylphenyl fragment to the bromo-functionalized coumarin (**7**). Cleavage of the respective ester protecting groups provided the target acidic TPACs (Scheme 6-2).

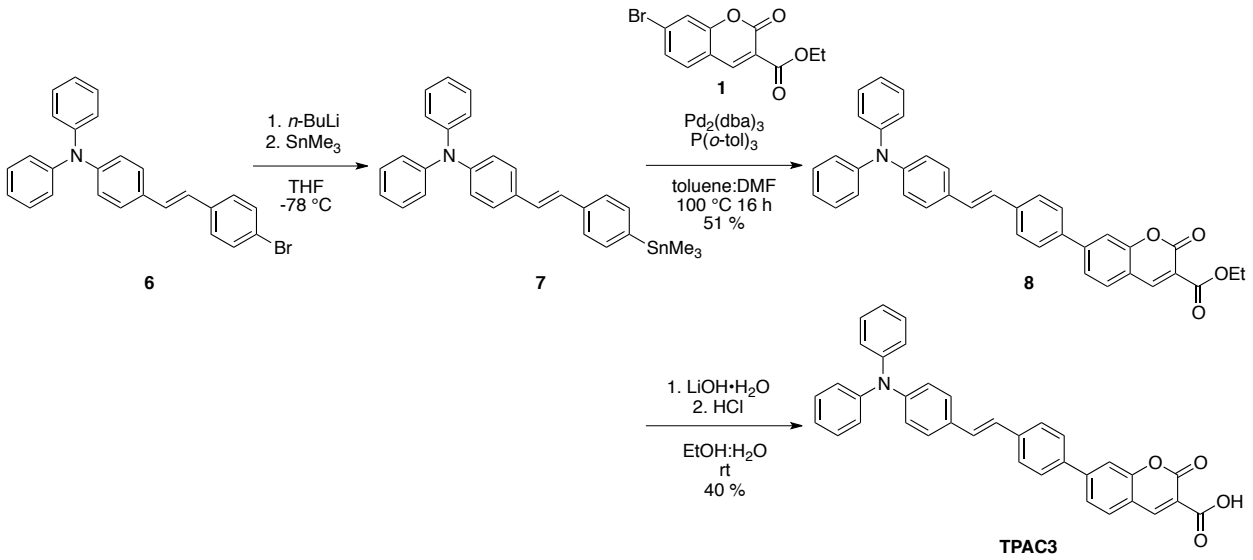

Scheme 6-2. Route for the synthesis of TPAC3.

Anatase titania particles were synthesized by base hydrolysis of titanium(IV) isopropoxide in methanol and characterized by transmission electron micros copy (TEM). The titania nanoparticles (d = 89 ± 16 nm) were functionalized using a standard mass transfer technique; particles were suspended in a 10 mg/mL dye solution (5:1 $CHCl_3$:MeOH) with a ~90-fold excess of the dye and heated at 50 °C for 16 h. The conjugates were then repeatedly washed with a $CHCl_3$/MeOH mixture to remove residual free dye molecules. Final samples were prepared by re-suspending the conjugates in $CHCl_3$ for photophysical studies.

6.3. Results

6.3.1. Ground-State UV-Visible Absorption

Absorption spectra of all dyes, both free and bound to TiO_2 nanoparticles, in chloroform are presented in Figure 6-2 along with their respective structures. **TPAC1** and **TPAC2** exhibit a single large absorption peak, assigned to a charge transfer (CT) transition that blue-shifts upon conjugation to the TiO_2 surface. The absorption spectrum of **TPAC3** exhibits two peaks: the lower energy band is assigned to the CT transition, and the higher energy band is assigned to a delocalized $\pi \rightarrow \pi^*$ transition on the basis of density functional theory (DFT) calculations at the B3LYP/6-311G++(d,p) level.[26] In contrast to the effect of titania conjugation on **TPAC1** and TPAC2, the absorption spectrum of the **TPAC3**-TiO_2 conjugates broadens but does not blue-

shift appreciably. This result is in agreement with previously reported spectra from structurally similar dyes.[11,13]

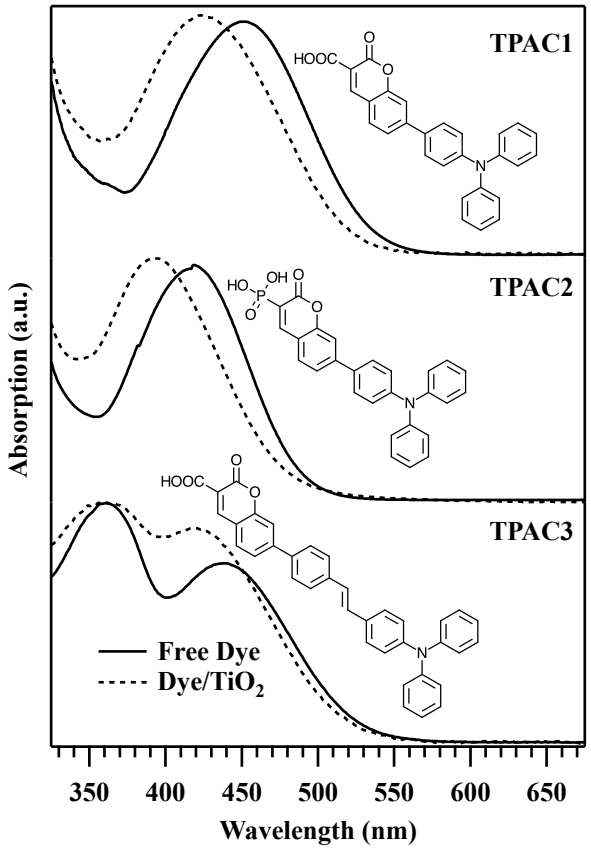

Figure 6-2. Structures and steady-state absorption spectra of **TPAC1** (top), **TPAC2** (middle) and **TPAC3** (bottom) for both free dye (solid lines) and dye-nanoparticle conjugate (dotted lines) samples.

6.3.2. Transient Absorption

Presented in Figure 6-3 are the dispersed transient absorption (TA) spectra between 830 and 940 nm for the free dyes (top) and the bound dyes (bottom). Solid contour lines indicate positive ΔOD, thick lines indicate a ΔOD of zero, and red dashed lines indicate negative ΔOD. The TA of **TPAC1** in this region is dominated by a single broad band that grows in at $\lambda > 930$ nm and blue-shifts slightly on the ~10 ps time scale. This band then decays in hundreds of picoseconds while simultaneously red-shifting. In contrast, the TA of bound **TPAC1** has no rising component and displays two bands, one on either side of the observed region. Neither peak shifts appreciably. For **TPAC2**, the TA is dominated by a single decaying band. Upon binding, this band shifts to shorter wavelengths and splits into two barely discernible bands centered at ~855 and ~900 nm. Notably, the TA of **TPAC3** changes from being absorptive early and emissive later to being always absorptive upon binding to TiO_2. It has been shown for TiO_2 thin films[27,28] that valence band electrons excited directly to the conduction band and to surface trap states absorb in this region. Other reports have assumed that electrons injected from photoexcited sensitizers into titania nanoparticles have similar spectral properties.[10–13] However, it is possible that the radical cation of the dye absorbs in this region as well, making unambiguous interpretation of the TA difficult.

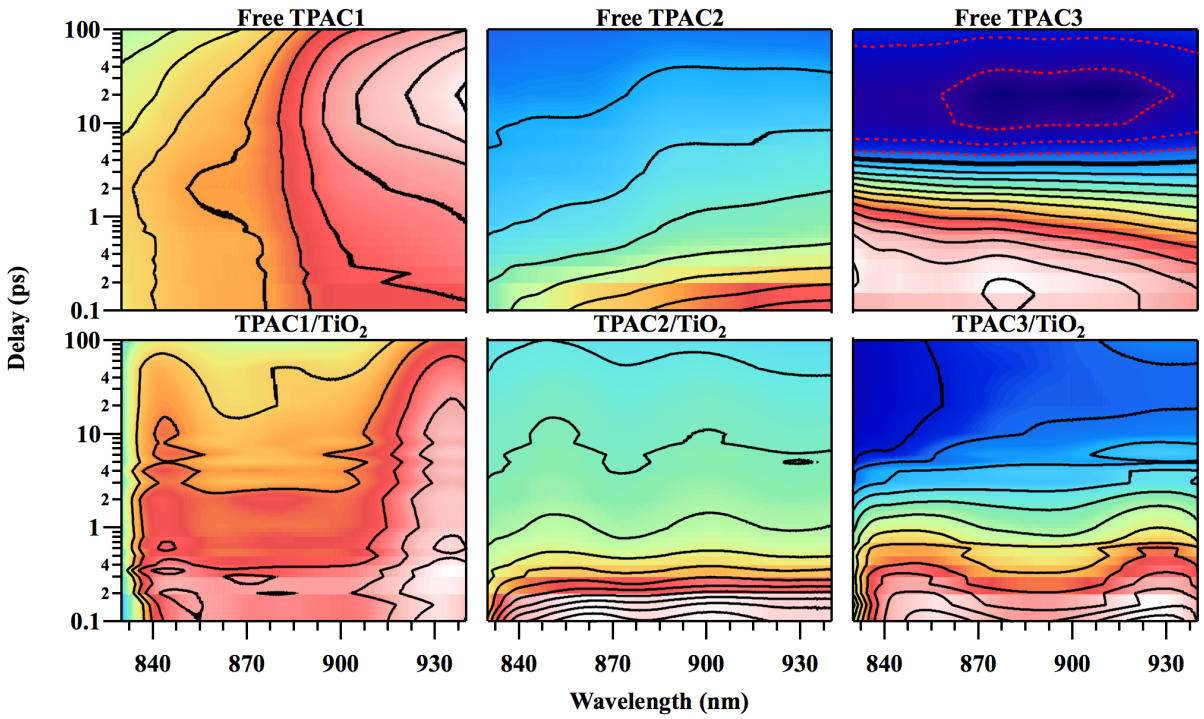

Figure 6-3. Contour plots of the transient absorption of the free (upper plots) and conjugated (lower plots) **TPAC1** (left plots), **TPAC2** (center plots) and **TPAC3** (right plots). Thin solid lines indicate positive ΔOD, thick lines indicate a ΔOD of zero and dotted lines indicate a negative ΔOD.

In order to simplify the analysis of the TA and comparisons with previous reports,[10–13] the TAs of the conjugated dyes were integrated between 830 and 940 nm, and the resulting transients were fit to the sum of four exponentials convoluted with a Gaussian instrument response function of the appropriate width.

Figure 6-4 presents the time evolution of the integral of the transient absorption (TA) from 830-940 nm of the conjugated TPACs. These decays were fit to the sum of three exponentials and a constant offset—used to model a very long time component—convoluted with the instrument response function. Algebraically,

$$TA(t) = S(t) \otimes \left(A_0 + \sum_{i=1}^{3} A_i e^{-t/\tau_i} \right) \quad (1)$$

and

$$\sum A_i = 1 \quad (2)$$

where *TA(t)* is the integral of the TA, *S(t)* is the instrument response function, and A_i and τ_i represent the fractional amplitude and the time constant, respectively, of the i^{th} decay component. Fits are shown as solid black lines and the dotted lines indicate zero.

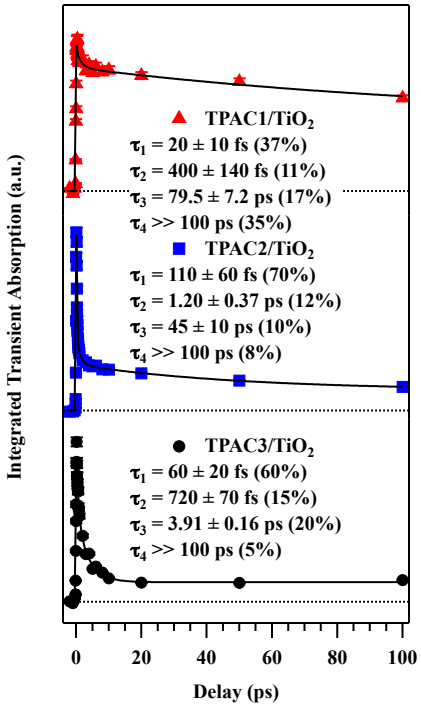

Figure 6-4. Transient absorption integrated between 830 and 940 nm of TPAC1/TiO_2 (top), TPAC2/TiO_2 (middle) and TPAC3/TiO_2 (bottom) are shown as the markers. The dotted lines show zero. Multiexponential fits are shown as the black lines and the extracted time constants are shown in the legend.

The results of these fits are summarized in Figure 6-5 as a bubble chart, where the center and area of each bubble indicate the time constant and fractional amplitude, respectively, of that decay component. **TPAC1** has the slowest overall decay; the fast component, τ_1, constitutes a small portion of the decay when compared to the other dyes, and the second largest component (35%) is the slowest (τ_{long}) 100 ps. Conversely, **TPAC3** has the fastest and most complete decay; $\tau 1$ is the largest component (60%), and τ_{long} only comprises 5% of the total intensity decay. Furthermore, τ_3 of TPAC3 is an order of magnitude shorter than that of the other dyes. **TPAC2** exhibits a fast decay as well; τ_1 makes up 70% and τ_{long} 8% of the total decay.

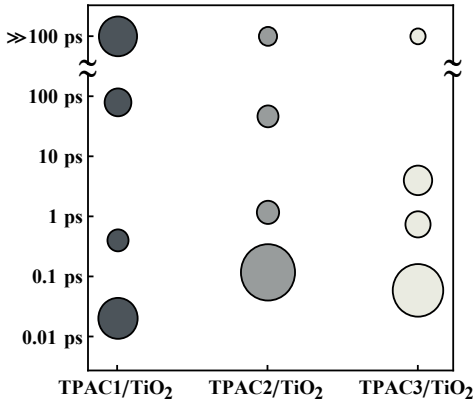

Figure 6-5. Summary of the **TPAC**/TiO_2 absorption transients integrated between 830 and 940 nm. The data are well modeled by a four-component exponential decay with the longest component fit as a constant offset. The vertical position of each bubble represents the time constant while the area represents the fractional amplitude of that decay component.

6.3.3. Transient Stimulated Raman Spectra of TPAC1 and TPAC2

Figures 6-6 and 6-7 present the baseline-corrected transient stimulated Raman spectra of free and bound **TPAC1** and **TPAC2**, respectively, in $CHCl_3$. The baselines for the ground state spectra were estimated by and interpolating a spline through points manually chosen as belonging to the baseline, similar to previous studies.[29–35] On the other hand, the baselines of the excited state spectra were estimated by fitting a sub-region of the spectra to one, in the case of the free dye samples, or two, in the case of the conjugates samples, Gaussian peaks for the signal and a third order polynomial for the baseline. This method has been previously used to analyze the FSRS spectra of 4-(Dimethylamino)benzonitrile.[36]

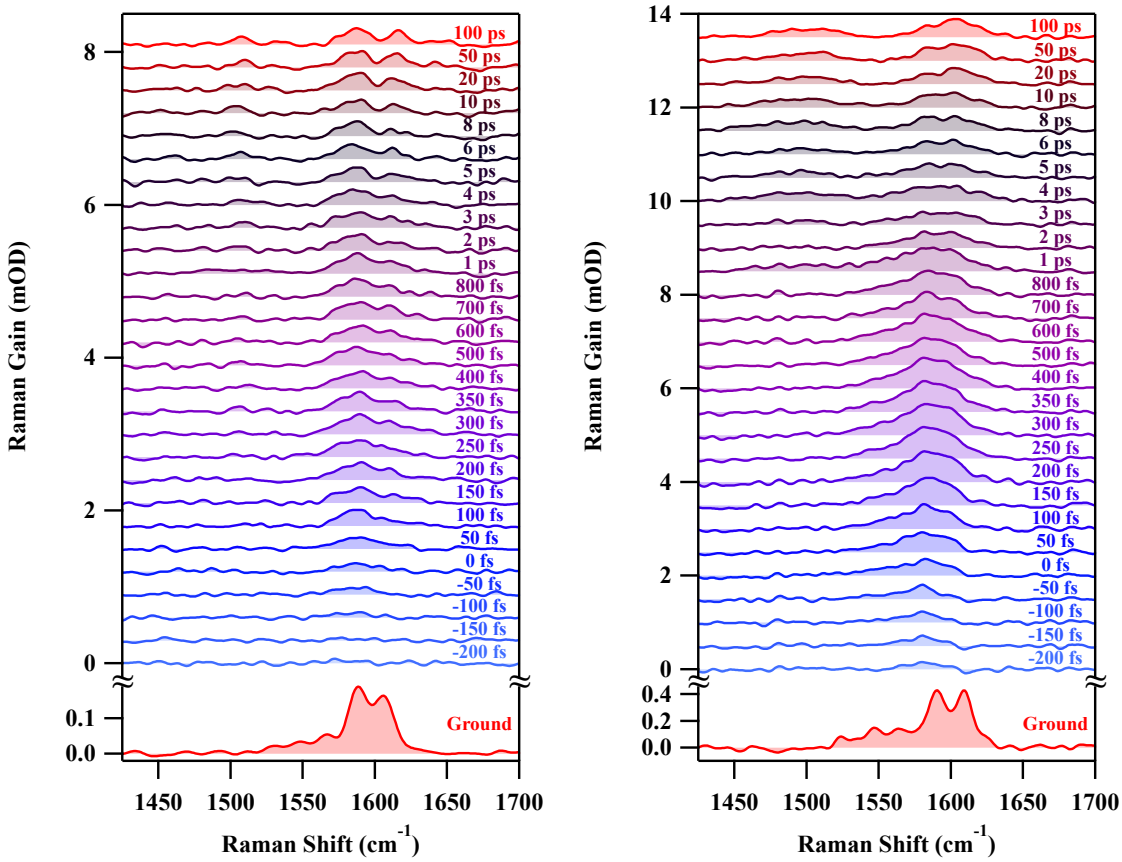

Figure 6-6. Raman spectra of **TPAC1** (left) and conjugated **TPAC1** (right) with baseline subtraction. Traces have been offset for clarity. Baselines (dotted lines) for the excited state were estimated algorithmically by fitting the spectra to a model function consisting of one or more Gaussian peaks for the signal and a 3rd order polynomial for the baseline. Ground state baselines were generated by fitting a spline through hand chosen points.

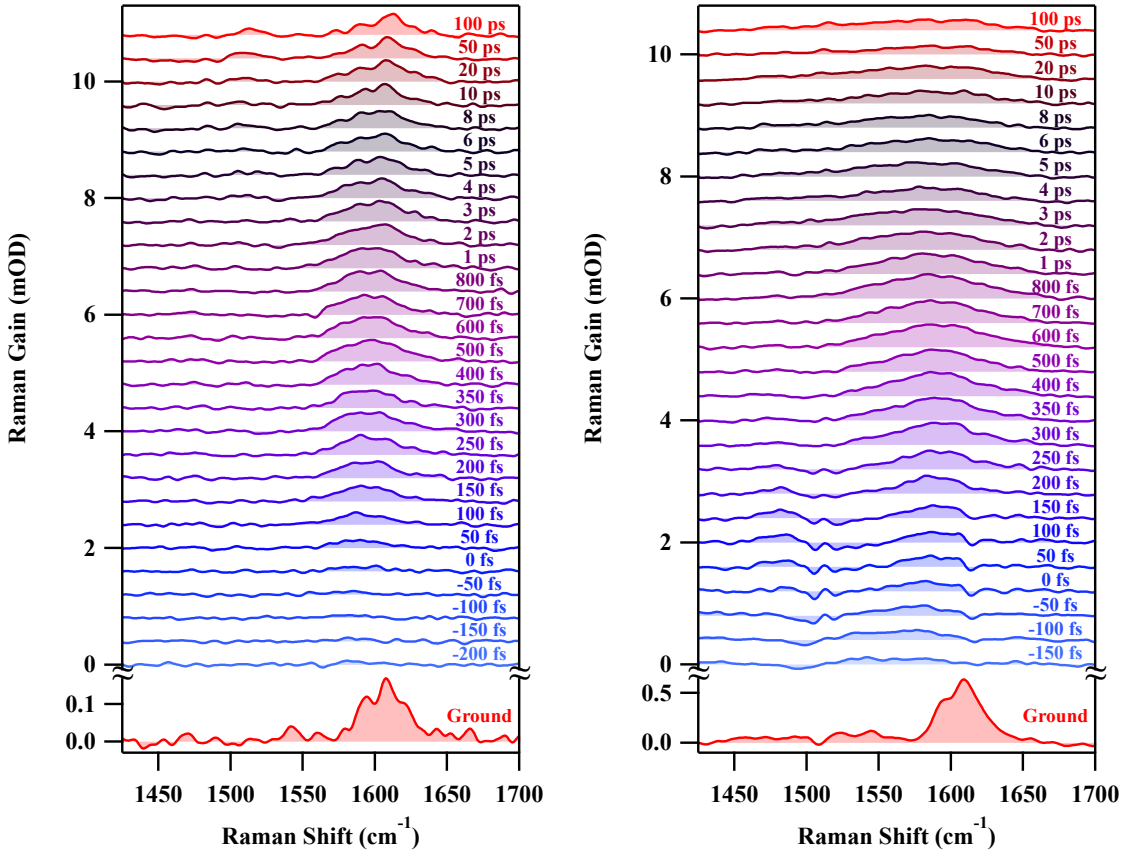

Figure 6-7. Transient Raman spectra of **TPAC2** (left) and conjugated **TPAC2** (right) with baseline subtraction. Traces have been offset for clarity.

Figure 6-8 presents selected transient stimulated Raman spectra of the same samples recorded at 100 fs, 1 ps, 10 ps and 100 ps. All spectra display an intense Raman mode near ~1590 cm^{-1}, which can be assigned to a delocalized C=C stretching motion along the conjugated backbone of the molecule. In the case of **TPAC1**, this stretching mode splits into two separate modes at longer times. Such behavior was not observed in the other samples, likely due to the fact that the free **TPAC1** data were taken at a higher resolution than the others. Upon binding to the TiO_2 surface, a new transient appears in the 1500−1520 cm^{-1} region of the **TPAC1** and **TPAC2** spectra.

To assist peak assignment in the Raman spectra, density functional theory (DFT) calculations[26] of the radical cation were performed at the B3LYP/6-311G++(D,P) level without symmetry restrictions on a pruned (99,590) grid. Presented in Figure 6-9 is a comparison of the observed excited state Raman spectra 100 ps after excitation, shown in red, of conjugated **TPAC1** (top) and **TPAC2** (bottom) with the predicted spectra of the corresponding radical cation, shown in blue. Radical cation Raman cross sections, shown as the black sticks, were calculated using DFT.[26] Furthermore, artificial spectra (blue curves) were generated using a 30 and 40 cm^{-1} FWHM Gaussian lineshape function for **TPAC1** and **TPAC2**, respectively. A comparison between the spectra of calculated radical cation and experimental data show that the mode in the 1500−1520 cm^{-1} region can be assigned to another delocalized C=C stretching motion while the mode at 1590 cm^{-1} retains the same character as in the neutral molecule.

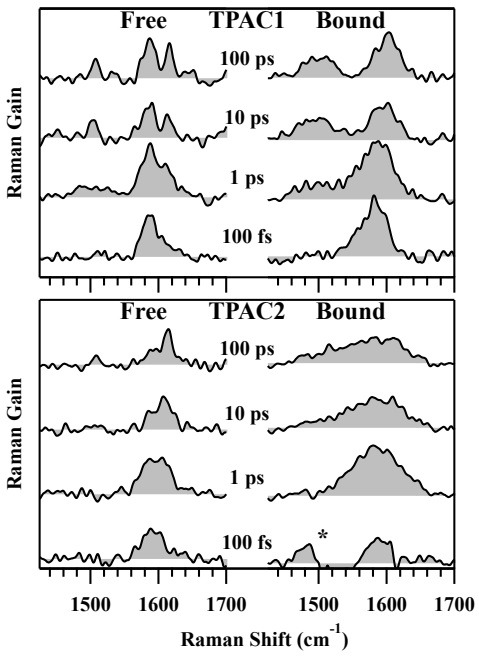

Figure 6-8. Transient stimulated Raman spectra of **TPAC1** (top) and **TPAC2** (bottom) in $CHCl_3$ at selected time delays. Free dye spectra are shown on the left and conjugated dye spectra are shown on the right. For all spectra there is a delocalized C=C stretching mode located at ~1590 cm^{-1}. For the **TPAC1**/TiO_2 and **TPAC2**/TiO_2 samples there is another intense delocalized C=C mode located at ~1500 and ~1520 cm^{-1}, respectively. The asterisk marks the time dependent solvent artifact due to impulsive excitation by the actinic pump.

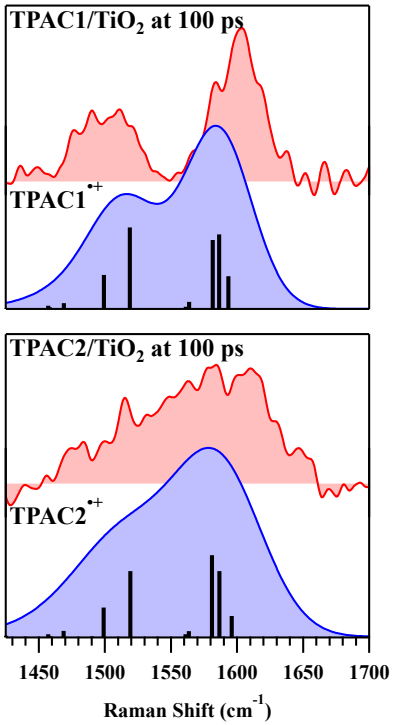

Figure 6-9. A comparison of the 100 ps spectrum of conjugated **TPAC1** (top) and **TPAC2** (bottom) with the Gaussian predicted Raman cross sections of the radical cations (shown as sticks) and spectra simulated by 30 and 40 cm^{-1} FWHM Gaussian line shape functions for **TPAC1** and **TPAC2**, respectively.

To extract time constants for the decay of the ~1590 cm^{-1} mode, the amplitudes of the Raman peaks shown in Figures 6-6 and 6-7 were fit to the sum of an exponential and a constant offset—used to model a very long time component—convoluted with the instrument response function (Figure 6-10). Algebraically,

$$I(t) = S(t) \otimes \left(A_0 + A_1 e^{-t/\tau}\right) \quad (3)$$

and

$$A_0 + A_1 = 1 \quad (4)$$

where *I(t)* is the intensity of the 1590 cm^{-1} mode, *S(t)* is the instrument response function, A_0 is the amplitude of the long time constant (modeled as a constant offset) and A_1 is the fractional amplitude associated with the τ time constant. The amplitudes and time constants are tabulated in Figure 6-10 and summarized as a bubble chart presented as Figure 6-11.

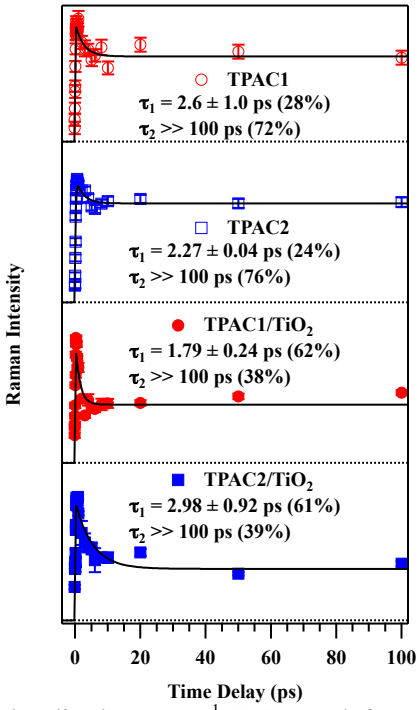

Figure 6-10. Kinetic analysis of the delocalized 1590 cm^{-1} C=C stretch for **TPAC1** (top), **TPAC2** (second from top), **TPAC1**/TiO_2 (second from bottom) and conjugated **TPAC2**/TiO_2 (bottom). The dotted lines show zero. Multiexponential fits are shown as black lines and the extracted time constants are shown in the legend

In all instances, the intensity of the ~1590 cm^{-1} mode can be well modeled by a biexponential decay (Figure 6-11). The shorter, accurately determined time constant is roughly the same for all samples at ~2.5 ps. Strikingly, the long time component represents nearly 75% of the decay for the free dyes but only ~40% of the decay for the conjugates. A direct comparison between Figures 6-5 and 6-11 shows that the transient Raman kinetics share little similarity with those of the TA; the decay of the TA is dispersive, when modeled by a multiexponential decay the extracted time constants span at least 4 orders of magnitude, while the transient Raman is best modeled by a biexponential decay.

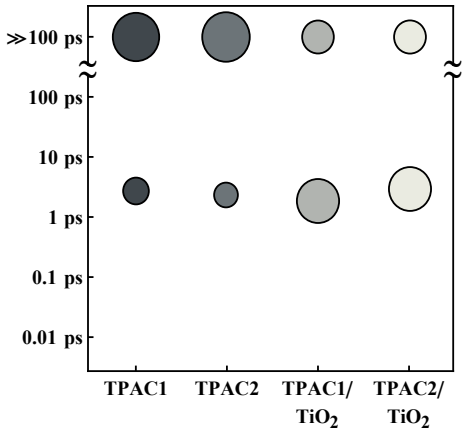

Figure 6-11. Summary of the intensity transients of the ~1590 cm^{-1} mode of **TPAC1** and **TPAC2** for both the free dyes and the conjugated dyes. In all four samples, the kinetics of the 1590 cm^{-1} mode are well described by an exponential function with two time constants, ~2.5 ps and one much greater than 100 ps. The vertical positions and areas of the bubbles represent the time constant and fractional amplitude of that decay component, respectively.

6.3.4. Transient Stimulated Raman Spectra of TPAC3

Figure 6-12 shows the selected transient stimulated Raman spectra of the same samples recorded at 100 fs, 1 ps, 10 ps and 100 ps, and presented in Figure 6-13 are the baseline-subtracted data of **TPAC3** and conjugated **TPAC3**, respectively. In this case, the data were sufficiently complex that both the ground and excited state baselines were estimated using the manual method described previously.[29-35] These spectra are rich in information containing many intense Raman modes over a wide range of frequencies. There is a notable similarity between the early time spectra for the free and bound dyes. While there appear to be slight differences at long times, the low signal-to-noise for the bound-dye samples makes baseline correction difficult, and therefore the significance of these deviations is hard to estimate.

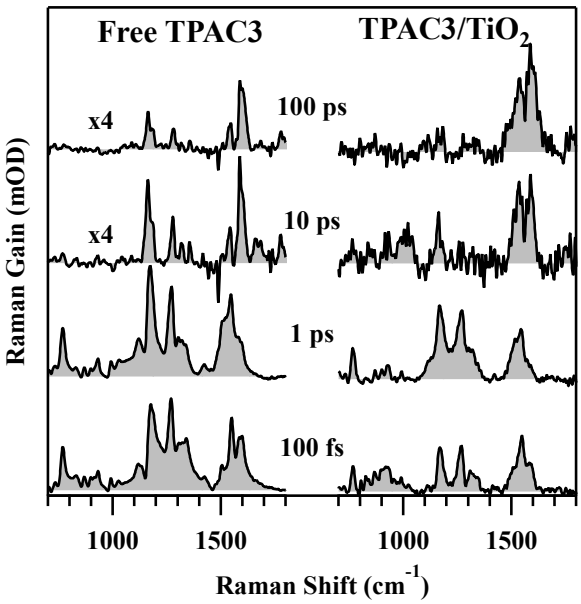

Figure 6-12. Transient Raman spectra of TPAC3 (left) and TPAC3/TiO_2 (right) at selected time delays. The band positions and intensities of the free and bound species are very similar.

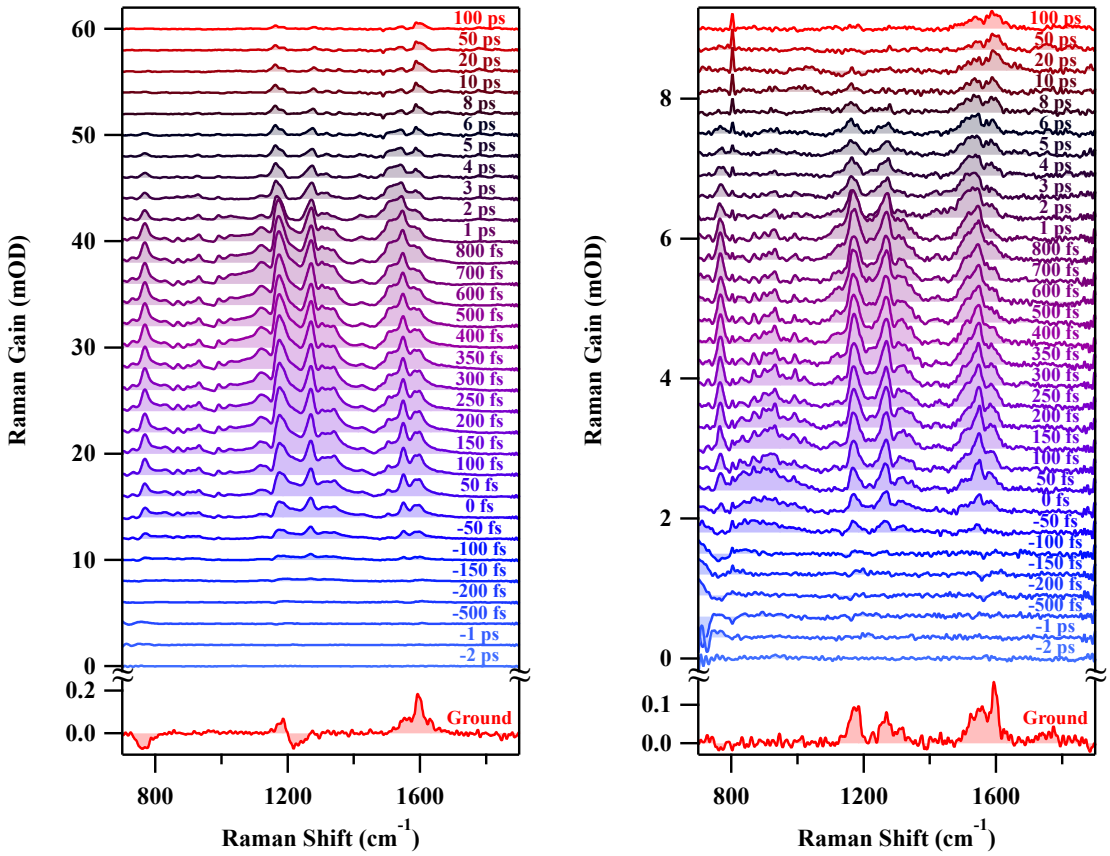

Figure 6-13. Raman spectra of TPAC3 (left) and conjugated TPAC3 (right) with baseline subtraction. Traces have been offset for clarity. Baselines were estimated by fitting a spline through hand chosen points.

Noticeably, these spectra are nearly identical to those of photoexcited *trans*-stilbene.[21] A comparison of the S1 Raman spectra of *trans*-stilbene[21] with free and bound **TPAC3** 3 ps after excitation is presented in Figure 6-14. Compared to the experiment performed by Weigel and Ernsting,[21] our conditions are different: chloroform was used instead of hexane, probing was performed in the 830−940 nm region as opposed to the 605−695 nm region, and the sample was excited using a pulse centered at 395 nm versus one centered at 280 nm. Nevertheless, the band positions and intensities of photoexcited S1 **TPAC3** match those of photoexcited S1 *trans*-stilbene nearly quantitatively with two exceptions: a new peak in the **TPAC3** spectra located at 766 cm^{-1} and a blue-shift of the olefinic CH deformation band to 1271 cm^{-1}. Other minor differences can be attributed to the higher resolution of the present experiment and different methods of baseline correction.

The kinetic analysis of *trans*-stilbene[21] is consistent with those of both free and bound **TPAC3**. Figure 6-15 presents the time evolution of the integral, from 700 to 1830 cm^{-1}, of the excited state Raman spectra of free and conjugated TPAC3. A similar analysis of photoexcited S_1 *trans*-stilbene has been presented by Weigel and Ernsting[21] who found a 0.33 ps rise and 0.92 ps decay time. The analysis of TPAC3 yielded a similar set of time constants of 0.25 and 2 ps. Note that in the analysis of *trans*-stilbene, the constant offset of the band integral was removed prior to analysis. In brief, the intensities of the transient Raman bands as a function of time are best modeled by a short exponential rise and a picosecond exponential decay with a long time offset. Even though our analysis differs slightly from that performed by Weigel and Ernsting,[21]

the extracted time scales are comparable, 0.33 and 0.92 ps for *trans*-stilbene in hexane and 0.25 and 2 ps for **TPAC3** in chloroform. The similarity between the excited-state potential energy surfaces (PESs) (as shown by the Raman spectra) and excited-state dynamics (as shown by the kinetic analyses) of *trans*-stilbene and TPAC3 suggests that they have similar photoreactivity—isomerization.

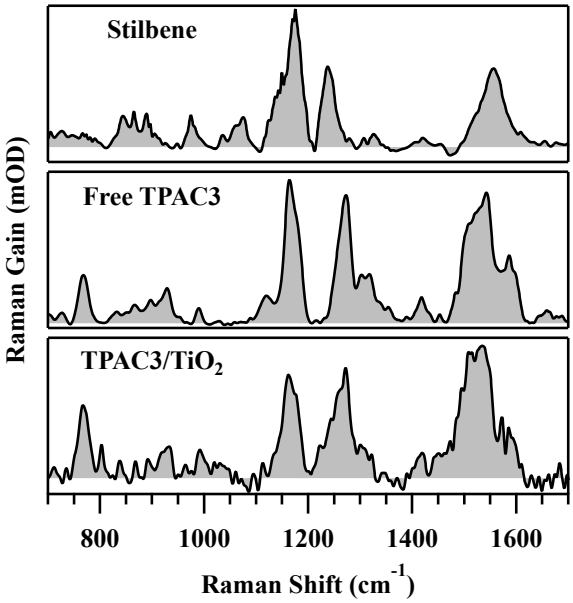

Figure 6-14. Comparison of the S_1 Raman spectra 3 ps after excitation of *trans*-stilbene in hexane, free TPAC3 and TPAC3 bound to TiO_2 in chloroform. Stilbene data was adapted from ref. 21.

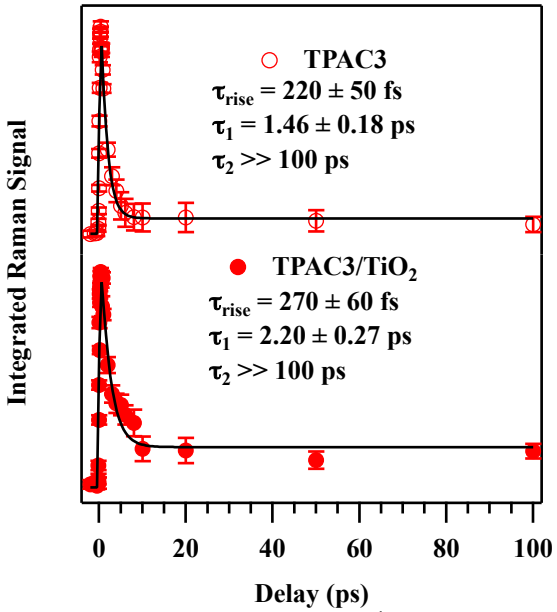

Figure 6-15. Raman signal integrated between 700 and 1830 cm^{-1} for TPAC3 (top) and TPAC3/TiO_2 (bottom) are shown as markers. Multiexponential fits are shown as solid lines and the extracted time constants are indicated in the legend. These data agree well with those reported by Weigel and Ernsting for *trans*-stilbene.[10]

6.4. Discussion

Time-resolved vibrational and electronic data provide new information on the dynamics of electron transfer (ET) across a molecular/semiconductor interface. In overview, the vibrational data for **TPAC1** and **TPAC2** are inconsistent with the conventional interpretation of the TA, which directly relates the decay in the 830−940 nm region to the recombination of electrons and cations. The Raman kinetics of the radical cation are slower than and different in character from those of the TA, suggesting that the TA decay is reporting on another process. Additionally, the similarity between the excited state structure and ultrafast structural relaxation of **TPAC3** with that of *trans*-stilbene suggests that isomerization of the vinyl linker competes directly with ET, reducing injection efficiency and photochemical stability for this system.

6.4.1. Analysis of the Kinetic Data from Transient Absorption and FSRS

The analysis of the TA for dye−nanoparticle conjugates is difficult because it is hard to determine whether the signal is due to the dye, the nanoparticle, or the combined system. It has been shown[27,28] that surface trapped electrons, and to a much lesser extent bulk electrons, absorb in the region studied. However, as is evident in the top of Figure 6-3, the free **TPAC** dyes also absorb here. Previous reports[10−13,29] have assigned the TA decay in this region to the recombination of electrons in TiO_2 with the molecular dye cations, assuming that the results for thin-film TiO_2[27,28] hold for nanoparticles. The dispersive nature of the decay was interpreted as being due to the heterogeneity of the particles' surface, leading to a distribution of recombination times.[10−13,29]

Comparing **TPAC1** to **TPAC2**, we find that the TA decay is faster for **TPAC2**, a dye that binds to TiO_2 through a phosphonic acid instead of a carboxylic acid, than **TPAC1**. **TPAC3**, which has a longer π-conjugation length, exhibits a much faster decay than **TPAC1**. Within the previously outlined framework, these results would imply that the electron recombination rate should be fast for **TPAC2** and faster for **TPAC3**. Therefore, the overall charge separation efficiencies of these two dyes are predicted to be lower than that of **TPAC1**.

In contrast, the evolution of the transient Raman spectra can be best described by a simpler set of two exponentials. For bound **TPAC1** and **TPAC2**, the appearance of a new mode in the 1500−1520 cm^{-1} region of the long time spectra indicates the formation of the radical cation. If the TA decay were indeed related to the recombination of electrons and holes, then we would predict that a highly multiexponential evolution of the transient vibrational signal ranging from 100 fs to 100 ps should also be observed. We thus conclude that the TA decay is due to a process other than recombination, while the transient Raman tracks the oxidation state of the dye. If this interpretation is correct, it means that the recombination rates for both carboxylic and phosphonic acid bound dyes are much slower than 100 ps. The experimental time resolution of the present study was insufficient to determine the effect of different binding moieties on injection rates.

6.4.2. Comparison of Excited State Kinetics between TPAC3 and trans-stilbene

Unlike **TPAC1** and **TPAC2**, the transient Raman spectra of **TPAC3** show no clear evidence for the formation of the radical cation. However, the time-resolved vibrational spectra of the S1 state of **TPAC3** and of *trans*-stilbene[21] (see Figure 6-14) are very similar, indicating that the S1 PESs, particularly in the region associated with the vinyl normal modes, of both species are nearly identical. This similarity is further supported by the approximate equivalence of the characteristic time scales for their spectral evolution: a 0.25 ps rise and 2 ps decay for **TPAC3**

and a 0.33 ps rise and 0.92 ps decay for *trans*-stilbene (see Figure 6-15 and ref 21, respectively). nIn *trans*-stilbene, this spectral evolution is due to vibrational cooling on the excited state and movement toward the S1/S0 conical intersection, which leads to isomerization. Because the shape of the PES determines chemical reactivity and because *trans*-stilbene and its derivatives are known to isomerize on the S1 surface with up to 50 % quantum yield,[38−40] these data suggest that **TPAC3** also isomerizes. A previous scanning tunneling microscopy (STM) study[41] on triphenylamine- and ruthenium-based dyes presented cursory evidence that such isomerizations are possible. Similarly, it has been observed that the fraction of the *cis* isomer of an indoline-based dye sensitizer increased under irradiation[42] and that replacing a double bond with a nonisomerizing indene group increased DSSC efficiency by an average of 16 %.[43] Furthermore, the high level of similarity between the transient Raman spectra and kinetics of **TPAC3** and *trans*-stilbene suggests that the ultrafast structural relaxation of **TPAC3** is dominated by the stilbene moiety and thus isomerization of the vinyl linker. It is likely that this process competes directly with charge separation, thereby reducing the efficiency and stability of the molecular dye responsible for electron injection. Vinyl linkers included in other dyes[2,8,10−13,44−46] are likely susceptible to this side reaction as well.

6.4.3. Proposed Model for Charge Transfer Dynamics at the Metal-Free Dye/TiO_2 Interface

The vibrational data support a model for the TPAC dyes with slow electron recombination. This model is in agreement with studies on ruthenium-based dyes[5] that have shown slow electron injection (0.1−1 ps) and much slower recombination (picoseconds−microseconds), in addition to studies of direct band gap excitation of TiO_2 thin films.[27,28] Furthermore, a visible TA study of aminophenyl acid sensitizers attached to TiO_2 thin films[8] found no evidence for subnanosecond charge recombination. In the case of the TPAC dyes, the TA decay could be due to electrons hopping from various surface trap states to the conduction band. The high level of heterogeneity in location and energy of the surface states throughout the sample may explain the multiexponential character of the TA decay. Within this new framework, the transient Raman tracks initial structural relaxation of the oxidized dye while transient absorption monitors the relaxation of electrons within the semiconducting material.

A model summarizing these observations is presented in Figure 6-16. Conjugation of the dye to the TiO_2 surface causes the LUMO of the free dye to rehybridize with the nearest surface trap state of TiO_2, creating a charge injection (CI) state, as shown by each of the dashed lines. Excitation to this state causes electron injection on the ∼10 fs time scale.[6,7] Because the injection process leaves a large amount of excess energy with the electron,[4,47] the hot electron can be subsequently transferred into the charge separated (CS) state, shown as the shaded curve. The CS state is one in which the dye has been formally oxidized and the nanoparticle formally reduced with the electron in the TiO_2 conduction band (CB). After entering the CS state, the electron cools rapidly, within 1 ps, through electron−phonon interactions.[48,49] The decay of the TA is due to electrons leaving the CI states and entering the CS state. Heterogeneity in trap state energy, and thus CI state energy, leads to highly multiexponential, dispersive, TA kinetics. More complete information on the distribution of trap state energies would allow for more sophisticated modeling of the system's dynamics and thus the TA decay. During this evolution, which is shown on the right as the charge transfer (CT) coordinate (Q_{CT}), the radical cation reorganizes along its internal degrees of freedom within ∼2.5 ps, as tracked by FSRS. For TPAC3, there is a unique nonradiative decay pathway that is shown as the isomerization coordinate (Q_{Iso}) on the left. This pathway competes directly with the electron injection pathway, thereby degrading efficiency and stability.

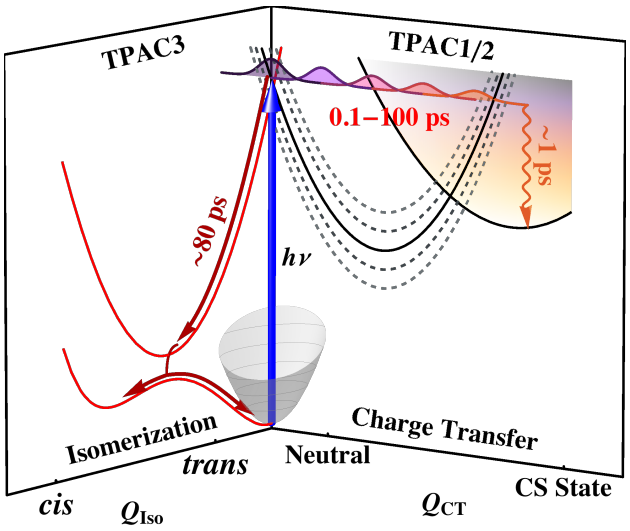

Figure 6-16. Schematic potential energy diagram showing the various processes occurring during and after electron injection from the dye to the nanoparticle. Absorption of a photon excites the system directly to a charge injection (CI) state formed from the LUMO of the dye and a surface trap state, shown as dashed lines on the right. The injection process leaves the electron with enough excess energy to be transferred into the charge separated (CS) state, shown as the shaded curve. The CS state is one in which the dye has been formally oxidized and the electron resides in the conduction band (CB) of the titania. Heterogeneity in trap state energy levels leads to a variety of transfer rates resulting in dispersive kinetics. After transferring, the hot electron quickly internally converts to the bottom of the CS state. During this evolution the radical cation reorganizes along its internal degrees of freedom within ~2.5 ps. TPAC3 has a unique non-radiative pathway shown at left which represents the photoinitiated *trans* to *cis* isomerization about the C=C bond. This new process competes directly with electron injection, lowering efficiency and decreasing the photostability of the dye.

6.5. Conclusion

We have investigated ultrafast interfacial electron transfer within a series of triphenylamine/coumarin dye−TiO_2 conjugates using both femtosecond transient absorption and stimulated Raman. The vibrational data are inconsistent with the common analysis of the TA, necessitating a new hypothesis in which the decay of the TA is attributed to hot electrons moving from the initially populated surface trap states to the conduction band and the picosecond process monitored by FSRS is the internal relaxation of the radical cation. Finally, our results indicate that the use of vinyl linkers as a means to extend π-conjugation in organic dyes for sensitizing semiconductors is deleterious because it introduces photoisomerization as an undesirable quenching mechanism.

6.6. Experimental

6.6.1. TPAC Syntheses

All commercially available reagents obtained from suppliers were used without further purification. Unless otherwise noted, all reactions were carried out under nitrogen with standard Schlenk techniques, and all glassware used in dry reactions were flame dried under high-vacuum prior to use. All organic extracts were dried over magnesium sulfate ($MgSO_4$) powder, and solvents were removed under reduced pressure with a rotary evaporator. Toluene, tetrahydrofuran (THF) and dimethylformamide (DMF) were purified and dried by passing

through two columns of neutral alumina under nitrogen prior to use. Flash chromatography was performed using Silicycle SiliaFlash ® P60 (particle size 40-63 μm, 230-400 mesh) silica gel.

All ^{1}H and ^{13}C NMR spectra were obtained in chloroform-*d*, unless otherwise noted, with a Bruker AVB-400, AV-500 or AV-600 instrument. ^{13}C spectra were measured with a proton-decoupling pulse program. All chemical shifts (ppm) were calibrated to the residual peak of the deuterated solvent. Data from high-resolution mass spectrometry (HRMS) using electrospray ionization(ESI) were obtained by the UC Berkeley mass spectrometry facility. Elemental analysis (CHN) was performed by the UC Berkeley microanalysis laboratory.

Ethyl 7-bromo-2-oxo-2H-chromene-3-carboxylate (**1**).

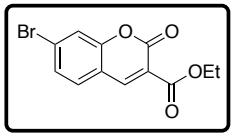

To an 8-dram vial, 4-bromo-2-hydroxybenzaldehyde (1.00 g, 4.98 mmol) was added to diethyl malonate (0.796 g, 4.98 mmol) under ambient conditions, and the resulting suspension was stirred for 10 min at rt. Piperidine (0.846 g, 9.95 mmol) was added to the reaction mixture drop-wise. The reaction mixture turned from orange to red, and yellow solid formed after ~1 eq. was added. The remaining piperidine was added, and reaction mixture was stirred at rt for 16 h. Concentrated HCl (6 mL, 12 M) was slowly added in a drop-wise fashion to the reaction mixture, which appeared as orange, viscous oil. Pink precipitates formed, and the suspension was vigorously stirred in conc. HCl for 1 h until the solid flakes were evenly suspended. Water was then added to the reaction mixture to fill up the vial, and the solid flakes turned from pink to off-white. The suspension was stirred at rt for 2.5 h and was filtered through a Buchner funnel to collect the solid. The crude material was passed through a plug of silica gel with dichloromethane as the eluent, and the product was obtained as a white, powder (463 mg, 31 %).

^{1}H NMR (400 MHz, $CDCl_3$), δ (ppm) = 8.48 (s, 1 H), 7.54 (ad, J = 0.4 Hz, 1 H), 7.47 (ad, J = 0.8 Hz, 2 H), 4.41 (q, J = 7.2 Hz, 2 H), 1.41 (t, J = 7.2 Hz, 3 H). ^{13}C (100 MHz, $CDCl_3$), δ (ppm) = 163.0, 156.0, 155.4, 148.0, 130.4, 129.0, 128.6, 120.3, 118.6, 116.0, 62.3, 14.4. HRMS (ESI, *m/z*): $[M]^+$ calcd for $C_{12}H_9O_4Br$ $[M]^+$: 295.9684; found, 295.9687.

Diethyl (7-bromo-2-oxo-2H-chromen-3-yl)phosphonate (**2**).

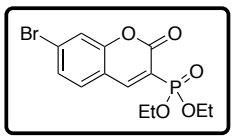

A dry 100mL RBF was charged with THF (35 mL) and CCl_4 (5 mL). To this flask, $TiCl_4$ (3.76 g, 19.8 mmol, 2.16 mL, 2 equiv.) was added at 0 °C dropwise via syringe, where upon addition generated an opaque yellow solution. A solution of 4-bromo-2-hydroxybenzaldehyde (2.0 g, 9.9 mmol, 1 equiv.) and triethyl phosphonoacetate (2.23 g, 9.9 mmol, 1.97 mL, 1 equiv.) in THF (5 mL) was then added dropwise. Lastly, a solution of pyridine (3.13 g, 39.6 mmol, 3.2 mL, 4 equiv.) in THF (7.5 mL) was slowly added, and the reaction was allowed to warm up to rt and stir overnight. Upon reaction completion, the mixture was quenched with H_2O (50mL). The aqueous layer was extracted three times with Et_2O, dried on Mg_2SO_4, and rotovapped to dryness. The residue was purified by SiO_2 column chromatography (3:97 MeOH:CH_2Cl_2) to obtain a clear solid (2.2 g, 6.09 mmol, 62% yield).

^{1}H NMR (600 MHz, $CDCl_3$): δ 8.44 (d, J = 16.8 Hz, 1H), 7.51 (s, 1H), 7.45-7.42 (m, 2H), 4.30-4.19 (m, 4H), 1.35 (t, J = 7.2 Hz, 6H). ^{13}C NMR (150 MHz, $CDCl_3$): δ 157.44, 157.34, 155.3, 152.5, 152.4, 130.1, 128.5, 128.4, 120.1, 116.8, 116.7, 63.5, 63.4, 16.32, 16.28. HRMS (ESI, *m/z*) calcd. for $C_{13}H_{15}BrO_5P$ $[M+H]^+$: 360.9835; found: 360.9847.

N,N-Diphenyl-4-(trimethylstannyl)aniline (**3**).

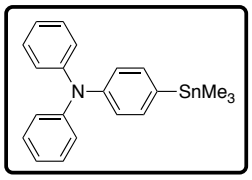

4-Bromotriphenylamine (500 mg, 1.54 mmol) was added to a 100 mL 3-neck flask and degassed with N_2. 30 mL of dry THF was added to the flask, and the resulting solution was cooled to -78 °C for 10 min. *n*BuLi (2.5 M in hexanes, 1.70 mmol, 0.680 mL) was added to the reaction mixture dropwise at -78 °C and then stirred at -78 °C for 1.5 h. Trimethyltin chloride (372 mg, 1.77 mmol) was added to the reaction mixture in one shot at -78 °C. The reaction mixture was stirred for 30 minutes before warming up to rt and stirring for 12 h. The reaction mixture was diluted with diethyl ether and washed with H_2O three times. The organic layer was dried over $MgSO_4$ and filtered. Removal of solvent under reduced pressure yielded the product as brown oil. The crude material was used in the subsequent reaction without further purification.

Ethyl 7-(4-(diphenylamino)phenyl)-2-oxo-2H-chromene-3-carboxylate (**4**).

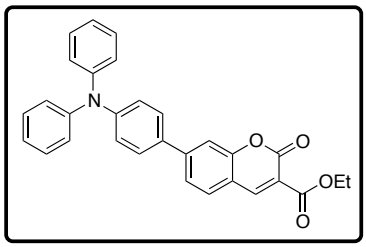

A 25-mL 3-neck flask connected to a condenser was charged with **1** (243 mg, 0.817 mmol), **2** (400 mg, 0.980 mmol), t*ris*(dibenzylideneacetone)dipalladium(0) ($Pd_2(dba)_3$, 2 mol%, 15.0 mg, 16.3 μmol) and tri(*o*-tolyl)phosphine (P(*o*-tol)$_3$, 8 mol%, 19.9 mg, 65.3 μmol), and degassed with N_2. Toluene (2.7 mL) and DMF (0.54 mL) were added to the flask, and the reaction mixture was immediately heated at 100 °C for 16 h. The reaction mixture was then cooled to rt and diluted with diethyl ether. The ether layer was washed with H_2O three times, dried over $MgSO_4$ and filtered. The crude mixture was purified by flash chromatography (silica gel, $CHCl_3$), and the product was recrystallized in absolute ethanol. The product was collected as yellow needles after vacuum filtration (1 crop, 230 mg, 61 %).

^{1}H NMR (600 MHz, $CDCl_3$), δ (ppm) = 8.55 (s, 1 H), 7.62 (d, *J* = 7.8 Hz, 1 H), 7.55 – 7.51 (m, 4 H), 7.30 (t, *J* = 8.1 Hz, 4 H), 7.16 – 7.13 (m, 6 H), 7.09 (t, *J* = 7.2 Hz, 2 H), 4.43 (q, *J* = 7.2 Hz, 2 H), 1.42 (t, *J* = 7.2 Hz, 3 H). ^{13}C (150 MHz, $CDCl_3$), δ (ppm) = 163.4, 157.1, 156.0, 149.2, 148.6, 147.3, 147.2, 131.5, 129.9, 129.6, 128.1, 125.3, 123.9, 123.2, 122.8, 117.2, 116.5, 113.9, 62.0, 14.4. HRMS (ESI, *m/z*) calcd. for $C_{30}H_{23}NO_4Na$ $[M+Na]^+$: 484.1519; found: 484.1521.

7-(4-(Diphenylamino)phenyl)-2-oxo-2H-chromene-3-carboxylic acid (**TPAC1**).

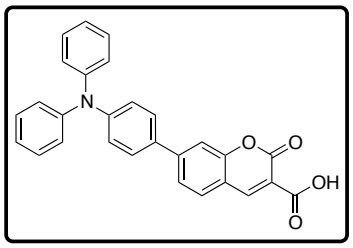

To a 100-mL RBF attached to a condenser, added **3** (200 mg, 0.434 mmol), lithium hydroxide monohydrate (911 mg, 21.7 mmol), absolute ethanol (22 mL) and distilled water (11 mL). The reaction mixture was heated at reflux for 2 h. The reaction mixture was then cooled to rt, acidified with 2M HCl to pH = 0 and diluted with chloroform. The reaction mixture was extracted with chloroform three times, and the organic layer was dried over $MgSO_4$ and filtered. The crude mixture was purified by recrystallized in absolute ethanol. The product was collected as small orange plates after vacuum filtration (1 crop, 130 mg, 69 %).

^{1}H NMR (500 MHz, $CDCl_3$), δ (ppm) = 12.29 (broad s, 1 H), 8.93 (s, 1 H), 7.76 (d, *J* = 8.5 Hz, 1 H), 7.68 (dd, *J* = 4.0 Hz, 1.5 Hz, 1 H), 7.64 (s, 1 H), 7.54 (d, *J* = 9.0 Hz, 2 H), 7.32 (t, *J* = 8.0 Hz, 4 H), 7.18 – 7.14 (m, 6 H), 7.12 (t, *J* = 7.5 Hz, 2 H). ^{13}C (150 MHz, $CDCl_3$), δ (ppm) = 164.6, 162.9, 155.5, 151.2, 149.7, 148.8, 147.1, 130.8, 130.6, 129.7, 128.3, 125.5, 124.4, 124.2, 122.5,

116.9, 114.0, 113.5. HRMS (ESI, *m/z*) calcd. for $C_{28}H_{18}NO_4$ $[M-H]^-$: 432.1241; found: 432.1234. Anal. calcd for $C_{28}H_{19}NO_4$: C, 77.59; H, 4.42; N, 3.23; found: C, 77.53; H, 4.50; N, 3.24.

Diethyl (7-(4-(diphenylamino)phenyl)-2-oxo-2H-chromen-3-yl)phosphonate (**5**).

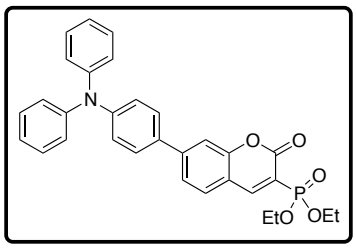

A dry 100 mL RBF was charged with *N*,*N*-diphenyl-4-(trimethylstannyl)aniline **2** (3.0 g, 7.40 mmol, 1.1 equiv.), coumarin phosphonate **3** (2.0 g, 6.73 mmol, 1 equiv.), $Pd_2(dba)_3$ (123 mg, 0.13 mmol, 2 mol%) and P(*o*-tolyl)$_3$ (164 mg, 0.54 mmol, 8 mol%). The flask was then evacuated and back-filled with nitrogen three times. Lastly, toluene (30 mL) and DMF (6 mL) were added to the flask and the reaction was allowed to stir at 110°C overnight. Upon completion, the reaction mixture was poured into H_2O (80 mL) and extracted three times with CH_2Cl_2. The organic layers were combined, dried on Mg_2SO_4 and rotovapped to dryness. The residue was purified by SiO_2 column chromatography (2:3 EtOAc:CH_2Cl_2) to obtain an orange-yellow solid (1.8 g, 3.43 mmol, 51% yield).

^{1}H NMR (300 MHz, $CDCl_3$): δ 8.52 (d, J = 17.1 Hz, 1H), 7.62-7.49 (m, 5H), 7.33-7.26 (m, 4H), 7.17-7.06 (m, 8H), 4.37-4.19 (m, 4H), 1.39 (t, J = 6.9 Hz, 6H). ^{13}C NMR (100 MHz, $CDCl_3$): δ 158.4, 158.2, 155.7, 153.0, 152.9, 148.7, 146.9, 146.7, 131.1, 129.4, 129.3, 127.8, 124.9, 123.6, 122.8, 122.5, 117.0, 116.2, 116.1, 115.1, 113.6, 63.2, 63.1, 16.24, 16.17. HRMS (ESI, *m/z*) calcd. for $C_{31}H_{29}NO_5P$ $[M+H]^+$: 526.1778; found: 526.1791.

(7-(4-(Diphenylamino)phenyl)-2-oxo-2H-chromen-3-yl)phosphonic acid (**TPAC2**).

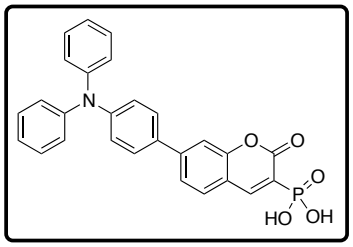

A dry 100 mL RBF was charged with compound **2** (300 mg, 0.57 mmol, 1 equiv.) and 20 mL of CH_2Cl_2. To this stirring solution, bromotrimethylsilane (523.6 mg, 3.42 mmol, 0.45 mL, 6 equiv.) was added dropwise via syringe at rt and allowed to stir overnight. Upon consumption of starting material, determined by thin layer chromatography, the mixture was rotovapped to dryness. The resultant orange residue was then solvated in MeOH, to which CH_2Cl_2 and petroleum ether were slowly added to precipitate a fluffy solid from solution. The solids were filtered off and washed with petroleum ether to provide a bright yellow solid (108 mg, 0.23 mmol, 40% yield).

^{1}H NMR (600 MHz, CD_3OD): δ 8.45 (d, J = 16.2 Hz, 1H), 7.76 (d, J = 8.4 Hz, 1H), 7.66-7.60 (m, 4H), 7.32-7.29 (m, 4H), 7.11-7.07 (m, 8H). ^{13}C NMR (150 MHz, $CDCl_3$): δ 160.8, 160.7, 157.0, 151.6, 151.5, 150.3, 148.7, 147.8, 133.1, 131.1, 130.6, 129.1, 126.2, 124.9, 124.1, 123.8, 121.3, 120.0, 118.1, 118.0, 114.5. HRMS (ESI, *m/z*) calcd. for $C_{27}H_{19}NO_5P$ $[M-H]^-$: 468.1006; found: 468.1011. Anal. calcd. for $C_{27}H_{20}NO_5P$ + H_2O: C, 66.53; H, 4.55; N, 2.87; found: C, 66.75; H, 4.50; N, 2.84.

(E)-4-(4-Bromostyryl)-N,N-diphenylaniline (6).

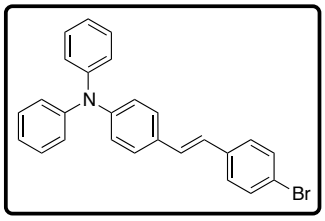

Synthesized according to reported procedures.[50]

(E)-N,N-Diphenyl-4-(4-(trimethylstannyl)styryl)aniline (**7**).

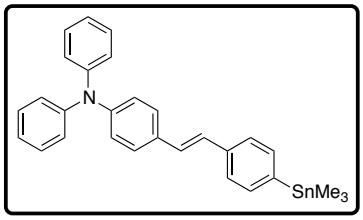

To a 50-mL 2-neck flask, added **6** (400 mg, 0.938 mmol) and degassed the content with N_2. Dry THF (15 mL) was added to the flask, and the resulting solution was cooled to -78 °C for 10 min. *n*BuLi (2.5 M in hexanes, 1.03 mmol, 0.41 mL) was added to the reaction mixture dropwise and stirred for 2 h at -78 °C. Trimethyltin chloride (215 mg, 1.08 mmol) was added to the reaction mixture at -78 °C. The reaction mixture was stirred for 15 minutes before warming up to rt and stirring for 1.5 h. The reaction mixture was diluted with diethyl ether and washed with H_2O three times. The organic layer was dried over $MgSO_4$ and filtered. Removal of solvent under reduced pressure yielded the product as yellow oil. The crude material was used in the subsequent reaction without further purification.

(E)-Ethyl 7-(4-(4-(diphenylamino)styryl)phenyl)-2-oxo-2H-chromene-3-carboxylate (**8**).

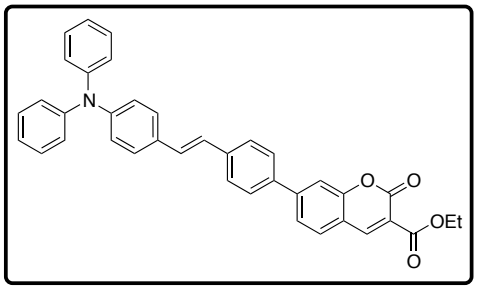

A 50-mL Schlenk tube was charged with **1** (232 mg, 0.782 mmol), **7** (478 mg, 0.938 mmol), Pd_2dba_3 (2 mol%, 14.3 mg, 15.6 μmol) and P(*o*-tol)$_3$ (8 mol%, 19.0 mg, 62.5 μmol), and degassed with N_2. Toluene (2.6 mL) and DMF (0.50 mL) were added to the flask, and the reaction mixture was immediately heated at 90 °C for 16 h. The reaction mixture was then cooled to rt and diluted with chloroform. The organic layer was washed with H_2O three times, dried over $MgSO_4$ and filtered. The crude mixture was purified by flash chromatography (silica gel, $CHCl_3$); the column was eluted with increasing solvent polarity: from $CHCl_3$ to 5 % acetone in $CHCl_3$ and then to 10 % acetone in $CHCl_3$. The product was dissolved in chloroform and recrystallized by layering with methanol. The product was collected as orange, plate-like crystals after vacuum filtration (1 crop, 361 mg, 82 %).

^{1}H NMR (600 MHz, $CDCl_3$), δ (ppm) = 8.56 (s, 1 H), 7.67 – 7.59 (m, 7 H), 7.41 (d, *J* = 9.0 Hz, 2 H), 7.27 (t, *J* = 8.4 Hz, 4 H), 7.15 (d, *J* = 16.8 Hz, 1 H), 7.12 (d, *J* = 7.8 Hz, 4 H), 7.07 – 7.02 (m, 5 H), 4.43 (q, *J* = 7.2 Hz, 2 H), 1.43 (t, *J* = 7.2 Hz, 3 H). ^{13}C (150 MHz, $CDCl_3$), δ (ppm) = 163.4, 157.0, 155.9, 148.5, 147.9, 147.6, 147.2, 138.8, 137.3, 131.1, 130.0, 129.7, 129.5, 127.7, 127.2, 126.0, 124.8, 123.6, 123.5, 123.4, 117.7, 116.9, 114.5, 62.1, 14.4. HRMS (ESI, *m/z*) calcd. for $C_{38}H_{30}NO_4$ $[M+H]^+$: 564.2169; found: 564.2172.

(E)-7-(4-(4-(Diphenylamino)styryl)phenyl)-2-oxo-2H-chromene-3-carboxylic acid (**TPAC3**).

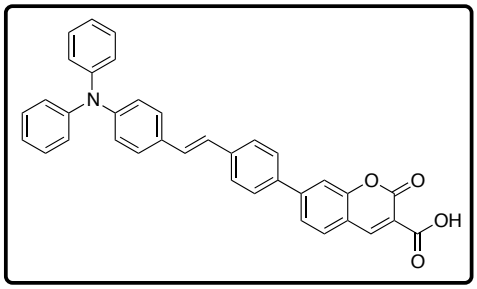

A 100-mL RBF attached to a condenser was charged with **8** (143 mg, 0.254 mmol), lithium hydroxide monohydrate (533 mg, 12.7 mmol), absolute ethanol (25 mL) and distilled water (6.3 mL). The reaction mixture was heated at reflux for 2 h and then cooled to rt. It was subsequently diluted with diethyl ether and extracted with 10 % NaOH solution three times. The aqueous layer was acidified with 2M HCl to pH = 0 and extracted with chloroform five times. The organic layer was dried over $MgSO_4$ and filtered. Removal of the solvent yielded an orange solid. The crude material was purified by recrystallization in $CHCl_3$/MeOH. The product was collected as red needles after vacuum filtration (1 crop, 54 mg, 40 %).

^{1}H NMR (600 MHz, $CDCl_3$), δ (ppm) = 12.27 (broad s, 1 H), 8.96 (s, 1 H), 7.80 (d, *J* = 7.8 Hz, 1 H), 7.74 (d, *J* = 7.8 Hz, 1 H), 7.72 (s, 1 H), 7.67 (d, *J* = 8.4 Hz, 2 H), 7.63 (d, *J* = 8.4 Hz, 2 H), 7.42 (d, *J* = 8.4 Hz, 2 H), 7.28 (t, *J* = 7.8 Hz, 4 H), 7.17 (d, *J* = 16.2 Hz, 1 H), 7.13 (d, *J* = 7.8 Hz, 4 H), 7.07 – 7.02 (m, 5 H). ^{13}C (MHz, $CDCl_3$), δ (ppm) = 164.5, 162.8, 155.4, 151.1, 148.8, 147.6, 139.4, 136.6, 130.9, 130.1, 129.5, 127.82, 127.75, 127.3, 125.7, 124.9, 123.5, 123.4, 117.4, 114.7, 114.1. HRMS (ESI, *m/z*) calcd. for $C_{36}H_{24}NO_4$ $[M-H]^-$: 534.1711; found: 534.1706. Anal. calcd for $C_{36}H_{25}NO_4$: C, 80.73; H, 4.70; N, 2.62; found: C, 80.45; H, 4.78; N, 2.64.

TiO_2 nanoparticles.

A 250-mL RBF containing a stir bar was charged with 100 mL MeOH (spectroscopic grade), 0.250 mL Nanopure water and anhydrous LiOH (2.63 mmol, 63 mg, Fisher Scientific, anhydrous LiOH powder was recrystallized from water and flame-dried under high vacuum at 100 mTorr). The mixture was sonicated (Branson 1210) for 2 h or until LiOH was completely dissolved. At room temperature, titania isopropoxide (1.823 mmol, 0.540 mL, 99.999%, Aldrich) was added dropwise to the LiOH solution. After final addition of the titania precursor, stirring was continued for an additional 3 min and then sonicated for an additional 10 min. Based on theoretical mass calculations, the crude reaction mixture had a concentration of 1.47 mg/mL (~10 mg/7mL). For a 90-nm anatase titania particle, footprint calculations yields 4.1×10^4 TPAC ligands/particle, and the molecular weight of these nanoparticles are calculated to be 9.4×10^8 g/mol based on unit cells.

Typical preparation for dye-TiO_2 conjugates.

A solution of **TPAC1** is first prepared. In a 1-dram vial, dissolved **TPAC1** (16.8 mg, 89 equiv, 433.45 mg/mmol) in 1.7 mL of 5:1 $CHCl_3$:MeOH mixture to make a 10 mg/mL solution. Seven 1 mL aliquots of TiO_2 nanoparticles were centrifuged at 8000 rpm for 5 min to collect 10 mg of the particles (microcentrifuge tubes, Molecular BioProducts, Cat#3444). The supernatant was removed, and the white pellets were resuspended in 400 μL of the **TPAC1** solution. The nanoparticle suspension was transferred to a 1-dram glass vial, sealed, and heated at 50 °C in an aluminum heating block. After 16 h, the vials were cooled to room temperature and divided the solution into 2 × 1.5 mL centrifuge tubes. To precipitate the nanoparticle conjugates, 400 μL of MeOH was added to each tube, and then the mixtures were centrifuged at 8000 rpm for 5 min. The supernatant was removed again, and the pellets resuspended in 400 μL MeOH/100 μL $CHCl_3$. Particles were then vortexed and sonicated for 1 min to disperse the particles evenly.

This washing procedure was repeated 4-5 times (with 400 μL MeOH/100 μL $CHCl_3$, and 450 μL MeOH/50 μL $CHCl_3$ for the last wash) until the supernatant became relatively colorless. After the final wash, each pellet was resuspended in 500 μL of $CHCl_3$, and two aliquots were combined and passed through a 0.45 μm PTFE syringe filter. This stock solution was diluted with $CHCl_3$ to an appropriate concentration for subsequent photophysical and Raman studies. If unused, the stock solution was stored at room temperature and in the dark.

*For the preparation of **TPAC2** conjugates.*
18.2 mg of **TPAC2** (89 equiv, 469.43 mg/mmol) was dissolved in 1.8 mL of 5:1 $CHCl_3$:MeOH mixture for 10 mg TiO_2. Unbound dye was removed by successive washing as described above. Here, 300 μL MeOH/200 μL $CHCl_3$ was used to clean the conjugates, except for the last wash, which used a mixture of 400 μL MeOH/100 μL $CHCl_3$. The **TPAC2** conjugates formed relatively large aggregates during the washes, and the final sample in $CHCl_3$ could not be filtered. The data were obtained with the washed but unfiltered conjugates.

*For the preparation of **TPAC3** conjugates.*
20.8 mg of **TPAC3** (89 equiv, 535.59 mg/mmol) was dissolved in 2.1 mL of 5:1 $CHCl_3$:MeOH mixture for 10 mg TiO_2. Here, 200 μL MeOH/300 μL $CHCl_3$ was used to remove unbound dye from the particle suspension. For the final wash, 300 μL MeOH/200 μL $CHCl_3$ was used before resuspending the final pellet in pure $CHCl_3$ and passed through a 0.45 μm PTFE syringe filter.

6.6.2. Femtosecond Stimulated Raman Spectroscopy.

FSRS measurements were carried out on samples of the **TPAC** dyes and their conjugates in CHCl3 with optical densities ranging from 0.45 to 2 per mm at 395 nm. The sample was agitated throughout the measurement in a 1 mm cuvette (Starna Cells, 21-G-1) using a small piece of stainless steel wire (diameter = 0.018 in.) as a stir bar inside the cuvette and a magnet attached to a dc motor as the actuator.

The FSRS instrument has been described in detail elsewhere.[51] Briefly, a regenerative Ti:sapphire amplifier (BMI, alpha/1000us) with a repetition rate of 1 kHz generates 900 μJ pulses at 790 nm with a duration of~60 fs. This beam is split to generate the three pulses necessary for FSRS. The actinic pulse (λ_{max} = 395 nm, 80−150 nJ/pulse) is generated by frequency doubling the laser fundamental in a 1 mm BBO crystal. The Raman pulse (λ_{max} = 790 nm, 10 cm−1 fwhm, 0.1−2 μJ/pulse) is generated by spectrally filtering the laser fundamental with a grating filter. The continuum probe pulse (830−940 nm, ~10 nJ/pulse) is generated by focusing a small portion of the laser fundamental into a 3 mm thick sapphire plate followed by compression in an F2 prism pair. The three pulses, all polarized parallel to the table, are focused in a planar noncollinear geometry into the sample using a 100 mm focal length achromatic doublet. Parallel polarization allowed for the highest signal-to-noise ratio. Because of the comparative nature of this study and the size of the nanoparticles used, rotational reorientation is not expected to significantly alter our results and conclusions. After passing through the sample, the actinic and Raman pulses are spatially filtered by an aperture, while the probe is recollimated with a 100 mm lens and dispersed by a spectrograph (Instruments SA, HR320) onto a front-illuminated CCD (Princeton Instruments, PIXIS 100F) synchronized to the amplifier such that each pulse can be recorded separately. Phase-locked chopping of the Raman pulse at half the repetition rate of the amplifier allows for collection of Raman spectra without

the need for a reference spectrum, as probe fluctuations are minimal (<1%) on a shot-to-shot basis. Timeresolved FSRS spectra were collected by varying the time delay between the actinic pulse and the Raman/probe pulse pair using a computer controlled delay stage (Melles Griot, Nanomotion II). Ground-state spectra are obtained by intermittently shuttering the actinic pump. Each reported spectrum is the average of 20,000−120,000 individual spectra (40,000−240,000 laser shots). Data collection is automated with LabVIEW.

Transient difference Raman spectra have had the ground state and solvent signals removed after being normalized using the 669 cm^{-1} peak of $CHCl_3$ as an internal reference to correct for both fluctuations in the Raman pump energy and the sample's transient absorption. The energy axis was calibrated using cyclohexane as a standard. The instrument response function (IRF) was measured using the optical Kerr effect between the actinic and probe pulses in $CHCl_3$ in the sample cell; a typical value for the IRF was 140 fs fwhm. Example measurements are presented in Figure 6-17.

For each experiment the instrument response function (IRF) was measured using a Kerr gating method. The actinic pump and Raman probe were aligned into the sample cell. An analyzer was placed after the collimating lens and adjusted to extinguish as many probe photons as possible, then the polarization of the actinic pump was set to 45° relative to the probe. When the pump and probe are overlapped in time, the nonlinear birefringence induced by the pump rotates the polarization of the probe increasing the intensity recorded after the analyzer. The delay between pump and probe was varied with a computerized delay state, and the dispersed probe photons were recorded on the CCD. Presented in Figure 6-17 are examples recorded in DMSO (left) and $CHCl_3$ (right). An advantage of this method is that the IRF is measured in the same sample cell and solvent used in the experiment.

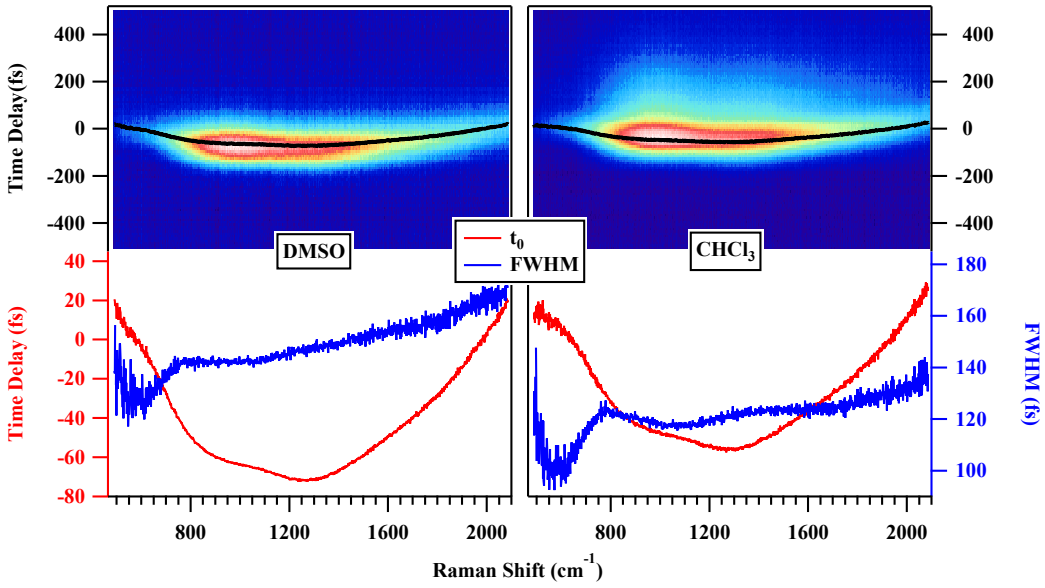

Figure 6-17. Representative examples of dispersed cross correlations measured in the sample cell in DMSO (left) and $CHCl_3$ (right). The contour plots shown at the top are the raw data, and the traces shown on the bottom are the extracted instrument response function parameters, the center (red) and the full width at half maximum (FWHM, blue). For the DMSO data the IRF at each pixel was modeled as a single Gaussian function. On the other hand, the $CHCl_3$ data was modeled as the sum of a Gaussian component, for the instantaneous electronic response, and an exponential decay component, for the impulsively excited vibrations. These data were taken on the same day, one after the other.

In the case of DMSO, the IRF at each pixel (i.e. vertical slice in Figure 6-17) can be accurately modeled as a Gaussian function indicating that the actinic pump is only interacting with the electronic degrees of freedom. On the other hand, for $CHCl_3$, the actinic pump can impulsively excite low frequency vibrational motions leading to an asymmetric IRF. This can be appropriately modeled by convoluting a Gaussian representing the IRF, with the sum of a delta function for the electronic component, and a decaying exponential for the vibrational component. Shown at the bottom of Figure S1 are the extracted widths and center positions of the per-pixel IRFs. The similarity between those recorded in DMSO, which only has an instantaneous electronic response, and $CHCl_3$, which has an additional slow vibrational response, indicates that the modeling detailed above is appropriate.

6.7. References

(1) Youngblood, W. J.; Lee, S.-H. A.; Maeda, K.; Mallouk, T. E. Acc. Chem. Res. 2009, 42, 1966.
(2) Hagfeldt, A.; Boschloo, G.; Sun, L.; Kloo, L.; Pettersson, H. Chem. Rev. 2010, 110, 6595.
(3) Gaal, D. A.; Hupp, J. T. J. Am. Chem. Soc. 2000, 122, 10956.
(4) Watson, D. F.; Meyer, G. J. Annu. Rev. Phys. Chem. 2005, 56, 119.
(5) Anderson, N. A.; Lian, T. Annu. Rev. Phys. Chem. 2005, 56, 491.
(6) Duncan, W. R.; Prezhdo, O. V. Annu. Rev. Phys. Chem. 2007, 58, 143.
(7) Schwarzburg, K.; Ernstorfer, R.; Felber, S.; Willig, F. Coord. Chem. Rev. 2004, 248, 1259.
(8) Myllyperkiö, P.; Manzoni, C.; Polli, D.; Cerullo, G.; KorppiTommola, J. J. Phys. Chem. C 2009, 113, 13985.
(9) Willig, F.; Zimmermann, C.; Ramakrishna, S.; Storck, W. Electrochim. Acta 2000, 45, 4565.
(10) Ziółek, M.; Tacchini, I.; Martínez, M. T.; Yang, X.; Sun, L.; Douhal, A.Phys. Chem. Chem. Phys. 2011, 13, 4032−4044.
(11) Ziółek, M.; Cohen, B.; Yang, X.; Sun, L.; Paulose, M.; Varghese, O. K.; Grimes, C. A.; Douhal, A. Phys. Chem. Chem. Phys. 2012, 14, 2816−2831.
(12) Wiberg, J.; Marinado, T.; Hagberg, D. P.; Sun, L.; Hagfeldt, A.; Albinsson, B. J. Phys. Chem. C 2009, 113, 3881−3886.
(13) Wiberg, J.; Marinado, T.; Hagberg, D. P.; Sun, L.; Hagfeldt, A.; Albinsson, B. J. Phys. Chem. B 2010, 114, 14358−14363.
(14) Li, R.; Lv, X.; Shi, D.; Zhou, D.; Cheng, Y.; Zhang, G.; Wang, P. J. Phys. Chem. C 2009, 113, 7469−7479.
(15) She, C.; Guo, J.; Irle, S.; Morokuma, K.; Mohler, D. L.; Zabri, H.; Odobel, F.; Youm, K.-T.; Liu, F.; Hupp, J. T.; Lian, T. J. Phys. Chem. A 2007, 111, 6832−6842.
(16) Ghosh, H. N.; Asbury, J. B.; Weng, Y.; Lian, T. J. Phys. Chem. B 1998, 102, 10208−10215.
(17) Mishra, A.; Fischer, M. K. R.; Bauerle, P. Angew. Chem., Int. Ed. 2009, 48, 2474−2499.
(18) Kukura, P.; McCamant, D. W.; Mathies, R. A. Annu. Rev. Phys. Chem. 2007, 58, 461−488.
(19) Fang, C.; Frontiera, R. R.; Tran, R.; Mathies, R. A. Nature 2009, 462, 200−204.
(20) Hoffman, D. P.; Mathies, R. A. Phys. Chem. Chem. Phys. 2012, 14, 6298−6306.
(21) Weigel, A.; Ernsting, N. P. J. Phys. Chem. B 2010, 114, 7879−7893.
(22) Frontiera, R. R.; Dasgupta, J.; Mathies, R. A. J. Am. Chem. Soc. 2009, 131, 15630−15632.
(23) Lockard, J. V.; Butler Ricks, A.; Co, D. T.; Wasielewski, M. R. J. Phys. Chem. Lett. 2010, 1, 215−218.

(24) Brown, K. E.; Veldkamp, B. S.; Co, D. T.; Wasielewski, M. R. J. Phys. Chem. Lett. 2012, 2362−2366.
(25) Jiang, X.; Yang, X.; Zhao, C.; Jin, K.; Sun, L. J. Phys. Chem. C 2007, 111, 9595−9602.
(26) Frisch, M. J.; Trucks, G. W.; Schlegel, H. B.; Scuseria, G. E.; Robb, M. A.; Cheeseman, J. R.; Scalmani, G.; Barone, V.; Mennucci, B.; Petersson, G. A.; Nakatsuji, H.; Caricato, M.; Li, X.; Hratchian, H. P.; Izmaylov, A. F.; Bloino, J.; Zheng, G.; Sonnenberg, J. L.; Hada, M.; Ehara, M.; Toyota, K.; Fukuda, R.; Hasegawa, J.; Ishida, M.; Nakajima, T.; Honda, Y.; Kitao, O.; Nakai, H.; Vreven, T.; Montgomery, Jr., J. A.; Peralta, J. E.; Ogliaro, F.; Bearpark, M.; Heyd, J. J.; Brothers, E.; Kudin, K. N.; Staroverov, V. N.; Kobayashi, R.; Normand, J.; Raghavachari, K.; Rendell, A.; Burant, J. C.; Iyengar, S. S.; Tomasi, J.; Cossi, M.; Rega, N.; Millam, J. M.; Klene, M.; Knox, J. E.; Cross, J. B.; Bakken, V.; Adamo, C.; Jaramillo, J.; Gomperts, R.; Stratmann, R. E.; Yazyev, O.; Austin, A. J.; Cammi, R.; Pomelli, C.; Ochterski, J. W.; Martin, R. L.; Morokuma, K.; Zakrzewski, V. G.; Voth, G. A.; Salvador, P.; Dannenberg, J. J.; Dapprich, S.; Daniels, A. D.; Farkas, Ö.; Foresman, J. B.; Ortiz, J. V.; Cioslowski, J.; Fox, D. J. Gaussian 09, Revision C.01.
(27) Yoshihara, T.; Katoh, R.; Furube, A.; Tamaki, Y.; Murai, M.; Hara, K.; Murata, S.; Arakawa, H.; Tachiya, M. J. Phys. Chem. B 2004, 108, 3817−3823.
(28) Tamaki, Y.; Furube, A.; Murai, M.; Hara, K.; Katoh, R.; Tachiya, M. Phys. Chem. Chem. Phys. 2007, 9, 1453−1460.
(29) Dasgupta, J.; Frontiera, R. R.; Taylor, K. C.; Lagarias, J. C.; Mathies, R. A. *Proceedings of the National Academy of Sciences* **2009**, *106*, 1784–1789.
(30) Fang, C.; Frontiera, R. R.; Tran, R.; Mathies, R. A. *Nature* **2009**, *462*, 200–204.
(31) Fujisawa, T.; Creelman, M.; Mathies, R. A. *J. Phys. Chem. B* **2012**.
(32) Hoffman, D. P.; Mathies, R. A. *Phys. Chem. Chem. Phys.* **2012**, *14*, 6298–6306.
(33) Kukura, P.; McCamant, D. W.; Yoon, S.; Wandschneider, D. B.; Mathies, R. A. *Science* **2005**, *310*, 1006–1009.
(34) Yoon, S.; Kukura, P.; Stuart, C. M.; Mathies, R. A. *Mol. Phys.* **2006**, *104*, 1275–1282.
(35) Kuramochi, H.; Takeuchi, S.; Tahara, T. *J. Phys. Chem. Lett.* **2012**, *3*, 2025–2029.
(36) Rhinehart, J. M.; Challa, J. R.; McCamant, D. W. *J. Phys. Chem. B* **2012**, *116*, 10522–10534.
(37) Huber, R.; Spörlein, S.; Moser, J. E.; Gratzel, M.; Wachtveitl, J. J. Phys. Chem. B 2000, 104, 8995−9003.
(38) Waldeck, D. H. Chem. Rev. 1991, 91, 415−436.
(39) Gegiou, D.; Muszkat, K. A.; Fischer, E. J. Am. Chem. Soc. 1968, 90, 12−18.
(40) Gegiou, D.; Muszkat, K. A.; Fischer, E. J. Am. Chem. Soc. 1968, 90, 3907−3918.
(41) Zuleta, M.; Edvinsson, T.; Yu, S.; Ahmadi, S.; Boschloo, G.; Göthelid, M.; Hagfeldt, A. Phys. Chem. Chem. Phys. 2012, 14, 10780−10788.
(42) El-Zohry, A.; Orthaber, A.; Zietz, B. J. Phys. Chem. C 2012, 116, 26144−26153.
(43) Lin, Y.-D.; Chow, T. J. J. Mater. Chem. 2011, 21, 14907−14916.
(44) Teng, C.; Yang, X.; Yang, C.; Li, S.; Cheng, M.; Hagfeldt, A.; Sun, L. J. Phys. Chem. C 2010, 114, 9101−9110.
(45) Hagberg, D. P.; Yum, J.-H.; Lee, H.; De Angelis, F.; Marinado, T.; Karlsson, K. M.; Humphry-Baker, R.; Sun, L.; Hagfeldt, A.; Grätzel, M.; Nazeeruddin, M. K. J. Am. Chem. Soc. 2008, 130, 6259−6266.
(46) Tian, H.; Yang, X.; Chen, R.; Zhang, R.; Hagfeldt, A.; Sun, L. J. Phys. Chem. C 2008, 112, 11023−11033.

(47) Tisdale, W. A.; Williams, K. J.; Timp, B. A.; Norris, D. J.; Aydil, E. S.; Zhu, X.-Y. Science 2010, 328, 1543−1547.
(48) Nozik, A. J. Annu. Rev. Phys. Chem. 2001, 52, 193−231.
(49) Shah, J. Ultrafast Spectroscopy of Semiconductors and Semiconductor Nanostructures; Springer: Berlin, 1996.
(50) Jiang, X.; Yang, X.; Zhao, C.; Jin, K.; Sun, L. *J. Phys. Chem. C* **2007**, *111*, 9595–9602.
(51) McCamant, D. W.; Kukura, P.; Yoon, S.; Mathies, R. A. Rev. Sci. Instrum. 2004, 75, 4971−4980.